TECHNISCHE UNIVERSITÄT MÜNCHEN

PHYSIK-DEPARTMENT

Lehrstuhl für Funktionelle Materialien (E13)

Forschungs-Neutronenquelle Heinz Maier-Leibnitz

Fission Gas Behaviour and Interdiffusion Layer Growth in in-pile and out-of-pile Irradiated U-Mo/Al Nuclear Fuels

Tobias Zweifel

Vollständiger Abdruck der von der Fakultät für Physik der Technischen Universität München zur Erlangung des akademischen Grades eines

Doktors der Naturwissenschaften (Dr. rer. nat.)

genehmigten Dissertation.

Vorsitzender:	Univ.Prof. Dr. Wilhelm Zwerger
Prüfer der Dissertation:	1. Univ.-Prof. Dr. Winfried Petry
	2. Prof. Olivier Tougait Université Lille Nord de France

Die Dissertation wurde am 04.11.2014 bei der Technischen Universität München

eingereicht und durch die Fakultät für Physik am 05.12.2014 angenommen.

TECHNISCHE UNIVERSITÄT
MÜNCHEN

PHYSIK-DEPARTMENT

FORSCHUNGS-NEUTRONENQUELLE
HEINZ MAIER-LEIBNITZ (FRM II)

FISSION GAS BEHAVIOUR AND INTERDIFFUSION LAYER GROWTH IN IN-PILE AND OUT-OF-PILE IRRADIATED U-MO/AL NUCLEAR FUELS

Bei der Fakultät Physik der Technischen Universität München
eingereichte Abhandlung zur Erlangung der Würde
eines Doktors der Naturwissenschaften (Dr. rer. nat.)

vorgelegt von

Tobias Zweifel

Lehrstuhl für Funktionelle Materialien E13

Contents

Contents 3

Abstract 7

Abstract (German) 9

1. Introduction 11
1.1. The "Forschungs-Neutronenquelle Heinz Maier-Leibnitz" - FRM II 11
1.2. Research reactor fuel conversion 13
1.3. General fuel plate manufacturing and prior test irradiations 14
1.4. Objectives of this thesis 17

I. Scientific background 19

2. Uranium metallurgy 21
2.1. The principle of uranium fission 21
2.2. α- , β- , and γ - phase uranium 23
2.3. Uranium - Molybdenum alloys 25
2.3.1. U-Mo phase diagram 26

3. The Interdiffusion Layer - (IDL) 29
3.1. Radiation damage in metals 29
3.1.1. Energy loss theory 30
3.2. IDL growth during in-pile test irradiations 35
3.2.1. IDL recrystallisation 36
3.2.2. Diffusion couple experiments 37
3.2.3. Out-of-pile irradiation experiments: Heavy ion irradiation 37
3.3. Methods to remedy or suppress IDL growth 38

4. Fission gas behaviour 41
4.1. Bubble growth mechanism 41
4.1.1. General mechanics 41
4.1.2. Growth equation 44
4.1.3. Influence of stress 46
4.1.4. Dislocation loop punching 47

4.2. Gas bubble observation after prior test irradiations . . . 49
4.2.1. PIEs on in-pile irradiated U-Mo fuel . . . 49
4.2.2. Kr implantation into thermally annealed U-Mo/Al compounds . . . 50

5. Utilized techniques for sample analysis 55
5.1. Scanning electron microscopy (SEM) . . . 55
5.2. Electron probe micro analysis - EPMA . . . 58
5.3. Focussed ion beam milling - FIB . . . 58
5.4. Transmission electron microscopy - TEM . . . 59
5.5. X-ray diffraction - XRD . . . 61
5.5.1. XRD data analysis - Rietveld method . . . 63
5.6. Secondary ion mass spectrometry - SIMS . . . 65

II. Thermal treatments on IRIS4 fuel samples 67

6. IRIS4 fuel manufacturing and in-pile irradiation 69
6.1. Fuel manufacturing . . . 69
6.2. Fresh fuel characterisation . . . 70
6.3. In-pile irradiation . . . 72
6.4. Post irradiation examinations . . . 73

7. Thermal Treatments on IRIS4 fuel 77
7.1. Sample preparation for thermal treatments . . . 77
7.2. Thermal treatment setup and fission gas release monitoring . . . 77
7.3. Thermal treatment curves . . . 79
7.4. Post-ThT examinations . . . 82
7.5. Results on ThT500 . . . 83
7.5.1. EPMA SE . . . 83
7.5.2. EPMA elemental mapping . . . 84
7.5.3. XRD . . . 87
7.6. Results on ThT670 . . . 90
7.6.1. EPMA SE . . . 90
7.6.2. EPMA elemental mapping . . . 91
7.7. Discussion . . . 98
7.7.1. Temperature dependent microstructural evolution . . . 98
7.8. Conclusions about thermal treatments . . . 103
7.9. Outlook . . . 103

III. Ion bombardment on monolithic U-Mo/Al layer systems 105

8. Manufacturing and irradiation of monolithic U-Mo layers 107
8.1. Sample manufacturing of monolithic layers . . . 107
8.1.1. PVD sputtering technique . . . 107
8.1.2. U-Mo layer thicknesses . . . 109
8.2. Heavy ion irradiation conditions . . . 111
8.2.1. The MLL Tandem accelerator . . . 111
8.2.2. Experimental setup . . . 115
8.2.3. Irradiation parameters . . . 116

9. Evaluation of heavy ion irradiation 119
9.1. SEM examinations . . . 119
9.1.1. Influence of irradiation temperature . . . 120
9.1.2. Influence of particle flux . . . 121
9.1.3. Comparison with previous in-pile irradiations . . . 121
9.2. TEM analysis . . . 125
9.3. High energy nano-XRD analysis . . . 128
9.4. Comparison of TEM and nano-XRD analyses . . . 129
9.5. Comparison with in-pile data . . . 131
9.5.1. Possible future experiments with heavy ions . . . 131

10. Kr implantation into heavy ion irradiated U-Mo/Al systems 133
10.1. Preliminary SRIM simulations . . . 133
10.2. The GANIL implantation facility . . . 135
10.2.1. Acceleration mechanism . . . 135
10.2.2. Implantation parameters . . . 135
10.3. SEM analyses . . . 137
10.4. SIMS measurements . . . 137
10.5. Comparison between Iodine and Krypton irradiation . . . 142
10.6. Comparison with other recent heavy ion irradiation studies . . . 143
10.7. Comparison with in-pile irradiated layer systems . . . 144
10.8. Comparison with IRIS4 experiment . . . 144
10.9. Conclusion . . . 146

IV. Summary 147

11. Summary of results 149
11.1. Atomized U-Mo powder . . . 149
11.2. Monolithic U-Mo/Al . . . 150
11.3. Comparison . . . 151
11.4. Conclusion . . . 151

12. Outlook 153

V. Appendices **155**

A. JNM article of SELENIUM particles analysed with high energy XRD **183**

B. Restart of MLL Tandem accelerator after spark **193**

C. Heavy ion irradiation setup and beam adjustment procedures **196**

D. TEM diffraction pattern evaluation **201**

E. XRD diffraction pattern analysis **204**

F. Sample polishing **207**

Abstract

Worldwide, highly enriched ^{235}uranium fuels are used in high performance research and test reactors in order to provide these facilities' high neutron fluxes. In a common global effort to minimize proliferation risks, the usage of highly enriched uranium (abbr. HEU) in civil nuclear fuel is envisaged to be substituted by low enriched uranium fuels (abbr. LEU). As the scientific quality of research and test reactors should not be reduced, i.e. the high neutron fluxes should be maintained, a new type of high density fuel is being developed at the moment. The alloy of uranium-molybdenum (abbr. U-Mo) is a prospective candidate of such a new fuel type. However, past test irradiations in material test reactors showed an insufficient irradiation behaviour of this new fuel under the conditions of high performance research reactors. Main reason for this irradiation performance is the growth of an interdiffusion layer (abbr. IDL) between the U-Mo fuel and its surrounding aluminium matrix. Due to this IDL generation, together with the accumulation of fission gases inside this layer, the test irradiations had to be stopped before the targeted final burn-up could be reached, as the fuel plates showed abnormal swelling behaviour at higher burnups.
This work is focussed on the study of two objectives: First, in-pile irradiated IRIS4 fuel samples were exposed to thermal treatment tests up to 1800°C to indentify temperature points where peak fission gas release from the samples occurred. These points could be determined to 500°C and 670°C respectively. Two successive treatments were performed until these two points in order to study the microstructural evolution of the IRIS4 fuel under these thermal conditions. It is shown that strong microstructural changes in the fuel occur at these two temperatures which strongly enhance fission gas precipitation.
Second, IDLs are generated in monolithic U-Mo/Al layer systems by the method of heavy ion irradiation. These out-of-pile created IDLs are very similar to the ones obtained after in-pile irradiation. Main focus of this part is to perform a systematic study of heavy ion generated IDLs with focus on the temperature and flux dependent IDL growth. As a next step, inert gas is further implanted into these IDLs. A comparative study is made between IDL and fission gas behaviour inside IDLs grown by heavy ion irradiation and in-pile irradiation.
Using scanning electron microscopy (SEM), transmission electron microscopy (TEM), x-ray diffraction (XRD), secondary ion mass spectrometry (SIMS) and electron probe microstructural analysis (EPMA), it is shown that the out-of-pile sample preparation techniques can very well be compared to the effects which occur during in-pile irradiation. Therefore, the presented methods offer an excellent possibility to predict the respective aspects of the fuel's behaviour during in-reactor irradiation, which enables a fuel pre-qualification process. These out-of-pile techniques provide a quick and time-efficient study

of the envisaged fuel solutions, as no further sample activation is caused by these out-of-pile techniques.

Abstract (German)

Weltweit verwenden viele Forschungs- und Testreaktoren Brennstoffe mit einem hohen Gehalt an ^{235}Uran. Grund für die hohe Anreicherung ist der erfordliche hohe Neutronenfluß dieser Einrichtungen. Ein gemeinsames internationales Projekt zielt darauf ab das Proliferationsrisiko zu minimieren, indem die Verwendung von hoch angereichertem Uran (Abk. HEU) in zivilen Brennstoffen minimiert und weitesgehend durch niedrig angereichertes Uran (Abk. LEU) ersetzt wird. Dadurch ist es nötig neue Brennstoffe zu entwickeln, die mit einem reduzierten ^{235}Urangehalt die Performance des Reaktors erhalten. Ein vielversprechender neuer, hochdichter Brennstoff besteht aus einer Legierung aus Uran und Molybdän (Abk. U-Mo). Allerdings zeigten in den vergangenen Jahren Testbestrahlungen dieses Brennstoffs ein unbefriedigendes Bestrahlungsverhalten unter den hohen Ansprüchen von Test- und Forschungsreaktoren. Hauptgrund hierfür ist die Entstehung einer Interdiffusionsschicht (Abk. IDL) zwischen dem U-Mo Brennstoff und der umgebenden Aluminium-Matrix. Diese Schicht akkumuliert die entstehenden Spaltgase, wodurch ein abnormales Schwellen des Brennstoffes beobachtet wird. Deshalb mussten die Testbestrahlungen angehalten werden, bevor der geplante finale Abbrand erreicht war.
In dieser Arbeit werden zwei Ziele verfolgt: Zuerst wurden Untersuchungen an bereits bestrahlten IRIS4 Proben unternommen. Dabei wurden die Proben bis zu einer Temperatur von 1800°C in einem Induktionsofen erhitzt. Ziel dieser Messung war es die markanten Temperaturbereiche zu identifizieren, bei denen ein massiver Ausstoß von Spaltgasen stattfindet. Zwei solche Ausstöße konnten bei 500°C und 670°C beobachtet werden. Daher wurden in einem folgenden Schritt weitere Proben bis zu diesen zwei Temperaturen erhitzt. Das Ziel hierbei war es die Evolution der Probenmikrostruktur zu analysieren, die zu einem solchen Ausstoß geführt hatte.
Der zweite Teil dieser Arbeit beschäftigt sich mit Schwerionenbestrahlung von monolithischen U-Mo/Al Schichtsystemen. In der Vergangenheit konnte bereits demonstriert werden, dass diese Methode ebenfalls zur Entstehung einer IDL führt, deren physikalische Eigenschaften sehr gut mit denen von IDLs verglichen werden können, die man nach einer in-pile Bestrahlung erhält. Das besondere Augenmerk wurde sowohl auf das temperaturabhängige, als auch auf das teilchenflußabhängige IDL Wachstum während einer Schwerionenbestrahlung gelegt. In einem folgenden Schritt wurde das Edelgas Kr in diese U-Mo/IDL/Al Schichtsysteme implantiert. Es wurde untersucht, inwiefern die Ergebnisse beider Bestrahlungtechniken betreffend IDL und Edelgasverhalten tatsächlich mit einer in-pile Bestrahlung verglichen werden können.
Zu den verwendeten Analysemethoden zählen Rasterelektronenmikroskopie (engl. SEM), Transmissionselektronenmikroskopie (TEM), Röntgendiffraktion (engl. XRD), sekundäre

Ionen Massenspektrometrie (SIMS) und Elektronenstrahlmikroanalyse (engl. EPMA). Es wird gezeigt, dass die Kombination aus Schwerionenbestrahlung und Edelgasimplantation in der Tat sehr gut zu vergleichen ist mit den Resultaten, die man während einer Reaktorbestrahlung erhält. Deshalb bilden die verwendeten Herstellungsmethoden eine sehr gute Möglichkeit Vorhersagen über die möglichen Ergebnisse einer Reaktorbestrahlung zu treffen. Dadurch ist es möglich eine Vorauswahl möglicher Brennstoffe zu treffen, bevor eine in-pile Bestrahlung durchgeführt wird. Da diese Herstellungsmethoden im Verhältnis zu Testbestrahlungen kosteneffizient sind und schnell Ergebnisse liefern können, bieten sie eine gute Option zur effizienten Forschung am neuen Brennstoff.

1. Introduction

Research and test reactors worldwide provide neutrons for a wide range of applications. Among them are experimental research on material analysis, industrial material preparation and medical applications. While nuclear power plants aim to produce electrical energy, the idea of research reactors is to produce a high neutron flux. This requires a different reactor core design. Therefore, the used kind of nuclear fuel is different. Nowadays, most nuclear power plants are operated on the basis of only slightly enriched ceramic UO_2 fuel, while research reactors usually require a significantly higher amount of the fissible ^{235}uranium in order to provide the desired high neutron flux with a reasonable reactor power. One of the newest high performance research reactors is the "Forschungs-Neutronenquelle Heinz Maier-Leibnitz" (FRM II) located in Garching near Munich, Germany.

1.1. The "Forschungs-Neutronenquelle Heinz Maier-Leibnitz" - FRM II

The FRM II neutron source provides an undisturbed thermal neutron flux of up to $8 \cdot 10^{14}\,{}^{\text{neutrons}}/_{\text{s}\cdot\text{cm}^2}$ while exhibiting a thermal power of only 20 MW [1]. The ratio of neutron flux to thermal power is the highest in the world. FRM II's reactor concept is mainly inspired by the reactors situated at the "Institute Laue-Langevin" (ILL) in Grenoble, France and the "High Flux Isotope Reactor" (HFIR) in Oak Ridge, USA.

The reactor design consists of a compact reactor core with only one single fuel element (see fig. 1.1). This fuel element has a cylindrical shape with an inner diameter of 118 mm, an outer diameter of 243 mm and an active height of 700 mm. Inside the fuel element, 113 involute curved plates contain the fuel (see fig. 1.2). The array of involute curved plates ensures a consistent, homogeneous cooling of the whole fuel element by light water, while heavy water is used as a reflector. The control rod moves inside the inner diameter of the fuel element.

In order to achieve the aforementioned high neutron flux to power ratio, a high ^{235}U density is needed in a small space, which is achieved by a combination of a high chemical uranium density and an enrichment of 93 weight percent (abbr. wt%). The uranium is present in an intermetallic compound with silicide (U_3Si_2), which is manufactured in

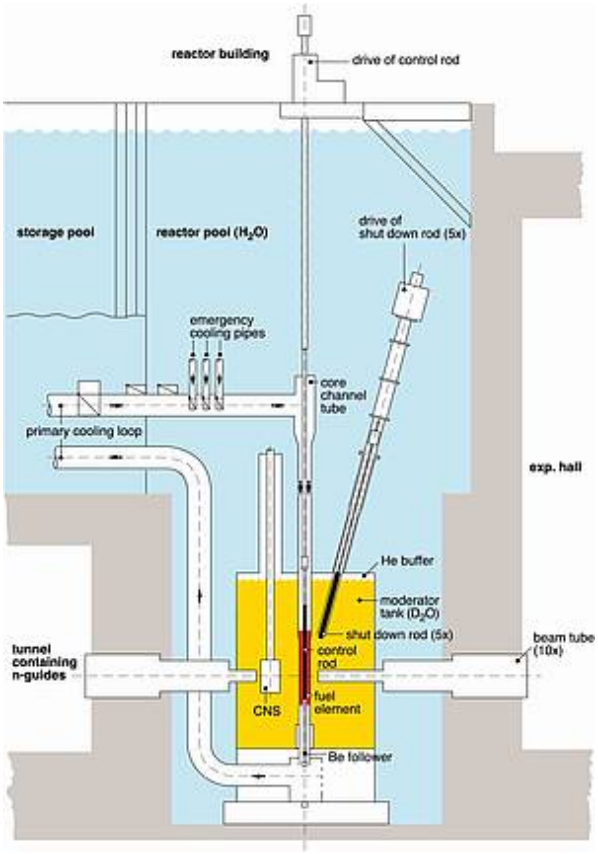

Figure 1.1.: *Cross-section view of FRM II's reactor [1].*

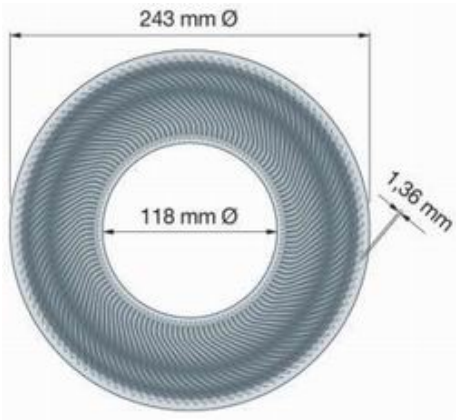

Figure 1.2.: *Sketch of FRM II's fuel element [1].*

ground powder form and later dispersed in an aluminium matrix. This material is referred to as the "meat". To prevent emission of fission products into the surrounding cooling water, the meat is further enclosed by an AlFeNi cladding. The uranium density inside the fuel element is $3.0\,{}^{g}/_{cm^3}$ in the region closer to the control rod and $1.5\,{}^{g}/_{cm^3}$ in the outer region near the reflecting heavy water. In total, 8.1 kg of uranium are inside a fuel element. After a reactor cycle of 60 days, a maximum fission density of $1.98 \cdot 10^{21}\,{}^{\text{fissions}}/_{cm^3}$ in the meat is reached [3, 4].

1.2. Research reactor fuel conversion

To support the global non-proliferation efforts, FRM II shows a unique commitment for conversion to lower enrichment in its nuclear operation license by operating its own scientific working group for reactor conversion. This is in close collaboration with international partners, e.g. the members of the "reduced enrichment for research and test reactors" program (RERTR) which was launched in 1978. As a requirement for conversion, the scientific quality of these facilites must be maintained which means that only a marginal loss in the provided high neutron fluxes may occur with lower enriched fuels.
The possible uranium enrichment in order to maintain these neutron fluxes is mainly determined by the reactor design and the available fuel density. In the case of FRM II, recent calculations have shown that the uranium density in dispersed U-Mo fuel has to be at least $8.0\,{}^{g}/_{cm^3}$ in order to provide operation with medium enriched uranium (MEU) fuel in the current core geometry [3]. As a consequence, the fuel must exhibit a significantly higher uranium density compared to what is currently reached with dispersed fuels. The first idea would be to increase the amount of U_3Si_2 particles inside the matrix. However, currently the technical limit of particle packing density increase is reached at 55 volume percent (abbr. vol%) which is equal to a uranium loading inside U_3Si_2 of $6.0\,{}^{g}/_{cm^3}$ [5] . However, the qualified limit for technical operation is $4.9\,{}^{g}/_{cm^3}$ which is below the required value of $6.5\,{}^{g}/_{cm^3}$.
Therefore, in order to reach the required uranium density, a new kind of high density fuel has to be developed. For metallurgic reasons (see chapter 2.2), utilizing pure uranium is not an option. Instead, an alloy of uranium and molybdenum (abbr. U-Mo) is at the moment the most prospective candidate [6]. However, until now, all test irradiations with this dispersed fuel targeting the conditions inside a high performance research reactor did not show the desired fuel performance. Main reason for this failure is the growth of an interaction layer (abbr. IDL) between the fuel and its surrounding aluminium matrix. The accumulation of fission gases in the IDL finally leads to an unacceptable swelling of the fuel at high fission rates, and several test irradiations had to be stopped even before the final envisaged burnup has been reached. Recent fuel manufacturing techniques, i.e. U-Mo particle coating and matrix modifications, proofed very efficient in delaying IDL formation. However, at high burnup, an accelerated plate swelling together with an IDL growth can still be observed. Main reason for this second swelling is the U-Mo particle

deformation leading to a coating failure in combination with enhanced matrix hardening by fission product implantation. In the framework of the HERACLES program, these two swelling factors are to be studied in detail.

1.3. General fuel plate manufacturing and prior test irradiations

A full-size fuel plate consists of the following components:

- For the **fuel** itself, two main concepts were approached: either U-Mo powders or monolithic U-Mo layers. Regarding U-Mo powder, two different options were persued, namely ground powder and atomized powder. While atomized powder production may provide spherical U-Mo particles with a diameter ranging from 50 to 150μm [36], ground powder production leads to irregular particle shapes [40]. In the monolithic case, a several 100μm thick U-Mo bulk material is used as meat [37].

- In the case of U-Mo powder, the particles have to be further embedded in a **matrix**. Just like in the case of the currently used U_3Si_2 fuel, the matrix consists mainly of aluminium. Most important task of the matrix is to guarantee thermal contact between the particles and the cladding. The usage of a matrix is therefore not necessary in the monolithic case due to the fact that the fuel is in direct contact with the plates' enclosing elements.

- Together, the fuel particles and the matrix form the **meat** of a fuel plate. This meat is futher enclosed by a **cladding** on top and bottom and by a **frame** in the meat's circumference. Both cladding and frame are a mandatory part as they prevent fission products from entering the primary cooling loop.

- As explained in more detail in chapter 3.3, additional manufacturing steps are necessary to improve the in-pile irradiation performance. It has been shown that both U-Mo particle coating (i.e. by Zr), and the addition of another element (i.e. Si) to the matrix proofed beneficial for in-pile performance [41].

- In the framework of the HERACLES' fuel development group, it is envisaged to pre-anneal the U-Mo before in-pile irradiation is carried out. This thermal treatment is aimed to mitigate microstructural defects inside the U-Mo to enable a better irradiation behaviour.

Tab. 1.1 summarizes several exemplary irradiation conditions and plate characteristics of both powder and monolithic U-Mo fuel plates. The according references in tab. 1.1 may provide lacking information.

Irradiation name	Year	Fuel/matrix type (values in wt%)	Loading (gU/cm^3)	Reactor	Final fission density (10^{21} f/cm^3)	LEU Equivalent burnup (% ^{235}U)	Cladding temperature (°C)	Heat flux (W/cm^2)
UMUS [32]	1999	ground U(7-9)Mo / pure Al	8	HFR	not reported (fuel plate failure)	20	110	250
IRIS 1 [33]	1999	ground U(7-9)Mo / pure Al	8	OSIRIS	4.5	67.5	74	145
IRIS 2 [34]	2001	atomized U7Mo / pure Al	8.3	OSIRIS	2.9	40	93	238
FUTURE [35]	2002	atomized U7Mo / pure Al	8.5	BR2	1.41	33	130	340
IRIS 3 [36]	2005	atomized U7Mo / Al(0.3 or 2.1)Si	8	OSIRIS	2.8 (Al(0.3)Si) 3.9 (Al(2.1)Si)	40.2 (Al(0.3)Si) 56.5 (Al(2.1)Si)	83	200
RERTR-6 [37, 38]	2005	monolithic U(7-10)Mo	≈ 17	ATR	2.8 - 3.9	35-49	<200	140 - 170
RERTR-7A [39]	2006	monolithic U10Mo	17	ATR	0.3 - 4.0	3-28	120	130 - 300
RERTR-7B [39]	2006	dispersed U7Mo/ Al(2.1)So	≈ 6	ATR	0.3-0.6	4-8	90 - 120 [64]	190 - 230
IRIS-TUM [40]	2008	ground U8Mo / pure Al or Al(2.1)Si	8	OSIRIS	5.9	88	98	260
IRIS4 (this work)	2010	atomized U7Mo pure Al or Al(2.1)Si	8	OSIRIS	3.3	55	100	260 - 270
E-FUTURE [41]	2010	atomized U7Mo / Al(4 or 6)Si	8	BR2	5.54	71	130	472
E-FUTURE II [42]	2011	atomized U7Mo / Al(6 or 12)Si	8	BR2	5.54	71	130	472
SELENIUM [43]	2012	atomized U7Mo pure Al	8	BR2	2.5	70	130	470

Table 1.1.: *Overview of selected previous in-pile test irradiations on ground and atomized U-Mo dispersion fuel, as well as for monolithic fuel, showing the evolution of fuel manufacturing and irradiation history over the years. Final fission density, burnup, temperature and heat flux values are given for maximum flux planes (MFP). In some cases, an additional element was added to the matrix to improve irradiation performance. The IRIS4 irradiation campaign is described in greater detail in chapter 6.2.*

Some of the test irradiations shown in tab. 1.1 were stopped at the indicated fission densities/burn-up when excessive, i.e. abnormal, fuel plate swelling was detected (see fig. 1.3). A cross-section examination of the irradiated plates showed the microstructural effects of this excessive swelling behaviour. An example case is seen in the IRIS2 experiment. In the according cross-section shown in fig. 1.4 - A, a so-called "break-away swelling" is clearly visible at the high flux region where the fuel matrix shows strong disbandment. Exemplary images on all three fuel kinds (dispersed and atomized powder, monolithic layer) were taken at 50% burn-up regions and are shown in fig. 1.4 - B to - D.

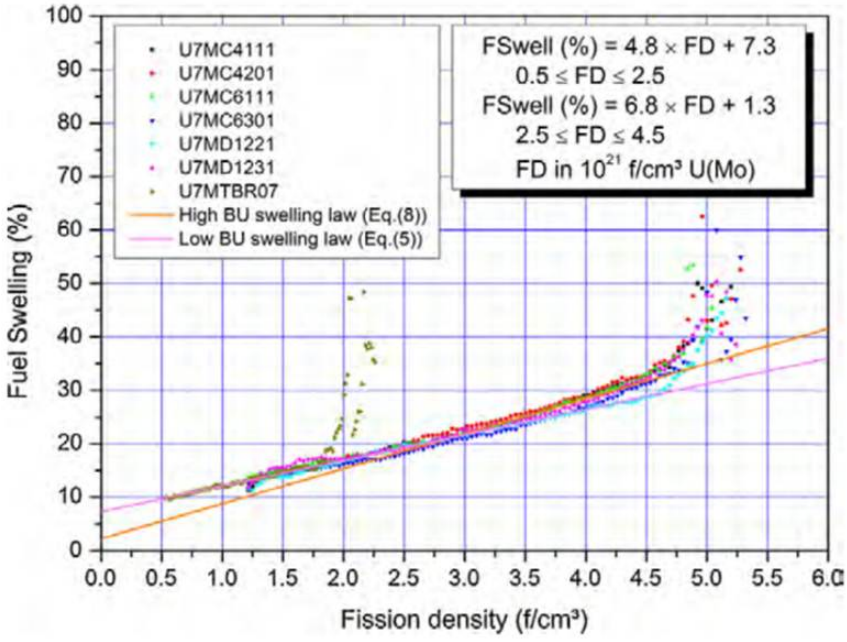

Figure 1.3.: *Exemplary fuel plate swelling curves for the E-FUTURE (left branches) and the SELENIUM (right branches) irradiation tests (see also tab. 1.1) [44]. In the E-FUTURE campaign, abnormal swelling started at around* $1.75 \cdot 10^{21}\,\mathrm{f/cm^3}$*, whereas in the SELENIUM campaign this swelling onset is delayed until* $4.5 \cdot 10^{21}\,\mathrm{f/cm^3}$.

Indeed, all three fuel kinds show the same signs made responsible for fuel plate swelling: the growth of an interdiffusion layer (abbr. IDL) between the U-Mo and the surrounding material (see also fig. 1.4 - B to - D), as well as the growth of large porosities during irradiation in which fission gases accumulate to form large bubbles. These in turn induce further pressure on the fuel. Bubbles are visible both inside the particles as well as at the U-Mo/IDL and IDL/matrix interfaces. In the later cases these bubbles seem to be larger in diameter as in the particles (see red circles in fig. 1.4 - B to - D). Both reasons for plate failure are explained seperately in chapters 3 and 4.

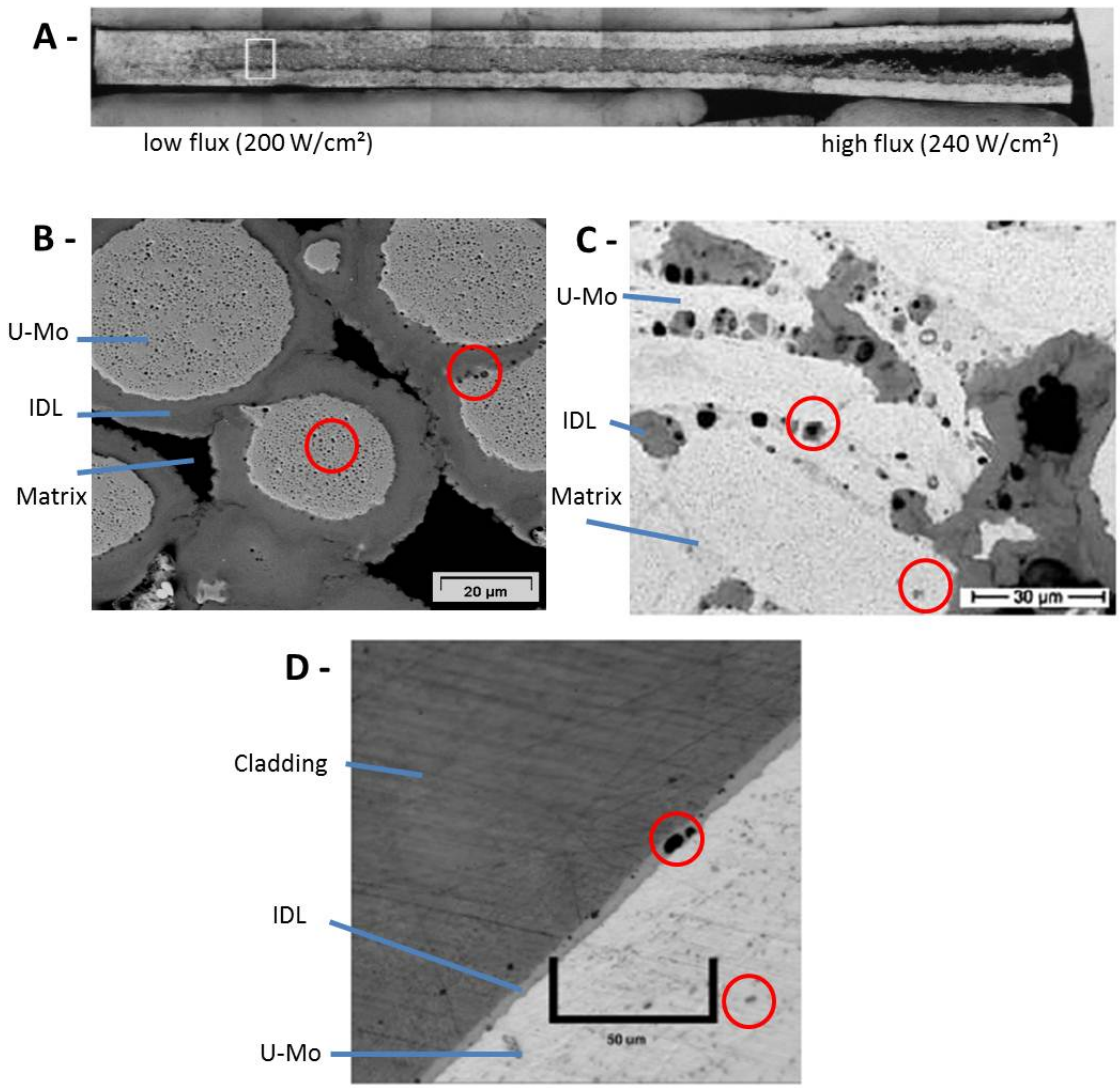

Figure 1.4.: *(A-) cross-section overview of an irradiated IRIS2 fuel plate [34]. At high flux regions, the matrix shows strong evidence of disbandment. Further SEM investigations on the fuel microstructures are shown for (B-) atomized powder [54], (C-) ground powder [40] and (D-) monolithic layers [37]. All images were taken in 50% burn-up regions. In all cases an IDL has been generated during irradiation between the U-Mo and the surrounding matrix/cladding. Moreover, in all cases excessive porosity formation is visible both in the particles and in the IDL (indicated by red circles).*

1.4. Objectives of this thesis

FRM II and the French "commissariat a l'energie atomique et aux energies alternatives" (CEA) developed a strong collaboration during the past years in order to investigate fuel behaviour on a common basis. Together, analyses on both in-pile and out-of-pile samples can be realised. Hence during this thesis, both kinds of irradiated samples were examined:

- For in-pile irradiated, dispersed U-Mo powder (IRIS4 campaign) measurements were performed at CEA. Aim of this study was to observe temperature dependent microstructural changes in irradiated fuel samples. Therefore, in total three IRIS4 fuel samples were exposed to thermal treatments. The first "thermal run" was carried out up to 1800°C in order to observe the main peaks in temperature of fission gas release. Two prominent release peaks were located at 500°C and 670°C. Thus, the two other samples were heated up to these two final temperatures in order to study the microstructure at these two temperatures and to conclude its effect on fission gas behaviour.

- Monolithic U-Mo/Al layer systems were irradiated out-of-pile by both heavy Iodine ions and Krypton ions. These two irradiation/implantation experiments were performed at the MLL Tandem in Garching near Munich, Germany and at GANIL in Caen, France. For Iodine irradiation, the main focus was to observe the IDL growth dependence on both irradiation temperature and particle flux, while Kr implantation was carried out to observe inert gas behaviour inside these created U-Mo/IDL/Al layer systems.

- Both approaches on in-pile irradiated IRIS4 fuel and out-of-pile particle bombarded U-Mo/Al layer systems are compared to each other, as well as with prior in-pile irradiation data of other irradiation campaigns. Based on this comparison, a conclusion is provided how representative these measurements are for predicting in-pile irradiation behaviour of future test plates.

Part I.

Scientific background

2. Uranium metallurgy

This chapter provides an overview of uranium fission, followed by a basic presentation of uranium metallurgy, closing with a description of Uranium-Molybdenum alloys as high density fuels for research and test reactors.

2.1. The principle of uranium fission

The theoretical background of uranium fission is very well explained in literature, e.g. in [7] upon which the following explanations are based. For completeness, the principle is shortly explained at this point as the produced fission fragments and according energies lead to the choice of elements for heavy ion irradiation explained in chapter 8.2.

Considering the nuclear binding energy for each nucleus, iron with an atomic mass number A of 56 is the most stable isotope (see fig. 2.1). Elements lower in atomic mass number could increase their binding energy by fusion. On the other hand, elements greater (or heavier) in mass number could increase their energy by fission. In the case of ^{235}U, the nuclear binding energy is 7.6 $^{\mathrm{MeV}}/_{\mathrm{nucleon}}$ [8]. The core is stabilized by the strong interaction which is around 100 times stronger than the Coulomb force which would otherwise drive apart the nuclei's protons. However, the range of strong interaction is only in the scale of 10^{-15}m and is therefore not to be considered at higher ranges in contrast to electromagnetic interaction. Therefore, the addition of a neutron to the core is far easier than the addition of a proton which would have to overcome Coulomb repulsion first.

Except for the nuclei ^{3}H and ^{4}He, every nucleus has a certain neutron capture cross section[1]. When absorbing a neutron, an energy amount E_n from the neutron is transferred to the nucleus. Depending on the nucleus' stability, this energy transfer can cause the fission of the nucleus[2].

[1] No capture cross section can be measured for ^{3}H and ^{4}He, as ^{4}H and ^{5}He are unstable, as strong force resonances in the timeframe of 10^{-23}s induce disintegration.

[2] Also, the neutron impact on and the energy transfer to the nucleus causes a deformation of the spherical core. Due to its surface energy, the core has some resistance against deformation. If strong enough, this deformation results in the Coulomb repulsion getting stronger than the strong interaction, which leads to fission.

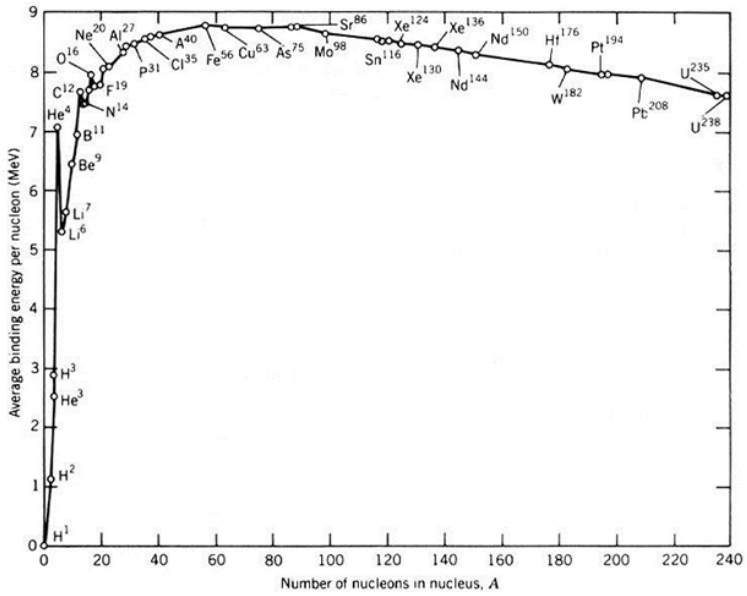

Figure 2.1.: *Average nucleon binding energy per nucleon versus atomic number. Elements found left of the most stable element Fe could become more stable by core fusion, while those on the right of Fe would undergo core fission [9].*

When ^{235}U absorbs a neutron it becomes ^{236}*U. The total energy release in case of a ^{236}*U fission is 202 MeV [8]. This energy is split among two, seldom three fission fragments with a total kinetic energy amount of 170 MeV, β-radiation, γ-radiation, neutrinos and an average of 2.4 neutrons per thermal fission, depending on the incoming neutron's energy. As shown in fig. 2.2, the two most common fission fragments are found at the mass numbers of 97 (i.e. Sr) and 139 (i.e. Xe). Especially ^{135}Xe generation is very unfavorable for reactor performance as it has a very high neutron capture cross section. Therefore, one also speaks of Xe "poisoning" of a fuel [7]. Between these two mass numbers, the amount of fission fragments strongly depends on the incident neutrons' energy. While thermal neutrons ($E \approx 25$meV [10]) generate two different fission fragments, fast neutrons ($E \approx 1 - 20$MeV [10]) more often generate two similar ones. In thermal reactors, thermal neutrons are used for inducing uranium fission, as the ^{235}uranium's neutron capture cross section for thermal neutrons is around 100 times higher than for fast neutrons.

Momentum conservation of the fission products leads to the lighter fission fragment having a kinetic energy of around 100 MeV, while the heavier one around 70 MeV. The according velocities are in the scale of 10^7 m/s which equals 1/10 of light speed. Table 2.1 lists the most common fission products, among them some of those being more prominent in this thesis ($_{36}$Kr, $_{53}$I, $_{54}$Xe).

Isotope	$_{36}$Kr	$_{38}$Sr	$_{40}$Zr	$_{41}$Nb	$_{42}$Mo	$_{43}$Tc	$_{53}$I	$_{54}$Xe	$_{55}$Cs	$_{60}$Nd
Yield (%)	1.5	5.7	6.5	6.5	6.1	6.1	15.9	14.2	6.2	7.6

Table 2.1.: *List of the most prominent elements occurring after thermal uranium fission [11].*

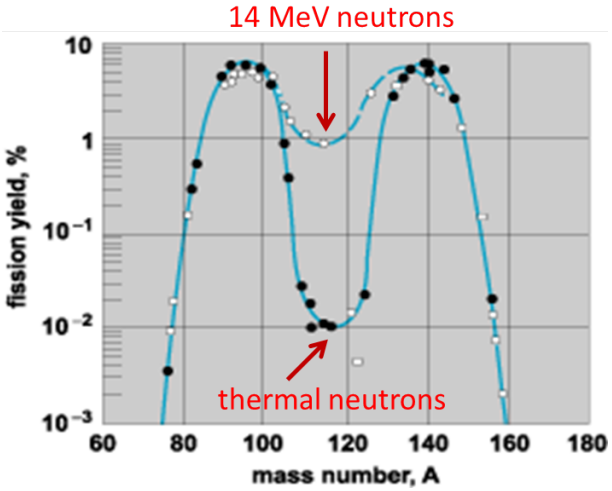

Figure 2.2.: *Occuring fission fragments after ^{236}*U fission. Please note that this distribution is normalized to 200%, as two fission fragments are generated [7].*

2.2. α- , β- , and γ - phase uranium

Due to their metallurgic properties, there exist three uranium phases which are named α-, β- , and γ after [12]:

The **α-phase** is thermodynamically stable at temperatures up to 667°C. Its orthorhombic lattice structure has four atoms in a unit cell (see fig. 2.3-A), and its space group symbol is Cmcm [14, 15, 16]. The according lattice parameters are $a = 2.852$Å, $b = 5.865$Å and $c = 4.945$Å with respective thermal expansion coefficients of $a = 35.6 \cdot 10^{-6}/°C$, $b = -8.4 \cdot 10^{-6}/°C$ and $c = 31.6 \cdot 10^{-6}/°C$ [18]. With increasing temperature, the α-phase expands in two dimensions while shrinking in the third one, leading to a high deformation at high temperatures. This anisotropic swelling effect is shown in fig. 2.4, where a highly textured and fine grained pure uranium rod has been exposed to thermal cycling between room temperature and 550°C. This strong deformation effect is the reason for not using pure uranium as a reactor fuel, although it would naturally have the highest uranium density of all possible fuels.

At temperatures between 667°C and 775°C, the stable phase is called **β-phase**. It has a tetragonal structure (P42/mnm space group) with 30 atoms per unit cell (see fig. 2.3-B). The according lattice parameters are $a = b = 10.7589$Å and $c = 5.6531$Å with expansion coefficients of $a = b = 23.6 \cdot 10{-}6/°C$ and $c = 10.4 \cdot 10{-}6/°C$ [17, 18]. Due to these different expansion parameters, the β-phase will also undergo anisotropic deformation during in-pile irradiation and is therefore also unsuitable as a reactor fuel.

Finally, above 775°C up to the melting point of 1132°C, the **γ-phase** is observed (see fig. 2.3-C). Its bcc structure (Im-3m space group) has the same lattice parameter for

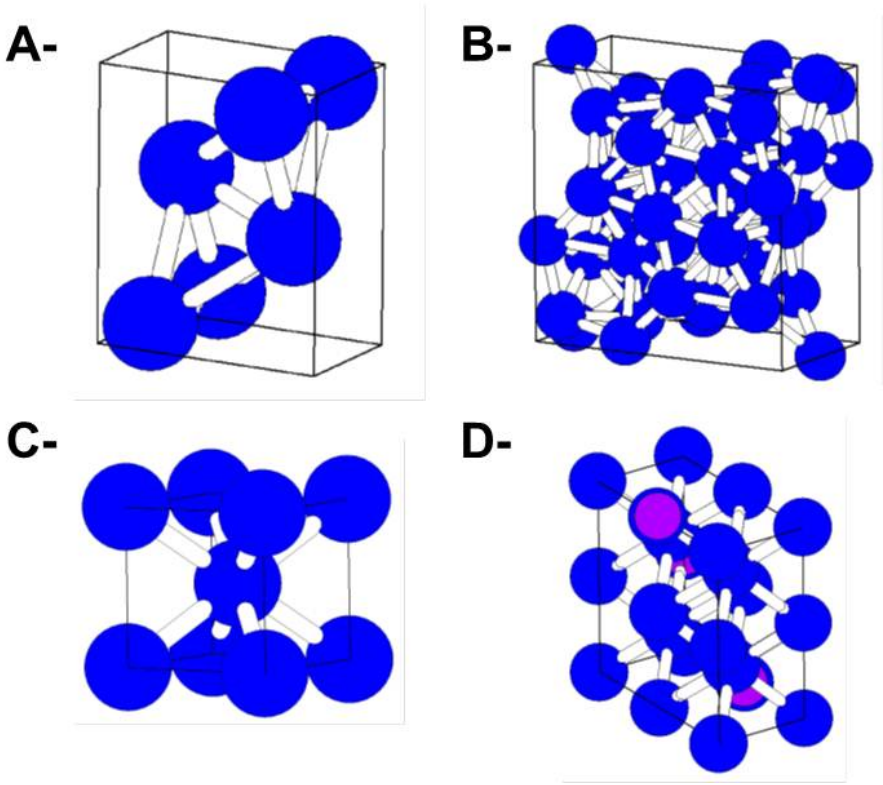

Figure 2.3.: *Sketches of the lattice structures of (A-) α-, (B-) β- and (C-) γ - phase uranium, as well as (D-) γ^0-U-Mo. Purple spots in (D-) mark the position of Mo atoms [13], [143].*

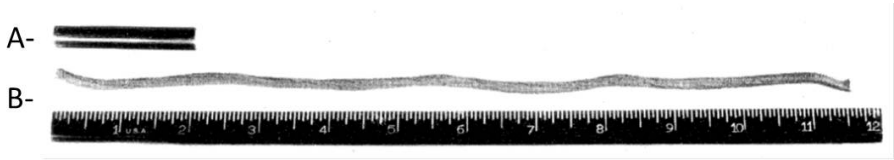

Figure 2.4.: *Image of α-U deformation. After around 3000 cycles at temperatures between 50 and 550°C, the solid bulk (A-) of highly textured uranium has grown around six times in size (B-) [15].*

all dimensions of $a = b = c = 3.474$Å at room temperature [18]. The according thermal expansion coefficient is $a = b = c = 21.6 \cdot 10{-}6/°\text{C}$. Thus, γ-phase uranium exhibits an isotropic expansion behaviour and according fuel expansion can be well predicted and controlled and is therefore suitable as a reactor fuel. Therefore, the main task is to stabilize this high temperature phase at room temperature.

2.3. Uranium - Molybdenum alloys

One possibility to stabilize the γ-phase is to alloy the uranium. Already in the 1950s, experiments have been undertaken to do so [12, 19]. Several alloying partners were taken into account, with the partners' according atomic percentages (at%) ranging from 5% to 30%. Fig. 2.5 shows some exemplary γ-U stability curves based on the U density inside the alloy at 500°C. As indicated, the U-Mo alloy shows the best γ-U stability with regard to density. Indeed, it was observed that a Mo content in the alloy ranging from 4.5 wt% to 15.5 wt% (or 10.5 at% to 31.5 at% respectively) stabilises the γ-phase at room temperature. With regard to fuel plate manufacturing criteria, a Mo contribution between 7 and 10 wt% is considered as an optimum [26].

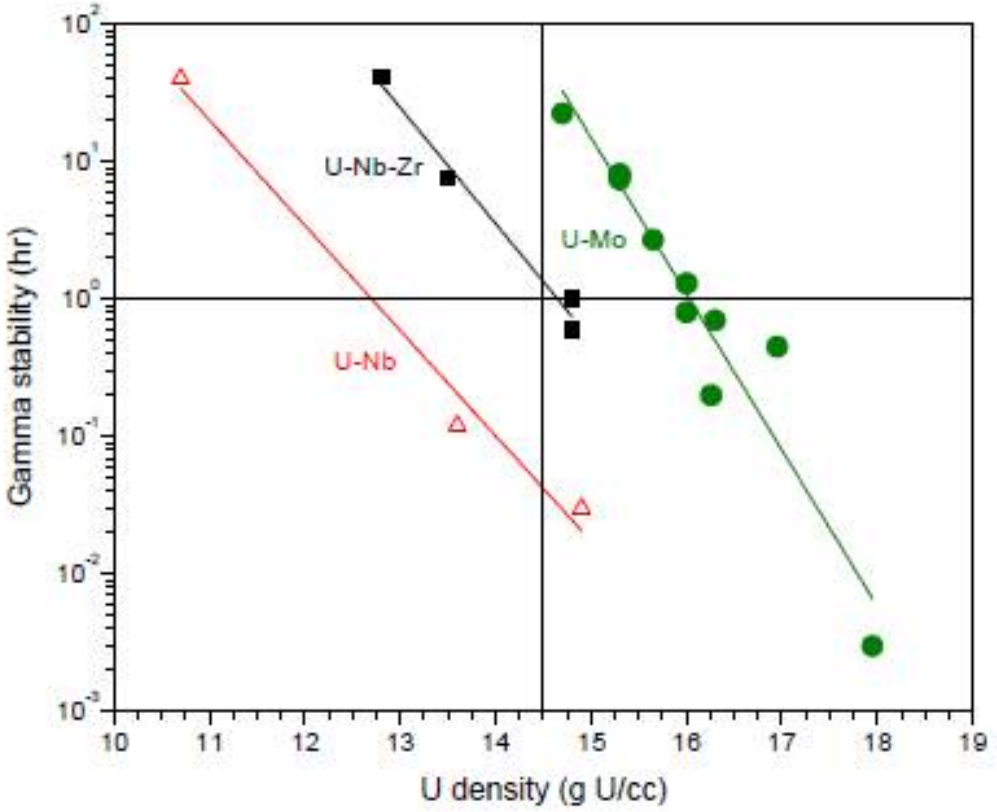

Figure 2.5.: *Relationship between γ-U stability and U density for different alloys at 500°C. U-Mo exhibits the highest density of all the three alloys [24].*

Below 4.5 wt% Mo, deteriorated phases like α'-U and α''-U are found. A similar behaviour is observed above 15.5 wt% Mo: in this case, phases like U_2Mo are detected. This in turn means that in general the U is not homogeneously alloyed. This behaviour was investigated in the 1960s when the final U-Mo alloys with a different Mo wt% were water-quenched from 900°C to room temperature[3].

[3]The cooling speed of water is around 1000 °C/s [21].

2.3.1. U-Mo phase diagram

Based on the informations obtained by quenching processes, a binary phase diagram can be depicted, which is indicated in fig. 2.6 - A. Here, the two identicated red lines symbolize U-7wt%Mo and U-8wt%Mo alloys respectively, as samples investigated in this thesis were composed of these two mixtures, with an according melting temperature of around 1135°C. As the γ-phase is metastable at room temperature, phase decomposition may occur which leads to uranium phases closer to the thermodynamic equilibrium, i.e. to the α- and U_2Mo phases. Several possible causes exist for inducing phase decomposition. The most prominent ones are thermal annealing at elevated temperatures over a long period and mechanical stresses, e.g. during plate fabrication processes at elevated temperatures. Time-temperature transition (TTT) diagrams provide excellent overviews over these decomposition processes. Fig. 2.6 - B shows a representative U-8wt%Mo TTT diagram which is very similar to the one for U-7wt%Mo. Grey colored lines in fig. 2.6 - B indicate transition measurements from the 1960s, while black lines indicate more recent studies, suggesting a shift of the C-shaped transition curves by 25°C towards higher temperatures. Phase decomposition due to thermal annealing does not start before around 50 minutes at 475°. At lower temperatures, this decomposition onset is further delayed.

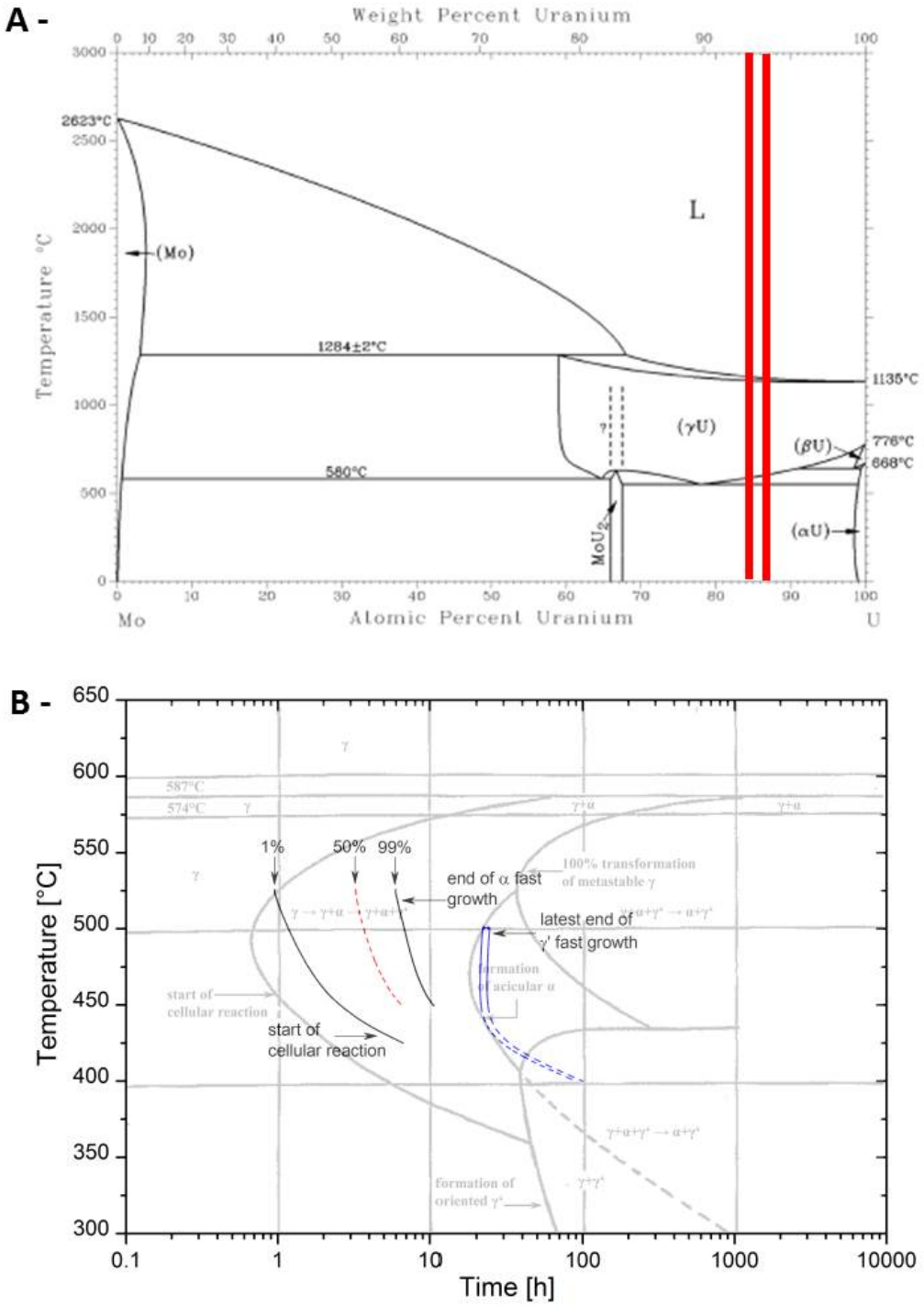

Figure 2.6.: *(A-) U-Mo binary phase diagram [24]. The two red lines correspond to U-7wt%Mo and U-8wt%Mo respectively. (B-) TTT diagram for a U-8wt%Mo compound. Grey lines indicate measurements from the 1960s [31], while black lines indicate recent studies [133].*

3. The Interdiffusion Layer - (IDL)

In this chapter, a brief explanation on the IDL growth and its properties is given, which is based on the theory of radiation damage in materials. Afterwards, the IDL problematics are shown as recent in-pile irradiation dealing with this topic are presented.

3.1. Radiation damage in metals

The following explanations describing the radiation damage event are mainly taken from [45, 46, 47, 48]. The radiation damage event is composed of several individual steps which take place in around 10^{-11} s after the fission event [49]. According to [48], the order of events in this small timeframe is:

- Energy loss through electronic interaction between particle and lattice atoms.
- Kinetic energy transfer from the fission product to a lattice atom. This may result in the lattice atom's displacement from its original lattice position if the kinetic energy amount is high enough.
- Displaced atom is becoming a so-called primary knock-on atom (PKA).
- Creation of additional knock-on atoms by the PKA's interaction with the lattice if the amount of transferred energy is still high enough ("damage cascade").
- Collection of point defects, i.e. vacancies and interstitials created by the PKA.
- After having lost all energy, the PKA remains as an interstitial inside the lattice.

Events occuring lateron are called "radiation damage effects" and include point defect migration, defect cluster formation and dissolution.

The damage event

The above mentioned damage steps and the according time frames of the individual steps are shown in fig. 3.1. These mentioned cascade steps lead to four major phenomena: the PKA creation and the damage cascade itself, followed by a thermal spike, a quenching phase and finally an annealing phase due to the locally increased temperature.

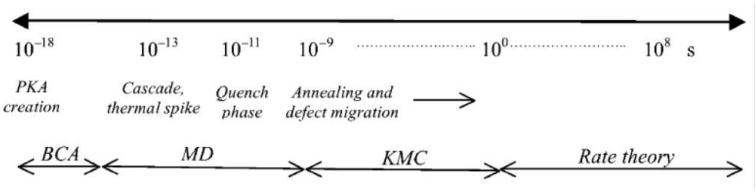

Figure 3.1.: *Time scale for damage evolution and according time intervalls [45].*

The initially created PKA and the resulting **damage cascade** last only for around 1 as. At the end of the cascade, several atoms may be found on **interstitial** lattice sites. This means on the other hand that there are some lattice sites which "lack" atoms, which are called **vacancies**. Right after the collision, the affected atoms transfer a part of the impact damage to their surrounding lattice neighbours. This transfer happens in a very short time (about 0.1 ps) which means that this high energy flux lets the affected areas behave like molten metal [45]. Therefore, this effect is called **thermal spiking**[1].
After this small timeframe, the energy is then transferred to the surrounding regions, and the affected zones return to their solid state and thermodynamic equilibrium is once again assured. The next effect taking place is therefore the **quenching phase**. In this 10 ps timeframe, several point defect or point defect clusters may be produced in the lattice. But in any case, these defects are far less in number than those created by the cascade [45].
Finally, the **annealing phase** will last from a few seconds until literally months or years as the defects migrate due to external temperature and re-arrange themselves inside the lattice[2].

3.1.1. Energy loss theory

The fission product can loose energy in different ways while travelling through a bulk material. Among them are collisions between nuclei, electronic excitation, ionization and Bremsstrahlung. The total energy loss per unit length $-(dE/dx)_{total}$ can be expressed as:

$$(-dE/dx)_{total} = (-dE/dx)_n + (-dE/dx)_e + (-dE/dx)_r \tag{3.1}$$

[1]Especially, the amount of flux, and therefore the thermal spiking effects are important for heavy ion irradiation which is described lateron.
[2]See also chapter 7 detailing the thermal annealing tests.

Here, the index n stands for the energy loss due to nuclear scattering, e for the electronic stopping and r for radiation induced energy loss.

The last term in eq. 3.1, the **energy loss due to radiation effects** $(-dE/dx)_r$, is just a very small amount for the experimental applications considered in this thesis and can therefore be neglected [45]. The main reason is that the energy of the lateron described heavy ion irradiation is not high enough to cause the radiation-induced effects like electronic excitation. This term is only interesting in the case of neutron radiation occurring in in-pile tests. Considering the other two contributions to the total energy loss, a clear distinction is made between the mechanisms behind the energy loss. In the high energy regime (electronic stopping power $S_e \gg$ nuclear stopping power S_n; distance ρ between two atom centers $\ll$ screening radius a), collisions are considered as pure Coulomb interaction processes. Contrary, the low energy regime ($S_e \ll S_n$; $\rho \approx a$) is ruled by collisions caused by nuclear stopping, which is the main source of deposited displacement energy, i.e. the main source for lattice distortions. In the following, it is assumed that each of the target nuclei acts independent of each other when slowing down or stopping the projectile. This is a good approximation for amorphous material and also a good first approximation for crystalline material [45].

The case of **high energy elastic collisions**[3] ($\rho \ll a$) is well described by Rutherford scattering. The energy transfer cross-section σ_s in this case is simply the same as in Coulomb scattering:

$$\sigma_s(E_i,T) = \frac{\pi b_0^2}{4}\frac{\gamma E_i}{T^2} \tag{3.2}$$

where b_0 is the impact parameter which considers charge states of both the involved particle and the lattice atom, γ the mass coefficient, E_i the incident particle's energy and T the amount of transferred energy between particle and target material. Based on σ_s, the energy loss by nuclear scattering becomes

$$\begin{aligned}(\frac{dE}{dx})_n &= n_V \cdot S_n(E_i) &&= \\ &= n_V \int_{\check{T}}^{\gamma E_i} T\frac{\pi b_0^2}{4}\frac{\gamma E_i}{T^2}dT &&= \\ &= \frac{n_V \pi b_0^2}{4}\gamma E_i \ln(\frac{\gamma E_i}{\check{T}})\end{aligned} \tag{3.3}$$

where n_V is the amount of atoms in a unit volume and $\check{T}$ is the minimum of transferable kinetic energy. Thus, at high energy the nuclear stopping is proportional to the density of atoms.

[3]Not to be confused with the high energy regime ($S_e \gg S_n$).

Considering the case of **low energy elastic collisions**, pure Rutherford scattering is insufficient to describe the effect. Lindhard et al. [50] developed an analytical function with a different σ. When applied to $(-dE/dx)_n$, the result is

$$\begin{aligned}(\frac{dE}{dx})_n = \; & n_V \cdot S_n(E_i) \; = \\ = \; & \frac{\pi^2}{4} a^2 n_V E_a \gamma\end{aligned} \tag{3.4}$$

where a is the screening radius of the observed area and E_a is the energy deposited in that area. The low energy function is thus linear proportional to n_V.

For the **electronic stopping power** $(-dE/dx)_e$, a first approximation is made by considering only the interaction of a heavy ion and a single electron. In this case, the formula for the stopping power depending on ion-electron interaction is given by:

$$\begin{aligned}(\frac{dE}{dx})_e = \; & \frac{n}{Z_2} \int_I^{\gamma_e E_i} T\sigma_s(E_i,T)dT \quad = \\ = \; & \frac{n}{Z_2} \frac{\pi b_0^2}{4} \gamma_e E_i \ln(\frac{\gamma_e E_i}{\bar{I}}) \quad = \\ = \; & n_V \pi \frac{Z_1^2 Z_2 \epsilon^4}{E_i} \frac{M}{m_e} \ln(\frac{\gamma_e E_i}{\bar{I}})\end{aligned} \tag{3.5}$$

Here, Z_1 and Z_2 are the particle charges, γ_e is an electron mass coefficient, and I is the mean excitation-ionization which is roughly around 11.5 MeV $\cdot Z_2$. However, this formula is not fully appropriate, as it does not distinguish between high and low projectile velocities. At high velocities all electrons in the target atom's shell interact, while at low velocities only electrons in the outer shells contribute to the scattering process. Lindhard et al. deduced a new expression for the potential energy V of the scattering process [51]:

$$V(r) = \frac{2(Z_1 Z_2)^{1/2} \epsilon^2}{r} \chi_{TF}[1.13(Z_1^{2/3} + Z_2^{2/3})^{1/2} \frac{r}{a_0}] \tag{3.6}$$

a_0 represents the Bohr radius, r the distance between the nuclei and χ_{TF} the Lindhard function which originates from Lindhard's electronic stopping cross section described in [51]. Therefore, the electronic stopping power of an incident ion is:

$$(-\frac{dE}{dx})_e = -8\sigma_e n_V (\frac{m_e}{M})^{1/2} E^{1/2} \equiv k n_V E^{1/2} \tag{3.7}$$

Thus, the electronic stopping power is proportional to the square root of the incident projectile's energy and the number of atoms n_V involved. To conclude, both nuclear and electronic stopping powers are linear proportional to the number n_V of atoms involved to stop the incident projectile.

Particle trajectories

As both electronic and nuclear stopping powers now have been described, it is further of interest how particles travel inside a solid. The comparison of the path in the solid for both high and low energetic ions is shown in fig. 3.2 below. For high energies, the ions are mainly stopped electronically. At low energies, nuclear collisions are the reason for the final halt of the projectile. Together, electronic stopping slows down the projectile until nuclear collisions significantly alter the projectile's trajectory resulting in the halt of the projectile. Illustrated in fig. 3.3 is the kind of dominant stopping mechanism at a particular penetration depth. A Gaussian distribution is applicable for the distribution of the implanted ions in the material, as illustrated in fig. 3.4 [45].

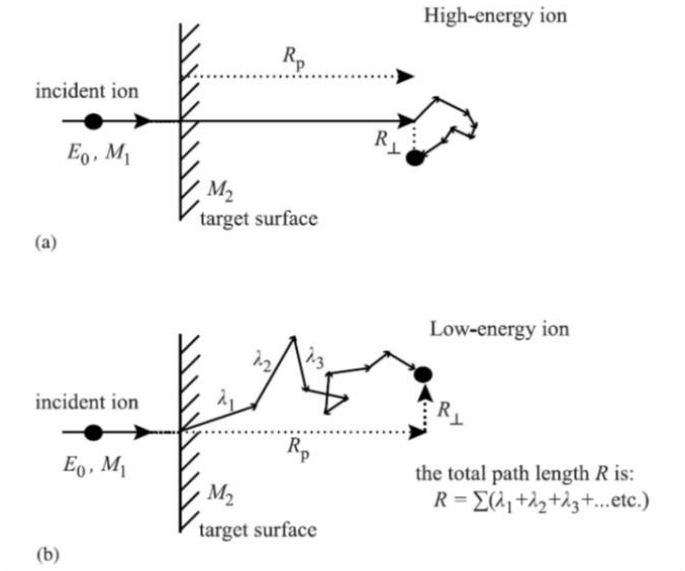

Figure 3.2.: *Comparison of projectile trajectories by high (a) and low (b) energetic ions inside a solid [45].*

Simulation of radiation damage with the SRIM-Code

Several methods exist to simulate radiation damage inside solids, among them the binary collision approximation (BCA), the kinetic Monte Carlo method (KMC) and the molecular dynamics method (MD) [45, 52]. As mentioned before, the time scale for a single damage

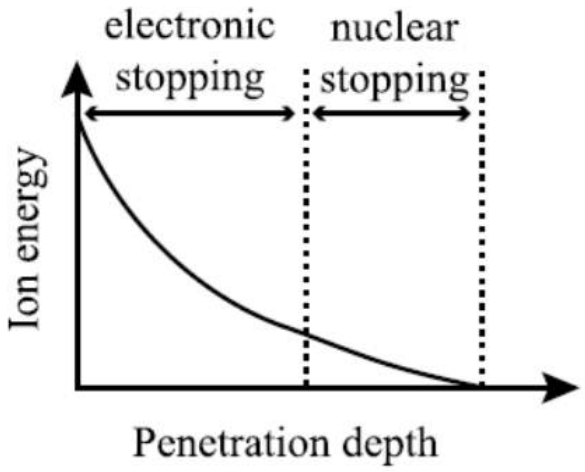

Figure 3.3.: *Zones of electronic and nuclear stopping dominance [45].*

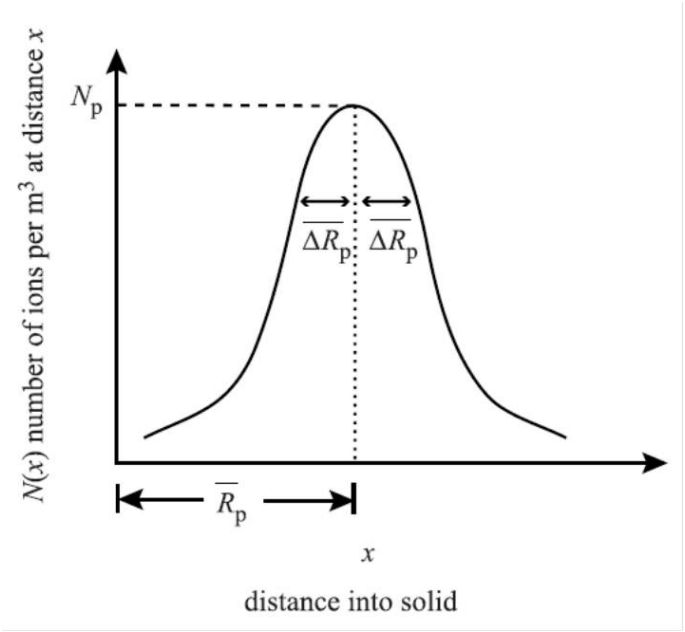

Figure 3.4.: *Gaussian distribution of the implanted ions inside the material. R_p is the average projectile penetration depth, while ΔR_p is the standard deviation and N_p the maximum concentration of implanted ions at the distance x [45].*

event is around 10^{-11} s. These three simulation methods are each accurate only for a distinct time intervall as it is shown in fig. 3.1. In this mentioned time frame of 10^{-11} s, the molecular dynamics method is the most accurate one. The SRIM (Stopping and Range of Ions in matter) - Code is in fact a Monte Carlo code based on molecular dynamics [53]. SRIM simulates displacement cascades very appropriately, as all atoms in the volume are considered, not just a two atom scattering process. In other words, this means that both attractive and repulsive forces towards the projectile are considered. In principal, the

total energy of the complete assembly of atoms is calculated by summing up all the atoms inside [45, 53]. The different accelerations of the atoms are calculated by solving Newton's equation $F = m \cdot a$. In the Monte Carlo Code, Netwon's equation is solved numerically in small time steps of around $5 \cdot 10^{-15}$ s. At the end of each time step, the resulting forces and accelerations are then the setpoint for the next iteration. The process is finished when all the targets and the projectile have been slowed down below the critical energy which is necessary to cause further displacements. However, if the projectile's kinetic energy E is increased, more atoms are taking part in the damage cascade which results in increased calculation time.
Basically, a cascade simulation begins with a temperature consideration of the arrangement of target atoms. It is assumed that all these atoms are in a state of thermal equilibrium before they are hit by the projectile. This equilibrium results in a certain amount of lattice vibrations. In the next step, the atoms are hit by the projectile with a certain amount of kinetic energy and under a certain incident direction. As all these calculations are based on a statistical process, many incident projectiles must be simulated to determine a reliable outcome (law of large numbers).
Therefore there are two possibilities to calculate damage cascades with this program: The first possibility is to use a quick calculation which just tracks the incident projectile's path through the material. Only the final ion positions are calculated. It does not take into account motion of knock-on atoms. The second option is the full damage cascade calculation in which all recoils are considered. The drawback is the high amount of calculation time[4]. In this thesis, a full damage cascade simulation was used (see chapters 8.1.2 and 10.1).

3.2. IDL growth during in-pile test irradiations

As explained above, during irradiation, the fission products transfer their kinetic energy to their surrounding material. This energy transfer causes the uranium and molybdenum atoms to be displaced into the surrounding Al matrix. After some time, which is directly dependant on burn-up, heat flux and fission density, an interaction layer between the U-Mo and the matrix is created (see fig. 1.4). Below the matrix melting temperature, the U-Mo-Al reaction is quite slow and diffusion-controlled, while simulations point out that an increase in temperature enhances the diffusion rate [55].
The IDL region is composed of a mixture of U, Mo, Al and possible additional elements which were added to the matrix, e.g. Si (see chapter 3.3). X-ray diffraction (XRD, see chapter 5.5), neutron diffraction and wavelength-dispersive X-ray spectroscopy (WDS, see chapter 5.2) analysis have been performed to investigate the elemental composition inside the IDL after in-pile irradiation at temperatures from 90 to 220°C [57, 58, 59, 60, 61, 62].

[4]For example, an up-to-date (as of 2014) office computer needs 5 hours to calculate a full damage cascade involving 10000 incident particles shot into an U-Mo/Al layer system. In contrast, a quick calculation with the same amount of particles can be performed in some minutes.

The most prominent interaction products detectable inside the IDL are mainly UAl_3 and with a far smaller amount (1 to 4 wt%) UAl_2 and UAl_4. Indeed, successive transmission electron microscopy (TEM, see chapter 5.4) experiments revealed the IDL's amorphous nature [63, 64]. Measuring a nearest neighbour distance in the amorphous IDL points out a value of around 0.250 nm.

An overview of IDL information obtained by PIE's in previous U-Mo test irradiations is provided in tab. 3.1.

Irradiation test	Fission density (10^{21} f/cm^3)	Heat flux (W/cm^2)	Max. Cladding temperature (°C)	IDL thickness (μm), structure (if measured)	nearest neigbor distance (nm)
IRIS 1 [33]	4.5	145	74	4 - 6	n.m.
IRIS 2 [34]	2.9	238	93	n.m.	n.m.
IRIS-TUM [40]	5.9	260	98	5 - 16.5, amorphous	0.24
FUTURE [63]	1.41	340	130	9 - 11 [35], amorphous	0.239 ± 0.004
RERTR6 [37]	3.4 - 6.3	140-170	<200	4 - 6, amorphous	0.251 [105]
RERTR7 [39]	0.3 - 4.0	130 - 300	90 - 120 [64]	≈ 3, amorphous [39]	n.m.

Table 3.1.: *IDL information obtained during post irradiation examinations for some exemplary irradiations (see also tab. 1.1). The nomenclature n.m. stands for "not measured". Fission density values are given for the examined area.*

3.2.1. IDL recrystallisation

Neutron diffraction studies were made in order to check if an amorphous IDL turns into a crystalline one when exposed to high temperatures [59]. Indeed, when performing a thermal annealing test up to 580°C, at 350°C an abrupt decrease of amorphous contributions to the neutron diffraction pattern and an increase of the crystalline UAl_3 diffraction peaks is observed. Therefore, it was concluded that a recrystallisation has occurred in the IDL. Therefrom, a model system was created to identify influential parameters for interaction layer amorphisation and crystallisation [66]. These parameters were identified as the irradiation temperature which counterbalances fission rate. On the one hand, a high fission rate produces many defects in the material per time unit, while thermal annealing may mitigate the fission rate damage. An intuitive sketch of this behaviour is shown in fig. 3.5. The strength of U-Al interaction, as indicated by the (U+Mo):Al atomic ratio, is strongly dependent on these two factors which point out a critical temperature necessary for IDL transition from the amorphous to the crystalline state. This value was estimated in [66] to be lower than 250°C during in-pile irradiation.

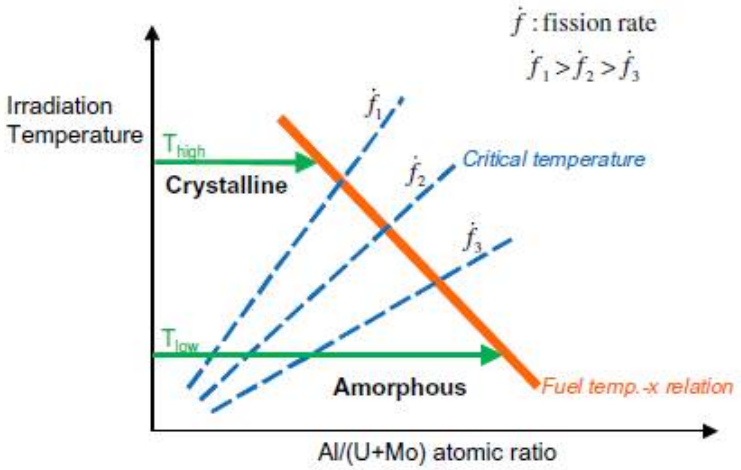

Figure 3.5.: *Model graph indicating the strength of U-Al interaction dependeing on fission rate and temperature [66]. Both high temperatures and high fission rates lead to crystalline IDLs.*

3.2.2. Diffusion couple experiments

Generation of an IDL in UMo/Al systems by thermal annealing has also been attempted several times [122, 56] [5]. Indeed, interaction layers could be created between the U-Mo and the Al matrix. However, the phase composition of these generated IDLs strongly depends on the annealing conditions. This has been proven by XRD analyses on this kind of IDLs. Different additional phases inside the IDL, like ternary $U_xMo_yAl_z$ compounds were detected, which normally do not show up during/after in-pile irradiation. Moreover, a non-marginal difference is observed when comparing the measured weight contributions of several phases, like UAl_3, occurring both in-pile and during thermal annealing. Therefore, this technique may be adequate to study microstructural evolution of manufactured fuel plates before in-pile irradiation, but is inadequate to predict in-pile grown IDL characteristics.

3.2.3. Out-of-pile irradiation experiments: Heavy ion irradiation

Since 2005, another technique is used to study IDL growth out-of-pile. It was demonstrated that bombardment with ^{127}Iodine ions at 80 MeV (flux $< 1.4 \cdot 10^{13}$ $^{ions}/_{s \cdot cm^2}$; final fluence $2 \cdot 10^{17}$ $^{ions}/_{cm^2}$) induces an IDL generation in U-Mo/Al test fuel samples (see also fig. 3.6) [142, 143, 68]. Complementary XRD analyses showed that no ternary $U_xMo_yAl_z$ compounds were created, in contrast to thermal annealing tests. Moreover, it was clearly evidenced that UAl_3 was the largest phase contribution to the IDL which was in good agreement with (U-Mo):Al atomic ratios measured after in-pile tests at similar irradiation temperatures [35, 66]. A drawback of heavy ion irradiation was that the observed UAl_3

[5] Also known as diffusion couple tests.

phase was almost fully crystalline with just some slight amorphous contributions. This observation was in contrast to in-pile IDLs which are amorphous at similar irradiation temperatures. Additionally, no clear conclusion can be made concerning the grown IDL thickness and the Iodine penetration depth into the sample, i.e. the IDL exhibits different thicknesses at a specific sample depth (see green circle in fig. 3.6).
The main advantage is that Iodine at 80 MeV is below the Coulomb barrier for nuclear reactions. Therefore, the samples are not further activated, which means post irradiation examinations can be performed right after the irradiation experiment. As heavy ion irradiation is a major part of this thesis, a full description is provided in chapter 8.2.1.

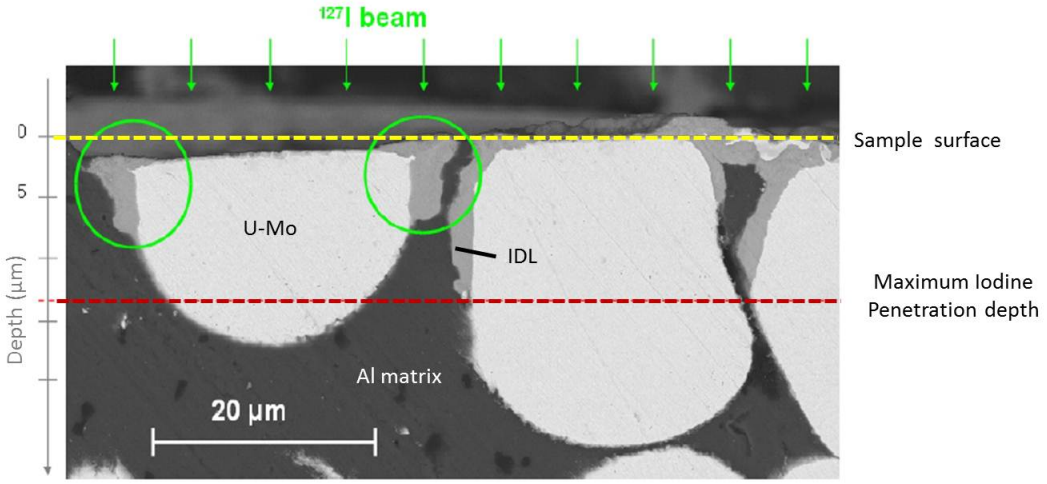

Figure 3.6.: *SEM cross section view of an heavy ion irradiated atomized U-Mo/Al sample. Between the U-Mo particles and the Al matrix an IDL has formed up (see green circles). The yellow dashed line indicates the sample surface which was exposed to the ^{127}Iodine particle bombardment. The red dashed line shows the maximum penetration depth of Iodine into Al of 13µm. Based on [143, 67].*

3.3. Methods to remedy or suppress IDL growth

Several fuel engineering methods were approached to improve the in-pile performance of U-Mo fuels with the goal to irradiate the plates to higher fission densities before excessive swelling occurs:

- Matrix manufacturing with an additional element. A Si addition (0.3 - 6 wt%) to the matrix proved beneficial for in-pile performance [36, 40]. This effect is caused by Si particle diffusion from inside the matrix towards the U-Mo/matrix interfaces where they accumulate to form a Si rich diffusion layer (abbr. **SiRDL**) [96]. This Si precipiation towards the U-Mo particles is based on the higher Si affinity towards U than Al. This protective layer around the fuel particles hinders U-Al interaction at

the start of the irradiation. However, the SiRDL is consumed during irradiation and IDL growth sets in as soon as this layer has vanished.

- U-Mo **particle coating** with a protective layer. In this case, the manufacturing process foresees to coat the particles before they are embedded in the matrix. Several options of particle coating are pursued at the moment. For example, in the SELENIUM project, ZrN or Si were applied as coating materials with coating thicknesses ranging from around 0.3 to 1 μm [36, 69, 107, 4] (see also appendix A). Indeed, it has been shown by both heavy ion irradiation experiments and in-pile irradiation that these coatings protect the fuel from U-Al interaction, as long as these coatings are intact. Locations of coating failures show strong evidence of IDL formation.

- Currently, it is tested whether a pre-irradiation U-Mo particle annealing before irradiation is beneficial to in-pile irradiation behaviour. This thermal treatments should mitigate microstrucural defects and therefore delay or negate U-Mo particle deformation which leads to coating failure and successive abnormal swelling (see chapter 1.3).

Tab. 1.1 indicates the fuel manufacturing evolution during the recent years. The above mentioned techniques enables fuel plate test irradiations at a high heat flux towards successively higher final fission densities in to range of around $5 \cdot 10^{21}\,{}^{\mathrm{f}}/_{\mathrm{cm}^3}$. However, at this value, excessive U-Mo particle deformation is observed which enforces test irradiation abortion. This particle deformation phenomenon is strongly investigated at the moment.

Generally said, both matrix and fuel particle engineering techniques significantly slow down IDL growth and therefore excessive swelling onset. However, the generation of fission gases and their accumulation inside the IDL is an ongoing problem to be solved.

4. Fission gas behaviour

Besides the interdiffusion layer growth during in-pile irradiation, the generation of fission gases like Xe and Kr is of great importance. These gases tend to gather in so-called "bubbles" with sizes up to some μm. As explained at the end of this chapter, large bubbles accumulate at the IDL/Al matrix interfaces. As the second experimental part of this thesis deals with examinations on fission gas in in-pile irradiated fuels, a theoretical background on this topic is provided in the following.
Several models have been developed in the past 30 years dealing with fission gas dynamics inside nuclear fuels. One common aspect of most of these theories is the role of voids inside the materials in which the fission gases accumulate in a second step. Indeed, a possible approach to desribe fission gas dynamics is to consider gas bubble mechanics almost identical to void mechanics. The only difference between voids and bubbles is the circumstance that voids are considered as gas bubbles without gas. Of course, this assumption is not adequate to the real physics behind this phenomenon. However, for providing a general understanding, it is an ideal approach. The fission gas theory which is presented in this chapter is mainly taken from [45] and [70], while some minor contributions come from [71], [72] and [73].

4.1. Bubble growth mechanism

Basically, the distinction between a void and a bubble is based on their according shapes: if enough gas is present inside a void, the gas pressure forces the void to become spherical. This allows both to be distinguished from each other by experimental examination methods, e.g. TEM (see chapter 5.4).

4.1.1. General mechanics

The Gibb's free energy G of a gas bubble is given by:

$$dG = V\,dp + \gamma dA. \tag{4.1}$$

Here, V represents the bubble volume, p the pressure, γ the bubble surface tension, and A the bubble surface area. Taking into account the thermodynamical principle

$$V\ dp = \ d(pV) - pdV \tag{4.2}$$

and utilizing

$$\begin{aligned} V &= \frac{4\pi R^3}{3} \\ pV &= \text{const} \quad \text{(ideal gas)} \end{aligned} \tag{4.3}$$

leads to

$$\frac{dG}{dr} \ = \ -4\pi R^2(p \ - \ \frac{2\gamma}{R}). \tag{4.4}$$

If a homogeneous distribution of free energy is further assumed inside the sphere, i.e. $dG/dr = 0$, the following relation is obtained:

$$p \ = \ \frac{2\gamma}{R}. \tag{4.5}$$

This in turn shows the equilibrium condition for a gas bubble, when the inner gas bubble pressure p is balanced by the surface tension γ of the bubble. In case of an existing stress σ upon the bubble, eq. 4.5 evolves into

$$p \ = \ \frac{2\gamma}{R} - \sigma. \tag{4.6}$$

As a next step, the number of gas atoms N_x inside the bubble is taken into account. The van-der-Waals equation gives a relationship between N_x and the according gas particle density ρ_g. Combining the definition of N_x

$$N_x \ = \ \rho_g \frac{4\pi R^3}{3} \tag{4.7}$$

with the ideal gas law

$$\begin{aligned} pV &= nkT \\ p &= \rho kT \\ p &= \frac{3nkT}{4\pi R^3} \end{aligned} \tag{4.8}$$

together with $\sigma = 0$ in eq. 4.6 (stress-free environment) results in

$$N_x = \frac{8\pi R^2 \gamma}{3kT}. \tag{4.9}$$

The abovementioned equation is only valid for ideal gases, i.e. for large values of R. In case of small R, the dense gas limit equation has to be considered, which is most dependent on pressure and temperature, while neglecting the surface term γ. However, in the following it is assumed that the gas bubbles are of adequate size for ignoring the dense gas case. A full description of the dense gas situation and its impact on eq. 4.9 is detailed in [45].

Both vacancy and interstitial flow affect the stability of a bubble, and hence the equilibrium condition. As a consequence, eq. 4.5 is dependent on the absorption rates of vacancies which in turn would provide more free space for gas atom addition to the bubble. Inside the bubble sphere radius R, it can be generally assumed that an amount of N_v vacancies exist which may be expressed as:

$$N_v = \frac{(4\pi R^3)/3}{\Omega} \tag{4.10}$$

where Ω is the atomic volume. Inserting eq. 4.8 in eq. 4.6 delivers an expression for the stress σ:

$$\sigma = \frac{2\gamma}{R} - \frac{3N_x kT}{4\pi R^3}. \tag{4.11}$$

Based on this formula, a critical bubble size radius R_c can be defined which indicates the regime where unstable bubble growth occurs. Solving $d\sigma/dR = 0$ delivers:

$$\begin{aligned} R_c &= (\frac{9N_xkT}{8\pi\gamma})^{1/2} \\ \Leftrightarrow \sigma_c &= (\frac{128\pi\gamma^3}{81N_xkT})^{1/2} \\ \Leftrightarrow N_x &= \frac{128\pi\gamma^3}{81\sigma_c^2kT}. \end{aligned} \tag{4.12}$$

Inserting R_c in eq. 4.9, the bubble size radius R_0 in thermodynamic equilibirum can be defined now:

$$\begin{aligned} R_c &= \sqrt{3}R_0 \\ \Leftrightarrow \sigma_c &= \frac{4\sqrt{3}\gamma}{9R_0}. \end{aligned} \tag{4.13}$$

Finally, by eliminating N_x in eq. 4.9 and 4.11, a direct relationship between σ_c, R_c and R_0 is obtained:

$$\sigma_c = \frac{2\gamma}{R_c}(1 - \frac{R_0^2}{R_c^2}). \tag{4.14}$$

In particular the last two equations are of special interest, as they depict critical values for bubble stability. Concerning stability, the following conclusions are made:

- For bubble sizes below R_c, application of stress σ_c force the bubbles to grow until they reach size R_c.
- If R_0 is greater than R_c or if σ_c is greater than $\frac{4\sqrt{3}\gamma}{9R_0}$, the bubbles may grow indefinitely until the growth is stopped by an external force, i.e. by lattice constraints. Excessive swelling may also lead to **bubble mass coelescence** which is shown lateron.
- For a constant σ, the critical size for a stable bubble can be determined.

4.1.2. Growth equation

Like in the case of void growth, a basic volume growth rate for gas bubbles can be deducted. Bubble growth is driven by an absorption of vacancies to a void which must be stronger than the absorption of interstitials to the void. Therefore, if a void grows by the absorption of vacancies, more free volume is available for fission gas accumulation inside this void.

The net growth rate A_{net}^{V} of a bubble is dependent on the vacancy (indexed as v in the following) and interstitial (i) concenctrations of both inside the bubble (C_v and C_i) and the bubble surface (C_v^{surf} and C_i^{surf}).

$$A_{net}^{surf} \;=\; A_{v}^{surf} \;- A_{i}^{surf} \;=\; 4\pi R D_v (C_v - C_v^{surf}) \;-\; 4\pi R D_i (C_i - C_i^{surf}). \tag{4.15}$$

The coefficient D represents the according diffusion coefficients of vacancies and interstitials. As D is of no significant importance in the following, it is not further detailed at this point. A very detailed description may be found in [45].

The vacancy and interstitial concentrations inside the bubble, C_v and C_i are proportional to the according formation energy E and temperature T:

$$C_{v,i} \;\propto\; \exp(\frac{E}{kT}). \tag{4.16}$$

A full derivation may also be found in [45]. At the bubble surface, the according concentrations C_v^{surf} and C_i^{surf}, are defined as:

$$C_{v,i}^{surf} \;= C_{v,i}^{0} \exp[\frac{\pm\Omega}{kT}(p - \frac{2\gamma}{R})] \begin{cases} + \text{ for vacancies} \\ - \text{ for interstitials} \end{cases} \tag{4.17}$$

where $C_{v,i}^{0}$ indicates the according thermodynamic equilibrium concentrations. As C_i^0 is very low in equilibrium, the term C_i^{surf} can normally be ignored. The total bubble growth includes the atomic volume Ω, and can then be written as:

$$\begin{aligned} \frac{d}{dt}(\frac{4}{3}\pi R^3) \;&=\; \Omega[4\pi R D_v (C_v - C_v^{surf}) \;-\; 4\pi R D_i (C_i - C_i^{surf})] \\ \Leftrightarrow \frac{d}{dt} R \;&=\; \frac{\Omega}{R}[D_v (C_v - C_v^{surf}) \;-\; D_i (C_i - C_i^{surf})]. \end{aligned} \tag{4.18}$$

where C_v^{surf} and C_i^{surf} represent the vacancy/interstitial concentration at the bubble surface, while C_v and C_i indicate the according concentrations in the bulk material.

Under the condition $dR/dt = 0$ in eq. 4.18, an expression for R_c can be found that also includes the vacancy supersaturation S_v:

$$R_c = \frac{2\gamma}{p + \frac{kT}{\Omega} \ln S_v} \quad \text{with } S_v \equiv \frac{D_v C_v - D_i C_i}{D_v C_v^0}. \tag{4.19}$$

A successive step substitutes p by the ideal gas equation shown in eq. 4.8. This leads to the definition of the bubble growth equation $g(R_c)$:

$$g(R_c) \; = R_c^3 - \frac{2\gamma\Omega}{kT \ln S_v} R_c^2 + \frac{3N_x\Omega}{4\pi \ln S_v} \equiv 0 \quad \text{for } \; R_c = 0. \tag{4.20}$$

Based on eq. 4.20, three cases are highlighted which are also plotted in fig. 4.1:

1. For case I, all three roots are real and the according curve has two intersections, called R_c^B and R_c^C, with the x-axis. This means that a void containing gas bubbles and which is situated between these two intersections shrinks back to a value of R_c^B. A void with the same amount of gas inside which is smaller than R_c^B grows until R_c^B is reached. Accordingly, a system above R_c^V **grows without any limit**.

2. In case II, the function has two identical roots and only one intersection with the x-axis. This intersection is at the point denoted R_c^* with an according amount of gas atoms N_x^*. In particular, in this case R_c^B and R_c^V are identical which means R_c^* indicates an instable state. In other words, N_x^* is the only allowed amount of gas bubbles inside the system in order to remain stable. Any change to this value leads to unlimited growth.

3. In the last case III, the function has no real root. This means that the amount of gas is high enough to immediately enforce sudden growth.

4.1.3. Influence of stress

Considering the influence of temperature and stress, [45] gives a very detailed deduction of the thermal bubble growth rate $\dot{R}_{th}$. The final equation is provided:

$$\dot{R}_{th} \propto \frac{(\sigma + p - \frac{2\gamma}{R})}{RKT}. \tag{4.21}$$

In particular, eq. 4.20 states that bubble growth occurs when the sum of stress σ and pressure p outbalance the bubble surface tension $2\gamma/R$, i.e. $\sigma + p \gg \frac{2\gamma}{R}$. Also, in this case

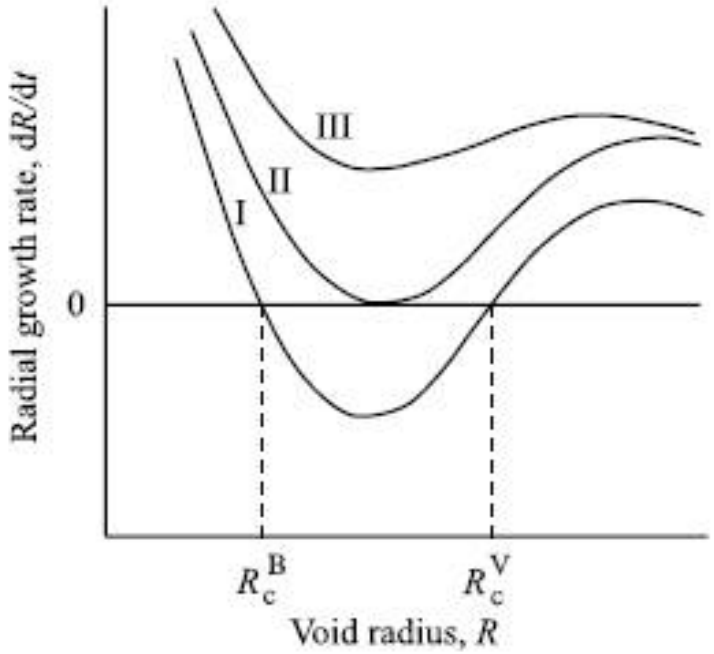

Figure 4.1.: *Growth rate depending on the cavity radius with an increasing amount of gas atoms inside [45].*

experiments were performed to verifiy the effect of stress on growth behaviour [83]. In these experiments, neutron irradiation was carried out on stainless steel. The result was that excessive swelling occurs with both increasing temperature and stress, even if no gas is present.

4.1.4. Dislocation loop punching

One last mechanism for bubble growth to be mentioned is the so-called "dislocation loop punching" process, which is detailed in [74]. If the gas pressure inside the cavity is high enough, it may have an effect on the surrounding lattice structure. By activating dislocations at sites normally not included in the cavity, these dislocations can be "punched out" of their positions, which means the bubble can grow further, as illustrated in fig. 4.2. The gas pressure necessary to trigger a dislocation loop is deducted to:

$$p > (2\gamma + \mu b)/r_0, \tag{4.22}$$

where μ represents the Shear modulus indicating the magnitude of shear stress, and b the Burgers vector indicating the magnitude and direction of lattice distortion caused by a

dislocation. Considering typical values of μ and b (≈ 1.5Å), the amount of pressure p must be an order of magnitude greater than $2\gamma/r_0$ before this mechanism is triggered.

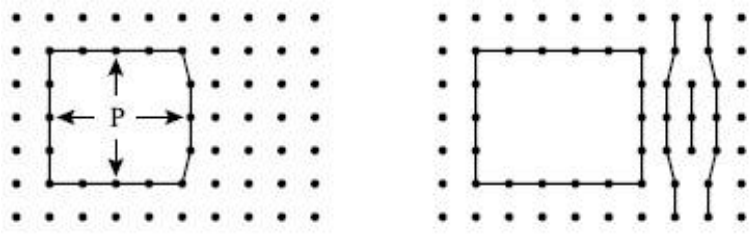

Figure 4.2.: *Sketch of the dislocation loop punching mechanism. A bubble can further grow by using its gas pressure p on the lattice structure to force dislocations nearby to be moved out of position [75].*

Bubble lattice structures

Several experiments consisting of neutron or ion irradiation of metals showed that a void superlattice structure has formed during irradiations [80, 81]. A general observation is that void superlattice structures, and therefore bubble superlattice structures as well, are more easily formed in bcc than in fcc metals. Although a full understanding of superlattice formation has not been achieved yet, some general comments can be provided: A system forced far off equilibrium conditions responds by forming these superstructures, provided that all these conditions are met:

- As a result of the cooling phase after a damage cascade, a vacancy agglomeration in clusters has occurred.
- An asymmetric production and diffusion of interstitials and vacancies.
- A dislocation bias which prefers interstitial absorption to interstitial sites rather than vacancy absorption to vacancy sites.
- Anisotropy of defect growth which prefer void growth over interstitial cluster growth.

Void superlattices are not observed after electron irradiation, and are therefore unambiguously attributed to neutron or ion irradiation. Moreover, it is observed that voids growing in distinct spatial directions, i.e. that form regular lattices, grow faster than randomly orientated ones [82]. Depending on the displacements per atom (dpa) value, superlattices have a lattice constant ranging from 5 to 8 nm with a void diameter from 2 to 6 nm. Several exemplary bubble superlattice observations on in-pile irradiated U-Mo fuel are shown in the following.

4.2. Gas bubble observation after prior test irradiations

Several important experiments considering gas bubble formation are presented below. Experiments were carried out both on in-pile irradiated U-Mo fuels, as well as on heat treated U-Mo alloys which were further exposed to Kr bombardment.

4.2.1. PIEs on in-pile irradiated U-Mo fuel

Similar to the previous chapter, a short overview over some exemplary PIE on fission gas analyses is provided. Tab. 4.1 lists some of those results considering bubble size and bubble distribution.

Irradiation test	Local fission density (10^{21} f/cm^3)	Max. Cladding temperature (°C)
FUTURE [35], [63]	1.41	130
IRIS-TUM [40]	5.9	98
RERTR6 [64]	4.5	109
RERTR7 [64]	3.3 (low flux) - - 6.3 (high flux)	90 - 120
Irradiation test	bubble size in (amorphous) IDL (nm)	bubble size S and superlattice parameter P in U-Mo particles (nm)
FUTURE [35], [63]	not measured	S: 2; P: 6-7
IRIS-TUM [40]	$>$ 1000	S: 3; P: 7
RERTR6 [64]	$>$ 100	S: 3.5; P: 11.5
RERTR7 [64]	54 - 159 (low flux) $>$ 200 (high flux)	S: 3.1 $\pm$ 0.4 ; P: 12.1 (low flux) S + P: not measured (high flux)

Table 4.1.: *Exemplary PIE data on fission gas distribution inside U-Mo fuel.*

A visualisation of these values is given in fig. 4.3 depicting investigations made on irradiated FUTURE samples consisting of atomized U-Mo powder, as well as in fig. 4.4 in fig. 4.5 showing exemplary results of irradiated RERTR6/7 fuel on monolithic U-Mo fuel. The major obersevations are in detail:

- Inside the U-Mo particles, a **grain subdivision** has occured (fig. 4.3 - A and fig. 4.4 - A). Moreover, at all the intergranular cell boundaries, porosities are observed which are filled with gas. These cell boundaries were exposed to locally higher stress than the grains themselves which means they are preferred locations for void growth (see chapter 4.1.3). These porosities are successively filled with fission gas. The intergranular grain size itself is dependent on the flux. While in low flux regions these grains are in the range of some μm in diameter. At higher flux, an additional

intergranular grain subdivision occurs. Here, the final grain diameter is around 100 nm [64].

- As seen in fig. 4.3 - B, these intergranular cells are enriched in Mo while the cell boundaries themselves are Mo depleted.

- A bubble superlattice structure has formed in the U-Mo particles. While the bubble sizes and the lattice parameter are already shown in tab. 4.1, the bubble superlattice orientation is parallel to the U-Mo one. However, while the U-Mo exhibits a bcc structure, the bubble superlattice is in fcc structure [105]. At the moment, the reason for this phenomenon is not known.

- Considering the bubble diameter, a strong dependence on the flux is observed. Inside the particles, at low flux the diameter is in the range of some nm, but a strong growth is evidenced in the high flux regime (see fig. 4.4 - B). Moreover, in the amorphous IDL, bubbles sizes are in the range of up to several 100 nm in diameter.

- According to [84], the bubble growth is enhanced by **recrystallisation** inside the U-Mo grains which forms smaller grains. Therefore, many more cell boundaries are created as part of the recrystallisation step (increasing interstitial loop punching). At around $2.1 \cdot 10^{21}$ f/cm³ swelling is minimal, while at around $5 \cdot 10^{21}$ f/cm³ recrystallisation is complete and the swelling rate becomes maximal. Furthermore, an equation is provided for estimating fuel swelling depending on the fission density:

$$(\frac{\Delta V}{V_0}) = 4.0 \cdot f_d \text{ (in } 10^{21} \text{ f/cm}^3) \tag{4.23}$$

4.2.2. Kr implantation into thermally annealed U-Mo/Al compounds

Besides in-pile irradiation, another possibility to study fission gas behaviour is the method of inert gas implantation into fuel samples. One approach is very well described in [85]: Here, different alloys composed of depleted uranium (DU) and Al, Si or Mo were prepared by arc melting [86] followed by annealing for 200 hours at 500°C. Successively, thin foils were prepared out of these compounds for Kr implantation at 200°C and an energy of 500 keV. According to SRIM, a fluence of $2.5 \cdot 10^{14}$ ions/cm² would induce at least 1 DPA for the most prominent phases which are supposed to appear after thermal annealing: UAl_3, UAl_4, $U_6Mo_4Al_{43}$ and UMo_2Al_{20}. With the final fluence of $2.5 \cdot 10^{16}$ ions/cm², an average 100 dpa were expected which equals a dose rate of $4 \cdot 10^{-3}$ dpa/s.
The result was that all the phases commonly found after in-pile irradiation ($U(Al,Si)_3$, UAl_4) are very stable with increasing dpa. Both phases remain crystalline even at 100 dpa. Moreover, the formation of an fcc bubble superlattice structure in the $U(Al,Si)_3$ compounds

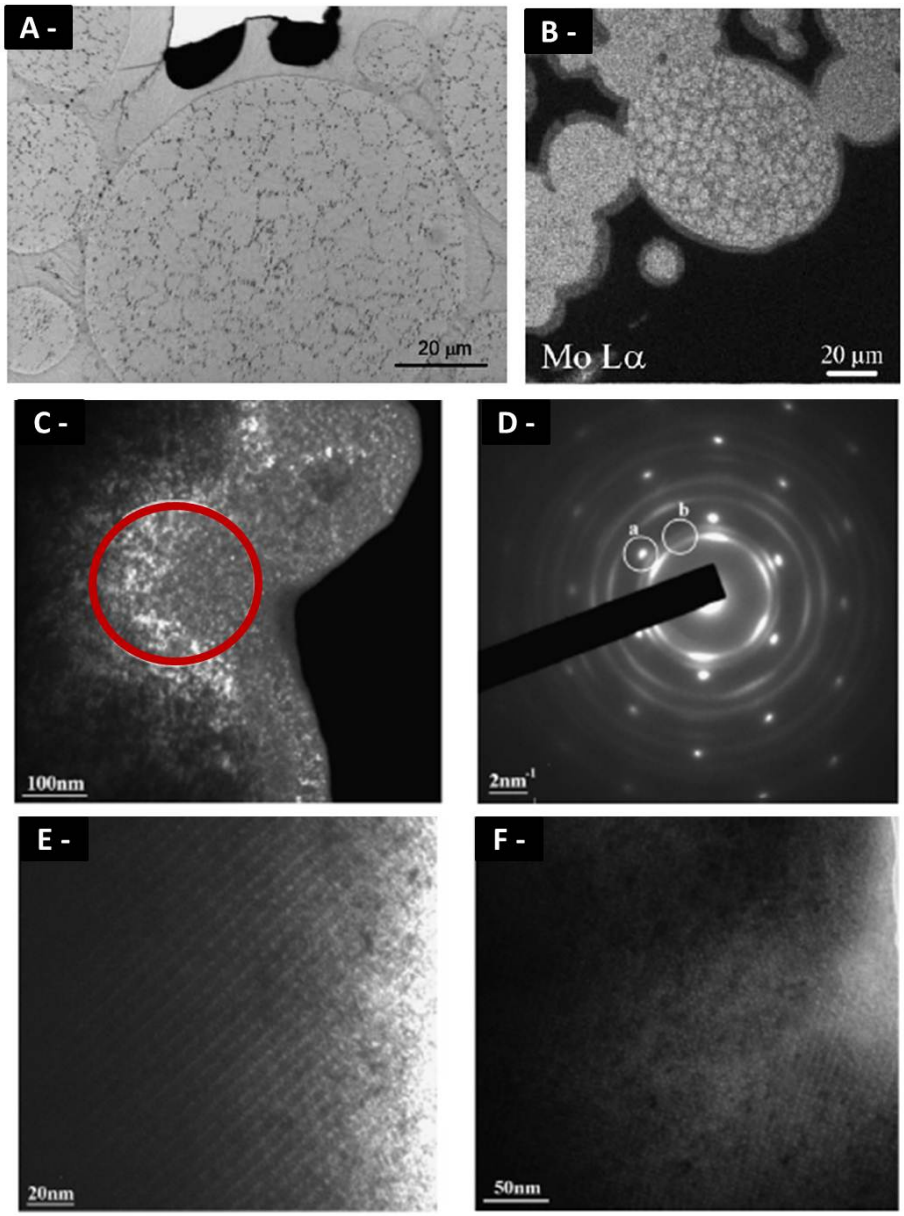

Figure 4.3.: *Microstructural investigations on irradiated FUTURE fuel samples. (A -) Optical microscopy on U-Mo. Inside the particles, grain subdivision has occurred. At these intergranular cell boundaries, porosities can be detected which are filled with fission gas. (B -) An EPMA mapping showing the Mo concentrations inside the particles. Inside the intergranular cells, a larger Mo amount can be detected than at the cell boundaries. TEM dark field imaging (C -) and a corresponding TEM diffraction pattern (D -) obtained in the area highlighted in red in (C -). The U-Mo's granular structure is well observed. (E -) and (F -): TEM bright field images of two different U-Mo particles. The bubble superlattice structure is evidenced [35, 63].*

was observed. The according bubble diameters were measured to some nm. In contrast, the phases expected after thermal annealing ($(U,Mo)(Al,Si)_3$, UMo_2Al_{20}, $U_6Mo_4Al_{43}$) show

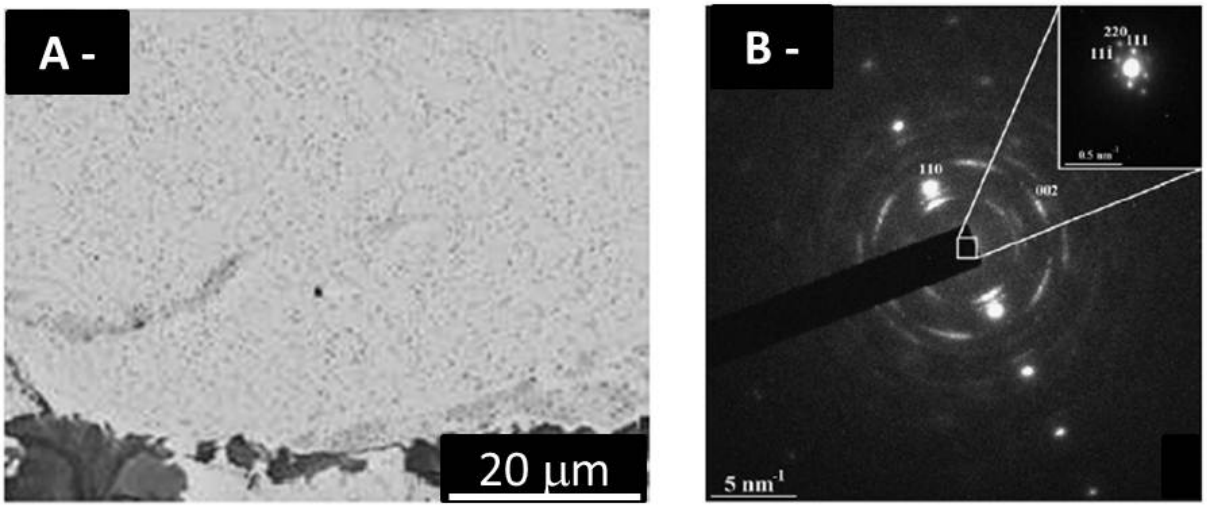

Figure 4.4.: *Microstructural investigations on irradiated IRIS-TUM fuel samples. (A -) SEM BSE image of a U-Mo particle where a grain subdivision has occurred. Also at these intergranular cell boundaries, the detected porosities are filled with fission gas. (B -) A corresponding TEM diffraction pattern showing a gas bubble superlattice structure [40].*

a high instability. Around 1 dpa was enough to transform these phases to the amorphous state. In this amorphous state, large bubbles with around 500 nm in diameter were created.

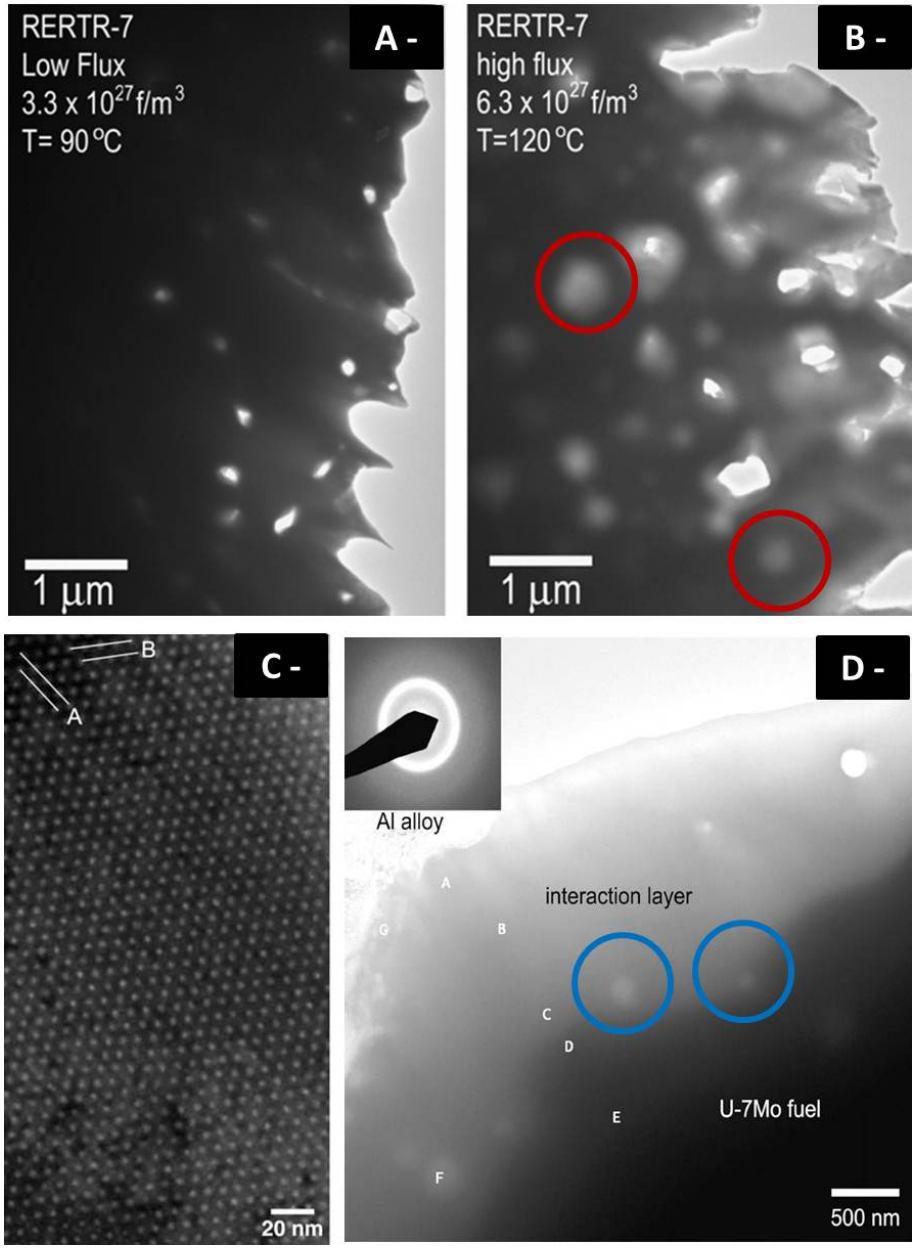

Figure 4.5.: *TEM investigations on irradiated RERTR7 fuel on both (A -) low flux and (B -) high flux regions. High flux regions show significantly bigger fission gas bubbles (see red circles). (C -) Inside the U-Mo particles of the RERTR6 fuel plates a bubble superlattice is seen as well. (D -) Large bubbles are visible inside the amorphous interaction layer (see blue circles) [105, 64].*

5. Utilized techniques for sample analysis

Before presenting the two main topics of this thesis, thermal treatments on IRIS4 samples and heavy ion irradiation of monolithic U-Mo/Al systems, the experimental techniques are introduced with which the corresponding samples were analyzed. These experimental techniques include optical microscopy (OM), scanning electron microscopy (SEM), transmission electron microscopy (TEM), x-ray diffraction (XRD), energy dispersive x-ray diffraction (EDX), focussed ion beam milling (FIB), electron probe microstructure analysis (EPMA) and secondary ion mass spectrometry (SIMS). As optical microscopy is a trivial technique, it is not explained in the following. Also, the descriptions of the facilities used for thermal treatments and ion bombardment are very specific for the individual experiment. Therefore, they are not explained in this chapter, but rather in the chapters dealing specificially with the related topic.

5.1. Scanning electron microscopy (SEM)

SEM allows to study the specimen microstructure with a high magnification down to the nm scale. However, as detailed in the following, only the sample surface and volumes in a depth of some μm can be examined. Many publications describe SEM techniques, and the following descriptions are based on [127], [128] and [129]. The principle of SEM investigation is the point-by-point scanning of a specimen with electrons and analyzing the intensities of the detected signal from the respective points. The different intensities are translated in different scales of grey and electronically assembled in an image matrix. In SEM, a higher magnification is achieved by a stronger electron beam focussing. The procedure for signal generation and detection is explained in the following:
For emitting electrons, two major techniques are used [1]: thermal emission or field emission. The method of **thermal emission** uses a tungsten cathode which is heated up and therefore emits the electrons. The resulting electron cloud has an average diameter of around 50 μm. In a next step, the electrons are accelerated by a voltage and focused by electromagnetic lenses towards the target. The method of **field emission** is based on the

[1] There are other techniques for emitting electrons, like Schottky emission. However, for the SEM systems used in this thesis, only the two mentioned methods were available.

quantum mechanical tunneling effect. In this case, a strongly pointed tungsten cathode is used. By applying an electrical field, a potential barrier is generated near the pointed cathode. Electrons close to the Fermi energy can tunnel through this barrier into the free space outside the cathode where they are further accelerated. The effective diameter of this electron source is around 2.5 nm and therefore 200 times smaller than in the case of thermal emittance. Thus, a very focussed beam can be generated which allows a far higher resolution when investiganting a sample. For both methods, an accelerating voltage between 1 and 30 kV can be used, resulting in an electron energy between 1 and 30 keV respectively.

For the following explanations please also consider fig. 5.1. When the electron beam from the gun (highlighted in blue in fig. 5.1 - A) hits the sample surface, a series of interaction processes occur. Two of these interaction processes lead to the emittance of so-called secondary electrons and back-scattered electrons out of the sample bulk.

As shown in fig. 5.1 - B, **secondary electrons** (abbr. **SE**) are generated by inelastic scattering effects between the primary electrons and the electronic shells of the atoms inside the material. The generated SE have an average energy of 2 - 5 eV. Due to this low energy, only SE close to the sample surface can escape the bulk material. Depending on the acceleration voltage, i.e. the primary electron beam energy, and the density of the sample material, SE from a depth of up to 10 nm can be emitted. When emitting from the material, the low energetic SE can be attracted towards the SE detector (e.g. a photo multiplier) by applying a low positive voltage of around 300 V. As a consequence, only sample surface information can be gained by SE investigation methods.

In contrast, **back-scattered electrons** (abbr. **BSE**) are the result of elastic scattering processes between the primary electrons and the electronic shells. When colliding, the primary electrons loose some amount of their kinetic energy and can be emitted from the material under a slightly different angle compared to their incident trajectory (see fig. 5.1 - B). When emitting from the material, these BSE have an average energy close to the primary electron energy and their mean trajectory points back to the electron gun (5.1 - A). Therefore, a typical BSE detector consists of a ring detector which is placed around the primary beam trajectory. When a BSE hits this ring detector, the Si atoms inside the BSE detector are ionized and a signal is generated. Depending on the bulk density and the primary beam energy, BSE from a depth of up to 10 μm can be emitted from the material.

Another occurring effect of high energetic interaction is the generation of x-rays inside the material. As shown in fig. 5.1 - C, incident electrons can excite shell electrons to a higher state, e.g. from the K- to the L-shell. Upon relaxation, a K_α x-ray photon is generated. The associated x-ray energy is characteristic for each element. Therefore, an elemental analysis of the investigated material can be made by this so-called **energy dispersive x-ray spectroscopy** (abbr. **EDX**). Also, depending on the detected peak intensity, the weight fraction of each element can be calculated. EDX is an efficient technique to simultaneaously measure several elements inside the material. However, depending on the accelerating voltage, and therefore the primary beam energy, a large volume inside the material is excited which can emit x-rays.

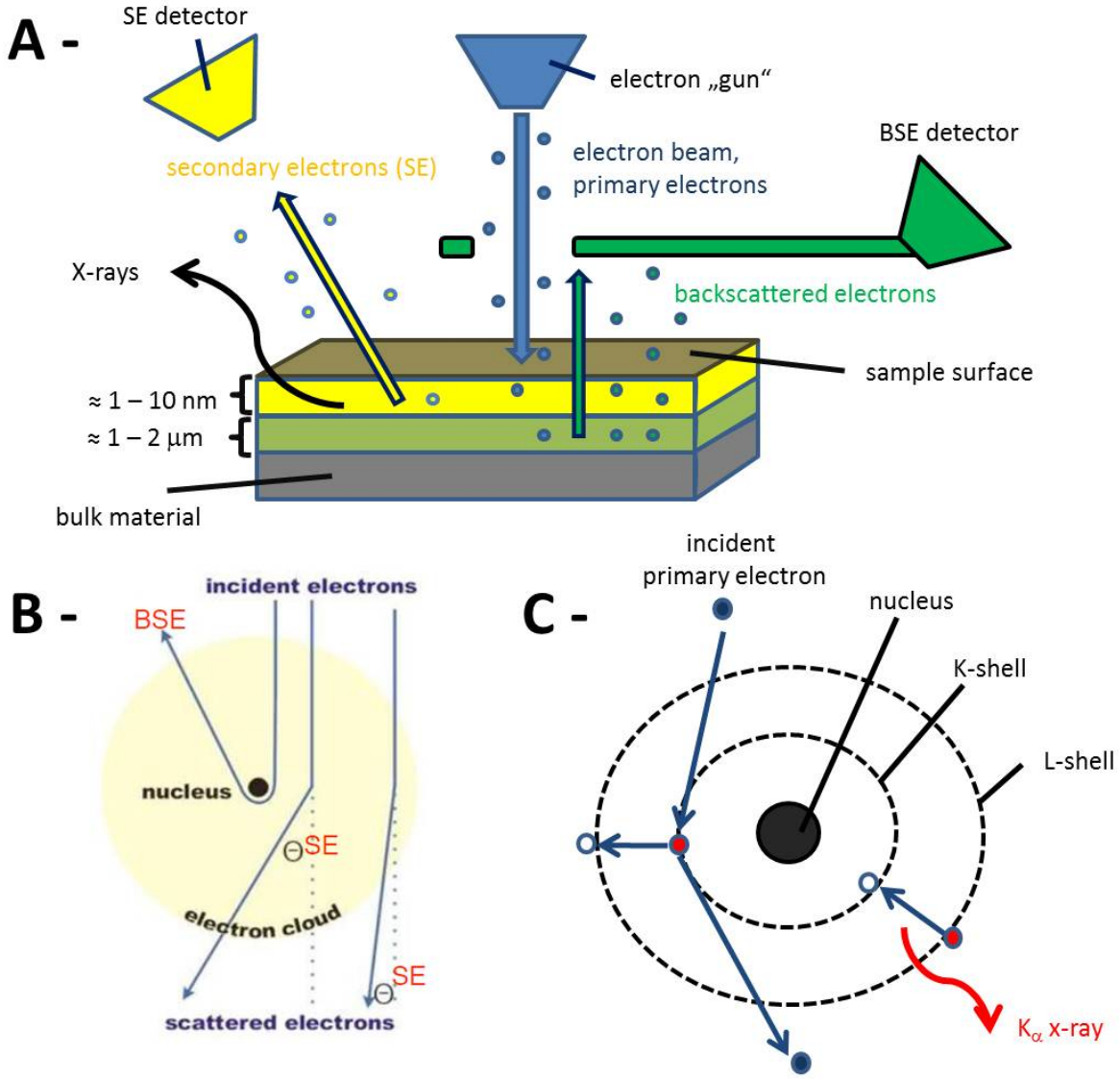

Figure 5.1.: *Sketches of SEM mechanisms. (A-) A general overview of how primary electrons emitted from the gun (indicated in light blue) hit the sample structure. Based on the primary electron energy, i.e. the accelerating voltage, the penetration depth is up to 2 µm. While traversing the sample, several secondary effects inside the sample are triggered (see also (B-)). From a depth of up to 10 nm inside the material, low energetic secondary electrons (SE) can leave the sample and are attracted to and absorbed by a positively charged SE detector. Backscattered electrons (BSE) from a depth of up to 2 µm are high energetic and mainly emitted in trajectory close to the primary electron beam where they can be detected by a backscattered electron detector. (C-) Also, incident beam electrons can excite electrons from atom shells inside the material. Upon relaxation, the electron can emit an x-ray photon that can also be detected. Therefore, information about the elemental composition inside the bulk material can be acquired. (B) is directly taken from [127], while (C-) is based on [127].*

If the accelerating voltage is too low, only low energetic x-rays can be generated which contribute a non-marginal error to the signal. For this reason, an acceleration voltage of 20 kV is normally used. Moreover, as all x-rays wavelengths are measured at the same time, the contribution of Bremsstrahlung to the detected signal reduces the quality of the signal. As a consequence, both Bremsstrahlung and large interaction volume result in an EDX detection limit of 0.1 to 0.2 wt%. In other words, EDX is time efficient, but can only provide qualitative, and no real quantitative sample analysis (in contrast to EPMA, see chapter 5.2). Also, EDX is no adequate investigation technique for light elements ($Z < 20$), as in these cases the generation of Auger electrons outbalances x-ray generation. In this thesis no such light elements are of interest.

5.2. Electron probe micro analysis - EPMA

Basically, EPMA has the same experimental setup as SEM and EDX: a material is exposed to an electron beam and the occurring interaction processes also lead to the generation of x-rays. Furthermore, EPMA SE and EPMA BSE analysis of a sample can be made as well. However, EPMA offers the possibility to indicate elemental wt% inside an investigated structure down to a scale of 0.01 wt%, which is 10 times more precise than EDX analysis [130]. In principal, EPMA uses the technique of **wavelength dispersive x-ray spectroscopy** (abbr. **WDX**). Unlike EDX, where all wavelengths are measured at the same time, WDX is set to measure just one single wavelength at a time which is realised by crystals set to a precise wavelength to detect only the signal of interest and compare the intesity to a known standard reference. This enables the high precision quantitative elemental analysis. As a consequence, this results in a far increased data acquisition time. Furthermore, WDX demands are far more precise and a more sensitive sample preparation as EDX analysis [130]. For example, a common preparation technique is to embed the samples in a Wood alloy consisting of Sn and Bi. This embedding technique affects other investigation techniques, like XRD, performed on the sample (see also chapter 7.5.3).

5.3. Focussed ion beam milling - FIB

FIB is commonly used to prepare small specimens down to the nm scale out of bulk materials. These smalls specimens are mandatory for high resolution analyses like TEM. This sample preparation method can also be included inside a SEM setup. Simply said, an additional ion gun is placed in a 45° angle relative to the primary electron gun. An additional FIB BSE detector can be mounted in the system to provide an according FIB image. Normally, Ga ions are used for FIB operation. Unlike electrons, ions have a far higher mass and can heavily damage the sample while the ion beam is switched on, even if only a small current is used. The sample is tilted so that the incoming ion beam current

hits the sample surface perpendicularly, which means that the according SEM SE image is tilted under a 45° angle compared to the FIB image. The use of an additional SEM imaging system is mandatory, as the sample cannot be observed by FIB SE imaging during the FIB sample preparation process itself.
The procedure of FIB milling includes a gas inlet system (see also fig. 5.2). This system, in combination with the ions, enables several different materials to be either deposited on the selected area, or "milling" of an area. In other words, the respective exposed regions are sputtered and material is released from the bulk sample. In the framework of this thesis, FIB was used for TEM sample preparation, which means that thin foils (called "lamellas") with an average thickness of 90 nm were retrieved from the bulk material.

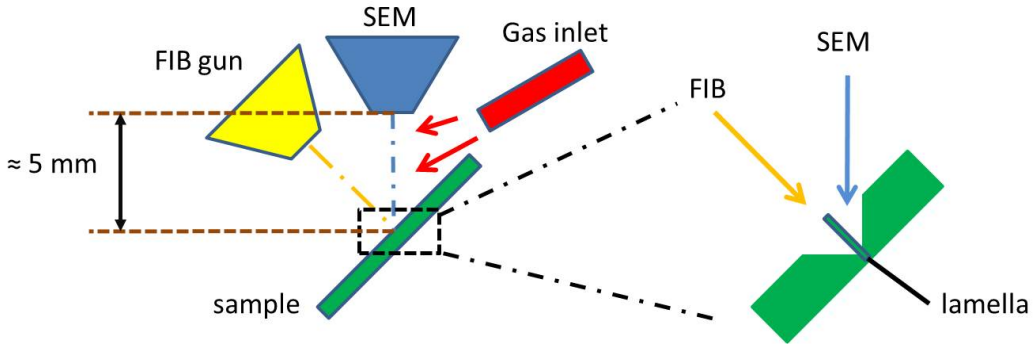

Figure 5.2.: *Sketch of FIB operation: The specimen is tilted inside a SEM system so that the sample surface and the ion beam include a 90° angle. Normally, FIB and SEM include a 45° angle. On the same time as FIB imaging, SEM imaging can be performed under a 45° angle to the sample surface. The distance between SEM gun and sample observation is normally around 5 mm. This ensures that FIB and SEM show exactly the same spot on the sample surface when FIB milling is undergoing. A gas inlet system can provide working gas for the operation processes. With a low FIB current, gas material can be deposited on the sample, while a high FIB current ensures sample milling. In the later case, the working gas assists the milling process. The final result of FIB milling are very small objects in the nm scale. The sketch is based on [127].*

5.4. Transmission electron microscopy - TEM

Contrary to SEM, the technique of TEM analysis allows sample analysis with a high energetic, parallel electron beam which traverses a thin specimen [131]. While traversing the specimen, the electrons' trajectories slightly shift due to Rutherford scattering. Due to inelastic scattering, some electrons loose kinetic energy. Elasticly scattered electrons which leave the specimen under the same angle and which are coherent can be focussed in their according common plane by objective lenses (see fig. 5.3 - A). The resulting electron diffraction pattern can be used to identify the crystal structure of the observed areas. The typical TEM spatial resolution is around 0.05 nm. Normally, TEM acceleration voltages

range from 300 to 500 kV. According sample thicknesses may therefore range from 60 to 100 nm. In the case for high Z density structures, like U-Mo, a thinner sample is of advantage, as electrons scatter more in denser materials.

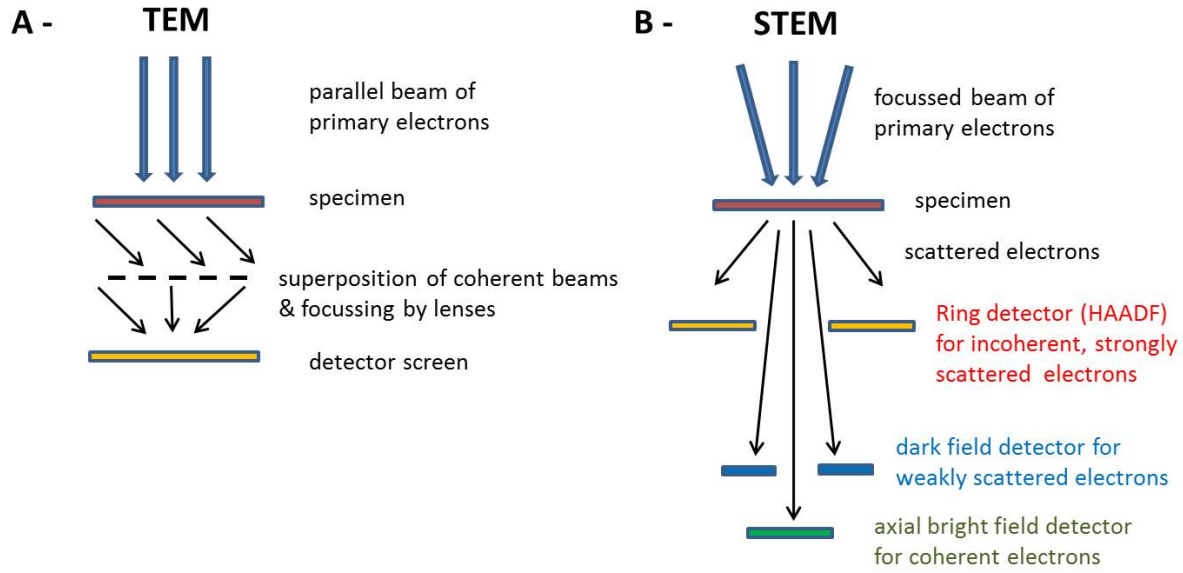

Figure 5.3.: *(A-) In TEM, electrons are accelerated by a high voltage ranging from 300 to 500 kV. The primary electrons' beam trajectories are considered as parallel to each other due to the beam size. When traversing an average 80 - 100 nm thin foil, the electrons are diffracted and can be focussed by objective lenses. A diffraction pattern can be acquired which shows the crystal structure of the examined area. (B-) In STEM, the primary beam is highly focussed so that point-by-point scanning of the specimen can be achieved. The transmitted electrons can be observed by bright field analysis technique or by high angular annular dark field (HAADF) analysis. The later technique allows phase analysis as the scattered electrons detected by HAADF are strongly dependent on the density of the scanned material.*

A derivate of TEM is the so-called **scanning transmission electron microscopy** (abbr. **STEM**). Contrary to standard TEM, STEM uses a high focussed primary electron beam with a beam diameter of around 0.22 nm [131]. Due to the focussed beam, it is possible to scan a structure point-by-point just like in SEM mode. In STEM, the primary electron beam also traverses the specimen, as indicated in fig. 5.3 - B. However, as the primary electron beam is focussed to a small area, the scattering effect inside the sample is very high and the resulting images are different from the ones obtained by standard TEM procedures. As a result, STEM offers the possibility to do bright field imaging, as well as dark field imaging, as well as a so-called high-angular annular dark field (HAADF) analysis. In particular, HAADF is useful for phase analysis of the examined specimen, as the scattering effect of HAADF detected electrons strongly depends on the density of the material, i.e. on the interaction with shell electrons. For example, as uranium has a high amount of shell electrons, HAADF is a very appropriate technqiue to distinguish between uranium (Z=92), aluminium (Z=13) and the IDL (i.e. mostly UAl_3).

5.5. X-ray diffraction - XRD

The technique of XRD is based on Bragg's law. A schematic of Bragg's law is given in fig. 5.4 - A, while a sketch for its derivation is shown in fig. 5.4 - B [132]. From geometric optics it is known that incident rays, like x-rays, which hit a surface under an angle of θ are reflected under the same angle. In XRD, reflection and diffraction is caused by interaction processes between the incident x-rays and the electron shells of the atoms inside the specimen. Due to a high beam energy of several keV, the x-rays can also penetrate a bulk material structure. Therefore, as shown in fig. 5.4 - B, it is possible to use classical geometric optics to calculate the path difference between a ray travelling through the specimen and one which is reflected at the specimen surface:

$$\begin{aligned} AB + BC - AE &= 2AB - AE = \\ &= 2\frac{d}{\sin\theta} - 2AD\cos\theta \; = \\ &= \frac{2d}{\sin\theta}(1 - \cos^2\theta) \; = \\ &= 2d\sin\theta \; \equiv \; n\,\lambda. \end{aligned} \tag{5.1}$$

If the analysed specimen has an ordered lattice structure, i.e. is not amorphous, reflected x-rays have a set path difference between each other. This amount of path difference is directly proportional to the lattice constant d of the material. Constructive interference of different reflected rays is given for all path differences which fulfill eq. 5.1, i.e. whose path difference is a multiple of the x-ray wavelength. The collected x-ray pattern can be analysed in order to determine the phases inside the analysed specimen and, by evaluating the peak intensity contribution of each phase, their according at% inside the examined area.

Several methods exist to analyse structures by XRD, among them the Laue, Bragg-Brentano, or the Debye-Scherrer method. The samples presented in this thesis consist of several different phases which contribute to a diffraction pattern. Additionally, these different phases are not ordered in a unique spatial direction all over the sample. Moreover, each of the different phases can also exhibit grain structures. Therefore, when considering XRD, it is appropriate to consider these samples as polycristalline structures. Hence, the Debye-Scherrer and Bragg-Brentano methods used for powder diffraction were applied in this thesis and are explained in the following. In powder diffraction, the acquired patterns of a polycristalline structure show diffraction rings. This is in strong contrast to the Laue method, where the diffraction pattern of a monocrystal shows only characteristic diffraction points indicating the lattice structure of the analysed specimen.

For low energetic beams (around 8 keV), the x-rays cannot penetrate a sample bulk structure. Rather, surface examinations can be made. The best method to collect reflected

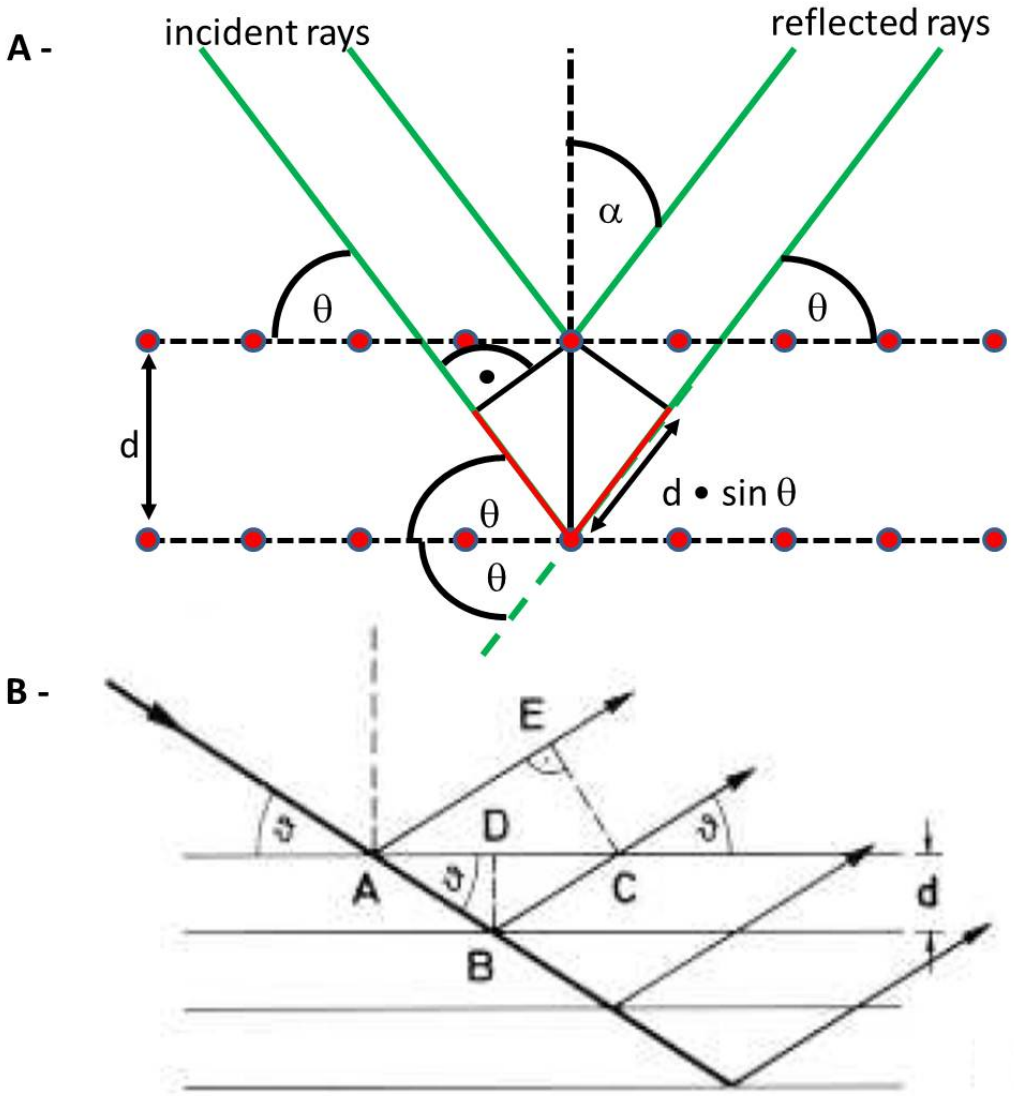

Figure 5.4.: *Sketches describing Bragg's law: (A-) Incident x-rays can penetrate into the specimen where they interact with the material atoms' electronic shells. In a lattice structure, all the reflected x-rays are diffracted under the same angle which results in a path difference between those rays being emitted from inside the material and those which are reflected at the sample surface. This path difference depends on the lattice constant d. XRD patterns can very well be collected for rays of constructive interference. (B-) Sketch to visualize the aforementioned derivation of Bragg's law [132]. The angle between incident and reflected beam is 180° - 2θ.*

low energetic x-rays is by the **Bragg-Brentano** setup sketched in fig. 5.4. In order to limit the irradiated part of the specimen, an aperture is positioned between the x-ray source and the specimen. X-rays hit the sample under a very narrow angle of around 2.3 °. Due to the different phases, and therefore the different lattice parameters, the reflected

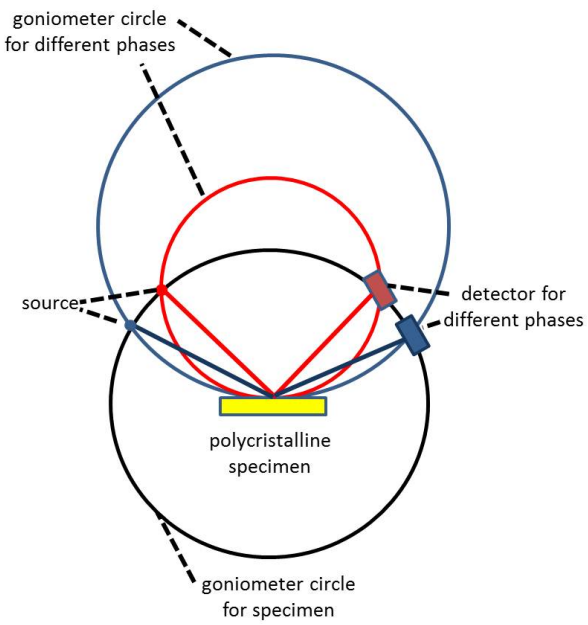

Figure 5.5.: *Sketch of the Bragg-Brentano setup, a θ-2θ powder diffraction method. To detect each individual phase, both x-ray source and detector of this phase have to be placed on their own goniometric circle. Two exemplary goniometric circles are highlighted in green and blue. As the specimen itself is placed in the center of its own goniometric circle, both the x-ray source and the according detectors are to be situated at this goniometric circle's radius (highlighted in black). A common method is to rotate the specimen while the source and the detector are fixed in place [132].*

x-ray beams are slightly shifted to each other. In order to fulfill the 2θ criterion for the incident and the reflected beam, both x-ray source and detector for each individual phase have to be placed on their own goniometric circle. Two exemplary circles are highlighted in red and blue in fig. 5.4. The specimen itself is in the center of its own goniometric circle (highlighted in black in fig. 5.4) with the x-ray source and the detector being situated at the specimen's circle's radius. Thus, in order to acquire the diffraction patterns, it is also necessary to shift the source and the detector on this black goniometer circle. One possibility is to use a circular (360°) detector positioned exactly on the goniometer circle so that it acquires the different phases at the same time. However, a far easier and therefore the most often used technique is to rotate the specimen to achieve the same effect.

Contrary to the Bragg-Brentano method, the **Debye-Scherrer** geometry uses transmission mode of incoming high energy x-rays (e.g. 21 keV). Therefore, the analyzed specimen has to be very thin, so that the x-rays can penetrate through the specimen. An exemplary sketch of a Debye-Scherrer setup is shown in fig. 5.6. As it can be seen, when the x-ray beam traverses the specimen, several reflected beams are generated due to the different phases and their according spatial orientation, each having a 2θ shift between incident beam and reflected beam (see fig. 5.6).

5.5.1. XRD data analysis - Rietveld method

In the scope of this thesis, the programs "Fit2D" [134] and "FullProf" [135] were used to evaluate the collected x-ray patterns. First, Fit2D is utilized to convert the obtained 2D diffraction image into a XRD pattern indicating the phase intensities and the peak

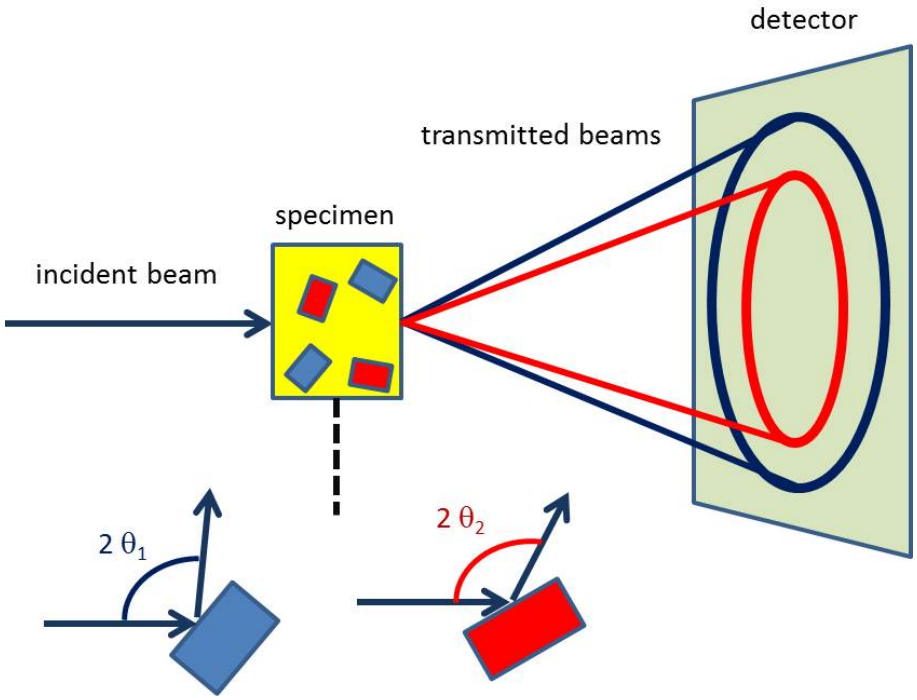

Figure 5.6.: *Sketch of the Debye-Scherrer method. The incoming x-ray beam can traverse the specimen if the beam energy is high enough and the sample thin enough. Due to the different phases and according spatial orientations inside, diffraction rings may be acquired on a flat detector behind the sample. Sketch is based on [133].*

locations. In a next step, FullProf is used to analyse the patterns by the Rietveld method. The basic idea is to use the method of least squares refinement to evaluate a diffraction pattern of a crystalline object. The Rietveld analysis technique uses a theoretically calculated diffraction pattern, which is generated by the phase information provided by the user. The refinement itself is based on the variation of the phase parameters which are further refined in iterative steps so that the theoretical pattern can be matched with the measured one. Therefore, qualitative and quantitative analysis of a diffraction pattern can be performed at the same time, as all phases can be refined simultaneously. Quantitative analysis is feasible by evaluation of the according measured peak intensities of each phase. An example for calculation of weight contribution of each phase to the final pattern can be found in [136].
In the final refinement pattern, the calculated theoretical one, the experimental one, and the difference between both are shown, from which one can conclude about the refinement quality. Additional refinement steps may be necessary to improve the fit quality.

5.6. Secondary ion mass spectrometry - SIMS

To obtain quantiative elemental information from inside a bulk material, the SIMS technique is often used. The following description of the SIMS technique is based on [157, 158]:

A primary ion beam consisting of either Ga or Cs is used to sputter the target material. Depending on the material bonding strength, the primary ions' high impact energy in the range of 1 to 25 keV leads to emission of single atoms or whole atom clusters from the target (see fig. 5.7). Around 1% of the emissioned particles are charged and can be analyzed in a mass spectrometer. In the D-SIMS technique, which was used in this thesis, a very high primary ion current is set to maximize the secondary ion yield which enables a detailed profile analysis. By setting the mass filter to the desired element, i.e. Kr, a precise elemental quantification as a function of sample depth can be achieved.

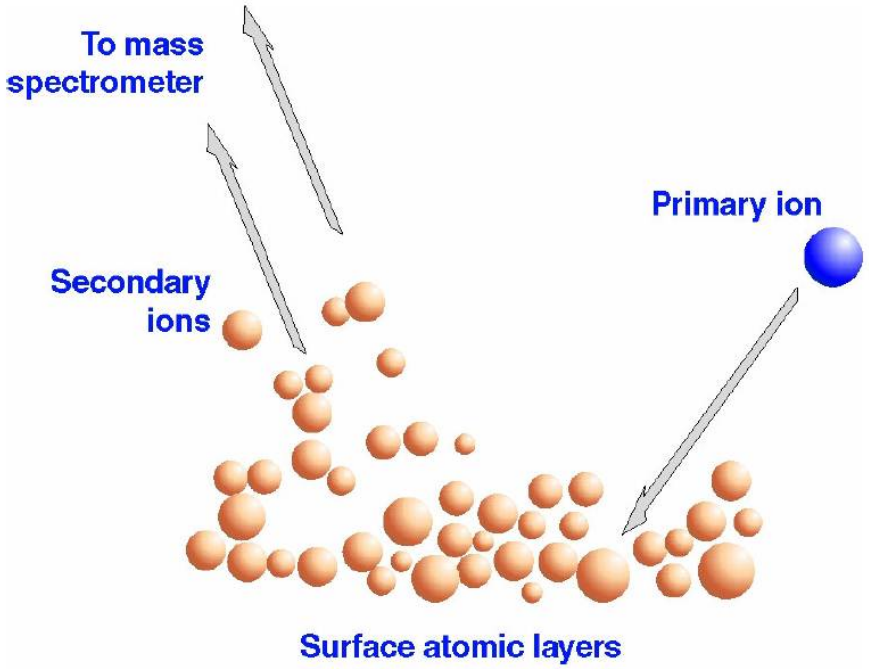

Figure 5.7.: *Sketch of the SIMS technique: An incident primary ion beam sputters the target material. Around 1% of the sputtered material is charged and can be analyzed by mass spectrometry [157].*

Part II.

Thermal treatments on IRIS4 fuel samples

6. IRIS4 fuel manufacturing and in-pile irradiation

The effect of U-Mo particle coating by an oxide layer as a method to slow down or prevent IDL growth has already been described in chapter 3.3. The goal of the IRIS4 irradiation test was to verify whether this effect can be further enhanced by the addition of Si to the matrix, an already known beneficial effect regarding in-pile irradiation behaviour (see also chapter 3.3). Therefore, this chapter provides an overview of the IRIS4 fuel manufacturing process and according post-manufacturing analyses in order to investigate the fuel microstructure. Furthermore, the subsequent in-pile irradation in the OSIRIS reactor is described together with the PIE results. While the fresh fuel characterization is presented here for the first time, the description of the in-pile irradiation conditions, as well as the PIE characterization are presented here for completeness and are mainly based on the according references.

6.1. Fuel manufacturing

For the IRIS4 fuel, atomized U-7wt%Mo particles were chosen which were provided by the Korean Atomic Energy Research Institute (KAERI) with an enrichment of 19.8wt% ^{235}U [87]. After the atomization fabrication, the particles were further oxidized during a thermal treatment process carried out under air at 200 - 250°C which lasted between 1 and 10 hours.
Four full size nuclear fuel plates were produced with this oxidized material. The particles were embedded in either a pure Al (A5) matrix (2 plates labelled 8053 and 8054) or in an AlSi alloy matrix containing 2.1 wt% Si (2 plates labelled 8043 and 8044). In all cases, the meat consisted of 50 vol% U-Mo which equals to an uranium loading of 8 $^{g}/_{cm^3}$ (see also tab. 6.1) [88]. For further enclosement of the meat, an AlFeNi cladding (97wt% Al, 1wt% Mg, 1wt% Ni, 1wt% Fe [90]) and an AG3NE frame (≈97wt% Al, ≈3wt% Mg; Si, Fe, Mn <1wt% each [91, 92]) were chosen, while the final fuel plate assembly was produced by hot co-rolling [89]. As a last step, a so-called “blister test” was performed in order to check whether the cladding and frame show no failure during this thermal treatment step performed at 425 ± 25°C for the duration of one hour. An illustration of the different fabrication steps is shown in fig. 6.1.

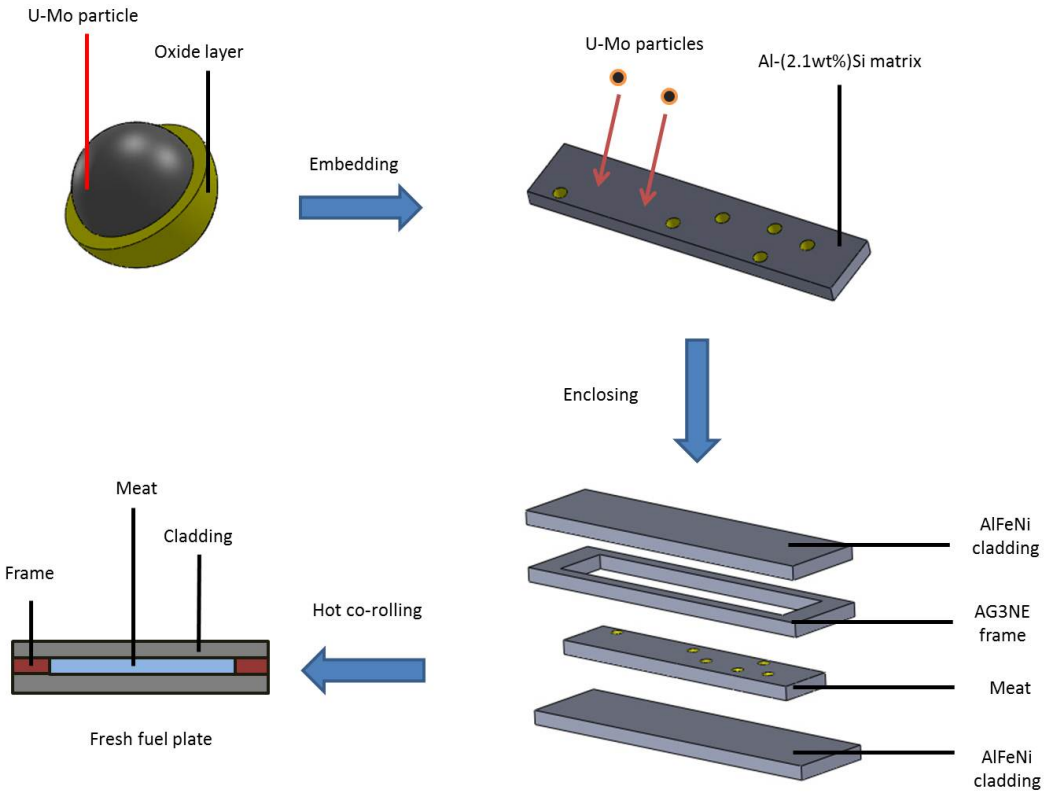

Figure 6.1.: *Illustration of the IRIS4 fuel manufacturing process. The oxide coated U-Mo particles are embedded in an Al matrix with a 2.1wt% Si addition. The created meat is then enclosed by an AG3NE frame and an AlFeNi cladding on both sides to prevent fission products to evade into the primary circuit. The image on the bottom left shows a cross-section view of the final fresh fuel plate.*

6.2. Fresh fuel characterisation

Before the in-pile irradiation test, the fresh fuel plates were characterised by high energy XRD, optical microscopy, EDX and EPMA. Considering high energy X-ray diffraction, it has been found that the coated U-Mo particles exhibited an average oxide layer thickness of 1.0 ± 0.1 μm after the initial oxide coating process [93]. Moreover, the main crystallographic phase of the oxide layer consisted of UO_2 [93]. However, identical XRD measurements performed on coated particles retrieved from the fuel plate indicated an oxide layer thickness of 1.5 ± 0.5 μm [94]. Also, XRD has confirmed a slight γ-U destabilisation into α''-U and U_2Mo during the manufacturing process at elevated temperatures (see also fig. 2.6 - B). This destabilisation results in intergranular grain subdivision, whereupon a Mo depletion at these grain boundaries is well detected (see fig. 6.2). Furthermore, the presence of an additional nitride layer has been detected, consisting of U_2N_{3+x} [94]. According EPMA and optical microscopy investigations also clearify the location of this nitride layer:

Fig. 6.3 depicts both SEM and EDX results on the location of the nitride layer. As seen, the nitride layer has grown around the UO_2 coated particles. As no nitride can be detected inside the particles, and the majority of nitrogen is located on top of the particles, it is concluded that the nitrogen layer has grown during the meat manufacturing step under ambient conditions. Otherwise, if this contamination would have occurred during the particle atomization process, nitrogen would have been detected inside the U-Mo particles. Another major observation is the presence of large cracks in the nitride layer. The exact reason for these cracks is not clear. One possibility is that these cracks appeared during the fuel plate cooling phase after the hot co-rolling manufacturing step.

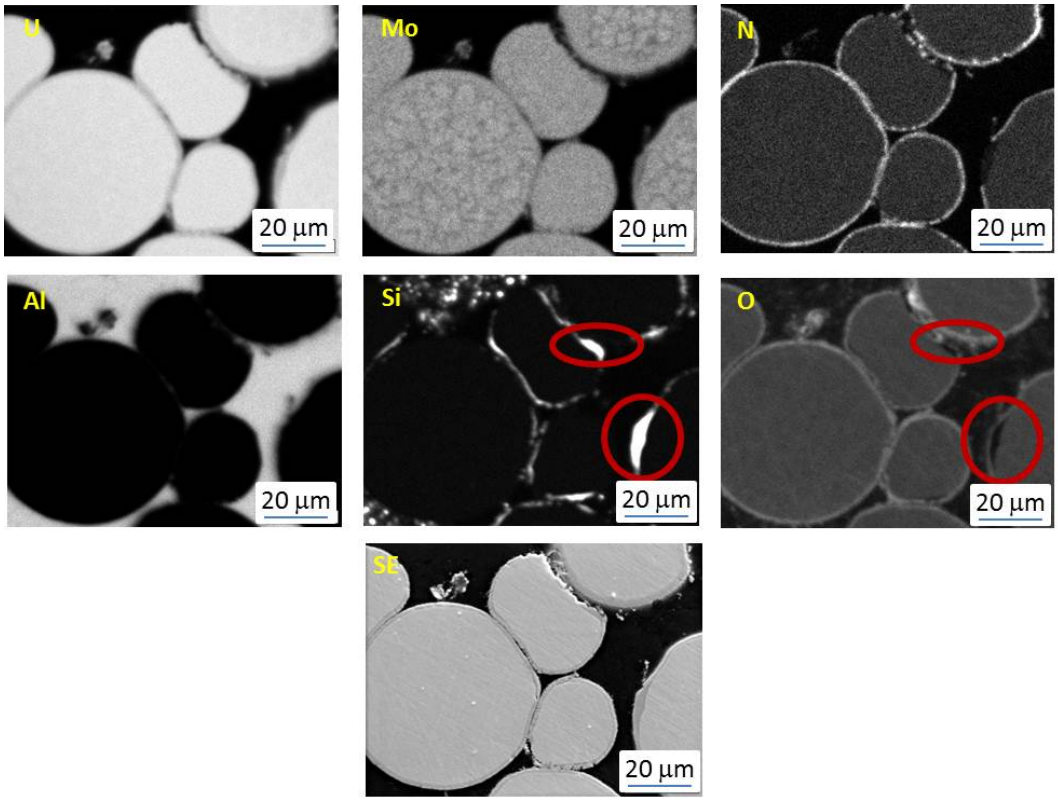

Figure 6.2.: *EPMA SE imaging and elemental mapping of fresh IRIS4 fuel meat. The different elements contributing to the meat can be distinguished from each other: U, Si, Mo, Al, N and O. A slight Si accumulation at the oxide layer around the particles can be seen (see red circle). Indicated in the Mo map is the intergranular grain subdivision leading to a Mo depletion at the grain boundaries inside the U-Mo particles.*

In fig. 6.2, EPMA SE and EPMA elemental maps of U, Mo, N, Al, Si and O are shown. No elemental mixing has occurred during the sample preparation step. Also, the formation of a Si enriched layer (abbr. SiRDL) around the particles is visible (red circles in fig.6.2). This effect has been observed previously several times in fresh U-Mo fuels. This intermetallic mixing layer is caused by Si particle diffusion inside the matrix towards the particles and is composed of $U_xMo_ySi_zAl_v$ [95, 96, 102, 103]. According HE-XRD measurements have quantified the SiRDL's average thickness on both oxidized [94] and non-oxidized U-Mo

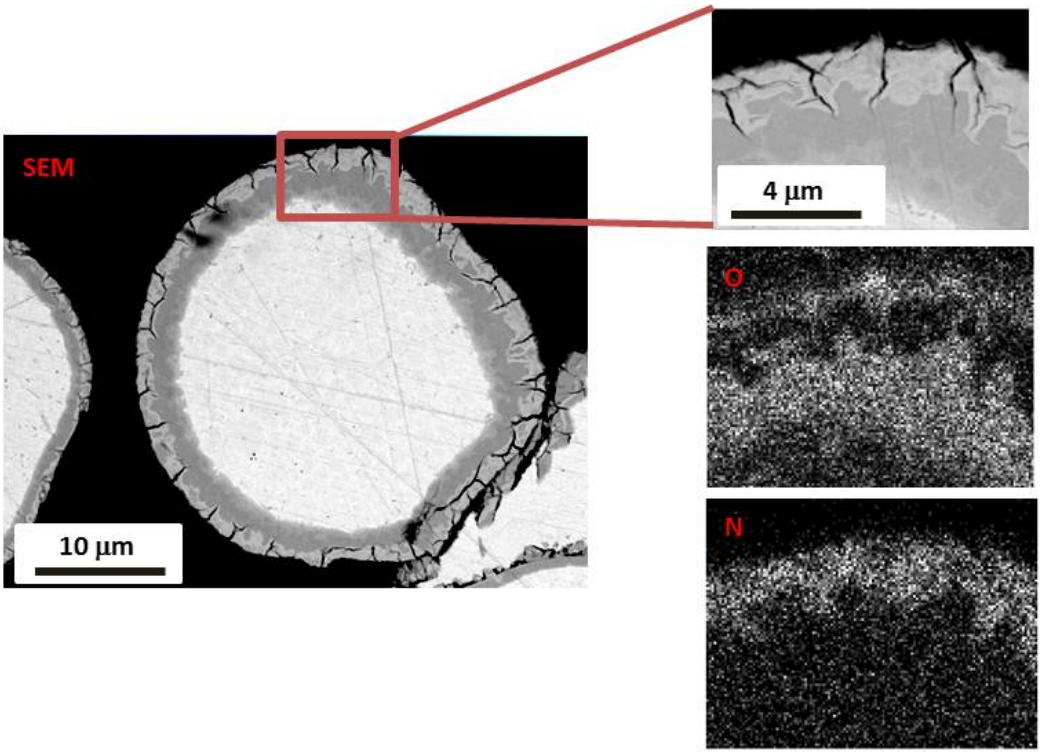

Figure 6.3.: *SEM BSE characterisation of fresh IRIS4 meat. The presence of a nitride layer which has grown on top of the oxidized particles is confirmed by EDX elemental mapping. The nitride layer exhibits cracks.*

particles inside an Al(2wt%)Si matrix [106]. It was found that the SiRDL is thinner in fuel plates consisting of oxidized particles (0.1 μm) than in non-oxidized ones (0.5 μm), resulting in an higher amount of remaining Si inside the matrix.

6.3. In-pile irradiation

All IRIS4 fuel plates were irradiated in the OSIRIS reactor in Saclay, France, from 2009 until 2010 [104]. Table 6.1 lists manufacturing process and in-pile irradiation data on both fuel plates with an Al-Si matrix. The two plates only have a slight deviation in some parameters, like heat flux. The only significant difference is the initial fuel porosity and the maximum plate thickness increase during irradiation. Mean burnup and fission density values, and not maximum values, are given in this table.

Parameter	**IRIS4 8043** [54]	IRIS4 8044 [54, 104]
Plate manufacturing process		
Mo/U-Mo (wt%)	7.3	7.3
U density (gU/cm^3)	7.7	7.9
Porosity (vol.%)	3.8	1.1
Si in matrix (wt%)	2.1	2.1
Plate thickness (mm)	1.31	1.31
Irradiation values		
Max. Heat flux (W/cm^3)	258	269
Max. Cladding surface temperature ($°C$)	100	100
Mean BU ($235U$%)	54.6	55.1
Fission density at MFP (10^{21} f/cm^3 in U-Mo)	3.31	3.34
Mean Thickness increase (μm)	132	269

Table 6.1.: *Summary of the in-pile irradiation conditions IRIS4 plates no. 8043 and 8044 (2.1wt% Si in matrix). Samples analyzed in this thesis were taken from plate no. 8043.*

6.4. Post irradiation examinations

In the following, only the results on **plate no. 8043** are presented in detail as the samples analyzed lateron were excusively obtained from this fuel plate. Fuel plate no. 8043 has been exposed to a heat flux of 258 $^{W}/_{cm^2}$ which resulted in a calculated cladding temperature of around 100°C [104]. For the PIE examinations, sample MA432 was cut near the maximum flux plane (see fig. 7.1) which was exposed to a burnup value of 62% with an according fission density of $3.6 \cdot 10^{21}$ $^{f}/_{cm^3}$ inside U-Mo [54].
Non-destructive examinations have shown an average plate thickness increase of 110 μm at the mean flux plane (MFP) with peak values of 163 μm [104]. Successive destructive examinations included optical microscopy (OM), scanning electron microscopy (SEM), X-ray diffraction (XRD) and electron probe microstrcuture analysis (EPMA).
SEM images taken in the main meat region of the fuel are shown in fig. 6.4. IDL growth occurred around the U-Mo particles. Surface fractions have been determined by EPMA elemental mapping to 35% for the IDL, 46% for U-Mo and 19% for the matrix respectively (see tab. 7.4).

Low energy XRD analysis performed in the IDL regions revealed no $U_xMo_yAl_z$ contribution, i.e. no crystalline structure, of this intermetallic phase. Therefore, it is assumed that the IDL is in an amorphous state, which was expected from other in-pile irradiation at similar irradiation temperatures [63, 105].

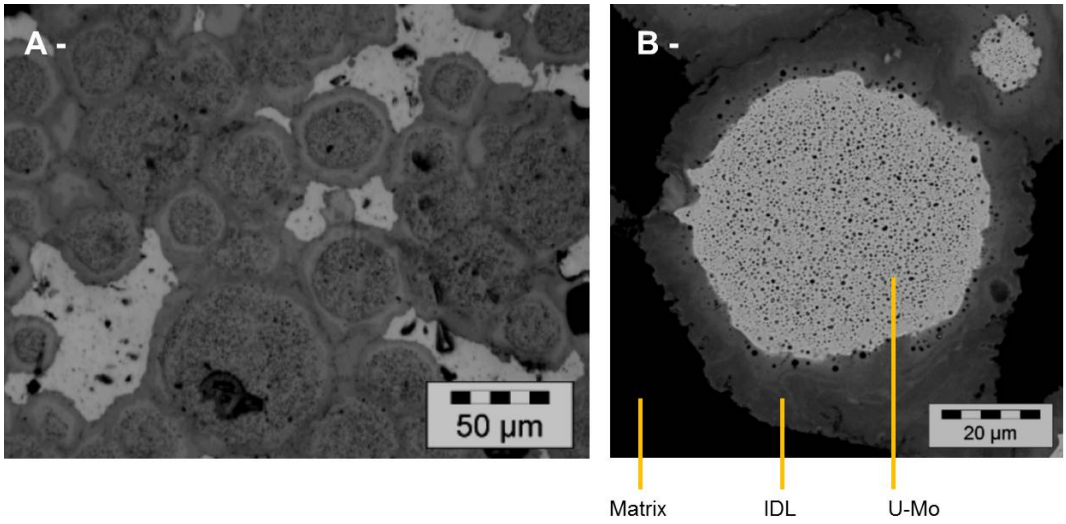

Figure 6.4.: *(A-) Optical microscopy and (B-) EPMA SE images taken in the main meat region of irradiated IRIS4 fuel [54]. (A-) The growth of an IDL around the particles is evidenced. (B-) Inside the particles and at the U-Mo/IDL interfaces, a large amount of porosities is visible. As shown in fig. 6.5, these porosities are filled with Xe gas.*

Considering **EPMA imaging**, an overview is shown in fig. 6.5. The following observations were made:

- A so-called "duplex" structure of the IDL becomes visible. The nomination "duplex" is chosen because the IDL has to be distinguished between an "internal" IDL located at the U-Mo/IDL interfaces and an "external" IDL at IDL/matrix interfaces.
- The external IDL is rich in oxygen which is not the case for the internal IDL (see fig. 6.5 - A).
- Oxygen is no longer present as a coating around the particles, but inside the external IDL.
- Another difference is the amount of Al inside these two IDLs: the internal IDL is poorer in Al than the external one (see tab. 7.6).
- Si precipitates have begun to accumulate at the external IDL, i.e. at the IDL/matrix interfaces, while the internal IDL shows no detectable Si amount (see fig. 6.5 - A). Furthermore, when comparing fig. 6.2 to fig. 6.5 - A, only a small amount of Si was consumed during in-pile irradiation. Indeed, there is no clear evidence of precipitate-free zones (abbr. PFZ) inside the matrix. During in-pile irradiation, Si diffusion towards the U-Mo particles is a wanted effect, as it stabilizes the particles and slows IDL growth (see also chapter 3.3). In the IRIS4 case, the fact that only a low Si diffusion to the particles is visible is attributed to the UO_2 layer around

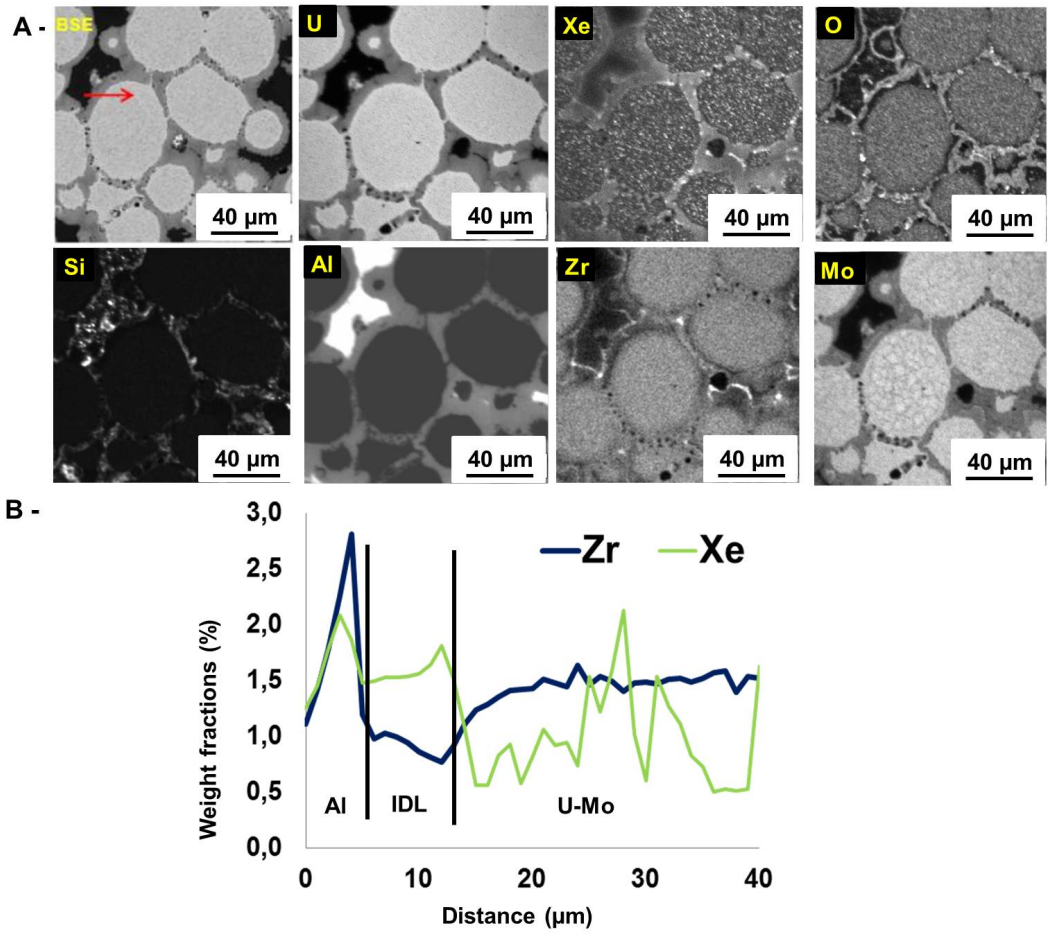

Figure 6.5.: *(A-) EPMA elemental mapping of irradiated IRIS4 fuel. All images were obtained in the meat center. A BSE image is shown together with X-ray maps for U, Xe, O, Si, Al, Zr and Mo. Indicated in the BSE image is the direction of the EPMA linescan shown in (B-). This scan indicates the Zr and Xe weight fractions inside the Al, the IDL and the U-Mo particle.*

the particles. This assumption is made because in similar irradiation tests, like IRIS3 [36], as well as after heavy ion irradiation [4], a total Si diffusion towards the particles has been observed [95]. Concluding, the normally beneficial addition of Si was diminished by the UO_2 layer.

- The presence of the nitride layer did not show any difference of the oxide layer's irradiation behaviour when compared to previous tests involving an oxide coating [109]. Experiments to evaluate the interest of nitride coating are ongoing [107, 108].

- Recrystallization inside the U-Mo particles, as indicated by U-Mo grain subdivision, and its influence on gas bubble size inside the U-Mo cores has been shown to occur in the $2.0 - 5.6 \cdot 10^{21}$ f/cm³ fission density range [97]. Considering the final fission density in plate no. 8043 of $3.76 \cdot 10^{21}$ f/cm³, recrystallization should have begun.

Regarding the elemental map for Mo (fig. 6.5 - A), the distribution of this element inside the particle cores is an indicator for the grain size, which is between 2 and 4 μm before irradiation (see fig. 6.2). For the irradiated case, it is seen that at least this original structure remains in some particles. This leads to the assumption that the process of recrystallization is not complete.

- Additionally, Xe gas bubbles have formed inside the U-Mo particles, at the U-Mo/IDL interfaces, as well as at the IDL/IDL interfaces (see fig. 6.5) - A.

- EPMA linescans were performed across the U-Mo particles, the IDL and the matrix, and an exemplary image is shown in fig. 6.5 - B. In the matrix, a Xe peak is found close to the IDL. This observation is attributed to fission product implantation in the matrix. Inside the IDL, the Xe concentration is almost homogeneous. This leads to the assumption of Xe precipitation into very small bubbles. To analyze fission gas diffusion inside fuels, the weight ratio Xe/Nd is most often used. Nd is considered as a burnup tracer, as this fission product is non-volatile, non-decaying, and has good emission characteristics for mass analysis [110]. However, this is only the case for UO_2 fuels. As seen lateron in chapters 7.5.2 and 7.6.2, Nd is volatile inside U-Mo and precipitates as well.

- Therefore, for analyzing Xe precipitation, the element Zr is used to calculate according Xe/Zr weight ratios, as this element is non-volatile inside U-Mo (see also chapters 7.5.2 and 7.6.2). The weight ratio Xe/Zr indicates the value of 0.7 inside the particles, and 1.3 on average in the IDL (see also tab. 7.7). This is in good agreement with those values measured in IDLs inside U-Mo/Al(Si) fuel plates in close irradiation temperature conditions, but with higher heat flux and burnup [99]: an average value of 0.7 was obtained inside the particles and 1.4 inside the IDL respectively.

7. Thermal Treatments on IRIS4 fuel

After the presentation of IRIS4 fuel manufacturing and in-pile irradiation conditions followed by post-irradiation examinations in the preceding chapter, the following one describes thermal treatments (abbr. ThT) carried out on the in-pile irradiated IRIS4 plate no. 8043. First, the thermal treatment conditions in CEA's LECA-STAR facility are explained. Second, a closer look is taken on the samples' microstructural evolution after ThT at 500°C and 670°C respectively which are the two main gas release temperatures. This chapter closes with a comparison between post-irradiation state, after ThT at 500°C and after ThT at 670°C.

7.1. Sample preparation for thermal treatments

In total, 3 samples were selected from the plate no. 8043 for further treatments and were labelled TMG434, TMD433 and TMD434. As indicated in fig. 7.1, these samples were located near the MFP, and their characteristics may be considered as identical in first approximation. Each sample was cut down to a size of 8×8 mm^2. Also indicated in fig. 7.1 is the sample labelled MA432, on which the PIEs presented in the last chapter were carried out. When considering the MFP, the position of MA432 is almost symmetrical to those of TMG434, TMD433 and TMD434. Therefore, all four samples are considered to have been exposed to the same irradiation conditions, which means the PIEs presented on MA432 are representative for the other three samples.

7.2. Thermal treatment setup and fission gas release monitoring

Successive thermal treatments were performed in the MERARG-2 setup located at CEA's LECA-STAR facility which is fully described in [112], [113] and [114]. A short explanation is given in the following, and an according setup sketch is shown in fig. 7.2. The whole setup is located in a hot cell and consists of an induction furnace connected to a γ-spectrometer for online fission gas release detection. The IRIS4 fuel samples were placed inside a sample

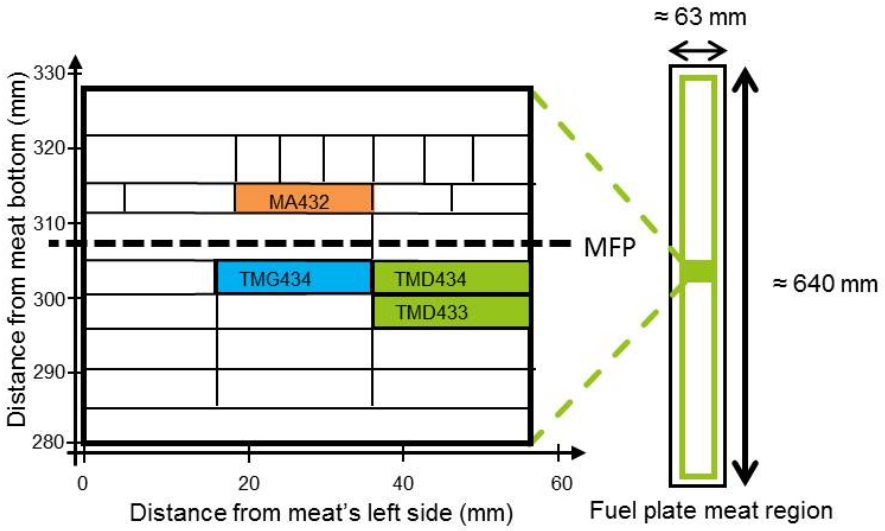

Figure 7.1.: *Sketch of the IRIS4 fuel plate no. 8043 indicating the regions from the samples were cut for further thermal treatments. The PIEs presented in the last chapter were performed on MA432 which was exposed the same irradiation conditions as TMG434, TMD433 and TMD434. The later three samples are heated up until 1800° C (TMG434), 670° C (TMD433), and 500° C (TMD434) respectively.*

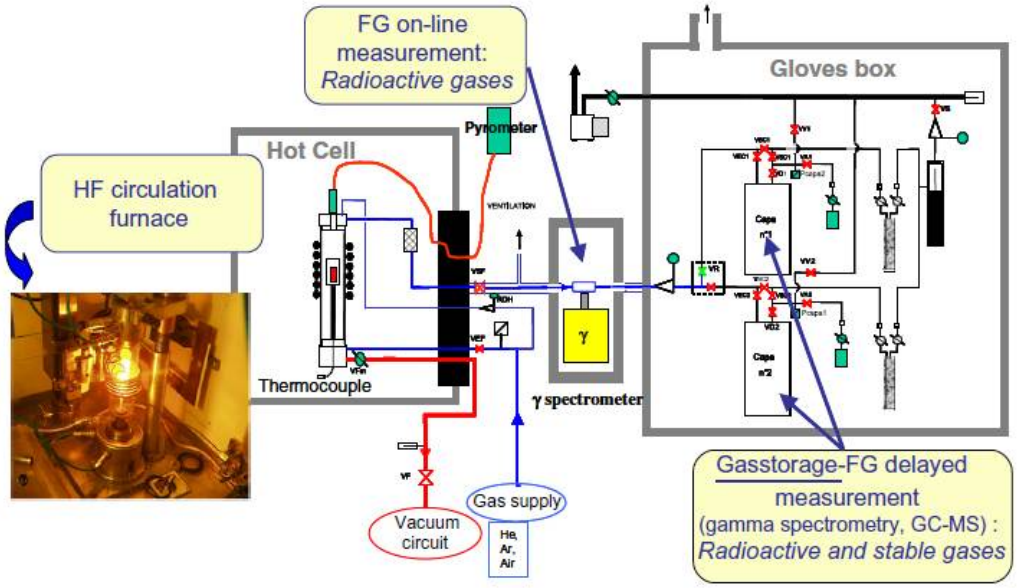

Figure 7.2.: *Sketch of the MERARG setup for thermal treatments and online fission gas release observation [114].*

holder made of molybdenum. This sample holder is placed inside a quartz tube, the actual furnace chamber. An induction coil is wrapped around this chamber, which is also coupled to the sample holder. Sample heating is achieved by high frequency (50 kHz) induction.

During heating, fission products naturally evade from the hot sample. These released fission products are exposed to a constant air or Ar gas jet which enables fission product transport through the furnace chamber, and through a μ-gas chromatograph (abbr. μ-GC) detection system to a storage capacity. During and at the end of the experiment, the capacity and the μ-GC may be isolated from the rest of the system. The capacity is fully unloaded and the integral quantity of the released gas is quantified by the μ-GC. This method takes into account the different detected fission products which each have a unique mobility. In other words, this provides an additional correction and verification opportunity, and two release curves are available as a function of temperature. They are labelled as "sample" (measured by the γ-spectrometer) and "capacity" (measured by the μ-GC).

7.3. Thermal treatment curves

For sample heating, a slow temperature increase of 0.1 $^{\circ C}/_{s}$ was chosen to obtain an accurate characterization of fission gas release. The first heating test, performed on sample TMG434 (location in fuel plate no. 8043 is shown in fig. 7.1), was executed until 1800°C. Goal of this first thermal run was to indicate the main temperature ranges in which main fission gas output is detected. This temperature of 1800°C is higher than the Al and U-7wt%Mo melting point and most of the forming compounds (see tab. 7.1). Therefore, it can be reasonably assumed that at this high temperature only a negligible rest of fission gas remains inside the sample. The release kinetics of ^{85}Kr in this first thermal run are shown in fig. 7.3 - A. Xe release peaks are identical to the ones for Kr indicating that Xe is located at the same positions inside the fuel as Kr, although only the Kr release peaks are shown here. Reason for this is that the measured Xe release quantity is not as precise as the one for Kr [114].

	Al-(2wt%)Si (matrix)	AlFeNi (cladding)	U-7wt%Mo	UAl_2	UAl_3	UAl_4
Melting point (°C)	$\approx$ 650 [115]	582 - 652 [116]	1145 [24]	1590 [98]	1350 [100]	731 [100]

Table 7.1.: *Melting temperatures of materials that could be present in thermally treated IRIS4 fuel. U-Al_x compounds are common U-Al interaction products occurring after in-pile irradiation. The exact cladding melting point depends on the wt% mixture of the different elements inside.*

Below 750°C, three temperatures are of interest: a broad peak below 400°C, a more intense peak at 500°C, and finally a very intense one at 670°C. The later two temperatures were chosen as the maximal temperatures for the two successive thermal runs and are described in detail in the following subchapters. Sample TMD434 was heated up until 500°C and sample TMD433 until 670°C. In the following, the individual thermal runs are abbreviated as ThT1800, ThT500, and ThT670. Both curves can be seen in fig. 7.3 - B and - C where

the reproducibility of the first thermal run is well seen, e.g. when comparing peak no. A2, B2, C2, as well as A3 and C3. The instantaneous ^{85}Kr output values measured in the two later runs are in excellent agreement with the first thermal run. Tab. 7.2 and tab. 7.3 sum up the measured output values. Indeed, the integral ^{85}Kr release was 1.5 to 1.7 $\cdot$ 10^{15} at/g for thermal runs up to 500°C (all ThT), while the value for the later peak was 7.8 (ThT 1800°C) and 8.5 (ThT 670°C) $\cdot$ 10^{15} at/g. The broad release peak below 400°C is associated with the loss of contact between the IDL and the matrix (see also chapter 7.5.1). During heating, above 670°C, several smaller release peaks are observed (labelled A4, A5, A6 and A7). These peaks are associated to the increased U-Al interaction and successive compound melting points (see chapter 7.6.2).
Finally, in the case of the ThT 500°C and ThT 670°C, the Kr release was measured that occurred during sample cooling down to room temperature. It yields 26 ± 3 % (ThT 500°C) and 6 ± 2 % (ThT 670°C) of the total released Kr quantitiy in the according runs. Chapter 7.7.1 provides interpretations on these release peaks.

Temperature (°C)	Fission gas release (%)	
	Per temperature interval	Integrated amount
T < 400	2.4	2.4
400 < T < 500	13.8	16.2
500 < T < 670	57.0	73.2
T > 670	26.8	100

Table 7.2.: *Measured fission gas release fraction in each temperature interval for the ThT 1800°C run.*

Thermal run no.	integral release (10^{15}at/g)		
	≤ 500°C	≤ 670°C	≤ 1800°C
ThT1800	1.7	7.8	10.4
ThT500	1.5	-	-
ThT670	1.6	8.5	-

Table 7.3.: *Integral fission gas release values during the ThT1800°C, the ThT500°C and the ThT670°C run. The unit "g" indicates that Kr release was normalized to the meat weight of each sample.*

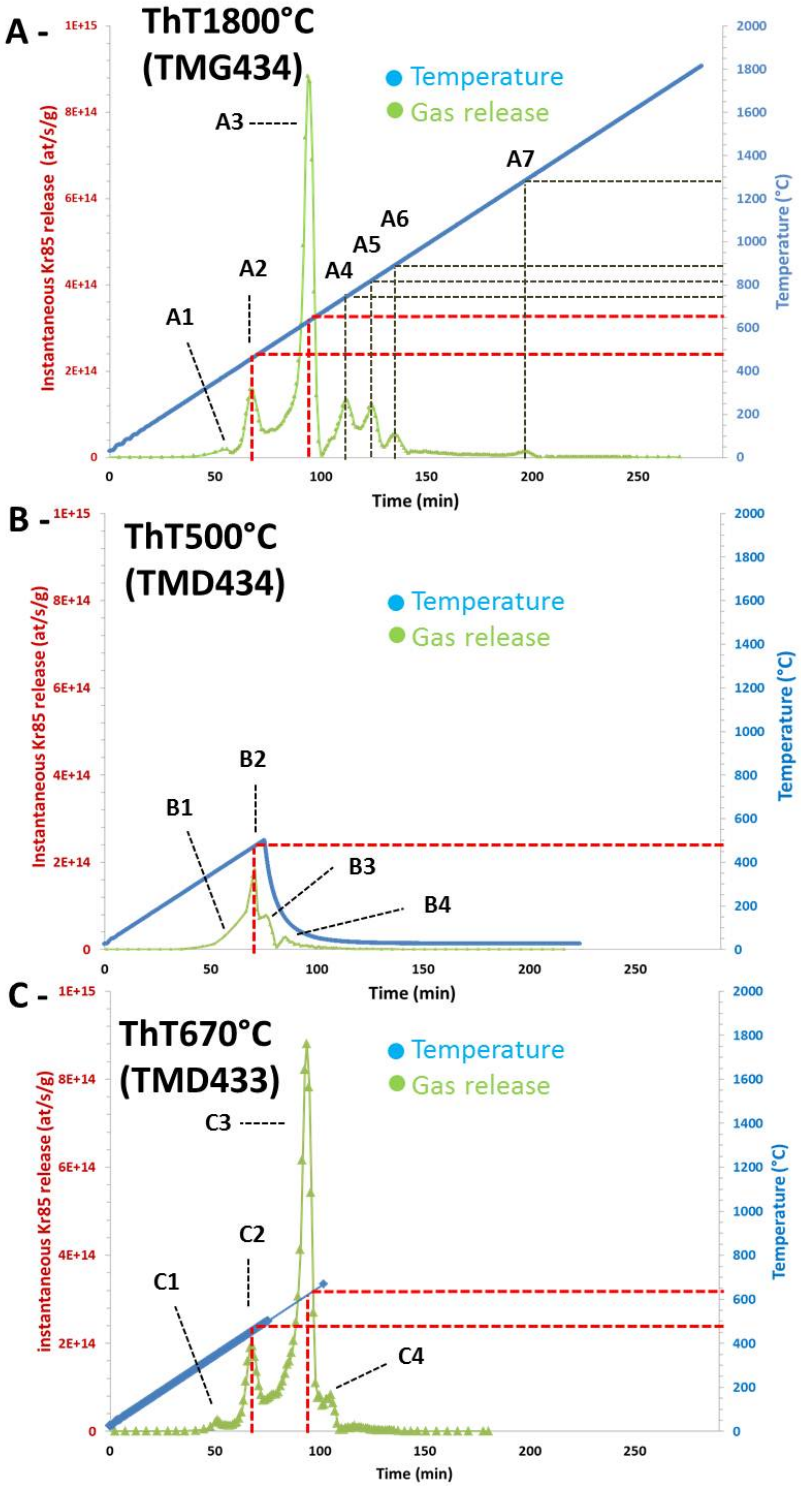

Figure 7.3.: *Measured ^{85}Kr release during the three different thermal treatment runs using similar irradiated IRIS4 fuel samples. The treatments were performed until a final temperature of (A-) 1800° C, (B-) 500° C, and (C-) 670° C. In each curve, the detected release peaks are indicated by a digit.*

7.4. Post-ThT examinations

Due to the high end temperature of the first run, no analyses concerning ThT1800 are presented here, as the sample melted down, and this first test run was aimed to identify the main release peaks. The two other samples were prepared for further investigations by standard metallography techniques: First, transversal cross section have been cut from the samples. To increase the effective observation area, these cross sections were not cut perpendicular to the sample cladding surface, but rather in a slight angle. This led to an artificially larger observable meat region (see also fig.7.4). The resulting cross section were further embedded in an eutectic Wood alloy (50wt% Bi, 26.7wt% Pb, 13.3wt% Sn, 10wt% Cd [101]) which is mandatory to perform EPMA analysis (see chapter 5.2).

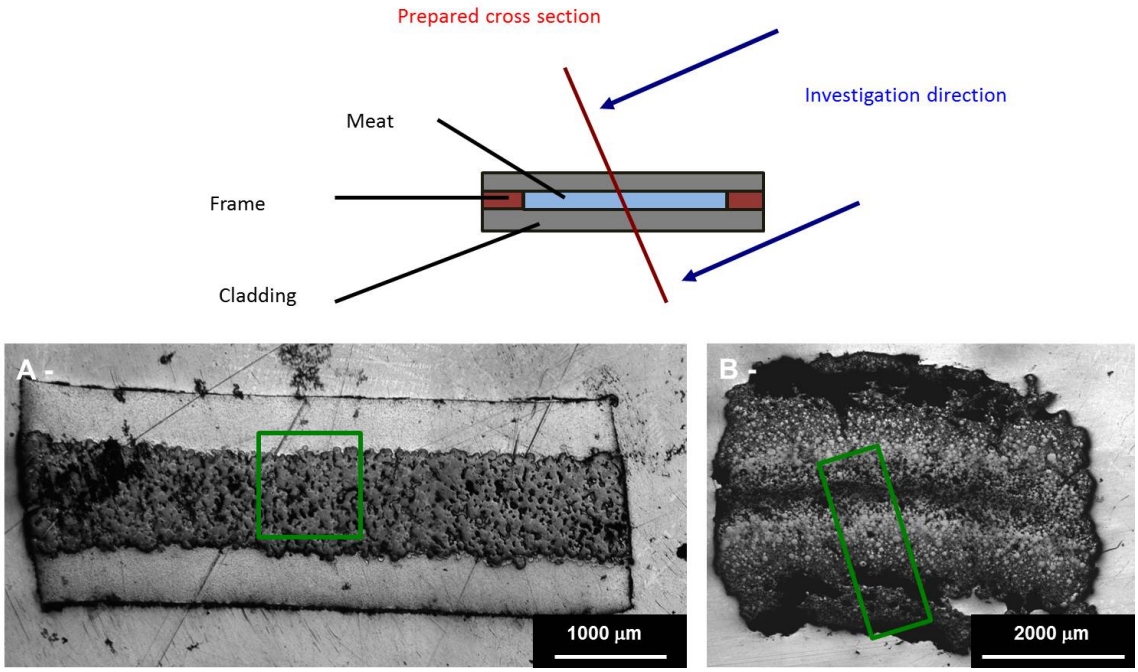

Figure 7.4.: *Global optical microscopy overview of transversal cross sections cut from the ThT500 (A-) and ThT670 sample (B-). Analyzed areas are highlighted in green. To gain an artificially magnified view of the meat region, the cross sections were not cut perpendicular to the cladding surface, but rather in a slight angle (see sketch).*

The first investigation was made by optical microscopy to obtain a global view of the samples. The sample ThT500 is shown in fig. 7.4 - A, while ThT670 is presented in fig. 7.4 - B respectively. In the ThT500 case, a clear distinction between the meat and the cladding can be made. This is no longer the case for ThT670, where a strong intermixing between the meat and the cladding region has occurred.
In the following, ThT500 and ThT670 will be examined by both EPMA and lab scale XRD. XRD techniques were performed inside a shielded "XRD 3003TT" setup in a horizontal Bragg-Brentano geometry (see chapter 5.5). A monochromatic X-ray beam ($\lambda = 1.54060$ Å) produced by a copper tube was used. Unfortunately, the signal-to-noise ratio was very

poor. EPMA was carried out by a "SX100R" device from CAMECA with an according acceleration voltage of 20kV and a beam current of 200 nA.

7.5. Results on ThT500

7.5.1. EPMA SE

EPMA SE images of sample TMD434 (see fig. 7.1) were taken in both the meat center and at the meat/cladding interface and are shown in fig. 7.5. Inside the U-Mo particles, big cracks of around 30 μm in length are visible. Fissures of the same length can be observed in the IDL. Contrary, the matrix exhibits no such fissures. The size of the fissures is the same in the meat center and in regions at the cladding interface. Considering the IDL surface fraction, a 30% increase compared to the pre-ThT state is visible (see fig. 6.5 and chapter 7.5.2). This further IDL growth by thermal annealing is in full agreement with chapter 3.2.2.

	Surface fraction in %		
	U-Mo	IDL	Al
After in-pile irradiation	46	35	19
After ThT at 500°C	48	46	5

Table 7.4.: *Surfrace fraction of U-Mo, IDL, and Al in the meat center determined by X-ray mapping analysis of Al and U. Large porosities are excluded from this analysis. No surface calculations were made in the ThT670 sample, as its microstructure is no longer homogeneous.*

Moreover, large and interconnected "holes" are observed at IDL/Al interfaces (indicated by blue circles in fig. 7.5. These holes are also detected after thermal treatments on fresh, non-irradiated U-Mo/Al fuels [117], but not in irradiated fuels without any thermal annealing. Indeed, when exposing fresh fuel to two successive thermal treatments (2 hours at 475°C followed by 4 hours at 550°C), the abovementioned effect is observed as well. This suggests that the appearance of these holes is not caused by fission gases. Instead, this effect is attributed to different thermal expansion coefficients of the compounds inside the sample (see tab. 7.5). This is further discussed in chapter 7.7.

Material	Thermal expansion coefficient α_T (10^{-6} K^{-1})
U-8wt%Mo	17.3
Al	27.5

Table 7.5.: *Thermal expansion coefficients for U-Mo and Al at 500° C [24]. At this temperature, Al has 1.6 times the value of U-Mo.*

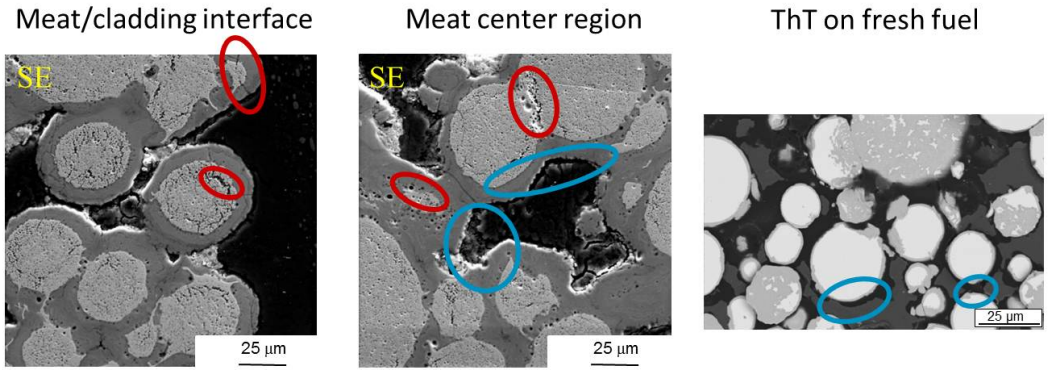

Figure 7.5.: *Two SEM images from the irradiated and thermally treated IRIS4 ThT500 sample: The middle image is representative for the meat center region, while the image at the right represents the meat/cladding regions. Highlighted in red are areas inside the sample where fissures occurred during the thermal run. Also, highlighted in blue are areas ("holes") where the IDL and the matrix lost contact with each other. These holes are also visible in non-irrdiated U-Mo/Al fuels after thermal treatments. An image of this behaviour is shown on the right [117]. Please note that the right image was taken in BSE mode, while the other two were taken in SE mode.*

7.5.2. EPMA elemental mapping

EPMA X-ray mapping results are shown in the two next images. In fig. 7.6, the distribution of Si and Al in both the meat center region and at the meat/cladding interface is shown. Accordingly, fig. 7.7 shows the Xe, Nd and Zr distribution in the same regions. According images of the as-irradiated state are shown in fig. 6.5.

- **Si**: The strongest difference compared to the pre-ThT state is the location of Si. After the thermal run until 500°C, no Si remains in the matrix any longer. It rather diffused towards the U-Mo particles and accumulated homogeneously in the internal IDL, with a concentration of up to 4 at%. At some locations, even larger Si precipitates exist at the IDL/matrix interface or even inside the IDL (see red circles in fig. 7.6). While a SiRDL is observed in post-manufacturing analysis of fresh fuel (see chapter 3.3), an enhanced Si precipitation was also observed in the IRIS4 fuel after in-pile irradiation (see chapter 6.4).

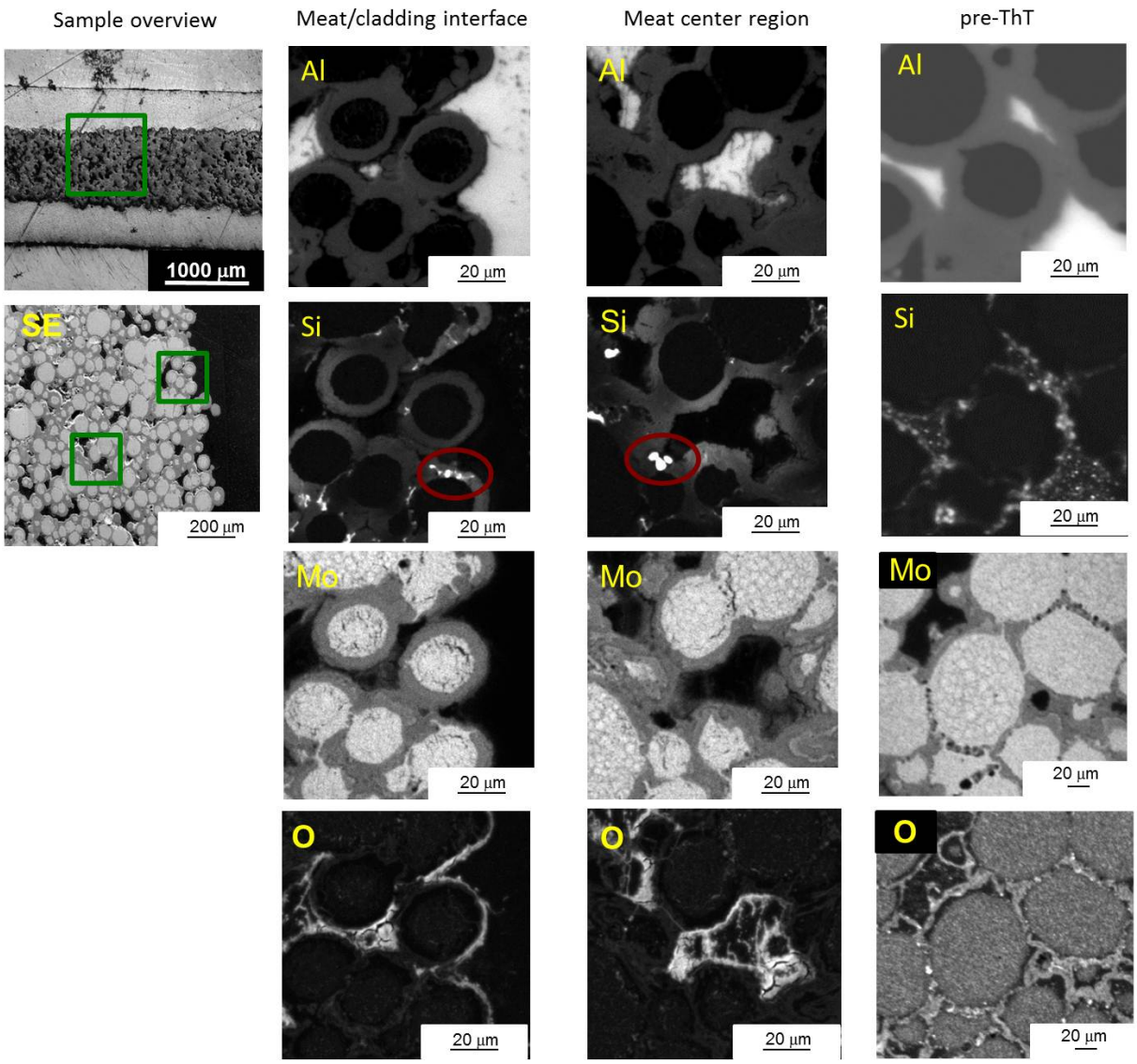

Figure 7.6.: *Al, Si, O and Mo EPMA elemental maps of the ThT500 sample and comparison with the pre-ThT state. On the left, the regions in which these maps were acquired are highlighted by green rectangles. In the Mo map, intergranular grains are visible inside the U-Mo particles. Si accumulation is well observed inside the IDL after thermal treatment. Red circles represent areas of massive Si accumulation. The two maps of the pre-ThT are taken from [54].*

- **O** and **IDL**: Oxygen has partially diffused from the external IDL into the matrix. As already seen in pre-ThT examinations, the external IDL is still richer in O than the internal one. This confirms the SE observation in chapter 7.5.1 that the IDL still exists in its duplex state. However, the whole IDL's surface fraction has increased, while an Al decrease has been detected. The according Al contribution to the measured elemental surface fractions decreased from 19% to 5%. An overview of these values is given in tab. 7.4 and tab. 7.6.

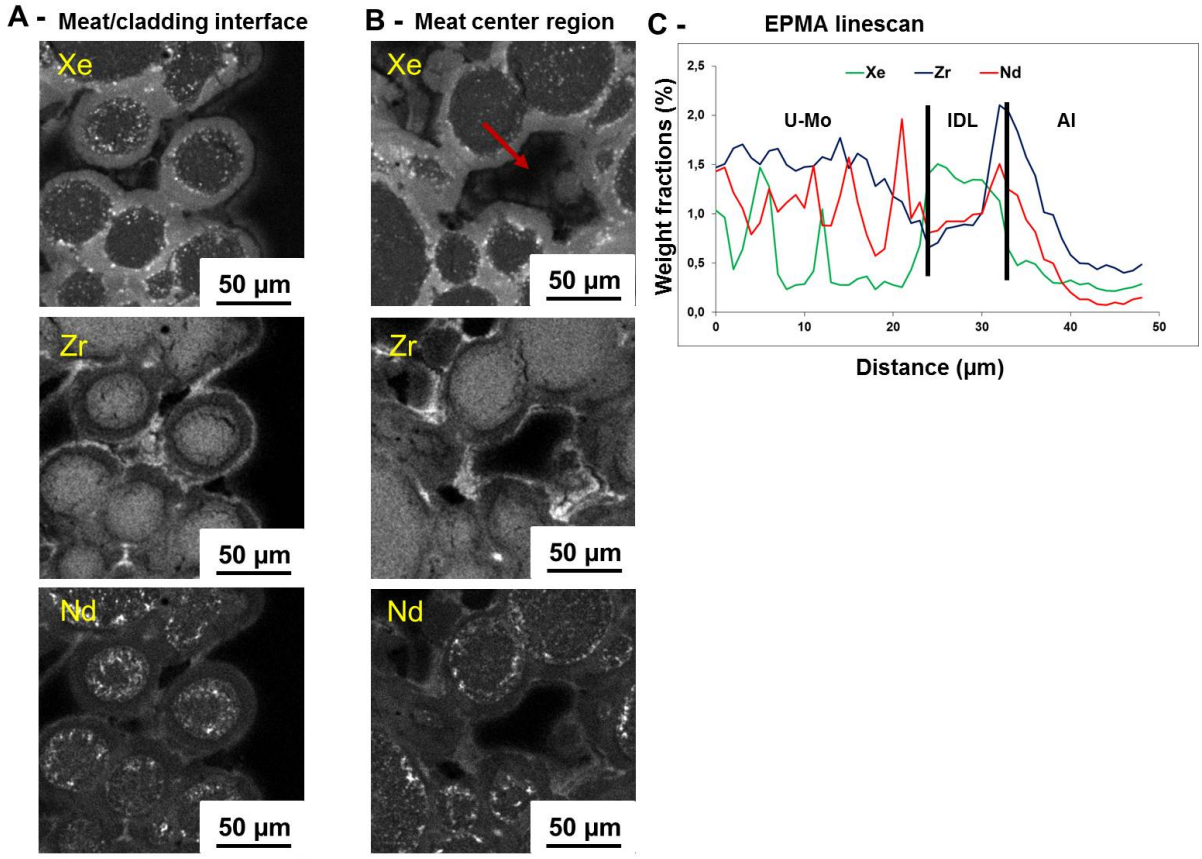

Figure 7.7.: *EPMA mapping of Xe, Nd and Zr distribution in the same regions already shown in fig. 7.6. Indicated by a red arrow is the direction of a linescan to determine the quantity of these elements inside the U-Mo particle, the IDL, and the matrix.*

- **Xe**: Fission gas bubbles are no longer homogeneously distributed in the U-Mo particles. As seen in fig. 7.7, inside the particles Xe can only be detected close to the U-Mo/IDL interfaces, while it has completely vanished from the particle cores. Inside the IDL, three different parts are detected. First, a large amount of bubbles can be seen close to the U-Mo/IDL interface. Second, a homogeneous Xe concentration of 1.3wt% is observed inside the IDL. This leads to the assumption of small Xe bubbles at this location[1]. Third, at the IDL/matrix interface, a value of up to 0.5wt% is measured. This value is significantly lower than the one for the pre-ThT state (see also fig. 6.5). Therefore, no Xe accumulation can be evidenced at this location after annealing at 500°C. This is attributed to the U-Al intermixing at this regions which enabled Xe gas release. However, EPMA can only deliver sample surface information due to a low beam penetration depth. Therefore, EPMA measurements do not deliver a definitive conclusion concerning fission gas behaviour inside the U-Mo particle core. If Xe gas had accumulated in large bubbles, these

[1]Bubbles with sizes smaller than 0.1μm cannot be detected by EPMA.

larger bubbles could have been destroyed by the sample cutting process and thus, the gas enclosed in these bubbles would have evaded from the sample immediately.

- **Nd**: Nd has accumulated in the outer part of the U-Mo particles, mainly near cracks. The according concentration is lower in the particle core than at U-Mo/IDL interfaces. A second Nd accumulation is visible at IDL/matrix interfaces. This indicates that Nd is not soluble in U-Mo fuels, contrary to UO_2 fuels [119]. Therefore, it cannot be used as burnup tracer.

- **Zr**: The Zr concentration inside the U-Mo particles is homogeneous for both the pre-ThT and ThT500 states inidicating that this element is soluble inside U-Mo and can be used as burnup tracer. An average weight fraction of 1.5% for both states is measured (see tab. 7.7). Inside the IDL, Zr has accumulated at the IDL/matrix interfaces, and an average weight fraction of 1.1% is measured there. This indicates a Zr diffusion towards the oxygen-rich external IDL.

- An **EPMA linescan** of Xe, Nd and Zr has been acquired beginning in the U-Mo particle cores, throughout the IDL and ending in the matrix. The according weight fractions are shown in fig. 7.7 - C. The Xe weight fraction inside the particles has a value of 0.17wt% on average which is lower than the pre-ThT value of 0.33wt% [54]. Inside the internal IDL, the obtained value of 1.8 is higher than in the pre-ThT state of 1.33 [54]. In the external IDL, the Xe amount of 0.5 is lower than in the pre-ThT state (0.8) [54].

- The **Xe/Zr weight ratio** for the pre-ThT, the ThT500 and the ThT670 state are listed in tab. 7.7 and individual elemental weight fractions are depicted in fig. 7.8. The average Xe/Zr weight ratio of 0.4 is found inside the particles (pre ThT: 0.7), while an average value of 0.8 is measured inside the internal IDL (pre ThT: 1.0 to 1.3). The value has significantly decreased in the particles and the external IDL, while it roughly remained the same in the internal IDL. Therefore, a comparison between Xe and Zr suggests that a thermal treatment at 500°C has induced Xe precipitation from the particle cores towards the internal IDL due to a Xe concentration gradient between these two areas. For Xe gas already inside the IDL, thermal treatment has reduced the amount inside the external IDL, which led to the assumption of fission gas release from these regions during the thermal runs.

7.5.3. XRD

As mentioned, due to the lab scale XRD setup, only a small number of counts could be collected, which delivers a poor signal-to-noise ratio. The phases indentified in the pattern shown in fig. 7.9 are α-U, γ-U-Mo, Al and UAl_3. Due to the in-pile irradiation and the thermal treatment at 500°C, the identification of α-U is well expected [118], as it

	(Al+Si)/(U+Mo) atomic ratio		Si concentration in %	
	Internal IDL	External IDL	Internal IDL	External IDL
After in-pile irradiation	4-5	5-6	-	-
After ThT 500°C	3-7	> 7	2-4	-
After ThT 670°C	3.3 - 9.6		1 - 5	

Table 7.6.: *IDL elemental composition as determined by quantitative EPMA linescans in in-pile irradiated IRIS4 fuels. Comparison between as irradiated and post-thermally treated fuel samples up to 500°C and 670°C respectively. In the 670°C case, no distinction is made between internal and external IDL; atomic ratio values show the evolution from the meat towards the cladding area. Accordingly, Si concentrations in the 670°C case are only releveant for IDLs around particles in the meat center (see also subchapter 7.6).*

		Weight fractions (wt%)					
		U-Mo core			IDL		
		Xe	Zr	Xe:Zr ratio	Xe	Zr	Xe:Zr ratio
pre-ThT	meat center	1.1	1.5	0.7	1.8	1.4	1.3
	near cladding	1.1	1.5	0.7	1.4	1.4	1
ThT500	meat center	0.6	1.5	0.4	1.0	1.2	0.8
	near cladding	0.6	1.2	0.5	0.9	1.0	0.9
ThT670	meat center	0.3	1.5	0.2	1.1	1.5	0.7
	near cladding	-	-	-	0.2	0.8	0.2

Table 7.7.: *Xe:Zr weight fractions as measured by EPMA at the three different states: as-irradiated, after ThT500 and after ThT670.*

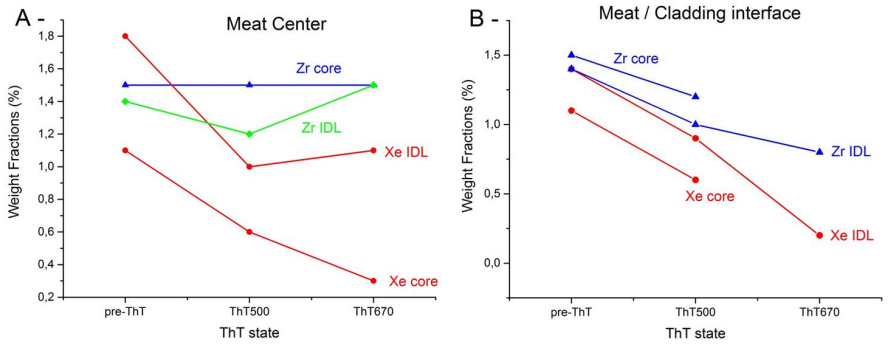

Figure 7.8.: *Xe and Zr average weight fractions in the (A-) meat center region and (B-) at the meat/cladding interface after the different thermal treatments.*

confirms the γ-U destabilisation under these conditions (see chapter 2.3.1). Accordingly, the γ-U-Mo lattice parameter decreased to 3.427Å from the former pre-ThT value of

3.44Å. This value is expected for in-pile irradiated γ-U-Mo fuel at temperatures around 100°C [24]. Also, the occurrence of UAl_3 as a common U-Al interaction is found. These peaks indicate a beginning IDL recrystallization which is expected at temperatures above 350°C (see chapter 3.2.1). However, according UAl_3 Bragg lines of the (1 0 0) and the (1 1 0) direction were not found in the pattern. The reason for this observation is still an open question. Further identified phases belong to Al, Bi and Sn. While Al is naturally found due to its contribution to the fuel matrix and cladding, the elements Bi and Sn are detected, as they are part of the Wood alloy in which the samples were embedded for EPMA analysis.

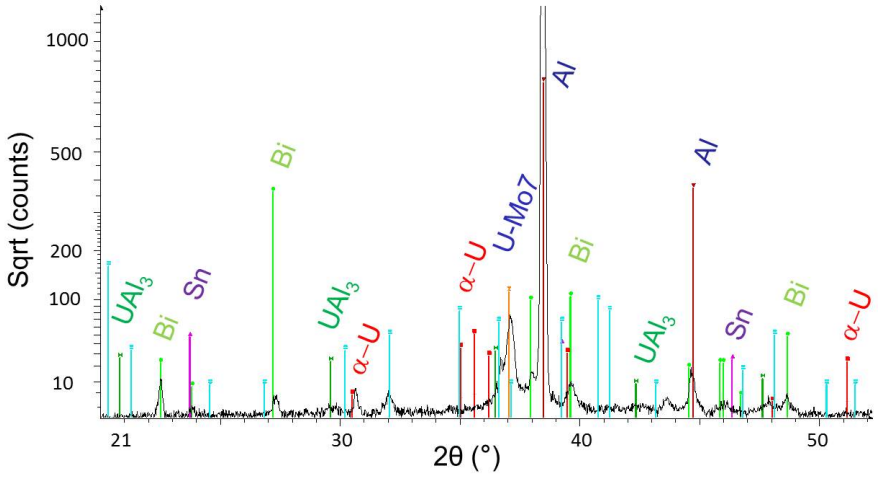

Figure 7.9.: *XRD refinement on the ThT500 sample. Identified phases include α-U, γ-U-Mo, UAl_3, Al, Sn and Bi. Please note the significant discrepancies between the expected peak height (in color) and the measured ones (in black).*

7.6. Results on ThT670

Identical to the ThT500 sample analysis, sample TMD433 (see fig. 7.1) has been characterized by the same methods. However, as already shown in fig. 7.4, this sample shows strong structural changes from the meat center regions towards the cladding interface due to the AlFeNi cladding melting point lying below 670°C (see tab. 7.1). Therefore, a more detailed description of the meat center and meat/cladding interfaces is given in the following.

7.6.1. EPMA SE

Only in the meat center region can the microstructure still be detected (see fig. 7.4 - B). An increasing U-Al interaction is observed in regions closer to the cladding interface. While the particle structure can still be observed in the meat center (see fig. 7.10 - B), at the meat/cladding interface a complete interaction occurred (see fig. 7.10 - A).

In the meat center, fissures can be detected as well (see red circles in fig. 7.10 - B). Compared to the ThT500 sample (see fig. 7.5), those fissures found in the meat center are not larger in size in comparable regions, even as the final temperature was higher. However, near the cladding interface, particles can hardly by detected, as huge porosities up to several tens of micrometers in diameter have formed (see green circles in fig. 7.10 - A).

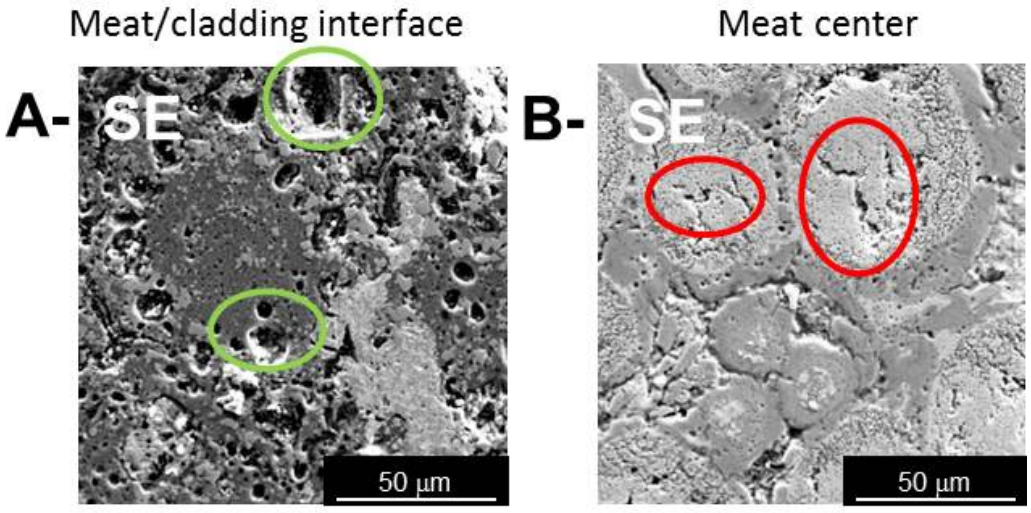

Figure 7.10.: *SE images of the ThT670 sample taken (A-) at the meat/cladding interface and (B-) in the meat center region. While the fuel microstructure can still be detected in the meat center, a total interaction occurred at the meat/cladding interface.*

7.6.2. EPMA elemental mapping

Large scale EPMA elemental maps shown in fig. 7.11 provide a global EPMA overview of this sample. In contrast, small scale EPMA mapping is presented in fig. 7.13, which provides an in-depth obersevation of selected regions highlighted by orange boxes in these two figures. The results for each element are:

- Most probably, **Al** has the same behaviour before strongly interacting with the U-Mo particles. Indeed, the interaction with the particles gets stronger the closer to the meat/cladding interface.
  - At the meat/cladding interface, a total interaction occurred. Al is now homogeneously distributed inside the particles (see fig. 7.13 - C), while the matrix shows almost no sign of this element. Indeed, a matrix cannot be easily identified any longer, as no clear distinction can be made between matrix and particles. Regions which most probably belonged to the matrix show large porosities.
  - In the meat center, a less drastic U-Al interaction happened. Only the beginning of U-Al interaction can be observed here (see white circles in fig. 7.13 - J).
- **O** and **IDL**:
  - Close to the initial cladding location, the oxygen is heterogeneous with concentrations up to 20wt%.
  - In the meat center, oxygen is homogeneously distributed inside the IDL which makes a clear distinction between external and internal IDL no longer possible.
- **Zr**:
  - In the meat center, the measured weight fraction inside the particles is 1.5wt% and is identical to the one inside the IDL.
  - At the meat/cladding interface, Zr has precipitated in the U-Al interaction areas. An average weight fraction is measured to 0.8wt%.
- At the cladding regions, several new compounds have formed. Comparing the elemental maps of Al (7.13 - C), U (7.13 - D), Si (7.13 - E) and Mo (7.13 - G), the regions rich in U are lacking Al and Mo. In contrast, regions rich in Si can be found at the same location as U. As conclusion, it can be assumed that $\mathbf{Al}_x\mathbf{Mo}_y$ and $\mathbf{U}_x\mathbf{Si}_y$ compounds have formed due to the different chemical affinities of the elements towards each other (see also chapter 3.3 about the SiRDL formation).

- Analysis of **Mg** and **Fe** (not shown) indicates that these elements, which are initially only present in the AlFeNi cladding and the AG3NE frame, have strongly diffused towards the meat center. In the meat center, both elements are mainly found in the remaining IDLs, but not in the U-Mo particle cores. This underlines the strong affinity of Mg towards Al which is higher than towards U [165].

- It is further of interest to quantify the **U-Al interaction strength**. When calculating the (Si+Al):(U+Mo) atomic ratios from the meat center towards the meat/cladding interface, the value increases from 3.3 in the center to 9.6 at the cladding (see also fig. 7.12 - B). For the meat center, these values were calculated in IDL regions, whereas for the cladding regions, no IDL could be detected any longer. Therefore, at the cladding regions, lesser data points could be acquired to calculate this value. Fig. 7.12 visualizes the increasing U-Al interaction from the meat center towards the cladding. This indicates the enhanced U-Al interaction when more Al is available, i.e. at the cladding. This is further discussed in chapter 7.7.1.

- In the case of **Xe** (see fig. 7.14), this element is only faintly detected at the cladding interface, while a still greater amount is located in the meat center. EPMA linescans have been performed in both the meat center, intermediate regions between center and cladding, and in the cladding interface. Two EPMA linescans, namely in the meat center and the cladding, are shown in fig. 7.15. The Xe weight fraction in the cladding was quantified to an average amount of 0.15wt%, whereas the value of 0.34wt% was measured in the meat center inside the U-Mo cores.

- In the meat center (region 5 in fig. 7.14) the **Xe:Zr weight ratio** is 0.2 insinde the particles and 0.7 inside the IDL. At the cladding interface, the value of 0.2 is measured.

- The diffusion of **Nd** at this temperature towards the U-Mo/IDL interfaces and also into the IDL has also been detected (no image is shown). According to the peaks in the linescans in fig. 7.15, both Nd and Xe clusters remain inside the material.

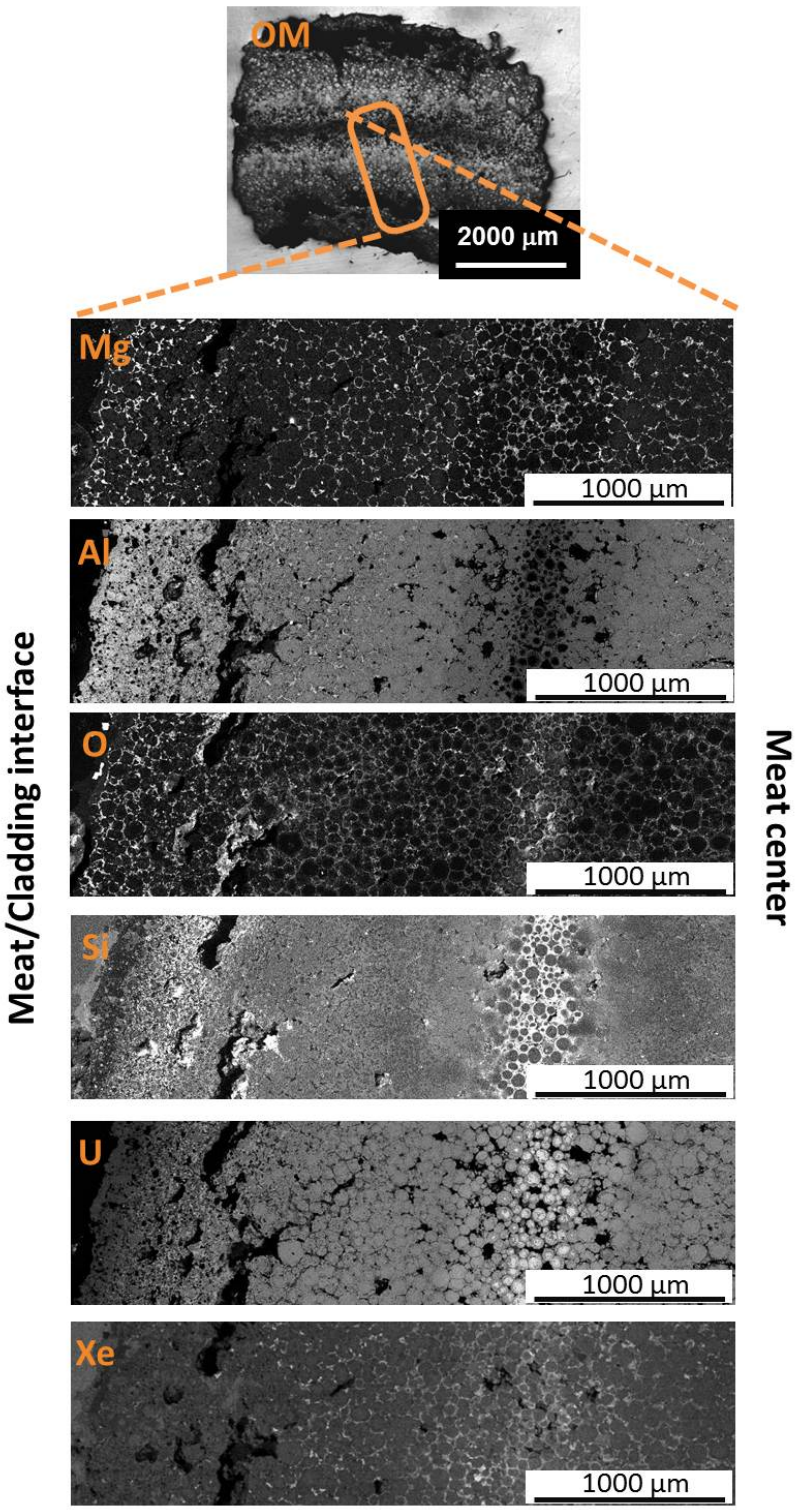

Figure 7.11.: *EPMA elemental mapping of the ThT670 sample in large scale. The left side of each map shows the meat/cladding interface while the right hand side shows the meat center. Elemental maps show the distribution of Mg, Al, O, Si, U and Xe. In the Xe map, five orange boxes are highlighted which mark the region for further small scale Xe investigations shown lateron.*

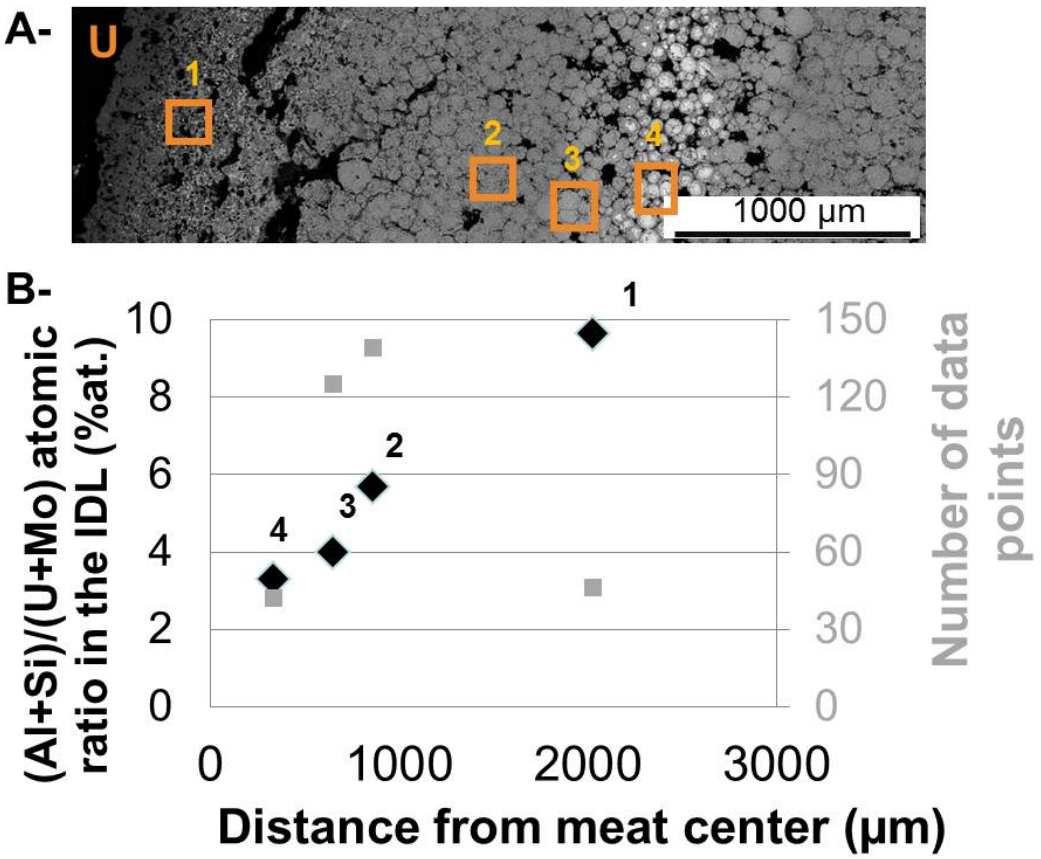

Figure 7.12.: *(A-) EPMA mapping of U. Indicated are 4 regions where a small scale investigation has been performed. (B-) Evolution of inceased U-Al interaction the closer one gets to the meat/cladding interface.*

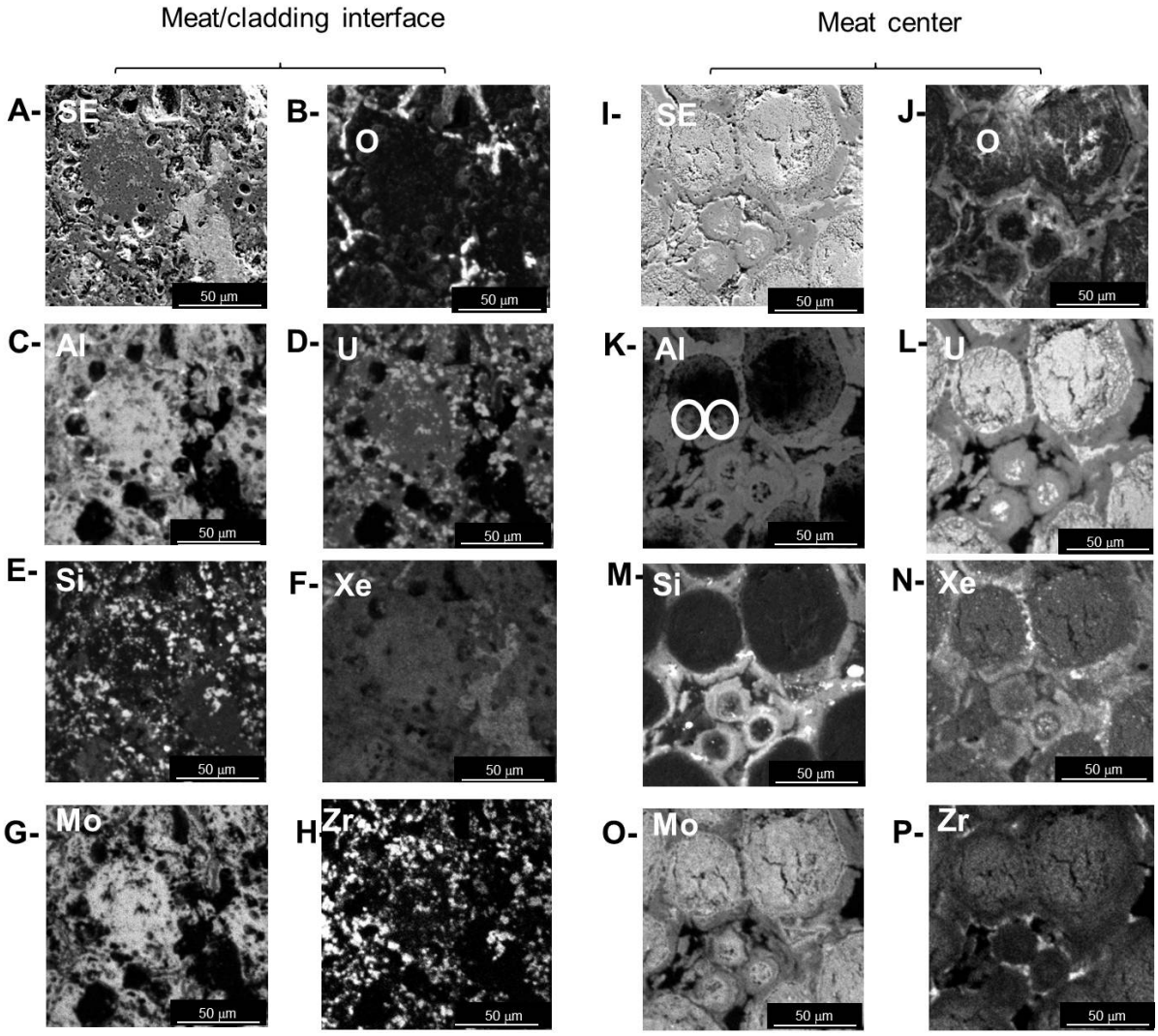

Figure 7.13.: *EPMA SE images (A- and I-) and EPMA small scale elemental mapping for the ThT670 sample. On the left hand side, the meat/cladding interface is shown, while on the right hand, the meat center is pictured. White circles in (K-) represent areas of starting Al diffusion into the U-Mo particles.*

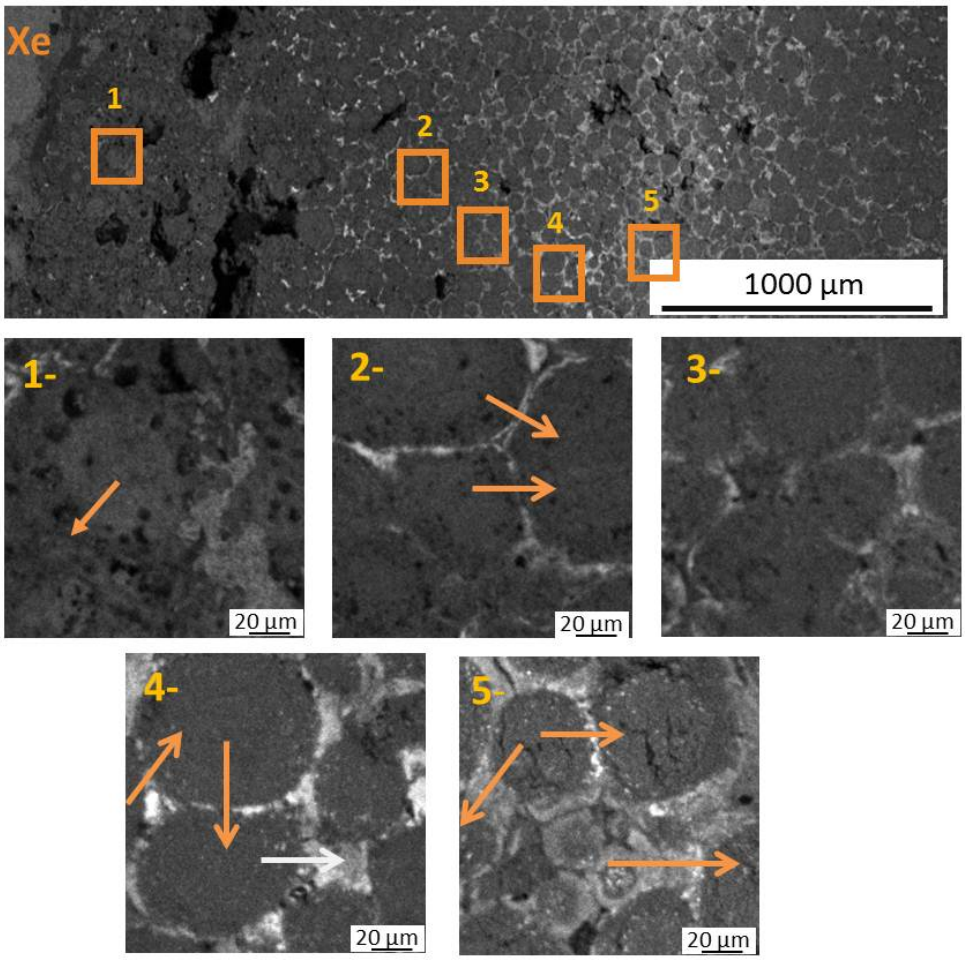

Figure 7.14.: *EPMA elemental mapping of Xe distribution. Below, small scale images of the same five selected regions as in fig. 7.12 are shown. Indicated by orange arrows are the direction of EPMA linescans performed in these regions in order to calculate Xe weight fractions and Xe/Nd weight ratios. In region 3 no linescan was obtained as this area was considered identical to region 2.*

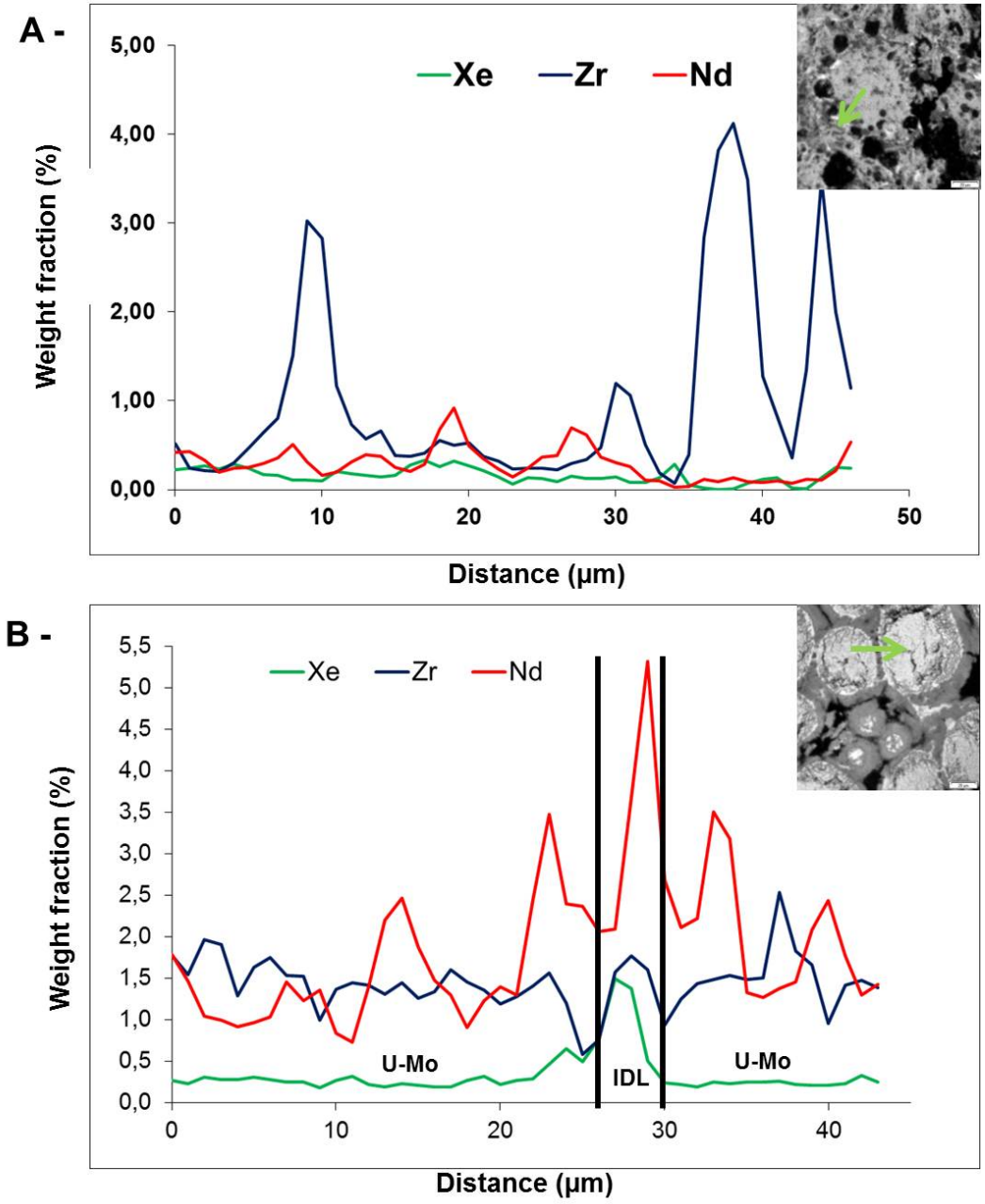

Figure 7.15.: *EPMA linescans showing the Xe and Nd weight fractions at (A-) the meat cladding interface and (B-) the meat center. Linescan directions are highlighted by arrows in according images. Image (A-) corresponds to region no. 1 and image (B-) to region no. 5 in fig. 7.14.*

7.7. Discussion

7.7.1. Temperature dependent microstructural evolution

Currently, little information is available considering microstructural evolutions in irradiated research and test reactor fuel after thermal annealing. Until now, most data considering this topic has been collected on an UAl_x/Al fuel plates which had undergone a coolant flow blockage incident [120]. For U_3Si_2, if thermal treatments (also called blister tests) were performed, only a few destructive examinations were made [89]. The results obtained in this thesis are illustrated and summed up in tab. 7.8 and tab. 7.11. Three topics are to be discussed in detail: the U-Mo particle behaviour, the IDL evolution and the Xe release mechanisms together with the behaviour of Si and O during thermal annealing.

Temperature(°C)	Integral/cumulated fission gas release (%)	Suspected location of released gas
< 400	2.4/2.4	Volumes close to sample surfaces
$400 < T < 500$	13.8/16.2	from IDL/matrix interfaces: • external IDL • large porosities at interfaces • from Al (implanted gases)
$500 < T < 670$	57.0/73.2	U-Mo particles closer to the cladding + IDL at total interaction regions
$T > 670$	26.8/100	U-Mo particle cores in the meat center until total interaction with Al/meltdown

Table 7.8.: *Measured total fission gas release and assumption of release locations inside the material.*

U-Mo particles

In-pile irradiation causes γ-U-Mo stabilisation together with an intergranular grain size decrease due to recrystallisation [121, 142, 143]. The thermal treatment at 500°C has caused a γ-U destabilisation resulting in the formation of α-U (see chapter 2.3.1). This has been shown by both XRD and EPMA elemental mapping. In the according Mo map (see fig. 7.6), the U-Mo intergranular grain boundaries are very well visible. Moreover, the onset of fissures inside the particles are observable. At ThT670°C, grains inside the particles are no longer visible. According fissures inside the particles have not grown in size when compared to the ThT step at 500°C.

IDL

At 500°C, an IDL thickness increase is observed all over the fuel meat compared to the pre-ThT state. However, this effect is also well observed after thermal annealing tests in fresh U-Mo systems [122]. In the following, the focus is on the microstructural changes at 670°C.
Generally, it is assumed that no strong thermal gradient existed throughout the whole sample. First, the overall sample thickness with 1.3mm was thin, but typical for plate type fuel. Second, the thermal conductivity of Al ($\approx 240\,^{W}/_{m\cdot K}$ [164]) and U-Mo ($\approx 10\,^{W}/_{m\cdot K}$ [24]) is known and considered sufficiently high. Despite the thermal conductivity of the IDL is not determined yet, it is assumed that the IDL contribution is not of importance at this low heating rate of $0.1°C/s$. For these reasons, only the available amount of Al is considered to be responsible for the heterogeneous U-Al interaction along the meat center - cladding direction. Three arguments are proposed to strengthen this statement:

- Elements from the cladding, for example Mg, are found in the interacted U-Mo particles after ThT670 (see fig. 7.11). Therefore, it is likely that Al from the cladding also diffused towards the meat center region. Additionally, U-Mo particles are likely to be mobile during the ThT as well, i.e. towards the cladding interface, as the cladding and the matrix melting temperature are below 670°C (see tab. 7.1).

- Thermal annealing tests of U-Mo/Al systems have also been performed recently by Ryu et al. [123, 124]. In that work, 4 different non-irradiated U-Mo/Al compacts with an according U loading from 10 to 50 vol% were exposed to thermal annealing until 700°C. SEM analyses of those samples have also shown a full interaction between the particles and the matrix for the lowest U loading, and the IDL quantity has decreased with increasing U loading. However, some differences between the experiment presented in this thesis and the work of Ryu exist: fresh versus irradiated fuel sample, different Mo content (10wt% versus 7wt%), coating (none versus oxide), matrix composition (pure Al versus Al2wt%Si), heating rates (10°C/min versus 6°C/min) and final temperatures (700°C versus 670°C). Nevertheless, the similarities between both experiments are striking. In this work, U-Mo particles close to the cladding exhibit the same behaviour as those from Ryu's experiment with a 10 vol% U loading. Also, in this work particles in the meat center behave similar to those in the annealed compacts with a 50 vol% U loading.

- By differential scanning calorimetry (DSC), Ryu has shown that a strong exothermic reaction occurred at 650°C for all compacts with 10 to 50 vol% U loading, i.e. also the same loading as the IRIS4 samples used in this work (50 vol%). It was also found that the interaction strength, e.g. the reaction heat, increased with decreasing U loading (see tab. 7.9). This can be associated with the strong fission gas release peak detected at 670°C (see fig. 7.3 - A and - C). As a conclusion, the lower the local U loading, the stronger is the interaction. This explains the observation that the meat

center could retain the U-Mo particle shape, while a total interaction occurred at the meat/cladding interface.

U loading (vol %)	Reaction heat (J/g)
10	150
30	240
40	175
50	100

Table 7.9.: *Measured reactions heat depending on U loading inside U/Al compacts [124].*

Si and O

At 500°C, the external part of the IDL remains enriched in O. At 670°C, the duplex IDL structure is less obvious in the meat center. Close to the cladding, some continious regions enriched in O remain even in the case of full U-Mo/Al interaction. O-enriched areas can be considered most probably as a marker of the previous U-Mo particle (and IDL) location. Therefore, this element helps in distinguishing the individual U-Mo particles (see fig. 7.11 and fig. 7.13). Moreover, this observation indicates a high oxygen solubility inside the material.
Considering Si, its full diffusion from the matrix towards and into the internal IDL at 500°C is observed. Such a homogeneous Si distribution inside an IDL has, to the author's knowledge, not been reported in literature. At temperatures of 670°C, in the fuel meat center this behaviour did not increase in strength. Contrary, at the cladding interface U_xSi_y compounds have formed with a low Al and Mo content. Also at 670°C, both Si and O cannot prevent U-Mo/Al interaction.

Xe release

Based on the microstructural observations in both annealed samples and the detected fission gas output peaks presented in chapter 7.3, regions of fission gas output are proposed (see also tab. 7.8):

- At temperatures below 400°C, 2.4% of the total fission gas output occurred. No clear explanation can be provided for the release peaks at 400°C (labelled A1, B1 and C1 in fig. 7.3). It was found that the Xe diffusion length in pure Al is in the range of several μm at this temperature [125]. Considering a 10 times higher density for U-7wt%Mo compared to Al, it is assumed that fission gas has been released from volumes close to the sample surfaces.

- Between 400 and 500°C, 13.8% of the total output occurred. The main locations of fission gas release are located at the IDL/matrix interface and inside the IDL where the aforementioned holes are located (see chapter 7.5.1). Therefore, fission gas has also been released from these parts of the sample through interconnected porosities (see fig. 7.5). The formation of holes is attributed to the different thermal expansion coefficients of the individual compounds inside the sample. The resulting internal stress enhances bubble growth (see chapter 4.1.3). This in turn leads to an enhanced gas pressure resulting in gas release. Fissures inside the U-Mo particle cores are generally not connected to these free volumes and therefore, only a small amount of fission gas release occured out of particle cores.

- Between 500 and 670°C, 57% of the total output were observed. Here, the output happened from regions where total U-Al interaction already occurred. Therefore, gas from the former U-Mo particle cores and the IDL could be released due to total interaction.

- For temperatures above 670°C, different compounds inside the material are expected to melt leading to fission gas release. According to fig. 7.3 - A and tab. 7.1, release peaks above 670°C are assumed to be related to the compounds listed in tab. 7.10. The presence of $MoAl_4$ and U_3Si could not be verified by XRD, as no pattern could be acquired in the ThT670 sample. The assumption of these two phases' presence is merely made based on the EPMA images shown in fig. 7.13 (see also chapter 7.6.2). Among the binary phase diagram database [126], no suitable compound could be identified which can be related to the peak at 820°C.

Release peak (°C) observed during ThT1800	Related compound meltdown
740	$MoAl_4$ [126]
820	unknown
900	U_3Si [126]
1270	U-7wt%Mo

Table 7.10.: *Assumed fission gas release from compounds melting at temperatures above 670° C (see also tab. 7.1).*

Observation item	After in-pile irradiation	After ThT at 500°C	After ThT at 670°C
EPMA observation on microstructure			
IDL	• amorphous • "duplex" layer structure: external IDL at IDL/matrix interfaces and internal IDL at U-Mo/IDL interfaces	• cracks inside IDL • IDL recrystallisation • duplex structure	• cracks not stronger than those at 500°C at comparable regions • duplex structure hardly observable
U-Mo	• small gas bubbles	• cracks inside particles	• cracks not stronger than those at 500°C at comparable regions • strong interaction with Al at cladding regions
Al	• interaction with U to form IDL	• no strong changes compared to pre-ThT state	• complete interaction with U-Mo at former matrix/cladding interfaces • starting diffusion into U-Mo in the meat center
Si	• large amount of precipitates remaining inside matrix	• complete diffusion into IDL • no Si remaining in matrix	• presence of U_xSi_y compounds within fully interacted particles close to initial cladding
O	• in the external IDL	• in the external IDL	• homogeneous distribution inside IDL in meat center • presence of O compounds in interacted particles at cladding
Xe	• bubbles homogeneously distributed inside U-Mo • bubbles at U-Mo/IDL interfaces • homogeneously distributed in IDL	• precipitation inside particle cores • bubbles at U-Mo/IDL interfaces • higher Xe diffusion from U-Mo cores to IDL • homogeneous distribution in IDL except at IDL/matrix interfaces	• almost complete release from remaining U-Mo particles • detectable inside IDLs in the meat center
Zr	• homogensously distributed in U-Mo • slight accumulation at IDL/matrix interfaces	• no strong changes compared to pre-ThT state	• strong precipitation in the total U-Al interaction areas near cladding • slight accumulation inside IDL
XRD analysis			
U-Mo	• no XRD pattern acquired	• γ-U-Mo destabilisation into α-U	• no XRD data
IDL	• amorphous	• recrystallisation	• recrystallisation

Table 7.11.: *Summary of EPMA and XRD analysis after in-pile irradiation [54], after thermal treatment at 500°C and after thermal treatment at 670°C.*

7.8. Conclusions about thermal treatments

In this part of the thesis, a synthesis of the IRIS4 irradiation experiment was presented. The fission gas behaviour inside the fuel when exposed to thermal annealing tests was observed to identify and locate temperature dependent fission gas release peaks from the fuel. In order to reach this goal, a detailed explanation of the different manufacturing steps and irradiation conditions has been provided. When heating up the fuel samples up to 1800°C, two strong fission gas release peaks were observed at 500 and 670°C. The interpretation of the fission gas release peak at 400°C remains questionable, but the peak at 500°C is attributed to large porosity formation occurring due to different thermal expansion coefficients of both the U-Mo and the Al matrix. The second peak at 670°C is attributed to the strong U-Al interaction process between the U-Mo particles and the matrix/cladding. Successive thermal treatments on two identical samples were stopped at 500°C and 670°C respectively. These two samples were further studied for the fission gas behaviour at these two temperatures.
Concluding, this part of the thesis is a first detailed study of the behaviour of annealed in-pile irradiated U-Mo/Al nuclear fuel plates.

7.9. Outlook

To improve the understanding of fission gas behaviour inside U-Mo/Al samples, the usage of other analytical methods is proposed. The used techniques in this thesis (EPMA and XRD) only offer the possibility to investigate sample surface structures. Information from inside the samples could not be acquired. Therefore, it is proposed to use secondary ion mass spectrometry (SIMS) to clarify the location and size of fission gas bubbles inside the particles after ThT at 500°C, as well as inside IDLs before any annealing. By a combination of EPMA and SIMS, a global overview over the temperature dependent fission gas behaviour could be obtained. By measuring the Xe quantity inside the bulk material, this could provide a conclusion about the Xe gas release through the holes and the fissures inside the U-Mo particles. In particular, it could provide a total fission gas output quantity out of these fissures.

Part III.

Ion bombardment on monolithic U-Mo/Al layer systems

8. Manufacturing and irradiation of monolithic U-Mo layers

The second topic of this thesis deals with the analysis of heavy ion irradiated U-Mo/Al layer systems. Goal of this study was to verify whether these out-of-pile irradiation technique provides comparable results regarding IDL formation as in-pile irradiation of dispersed U-Mo/Al systems. This chapter describes the production technique for monolithic layer systems, as well as the conditions for heavy ion irradiation of the layer systems used in this thesis. Later chapters in this part of the thesis deal with the experimental results obtained by particle bombardment. Additionally, Kr implantation into these out-of-pile generated U-Mo/IDL/Al layer systems is discussed.

8.1. Sample manufacturing of monolithic layers

In the following, the physical vapour deposition technique (PVD), also known as "sputtering", will be described as a method to produce monolithic layer systems. Although many methods of PVD exist, like thermal erosion, evaporation or cathodic arc deposition, the term "sputtering" is unique to PVD caused by particle bombardment. A special kind of sputtering was used to prepare the samples presented in this part of the thesis: the so-called DC magnetron sputtering. The first subchapter presents an overview about the DC magnetron sputtering technique itself and the used sputter reactor as well. As both items are fully described in [137], only a short summary is given. The successive subchapter presents an overview of the produced samples.

8.1.1. PVD sputtering technique

Basically said, the term "sputtering" means the abrasive of material surface atoms by particle bombardment. For many technical applications, inert gas is used which has three functions:

- For ion generation by glow discharge (see below).

- Inert gas ions themselves are used for target bombardment.
- Inert gas reactions are purely physical. Otherwise, non-inert gases may lead to secondary chemical reactions and may even form new compounds with the bulk material inside the target[1].

For metallic sputtering targets, i.e. U-Mo alloys, elastic collision processes between incident particles and target atoms are more important than inelastic ones. This is due to the swift distribution of collision energy between the incident particles and the bulk material electrons. In contrast, inelastic scattering processes would lead to locally excited areas inside the target and may lead to the ejection of clusters. As a consequence, the sputtered layer would globally exhibit an inhomogeneous thickness on the substrate. Therefore, it has to be guaranteed that the particle-target reactions stay in the elastic regime.

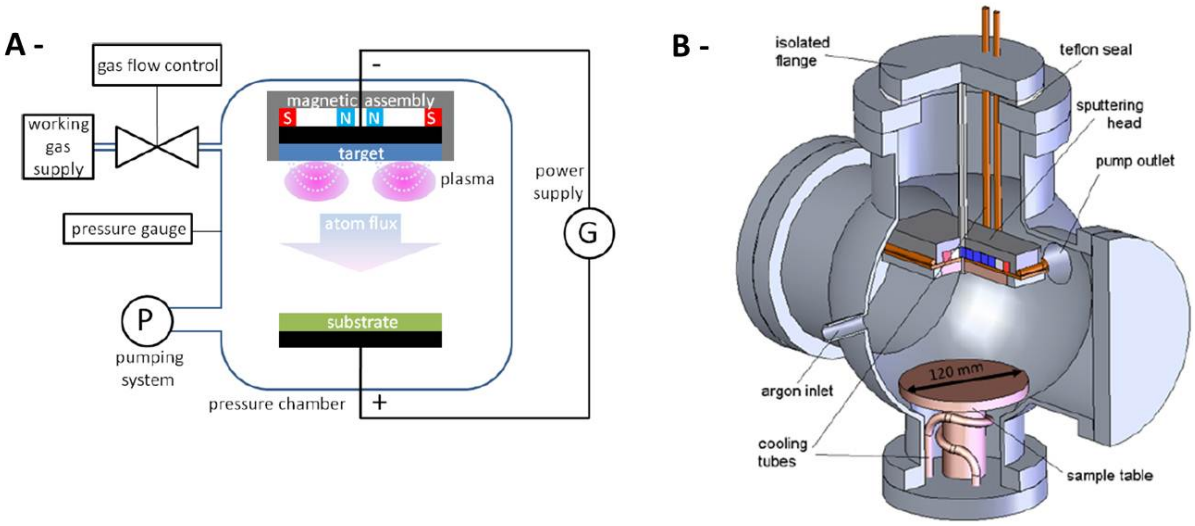

Figure 8.1.: *(A-) Sketch of the DC magnetron sputtering technique. (B-) Drawing of the used sputtering setup. Both sketches are taken from [137].*

A sketch of the **DC magnetron sputtering** technique is shown in fig. 8.1 - A. The whole sputtering process occurs inside a vacuum chamber with pre-operation pressure in the range of 10^{-6}mbar. This ensures that the pollution of the sputter-deposited layer with oxide and nitrogen compounds is neglibigle. In a next step, Ar gas is introduced into the system via a gas flow control system. In order to cause ion bombardment of the target, an Ar glow discharge plasma is generated. **Glow discharge** combines continuous ion production and homogeneous ion bombardment of the target. A DC electrical field is sufficient to induce glow discharge. Electrons are accelerated in this DC electrical field and can ionize the Ar gas atoms between cathode and anode, resulting in a glow discharge. As the Ar ions are used for target bombardment, the target is operated as the cathode and the substrate as the anode of the DC setup. As a constant stream of ions to the target has to

[1]This technique is used in reactive sputtering [137].

be ensured, only electrically conductive materials, like U-Mo, can be sputtered in this way. For non-conductive materials, the method of oscillating field sputtering has to be used. This is explained in more detail in [137]. Normally, glow discharge sputtering is a rather slow process. To increase the target bombardment rate, a magnetic assembly is coupled to the target which superposes the electrical field with a magnetic one. The Lorenz force drives the electrons in the plasma region into spiral trajectories along the magnetic field lines. This results in an increased number of electrons in magnetic field regions. As a consequence, a high degree of gas ionization is achieved. Most often, permamagnets in a double ring shape are used to generate the magnetic field, which leads to a torus shaped magnetic field in front of the target. In this torus region, an intense target erosion is observable. The drawback is a reduced homogeneous target erosion when compared to non-magnetic DC sputtering.
Fig. 8.1 - B shows a sketch of the used sputtering reactor in this thesis, which ceased operation in late 2012. The shown sputtering head consisted of the duo magnet ring upon which the U-Mo target was mounted. Also visible in the sketch are cooling tubes connected to both target and sample table. This is mandatory to counter target and substrate heating by ion bombardment. On the target, increased temperature may also result in the permamagnets exceeding the Curie temperature and may therefore result in failure of the magnetic assembly. In the worst case, a cooling failure could result in target melting and damage of the structural components. On the substrate, a too high temperature may result in inhomogenous monolithic layer growth. A more detailed explanation for this may be found in [137].
By means of this special DC magnetron sputtering reactor, the samples were produced under an operating pressure of $8.0 \cdot 10^{-3}$mbar and an applied DC voltage of 350V resulting in a power of 240W. Under these conditions, it took 10 minutes on average to sputter a 1μm thick monolithic U-Mo layer upon a 99.999% pure and 500μm thick Al substrate. All the Al substrates themselves were polycristalline with an average grain size diameter of 400μm as observed by confocal microscopy. The provided targets were fabricated uniquely out of depleted U-8wt%Mo provided by AREVA-CERCA.

8.1.2. U-Mo layer thicknesses

Before actually sputtering U-Mo layers, some preliminary considerations were made concerning the necessary and reasonable U-Mo layer thickness for successive heavy ion bombardment. As it is shown lateron in chapter 8.2, heavy ion irradiation at the MLL Tandem accelerator is performed with ^{127}Iodine at 80 MeV under a perpendicular incidence upon the sample surface.
Recently, simulations were performed to compare the damage events during heavy ion irradiation to in-pile ones [138]. According SRIM calculations regarding ion bombardment under these conditions on U-8wt%Mo/Al layer systems are shown in fig. 8.2 (see also chapter 3.1.1). The Iodine particles can penetrate to a maximum depth of 5.4 μm inside the U-8wt%Mo layer. In the following, the main results concerning ^{127}I irradiation at

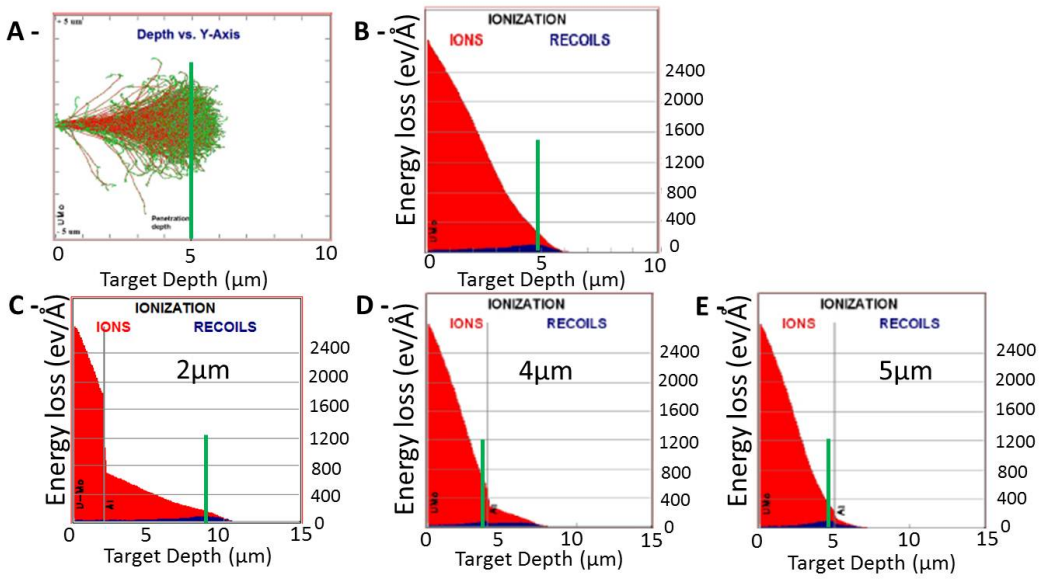

Figure 8.2.: *SRIM calculations showing the impact of Iodine ions with an energy of 80 MeV into an U-8wt%Mo layer. (A-) A two-dimensional plot showing the Iodine penetration depth into a pure U-8wt%Mo layer. The average maximum penetration depth is located at 4.95 µm. (B-) The ionization due to recoils is also at its maximum at this depth. (C-) to (E-): Ionization plots calculated for U-Mo layers of various thicknesses: (C-) 2 µm, (D-) 4 µm, (E-) 5 µm. Ionization by both ions and recoils are plotted [143]. Green lines indicate Bragg peaks for nuclear stopping power.*

80 MeV are listed:

- The type of stopping power changes at a depth of around 4.0 μm inside the U-Mo from mainly electronic to nuclear.

- Also, the nuclear stopping power reaches a maximum at a depth of 4.95 μm, while the maximum for the electronic stopping power is right at the irradiation surface. Considering the deposited Iodine particles inside the material, a maximum is detected at 4.95μm (see fig. 9.3), right at the same spot of the maximum nuclear stopping power, as indicated by the Bragg peaks in fig. 8.2 (see green lines).

- The most vacancies inside the U-Mo target material are caused by recoils. In particular, the most damage by recoils is caused inside an U-Mo layer thickness of 4 to 5 μm. Below 4 μm, the stopping mechanism is mainly electronical which does not result in comparable lattice atom displacements. 2 to 3 times more vacancies are produced during ion bomardment per particle as during in-pile irradiation [138].

- For studying the effect of electronic stopping power, layer thicknesses of 2 or 3 μm are considered as most representative.

- For comparing the final fluence of $1.0 \cdot 10^{17}$ ions/cm² (see chapter 8.2.3) to an in-pile fission density value, this final fluence is calculated to an equivalent peak $5.1 \cdot 10^{19}$ f/cm³ of the current FRM II fuel [4] (see also chapter 1.1)[2]. More detailed calculations are ongoing at the moment.

Inside materials, the nuclear stopping power is far more important than the electronic one, as these nuclear scattering processes cause far more damage to the material than Coulomb scattering. Nevertheless, it is of interest to compare the effect of heavy ion irradiation on U-Mo layers with a thickness from 1 to 3 μm on the one hand (electronic stopping power dominance) to U-Mo layers with thicknesses between 3 and 5 μm (nuclear stopping power dominance).
As a result, a total amount of 40 U-Mo/Al layer systems were produced by DC magnetron sputtering, with according U-Mo layer thickness of either 2 or 3 μm or 4 and 5 μm. The sample size in every case was 10×10 mm². Considering a 500μm thick Al substrate in every case, the toal thicknesses of the samples were roughly the same.

8.2. Heavy ion irradiation conditions

In the following, the MLL Tandem accelerator is presented where the Iodine irradiation was carried out.

8.2.1. The MLL Tandem accelerator

Several instruments and techniques are necessary to accelerate particles to energies in the MeV regime. An overview of the MLL beamguide is given in fig. 8.3. The basic principle is as follows:

- Negative ion generation in the particle source.
- Acceleration to the desired charge state and energy in the main acceleration tube.
- Traversion of a 90° magnet to guide the beam to the experimental chambers.

[2] In [4], a maximum FRM II fission density of $1.98 \cdot 10^{21}$ f/cm³ inside the meat is given. This equals to $3.96 \cdot 10^{21}$ fissionproducts/cm³ in the fuel kernels. A total energy deposition of 166 MeV per fission leads to a maximum energy deposition of $3.29 \cdot 10^{23}$ MeV/cm³ inside the meat (U-Mo + matrix). For the energy deposition inside heavy ion bombarded U-Mo/Al layers, a value of $1.3 \cdot 10^{22}$ MeV/cm³ inside U-Mo and $1.0 \cdot 10^{21}$ MeV/cm³ inside Al was calculated. Considering a 50vol% U loading, an average value of $9.4 \cdot 10^{21}$ MeV/cm³ was obtained. The mentioned fluence after heavy ion irradiation therefore corresponds to around 2.8% peak burnup of the FRM II fuel.

- Traversion of a switcher magnet in hall 1 to guide the beam towards the desired beam tube where the experimental setup is placed.

- Target bombardment at the experimental setup.

Three of these, the ion source, the main acceleration tube and the experimental setup are described in the following.

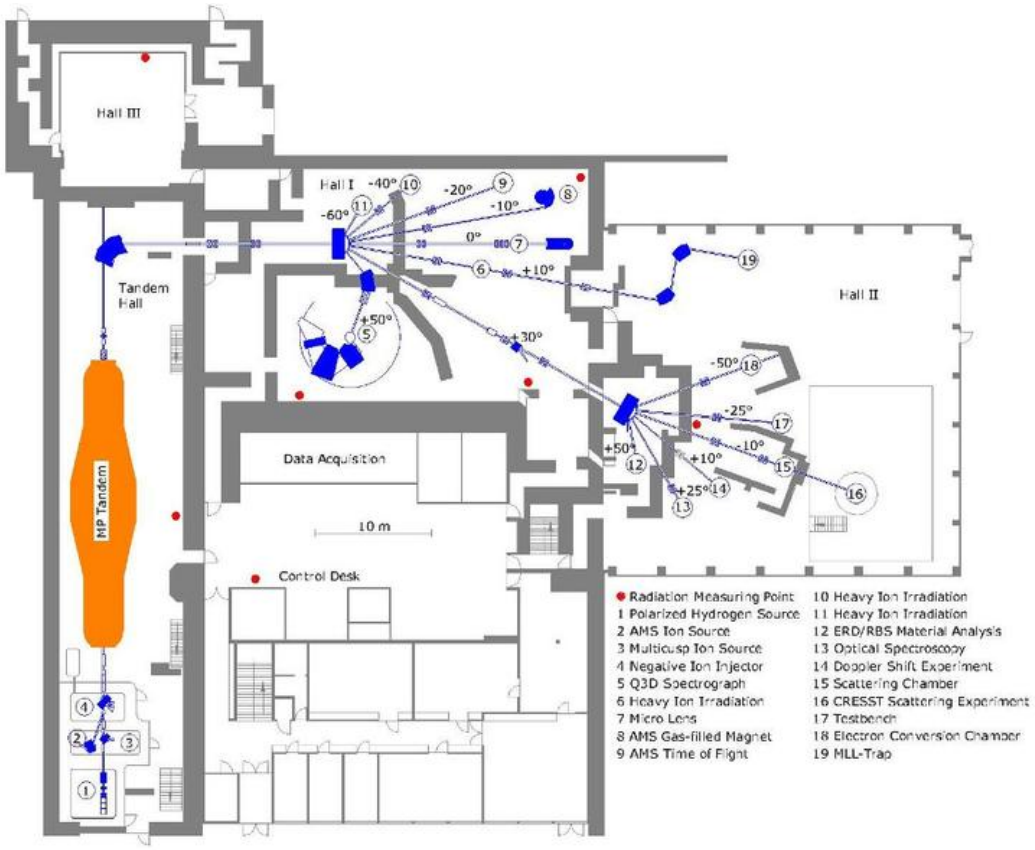

Figure 8.3.: *Overview of the MLL Tandem accelerator facility. Negative charged ions are generated in the ion source, while the main acceleration to the final energy and charge state takes place in the main Tandem tube. Afterwards, a 90° magnet leads the beam to hall 1. There, a switcher magnet guides the beam to the experimental setup at the +10° tube [140].*

The Ion source

First, a closer look is taken on the mechanism of particle extraction from a source material. The following explanation of this **ion source** is also depicted in fig. 8.4 - A. The particle source itself is a seperate vacuum chamber whose only connection to the rest of the accelerator is given by a tube 100 mm in diameter. Inside this vacuum chamber, a Cs

reservoir is electrically heated up so that Cs atoms can evaporate into the chamber. There, they condensate on the cold surfaces, i.e. also on a so called "Ionizer" and on the "target" from which the particles are generated in a successive step. Both Ionizer and target are connected to an electrical DC source ($\approx$ 5 kV[3]) with the ionizer functioning as the kathode and the target as the anode. Similar to the Cs reservoir, the electrical current enables the ionizer to reach an operating temperature of 1400°C in vacuum conditions. A direct result is that any Cs gas getting in contact with this chamber component is ionized and positively charged afterwards.
As a consequence, the charged Cs is attracted to the target. Due to the high impact energy, the target material is sputtered. As seen in fig. 8.4 - A, the sputtered particles have to traverse the already existing Cs layer on the target. While crossing, the particles might be able to drain electrons out of the Cs layer if the respective particles' electronegativity is higher than the one for Cs. This is normally easily achieveable, as Cs is one of the elements with the lowest electronegativity [139]. An overview of some exemplary elements resulting from thermal fission of ^{235}U with their according electronegativity is given in tab. 8.1. Besides the inert gases, Iodine has a high electronegativity of 2.66, which also means that a large amount of negative charged Iodine ions are yielded after crossing the Cs layer. Contrary, the yield of Sr with an electronegativity of 0.95 is poor and therefore it is not considered economic in any Tandem operation. Inert gases cannot be negatively charged and are therefore not used.
After leaving the target material, the negative charged ions are attracted towards the beam tube leading to the mean acceleration tube by means of an "extraction" voltage of around 15 kV. In a next step, the particles are focussed by electric quadrupol lenses and are further accelerated by a so-called pre-acceleration voltage of around 50 kV before they enter the main acceleration tube.

Element	Cs	Sr	Zr	I	Xe
Electronegativity	0.7	0.95	1.33	2.66	2.6
Thermal uranium fission yield (%)	6.2	5.7	6.5	15.9	14.2

Table 8.1.: *Overview of the electronegativity of frequent elements after thermal fission of ^{235}U (see also tab. 2.1). Cs which has one of the lowest electronegativites of all elements is put in first place as it is an essential part of Tandem accelerator operation and is therefore considered as a reference. For consistency, the total elemental yield after thermal uranium fission is shown as well. All values are according to Pauling's classification and are therefore without unit [139].*

[3]Exact voltage values depend on the type of element.

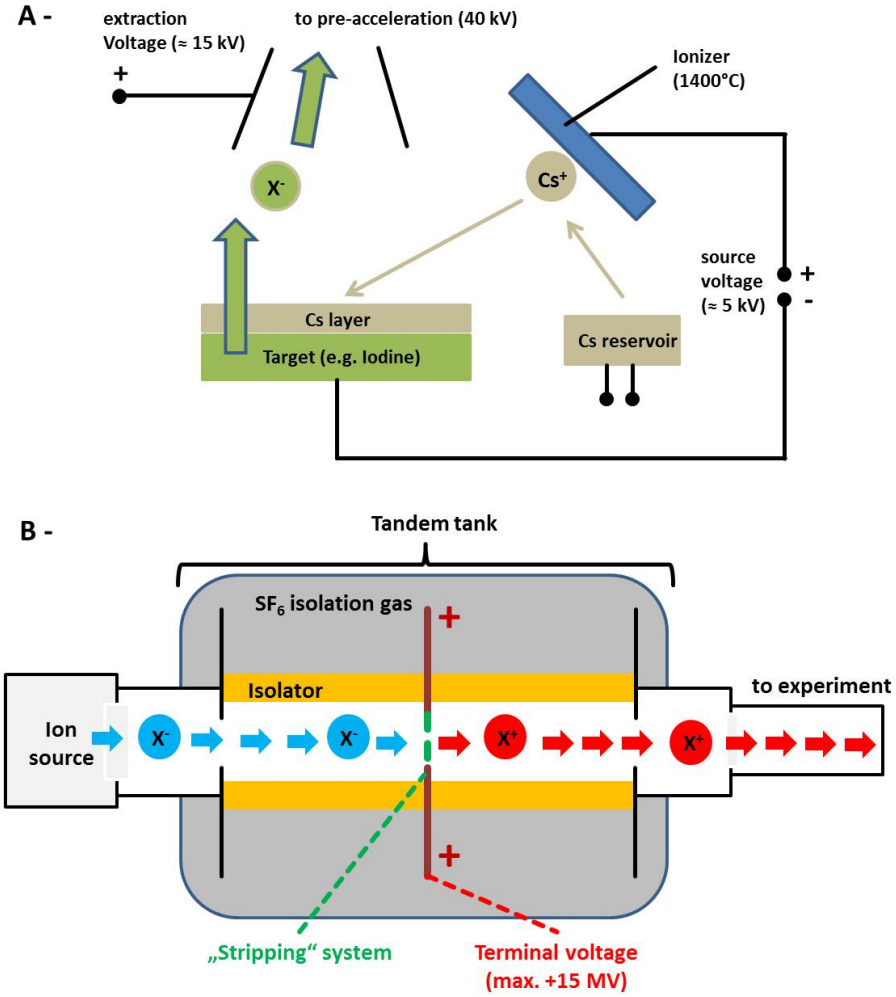

Figure 8.4.: *Sketches explaining the basic mechanism of Tandem acceleration. (A-) shows the method of particle extraction from a target via sputtering. Before entering the mean acceleration system shown in (B-) the particles are negatively charged. In the acceleration "tank", the particles are first accelerated towards a terminal voltage in the range of 3 to 15 MV. There, the particles traverse a "stripping" system after which they are positively charged. Then the second acceleration step forces the particles towards the experiment. As high voltages are applied, both an isolator and an SF_6 isolation gas have to be used to shield the beam tube from the environment. (B-) is based on [140].*

Main acceleration mechanism

The last acceleration step takes place in the main acceleration tube. This machine part is simply called "**Tandem**", and a sketch of the acceleration mechanism inside this tank is shown in fig. 8.4 - B. When entering the Tandem, the particles are accelerated by the "terminal" voltage towards the center. The terminal voltage can be adjusted between +3

and +15 MV. At the terminal, the ions traverse a "stripping" system. This stripping system has the function to drain electrons from the negative charged ions in order to produce positive charged ones for the second acceleration step. The nature of the stripping system depends on the particle current. For a low current, a solid carbon foil is used, while for a high current an Ar filled gas tube under low pressure is utilized. Main reason for these two different kinds of stripping system is the fact that carbon foils cease operation after around 5 minutes of high intensity particle bombardment, as the foils are severly damaged. Due to the required particle fluxes in this thesis, only the gas stripping system could be utilized. The drawback of using a gas stripping system is the increasing gas pressure during high intensity particle bombardment which accordingly reduces beam transmission through the terminal by an increasing amount of inelastic collision processes. Moreover, the gas stripping system permits only a lower amount of possible charge states than the foil stripper. This is due to the different densities of the stripping element: $3\,{}^{\mathrm{g}}/_{\mathrm{cm}^3}$ for carbon and $1.7\,{}^{\mathrm{g}}/_{\mathrm{cm}^3}$ for Ar. This results in different interaction strengths between the stripping element and the incoming particle.
During the stripping process, the resulting positive particle charge state depends on the terminal voltage. Normally, more than one single particle charge state is generated during the stripping process. A very detailed explanation of charge distributions may be found in [141]. After being positively charged, the terminal voltage once more accelerates the now positive charged ions towards the opposite side of the tank. As the terminal voltage is used twice to accelerate the particles, the term "Tandem acceleration" is used. Right after leaving the tank, the ions have to traverse the 90° magnet (see fig. 8.3) in which their trajectory is shifted by 90°. This magnetic field selects the desired ion charge state. Heavy ion irradiation at the MLL Tandem is performed with ^{127}Iodine at 80 MeV, as this element in combination with this energy is representative to simulate uranium fission damage in a fuel [143, 142]. When considering tab. 8.1, a very high yield of Iodine ions can be expected from the particle source. Therefore, Iodine is chosen for heavy ion irradiation. Indeed, a particle current of 3.5 μA ($= 2.2 \cdot 10^{19}\,\mathrm{I}^{-1}{}^{\mathrm{particles}}/_{\mathrm{second}}$) can be achieved before entering the acceleration tank. Two prominent terminal voltages, 9.9 MV and 11.3 MV, exist to generate charge states which result in a total Iodine energy of 80 MeV: I^{6+} and I^{7+}. In the scope of this thesis, both charge states and therefore both fluxes were considered during heavy ion irradiation. In the following, the charge states I^{6+} and I^{7+} are abbreviated as **7+** and **6+** respectively.

8.2.2. Experimental setup

Heavy ion irradiation was executed in an experimental setup as depicted in fig. 8.5 - A. A full explanation of the setup and the beam adjustments can be found in the appendix C. A short explanation is provided in the following:
During operation, the whole vacuum chamber is kept under high vacuum conditions of $8.0 \cdot 10^{-6}$ mbar. The beam itself traverses the irradiation chamber in the center, and

the samples to be irradiated were positioned exactly at this location. This is realized by a movable rod on which a small copper piece carrying a maximum of three samples is mounted. This allows successive irradiation of all three samples without the need to break the vacuum for sample change. Two Faraday cups, one before the irradiation chamber and one after, provide beam intensitiy (i.e. beam current) measurement. Temperature was measured at each of the three possible irradiation conditions by PT100 sensors which were placed between the sample and the Al sheet covering the samples. All Al sheets used in this thesis had a 6mm wide hole, so that the beam footprint on the samples is of this size. The distance between the beam spot and the sensor was around 1mm. Heating of the sample was realized by the beam power itself and an electrical heating wire on the sample holder. Meanwhile, cooling was performed by pressurized air pumped through the backside of the sample holder. Programmable logic controlling (PLC) automatically adjusted cooling and heating power to maintain a stable irradiation temperature. Alltogether, the irradiation temperature could be kept at a very stable level with just a ± 2°C deviation. However, the first samples irradiated during this thesis were mounted on an old sample holder version used in preceeding theses and is fully described in [142, 143]. With this sample holder, a stronger temperature deviation of ± 20°C was apparent (see also chapter C). According error bars in fig. 9.2 indicate samples which were irradiated with the old sample holder.

8.2.3. Irradiation parameters

The following parameters were chosen for the irradiation on the U-Mo/Al layer systems:

- An irradiation temperature between 90 and 200°C was chosen. These two limits have been set because in-pile irradiation on dispersed powder samples took place in the lower range between 90 and 120°C (see also tab. 1.1). For higher temperature regimes, results of heavy ion irradiation in the range of 200°C and above are already available [142, 143].

- As described in chapter 8.2.1, two Iodine charge states, 6+ and 7+, may lead to a total particle energy of 80 MeV. However, the higher charge state has only 1/3 of particle flux as the lower charge state. This in turn leads to an according reduction of the damage-by-time ratio inside the material (see also chapter 3.1). Irradiation with both charge states has been performed to evaluate its impact on IDL growth. The according fluxes are $2.0 \pm 1.0 \cdot 10^{11}$ $^{\text{ions}}/_{\text{s}\cdot\text{cm}^2}$ for the 7+ and $7.0 \pm 1.0 \cdot 10^{11}$ $^{\text{ions}}/_{\text{s}\cdot\text{cm}^2}$ for 6+ the charge state.

- For all cases, the final fluence was $1.0 \cdot 10^{17}$ $^{\text{ions}}/_{\text{cm}^2}$. This final fluence value was kept fix so that all heavy ion irradiation results can be compared to each other.

- The according energy deposition at the U-Mo/Al interfaces is different for the 2μm and 4μm thick U-Mo layers. Tab. 8.2 indicates the deposited energies at the U-

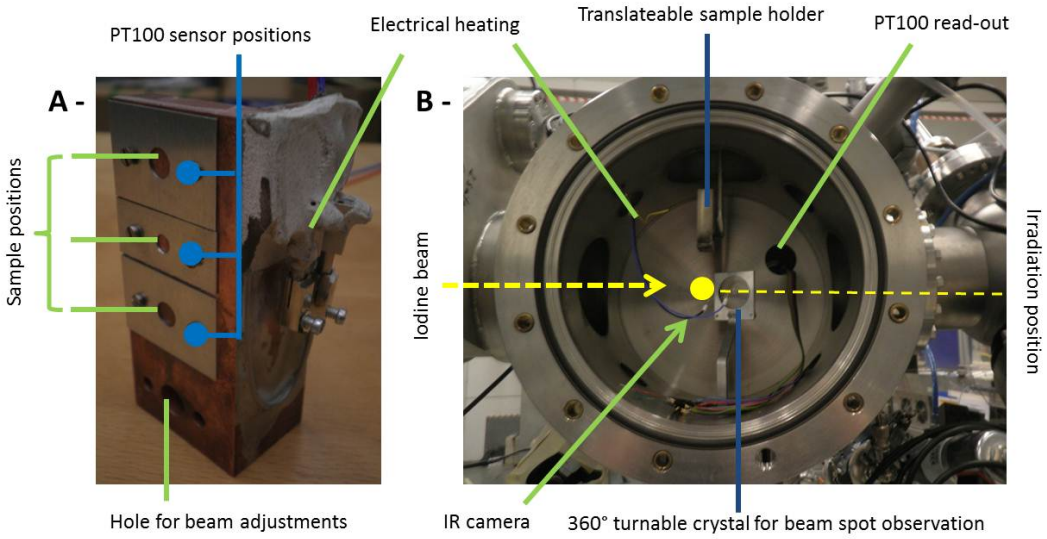

Figure 8.5.: *(A-) Image of the sample holder. Three irradiation position are possible. The samples are fixed to the holder by a thin Al sheet with a 6mm wide hole. This ensures the beam footprint on the sample is exactly of this size. The irradiation temperature is measured by a PT100 sensor positioned between the Al sheet and the sample holder (≈ 1mm distance to beam footprint). On the bottom of the sample holder, a 6mm wide hole was drilled. This is meant for beam adjustments and allows for on-line beam monitoring. Sample heating is achieved by both the beam power and an electrical heating wire on the sample holder's flank. (B-) Overview of the irradiation chamber. The beam traverses the chamber centrally where the irradiated sample is to be positioned. The sample holder is mounted on a translateable rod which can move the holder vertically. Integrated in the rod is a cooling tube. A turnable quartz crystal together with an IR camera allows for on-line beam spot monitoring.*

Mo/Al interfaces as calculated by SRIM. 1.1 $^{\mathrm{MeV}}/_{\mathrm{ion}}$ is deposited at a thickess of 2μm, while 2.3 $^{\mathrm{MeV}}/_{\mathrm{ion}}$ are deposited at a 4μm thickness (see also fig. 9.3).

Iodine charge state	Flux (10^{11} ions/s · cm^2)	Fluency (10^{17} ions/cm^2)	Deposited energy per ion (MeV/ion)	
			2μm U-Mo	4μm U-Mo
6+	7.0 ± 1.0	1.0	1.1	2.3
7+	2.0 ± 1.0	1.0	1.1	2.3

Table 8.2.: *Summary of heavy ion irradiation conditions and calculated deposited energy at the U-Mo/Al interface.*

9. Evaluation of heavy ion irradiation

Experimental techniques to analyze the irradiated samples consist of SEM, EDX, XRD and TEM (see chapter 5). Main focus is the investigation of the irradiation temperature and heavy ion flux dependent microstructural evolutions in these samples. The chapter concludes with a comparison between results obtained in-pile and out-of-pile.

9.1. SEM examinations

After heavy ion irradiation, SEM cross sections were prepared to observe the grown IDL. The standard procedure for cross section preparation starts with cutting the sample by a diamond saw.

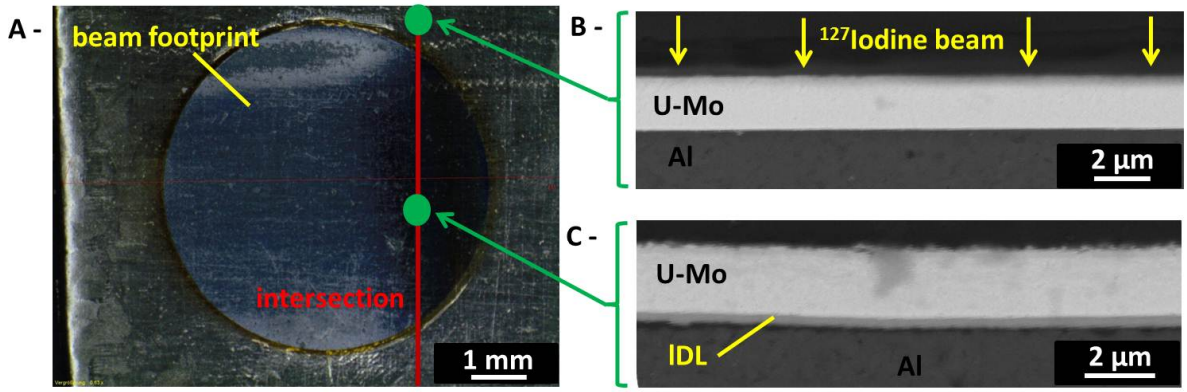

Figure 9.1.: *(A-) Optical microscopy image of a heavy ion irradiated monolithic U-Mo/Al sample. The beam footprint on the sample is uniformly 6mm in diameter. The red line indicates the intersection for successive SEM cross section preparation. The right, smaller part of the sample was embedded. Two representative SEM BSE images are shown in (B-): for the non-irradiated and in (C-): for the irradiated part. In the irradiated area, a 400nm thick IDL has grown between the Al substrate and the 2µm thick U-Mo layer.*

Fig. 9.1 - A shows a representative optical microscopy image of a sample irradiated at 180 ± 2°C with an according Iodine charge state of 7+. A red line in this image indicates the cutting intersection. As the beam footprint on the sample was very homogeneous with

a uniform 6mm diameter, it was sufficient to prepare a smaller part of the sample for SEM investigations, as the observed cross section of this smaller part was considered as representative for the whole irradiated area. This also allowed usage of the major part for follow-up investigations and/or experiments. After that, the next step consisted in embedding the cutted piece in a resin and polishing the cross section.

For indicating the different compositions inside the cross sections, both SEM BSE imaging and EDX linescans were carried out. A comparison between the non-irradiated and the irradiated part of the cross section is shown in fig. 9.1 - B and - C. The presence of a 400nm thick IDL is well visible in the irradiated part between the 2μm thick monolithic U-Mo layer and the Al substrate. This IDL is therefore uniquely attributed to heavy ion irradiation effects. All other possible causes, i.e. sputtering or temperature effects during irradiation, cannot be the cause: Instead, both causes would have a global effect on the sample. These general observations were made on all the heavy ion irradiated samples.

9.1.1. Influence of irradiation temperature

A plot summarizing the temperature influence on both 2μm and 4μm thick U-Mo layers is shown in fig. 9.2 - A. Both graphs show the evolution of the IDL layer thickness with increasing temperature from 110 $\pm$ 10 to 190 $\pm$ 25°C during irradiation with the 6+ charge state.

The following observations are made, and a discussion with in-pile experiments is provided in the following chapter 9.1.3:

- If an IDL is generated, the final thickness is below 1.5μm.
- Below 110°C no IDL is generated by heavy ion bombardment, even in the case of high particle flux.
- With increasing temperature, the final thickness is enhanced, e.g. with average values ranging from 0.2μm at 110°C to 1.1μm at 180°C for the high flux condition on 2μm thick U-Mo/Al systems.
- The initial U-Mo layer thickness, and therefore the main method of particle stopping power (electronic in the thinner layers, nuclear in the thicker ones), has an impact on the IDL growth. For example, when comparing the obtained IDL values for 120, 130 and 140°C a difference is well visible. For thicker U-Mo layers, the IDL exhibits only half the thickness than after irradiation in the thinner layer systems.
- The final IDL thickness is directly proportional to the irradiation temperature once interaction has started.

9.1.2. Influence of particle flux

Considering the flux, only the results in the 2μm thin U-Mo/Al systems could be investigated. More beamtime would be required to perform a comparative study in U-Mo layers of a different thickness. Once more a plot showing the IDL growth with increased irradiation temperature is shown in fig. 9.2 - B. Here, the blue line indicates the high flux state 6+, while the red line represents the low flux irradiations (7+). It becomes evident that the particle flux has an impact on the final IDL growth, as the final interaction layer thickness is far less than in the high flux samples. For example, at a temperature of 180°C, the obtained IDL thickness is 0.4μm. At the same temperature a value of 1.1μm is observed in the high flux case. Moreover, in the high flux case, a 0.4μm thick layer has already grown at 120°C. To conclude, a 3.5 times higher particle flux results in a 3 times thicker IDL on average at the same irradiation temperature which is in rough agreement with the flux ratios between the two charge states. This flux dependency is also in excellent agreement with in-pile measured IDL thicknesses where the same result has been obtained [146, 147].
SRIM calculations were carried out to calculate the nuclear energy deposition at the heavy ion irradiated U-Mo/Al interfaces, and delivered a value of 2.3 $^{\mathrm{MeV}}/_{\mu\mathrm{m\cdot ion}}$ for a 4μm thick U-Mo layer and 1.1 $^{\mathrm{MeV}}/_{\mu\mathrm{m\cdot ion}}$ for a 2μm thick layer. Therefore, the energy deposition is 2.1 times higher in the thicker layers. To conclude, the flux, and not the deposited energy (see chapter 9.1.1) is considered responsible for the IDL growth.

9.1.3. Comparison with previous in-pile irradiations

A comparison of these irradiation results with the RERTR6 and RERTR7A irradiation campaigns on monolithic U-Mo fuel is listed in tab. 9.1. It is well visible that the obtained final IDL thickness after the in-pile tests is around 3 to 4 times higher than after heavy ion irradiation. However, it has also to be mentioned that the final burnup was also 3 to 4 times higher in the in-pile tests. Assuming a linear IDL growth in both in-pile and out-of-pile irradiation experiments, the results of both techniques are in good agreement. However, the most important point is that during in-pile experiments, an IDL is grown at irradiation temperatures as low as 90°C (see also chapter 3.2), whereas during heavy ion irradiation, a minimum temperature of 110°C is mandatory to grow an IDL. Therefore, several differences have to be stressed when comparing in-pile to out-of-pile experiments:

- Ion bombardment is an one-dimensional effect on the target surface, which means that all the incident particles have the same irradiation angle with respect to the sample surface. In this thesis, the incident angle of 90° between the beam and the specimen surface was chosen to achieve the maximum penetration depth inside

the samples[1]. However, the incident beam still has a "preferred direction" when traversing the specimen. Although the knock-on atoms' trajectories inside the material are statistically oriented, the Iodine's momentum remains an important factor during heavy ion irradiation.

- This purely one-dimensional effect does not exist during in-pile irradiation. Although the fission products are finally implanted in the matrix, this effect has to be considered three-dimensional. In the in-pile case, the fission products are generated all over the layer with a statistical three-dimensional distribution of fission product trajectories, i.e. in an incident angle of 0° to 180° with respect to the U-Mo/Al interface. As a consequence, heavy ion irradiation on monolithic layers serves as a model system to simulate specific fission products being ejected towards the U-Mo/Al interfaces in a 90° angle. Detailed simulations to compare this effect to the in-pile case are ongoing at the moment.

- Moreover, the heavy ion irradiated U-Mo thickness was in all cases either 2 or 4μm. During in-pile irradiation, fission products are generated randomly inside the U-Mo particles and successively driven towards the interfaces (see also chapter 8.1.2).

- Temperature measurement: In both the out-of-pile and in-pile studies, the exact temperature at the irradiation areas cannot be measured. In the in-pile case, only the cladding temperature can be calculated. In the ion irradiation experiments, the temperature was measured 1mm next to the irradiated area. In the beam center, the true temperature is only slightly higher, as the thermal conductivities of Cu ($240 - 400\,{}^{\mathrm{W}}/_{\mathrm{m\cdot K}}$ [163]), Al ($240\,{}^{\mathrm{W}}/_{\mathrm{m\cdot K}}$ [163]) and U-Mo ($10\,{}^{\mathrm{W}}/_{\mathrm{m\cdot K}}$ [25]) are high (see appendix C).

- Influence of neutron irradiation: The influence of neutrons on radiation damages inside a material is also considered in the following. During heavy ion irradiation, neutronic contribution to the damage cascade (see chapter 3.1.1) is non-existent. During thermal ^{235}U fission, 2.4 neutrons with a total energy of 6MeV are created on average (fast neutrons) [7]. Comparing the mass of neutrons (1.0u) to uranium (238u), molybdenum (96u) and aluminium (27u)[2], the neutrons' contribution to nuclear stopping power damage inside the material is low and can be neglected.

[1] Prior heavy ion irradiation experiments have been carried out regarding ion irradiation under different angles than 90° [142, 143]. The outcome was that in this case, all the interdiffusion processes are taking place on the irradiated surface, and almost no in-depth effects can be observed. Therefore, a 90° incident angle is mandatory to achieve interaction inside the bulk material

[2] Atomic masses are provided for the monolithic layer systems consisting of ^{238}U, Mo and Al.

Irradiation	Final burnup (% ^{235}U)	Temperature (°C)	IDL thickness (μm)
RERTR6 [37]	35 - 49	<200	4 - 6
RERTR7A [39]	3 - 28	90 - 120	≈ 3
This work	<10 [4]	100 - 200	$\approx 1.0 \pm 0.4$

Table 9.1.: *Comparison of the obtained IDL thicknesses after in-pile irradiation and after heavy ion irradiation.*

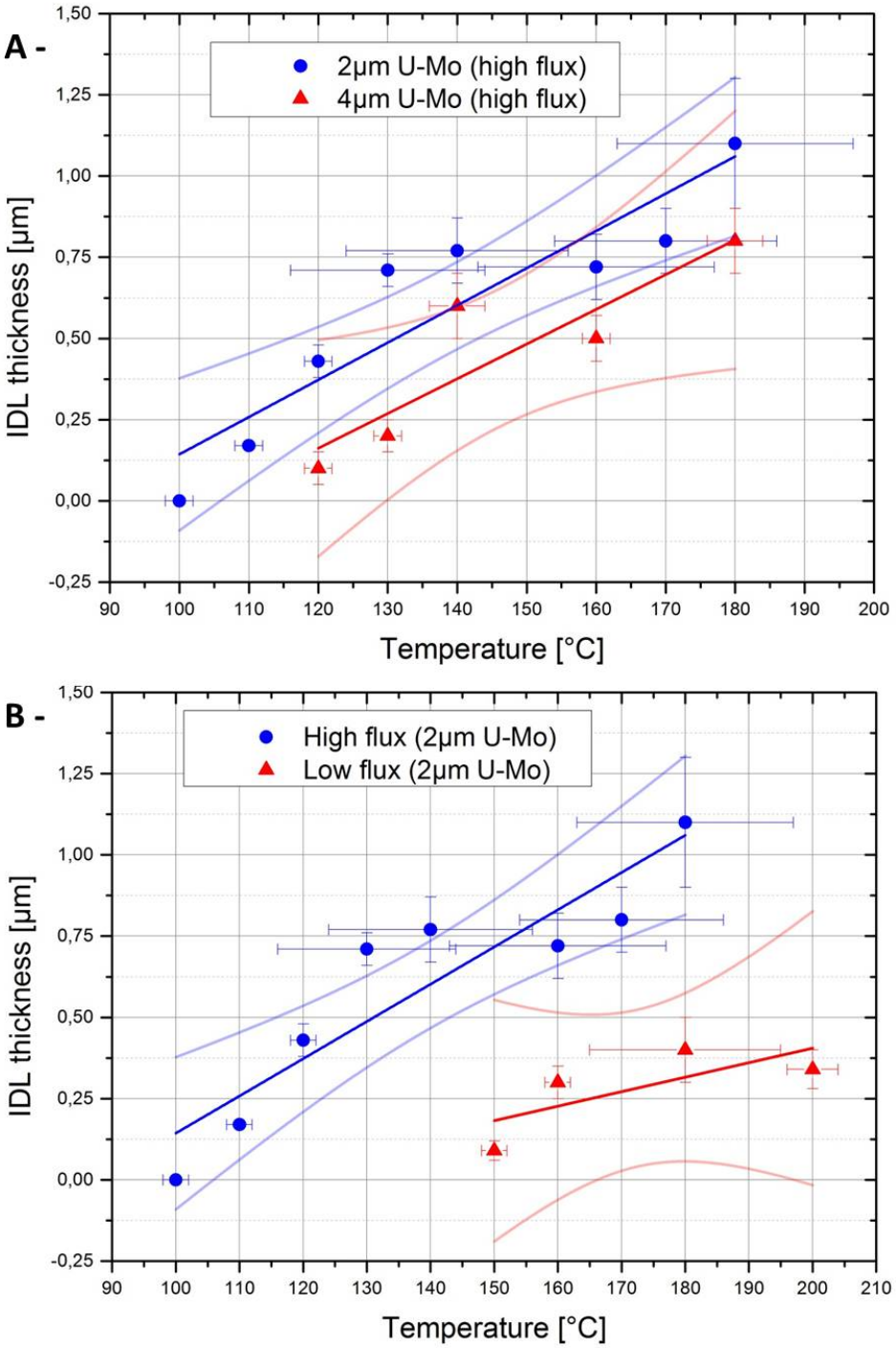

Figure 9.2.: *(A-) Plot showing the IDL thickness evolution with increasing temperature for both 2µm (in blue) and 4µm (in red) thick U-Mo layers. (B-) Plot comparing the influence of flux on 2µm U-Mo systems. The blue line indicates the high flux condition (6+) already shown in (A-), while the red one represents the low flux condition (7+). All sample types were irradiated until a final fluence of* $1.0 \cdot 10^{17} \frac{ions}{cm^2}$*. Large error bars on the x-axis indicate irradiations performed with the old setup (see chapter 8.2.2). Linear fits with 95% confidence bands are shown.*

9.2. TEM analysis

As detailed in [142] and [143], previous heavy ion irradiation experiments were performed at a 20 times higher flux ($\approx 1.4 \cdot 10^{13}$ $^{ions}/_{s \cdot cm^2}$) than the high flux case discussed in this thesis. After irradiation at this high flux, a mainly crystalline IDL was generated during ion bombardment [68] (see also chapter 3.2.3). This phenomenon is also described in chapter 3.2.1. Both high irradiation temperature and high flux may result in a crystalline IDL. However, in-pile generated IDLs are amorphous (see chapter 3.2). Therefore, it was necessary to create an amorphous IDL with heavy ions. In this thesis, lower fluxes were applied than in previous heavy ion irradiation tests [143, 142]. Both TEM and XRD measurements were performed to investigate this topic (see also chapters 5.4 and 5.5).
Recently, it has been demonstrated that thin foils for TEM investigations can be prepared by FIB out of both thermally annealed diffusion couples [148, 149], as well as out of in-pile irradiated monolithic U-Mo/Al fuel samples [150]. Hence, this examination technique was considered as well for analyzing the heavy ion irradiated samples. In the following, all presented results were acquired from an U-Mo/Al layer system irradiated at 140°C with the charge state 6+. This specific sample exhibits an U-Mo layer thickness of 5μm. SRIM calculations shown in fig. 9.3 indicate a maximum nuclear stopping power at this depth, right at the initial U-Mo/Al interface.
First, analogue to chapter 9.1, standard cross section preparation techniques were carried out to investigate the resulting IDL grown by heavy ion irradiation. As shown in fig. 9.4 - A, under these specific irradiation conditions, a 0.7μm thick IDL has grown between the Al substrate and the U-Mo layer which is in full agreement with the other IDL thicknesses obtained after heavy ion irradiation (see chapter 9.1.1). By FIB techniques, a thin foil was prepared out of an irradiated part of the sample which is highlighted in red in fig. 9.4 - A. The initial thin foil size was 10μm $\times$ 5μm with an according thickness of 2μm. Successive thinning led to an average foil thickness of 100nm which qualifies for TEM investigations at 300kV.
A TEM HAADF[3] image of the prepared thin foil is shown in fig. 9.4 - B. Visible on the left side of this image is no uniform shape of the three different layers. This artefact happened during thin foil preparation and is attributed to the different layers' material densities. This results in different thinning ratios for each layer.

Successive TEM EDX and TEM electron diffraction patterns on each layer were collected, and the according images are summed up in fig. 9.5. An **EDX linescan** across the three layers with a 88nm stepping (see fig. 9.5 - B) indicates the qualitative contributions of U, Mo, Al and O. However, as EDX can only provide qualitative measurements (see chapter 5.1), no quantitative (U+Mo):Al ratio can be concluded from these data. Instead, only elemental mixing of U and Al inside the IDL is confirmed.

[3]See chapter 5.4 for details.

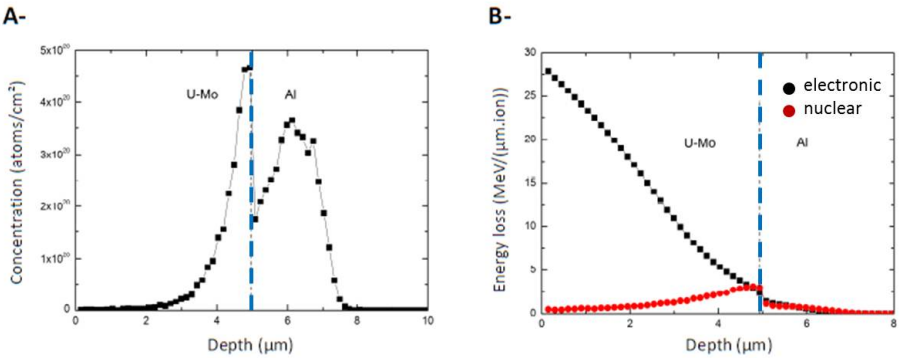

Figure 9.3.: *SRIM calculations performed on Iodine irradiation on a 5µm thick U-Mo layer on an Al substrate. (A-) Iodine distribution and (B-) energy loss are depicted. The blue line indicates the U-Mo/Al interface.*

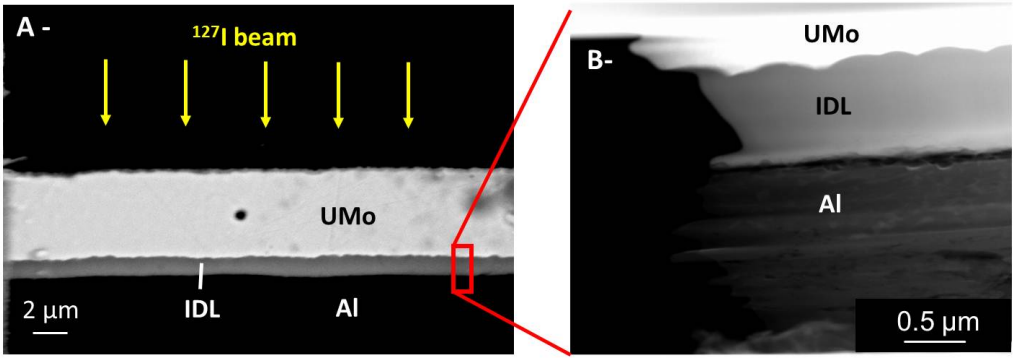

Figure 9.4.: *(A-) SEM BSE image of a sample irradiated at 140°C (charge state 6+). A 0.7µm thick IDL has formed during irradiation. The region highlighted in red represents the area from which a 100nm thin foil for TEM investigations was prepared. (B-) STEM HAADF image of the mentioned foil well indicating the three different layers. The left hand side in (B-) does not show a uniform layer thickness. This is an artefact produced by thin foil preparation.*

The exact location of the three collected electron diffraction patterns for each layer is shown in fig. 9.5 - A where the respective areas are highlighted by red circles.

- Considering the **Al** diffraction pattern (fig. 9.5 - C), a polycrystalline single phase fcc structure is revealed. Additionally, grain subdivision has occurred when comparing the according size to the unirradiated post-manufacturing state. The grain size was around 400μm before irradiation, while post-irradiation examination indicates a size below the μm range. To conclude, the according size decreased by around 1000 times. This effect is attributed to heavy ion irradiation effects.

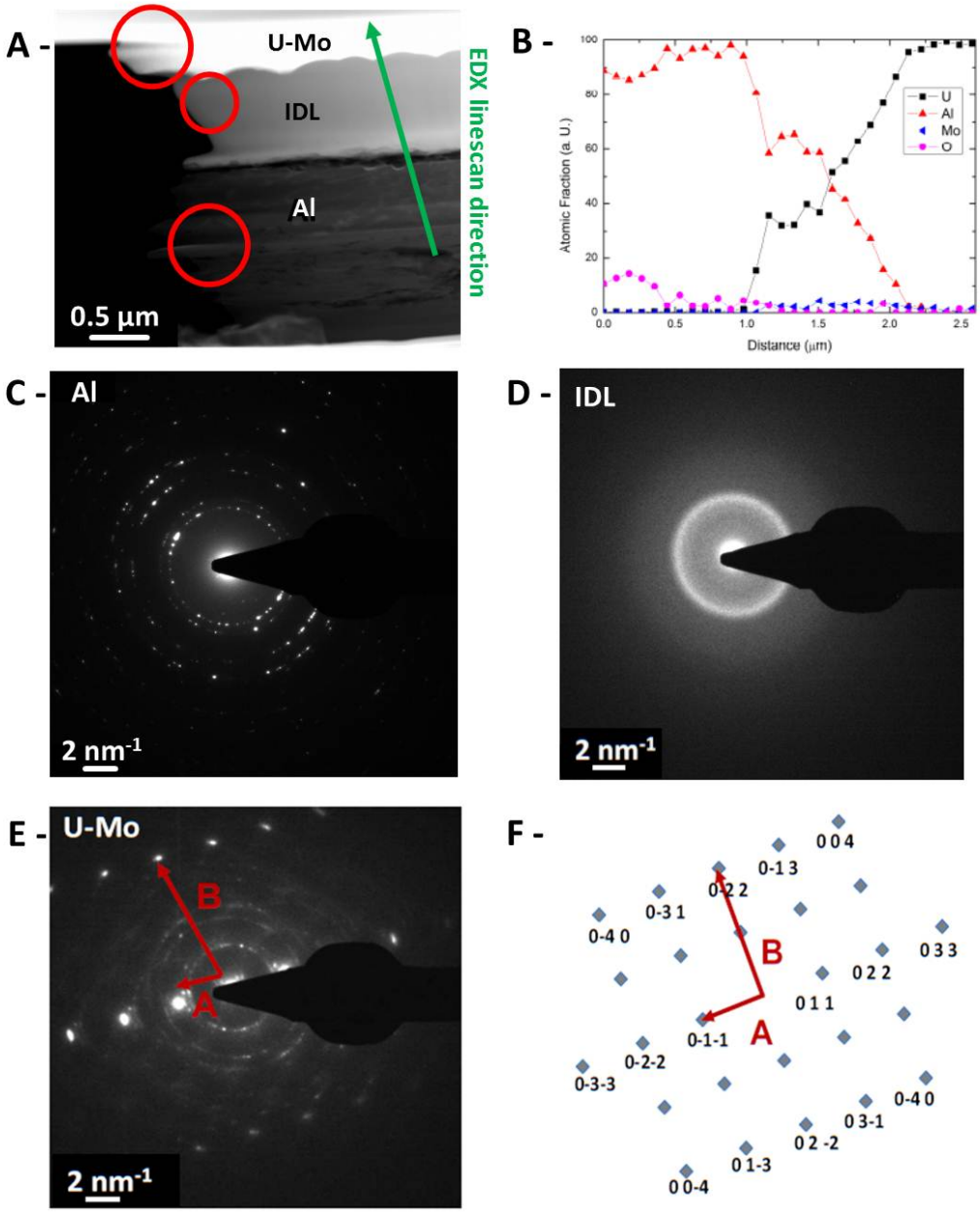

Figure 9.5.: *(A-) STEM HAADF image of the thin foil with indicating the areas for EDX linescan direction (B-) and TEM diffraction pattern collection of the U-Mo, IDL and Al layer (C- to E-). The literature diffraction pattern for the U-Mo (1 0 0) crystall axis is shown in (F-) [151]. A slight shift of approximately 10° between the two directions A and B is observed in the sample's U-Mo pattern when compared to the (1 0 0) literature diffraction pattern.*

- Investigation of the **IDL** reveals an amorphous phase (fig. 9.5 - D). Calculation of the nearest neighbor distance (i.e. the d_{hkl}) delivers a value of 0.250 ± 0.02 nm[4]. A comparison with in-pile obtained values is provided in chapter 9.5.

[4]A full description for derivation of this result may be found in appendix D

- Regarding the **U-Mo** diffraction pattern (fig. 9.5 - E), two observations are made. First, diffraction rings are observed in the image center which were identified as nanocrystalline UO_2 (space group: Fm-3m). The oxidation of uranium is attributed to sample storage under ambient conditions. Second, micrometer sized U-Mo grains (Im-3m) are seen as well. Comparing the observed pattern to literature values for γ-U-8wt%Mo (fig. 9.5 - F), TEM pattern acquisition in the (1 0 0) crystall zone axis is confirmed, although the absence of whole series of lattice reflections is observed. Additionally, a slight lattice distortion in the lattice structure is obvious when compared to the literature pattern. Two directions labelled "A" and "B" are drawn in fig. 9.5 - E and - F. For a common bcc lattice structure, which is the case for γ-U-Mo, the angle between direction A and B is 90°. In the shown TEM pattern the angle between these two directions is rather 80°. Also, from the acquired TEM pattern the d_{hkl} values were determined to 0.244nm for direction A and 0.128nm for direction B, while literature indicates values of 0.242nm for direction A and 0.121nm for direction B. Especially for direction A the value is in excellent agreement with the literature one. However, for direction B the value is notably smaller. These observed effects, the absence of lattice reflections and the lattice distortion, are attributed to the ion bombardment damage during out-of-pile irradiation. As described in chapter 8.1.2, the nuclear stopping power of Iodine at 80 MeV is strongest at this U-Mo layer thickness, i.e. most damage is caused inside the target material.

9.3. High energy nano-XRD analysis

A complementary analysis to the TEM investigation of this thin foil was made by high energy nano-XRD performed at the ID22Ni beamline at the ESRF in Grenoble, France [152]. In particular, it was of interest to verify the amorphous nature of the IDL by this technique. All data was collected in Debye-Scherrer transmission mode[5] using a 29.6 keV ($\lambda = 0.4189$ Å) monochromatic beam with an according beam footprint on the sample of 0.1μm $\times$ 0.15μm in size. Patterns were collected in both the U-Mo layer and the IDL with a counting time of 20 seconds for each pattern. No patterns were collected for the Al substrate because the 88nm thin foil combined with the high beam energy resulted in a very low interaction between the beam and the Al. As a consequence, the obtained patterns had a too low Al intensity to provide reliable information.

- Considering the **U-Mo** diffraction pattern shown in fig. 9.6 - A, two prominent pattern contributions are identified: γ-U-8wt%Mo with a lattice constant of 0.342nm and the element Cu. The detection of Cu is clearly attributed to the TEM sample holder grid on which the TEM thin foil was glued on. A third contribution is observed as well, with the most intense peak being located at 0.280 nm. However, this phase

[5] see chapter 5.5

is not identified yet[6]. Similar results reporting about an unknown phase located at this position were also observed before in both atomized γ-U-Mo powder [93, 153] and U-Mo ingots [21]. In particular, it is not fully clear whether the presence of this phase is due to the U-Mo lattice distortion already observed by TEM or due to an additional trace phase.

- Evaluation of the **IDL** diffraction pattern (see fig. 9.6 - B) confirms the presence of an amorphous phase. By Rietveld analysis, the nearest neighbour distance is calculated to 0.247 ± 0.02 nm. Two additional phases are prominent in the diffraction pattern: UO_2 and Cu from the TEM sample holder grid. For UO_2, a lattice constant of 0.545 nm was determined which is quite low for this phase. More likely a strong contribution of U_4O_9 and U_3O_7 phases to the analyzed UO_2 pattern is assumed [154]. This phase overlap in turn leads to this measured low lattice constant value. To conclude, a strong over-oxidation of the thin foil is very probable if one consideres the thin foil's surface-to-volume ratio.

- For both analyzed patterns, the preferred orientation corrections were applied to improve the refinement quality of the Cu and γ-U-Mo Bragg lines, as the thin foil exhibited strong texturing (see the 2D diffraction patterns of each Rietveld analysis that are provided as insets in fig. 9.6).

9.4. Comparison of TEM and nano-XRD analyses

When comparing both TEM and XRD results, the following common observations are made:

- The **U-Mo** layer exhibits a strong oxidation. Most probably the oxidation phase made a transition from UO_2, which is commonly detected on U-Mo, towards U_4O_9 and U_3O_7. This effect is attributed to sample exposure and storage under ambient atmosphere. Additionally, a distortion of the bcc γ-U-Mo lattice structure is detected. This distortion is attributed to heavy ion irradiation effects. However, further TEM analyses in the non-irradiated part of the sample have to be performed to verify this statement.

- Regarding the **IDL** layer, both techniques delivered the same result: an amorphous phase was detected with a nearest neighbor distance of 0.249 ± 0.02nm when calculating the arithmetic mean of both TEM and XRD results. Considering the individual values for both techniques, the obtained results are in excellent agreement.

[6] as of April 2014

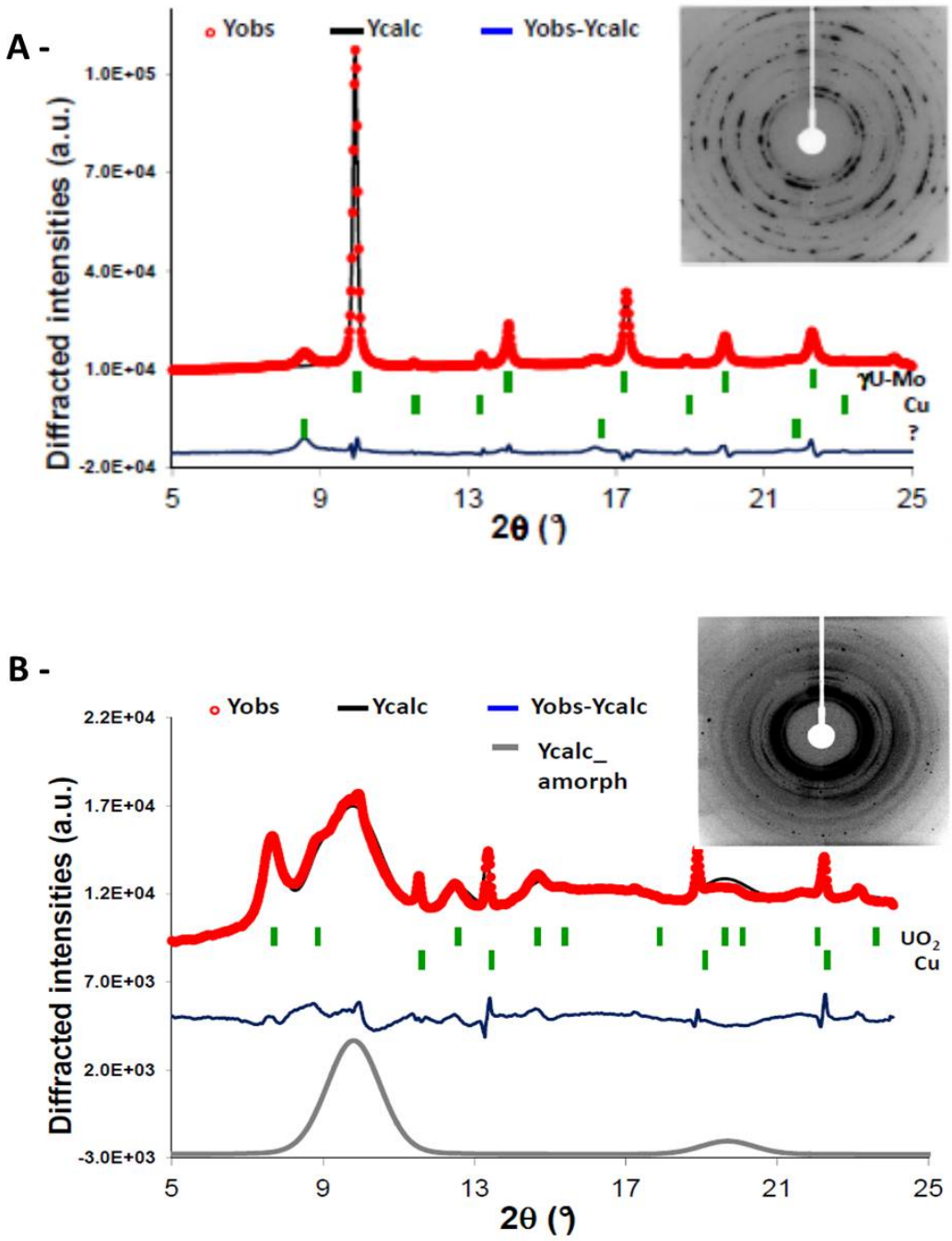

Figure 9.6.: *Nano-XRD diffraction patterns of the (A-) U-Mo layer and (B-) the IDL layer as analysed by the Rietveld method. For both patterns, the original acquired 2D diffraction pattern is added as an inset on the top right of each image. Both patterns show a significant Cu contribution due to the TEM sample holder on which the thin foil was glued on. (B-) In the IDL layer, the contribution of the amorphous phase is plotted seperately as it has a very strong share of the pattern.*

9.5. Comparison with in-pile data

In the past years, TEM examinations were performed on in-pile irradiated dispersed U-7wt%Mo powder in an Al matrix. Two of them are considered in the following when comparing the results to those presented in this chapter: the experiments of van den Berghe et al. ([63]) who examined U-Mo powder in a pure Al matrix, and those of Gan, Keiser et al. ([105, 64]) who studied an Al matrix with a 2wt% Si addition. During these in-pile tests, the irradiation temperature ranged from 90 to 130°C with a final fission density from 0.4 to 6.31 $\cdot$ 10^{21} fissions/cm^3. Table 9.2 shows a comparison of these investigations with the results explained before, while fig. 9.7 shows the comparison of the according TEM images. In all cases, the formation of an amorphous IDL is observed with an according nearest neighbour distance ranging from 0.239 to 0.251 nm. As a conclusion, it can be said that the result of heavy ion irradiation regarding this value is in a good agreement with according in-pile data, although in the upper range of the in-pile IDLs' nearest neighbour distances.

Fuel composition	Final fission density (10^{21} f/cm^3)	Irradiation temperature (°C)	IDL structure	Nearest neighbour distance (nm)
atomized U-7wt%Mo powder in Al matrix ([63])	1.41	below 130	amorphous	0.239 ± 0.004
atomized U-7wt%Mo powder in Al(2wt%Si) matrix ([64])	3.32 (low flux regime) 6.31 (high flux regime)	90 (low flux) 120 (high flux)	amorphous	not measured
atomized U-7wt%Mo powder in Al(2wt%Si) matrix ([105])	4.5	109	amorphous	0.251
ground U-8wt%Mo powder in Al(2wt%Si) matrix [40]	5.9	98	amorphous	0.24
U-8wt%Mo/Al layer system (this work)	5.1 [4]	140	amorphous	0.248 ± 0.02

Table 9.2.: *Overview and comparison of IDL characteristics obtained either by in-pile irradiation or by heavy ion irradiation. Irradiation conditions (temperature, final fission density) are mentioned as well. The nearest neighbour distance inside the IDL obtained by heavy ion irradiation is in good agreement with those obtained in-pile.*

9.5.1. Possible future experiments with heavy ions

Especially the results concerning the IDL, as obtained by TEM and nano-XRD, demonstrate that heavy ion irradiation can very well simulate the out-of-pile IDL growth with properties very similar to those IDLs generated during in-pile irradiation. Concerning the resulting IDL thickness with respect to irradiation temperature and particle flux, additional work is strongly encouraged. In particular, all the samples presented in this thesis were irradiated to the same final fluence of $1.0 \cdot 10^{17}$ $^{\text{ions}}/_{\text{cm}^2}$ at the same flux. However, no studies have been carried out for low fluence irradiation conditions. These experiments would provide valuable data concerning the IDL growth kinematics during the very first hours of irradiation, i.e.

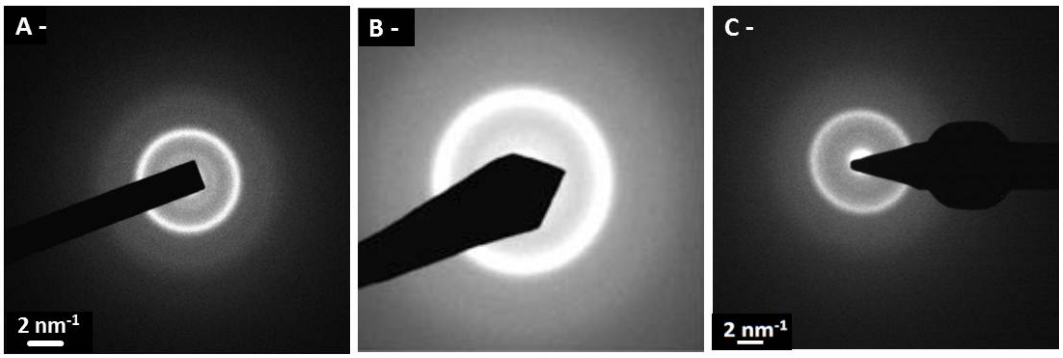

Figure 9.7.: *Comparison between TEM images obtained inside IDLs generated as a result of either in-pile irradiation ((A-, [63]) and (B-, [105])) or heavy ion irradiation (C-). No scale for image (B-) is indicated in the according reference.*

if compared to in-pile experiments with very low fission densities.
Additionally, it would also be of great interest to observe the IDL transition from the amorphous to the crystalline state during heavy ion irradiation with respect to irradiation temperature and particle flux. This would complement preceding heavy ion irradiation experiments performed under high flux conditions ($\approx 1.2 \cdot 10^{13}$ ions/s·cm²) on dispersed U-Mo/Al systems [142, 143] during which a mostly crystalline IDL was obtained. As a consequence, the flux must then be chosen between $1.2 \cdot 10^{13}$ ions/s·cm² and the aforementioned values for the charge states 6+ ($7.0 \cdot 10^{11}$ ions/s·cm²) and 7+ ($2.0 \cdot 10^{11}$ ions/s·cm²). Moreover, as amorphous IDLs can be generated by heavy ion irradiation, the option of further implanting inert gas into the heavy ion irradiated U-Mo/Al layers is also of importance. This provides a more complete general view whether heavy ion irradiation in combination with gas implantation could simulate in-pile irradiation observations. This new approach is presented in the following.

10. Kr implantation into heavy ion irradiated U-Mo/Al systems

Mentioned in the last chapter was the possibility to further implant inert gas into monolithic U-Mo/Al layer systems which were already exposed to heavy ion irradiation. Major goal of this method is the observation of inert gas behaviour in the IDL and U-Mo layer and comparison of results to in-pile irradiated data. In particular, it would be of interest to observe whether these gas particles would also form "bubbles", and whether an accumulation at the interfaces between the different layers could be detected.
Therefore, this thesis' last experimental chapter provides results on this approach. First, an explanation is presented about the choice of Kr as inert gas and the necessary particle energy to successfully implant this element into the desired sample depth. Second, the GANIL facility is described where the gas implantation took place. Finally, experimental results are presented and compared to in-pile experiments.
The samples presented in the following were not analyzed after Iodine implantation, as sample cutting would have reduced the area of interest for successive measurements after Kr implantation. Instead, samples with a 2 and 4μm thick U-Mo layer were bombarded with Iodine at the same conditions (high flux and at a temperature of 140$\pm$2 °C) as already presented in chapter 9. The samples selected for this study were irradiated with the new I irradiation setup which allowed a long-term stable irradiation temperature (see chapter 8.2.2). Therefore, it was assumed that an approximately 0.8μm thick and homogeneous IDL has grown during Iodine irradiation. As depicted in fig. 10.3, this assumption was correct. No low flux generated IDLs were selected, as the average thickness of 0.3μm was considered as too thin for this first implantation experiment. A thicker IDL provides a more precise result, as a thicker IDL can accommodate more Kr than thinner ones.

10.1. Preliminary SRIM simulations

Similar to the calculations presented in chapter 8.1.2 regarding Iodine implantation into as-fabricated U-Mo/Al systems, SRIM full damage cascade simulations regarding Kr implantation into U-Mo/IDL/Al layer systems were carried out. Basis for these calculations was the assumption of an either 2 or 4μm thick U-Mo layer which has been naturally oxidized due to storage under ambient conditions (see also fig. 9.5). This oxide layer

has been determined to an average thickness of 0.5μm[1]. For the IDL thickness, a value of 0.8μm was chosen for both cases, and the crystallographic phase UAl_3 was used to simulate this IDL, as this phase is most commonly found after heavy ion irradiation (see chapter 3.2.3).
SRIM calculations for Kr penetration depth and ionizations are shown in fig. 10.1. An implantation energy of 45 MeV was considered, as at this energy the Kr ions reach a peak stopping inside the IDL for 2μm thick U-Mo layers, i.e. the highest amount of Kr is then expected inside the IDL. The ionization caused by recoils is at its maximum at the U-Mo/IDL interface. Considering ion and knock-on atom trajectories, a maximum collision depth of 6μm inside the material can be determined. To conclude, this implantation energy is sufficient to deposit Kr inside the IDL. In the 4μm thick U-Mo layer systems, the implantation peak is located 0.5μm before the U-Mo/IDL interface. As the peak implantation depths for both cases only differ by 0.5μm, both layer system types are considered as similar.

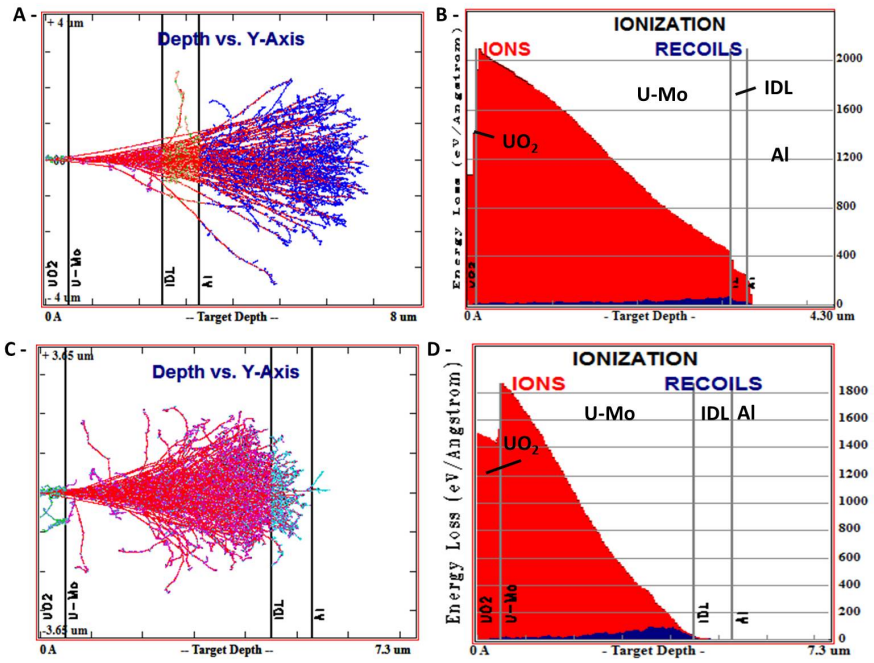

Figure 10.1.: *SRIM full damage calculations performed on layer systems consisting of a 0.5μm UO_2 layer, an either 2 (A- and B-) or 4μm (C- and D-) thick U-8wt%Mo layer, a 0.8μm thick IDL and an Al substrate. (A-) The mean Kr implantation depth for the thinner U-Mo layer lies at the U-Mo/IDL interface, while knock-on collisions may occur until a depth of 7μm. (B-) Ionization calculation by ions and recoils. Recoil damage is at its maximum at the U-Mo/IDL interface. (C-) For the thicker U-Mo layers, the mean implantation depth lies 0.5μm before the U-Mo/IDL interface, which is further verified by the calculation of ionization and recoil damage (D-).*

[1]i.e. a 0.5μm thick UO_2 layer has grown on top of a 2 or 4μm thick U-Mo layer

10.2. The GANIL implantation facility

As a first approach for inert gas implantation, one beam time has been granted at the Grand Accélérateur National d'Ions Lourds (GANIL) facility. A short description about inert gas implantation at GANIL's IRRSUD beamline is presented in the following [155].

10.2.1. Acceleration mechanism

Unlike the MLL Tandem accelerator presented in chapter 8.2.1, the GANIL facility utilizes plasma generation and acceleration. Just like in the case of DC magnetron sputtering (see chapter 8.1.1), plasma is generated by electromagnetic fields which ionize the inert gas particles inside the particle source, e.g. a gas container system. Further heating of the containment system up to around 1500°C results in augmented ion energy, which allows the ions to escape the containment system. After the ionization process, a broad distribution of particle charge states is present. The higher the charge state, the more unstable the ion is, resulting in a low yield of high charge states. Right after release from the containment system, the plasma enters the main acceleration system consisting of a series of cyclotrons in combination with quadrupol magnets. Together, these two types of devices further accelerate and focus the beam throughout the GANIL facility.
The irradiation took place at the IRRSUD beamline whose irradiation setup is depicted in fig. 10.2 - A. Just like at the MLL Tandem accelerator, the beam traverses the irradiation chamber centrally and hits the sample surface perpendicularly. The samples themselves are mounted on a sample holder which has an integrated thermal element for measuring the irradiation temperature (see fig. 10.2 - B). The beam size can be expanded so that the target area can be homogeneously irradiated. The beam current and the irradiated area on the sample holder can be measured and calculated by Faraday cups operating right in front of the irradiation chamber.

10.2.2. Implantation parameters

During the available beam time, only one pre-set kind of element and one particle energy could be chosen which remained the same during the actual irradiation period. While Xe is more representative as implantation element because of its around 20 times higher uranium fission yield than Kr (see chapter 2.1), it is far more demanding considering acceleration up to the MeV range. Main reason is that both elements are inert gases and have to be excited to the same charge state in order to provide the demanded beam energy. However, as Xe has a 1.5 times higher atomic mass than Kr, it is far more difficult to accelerate than Kr [156]. As both Kr and Xe are chemically equivalent, most effects are

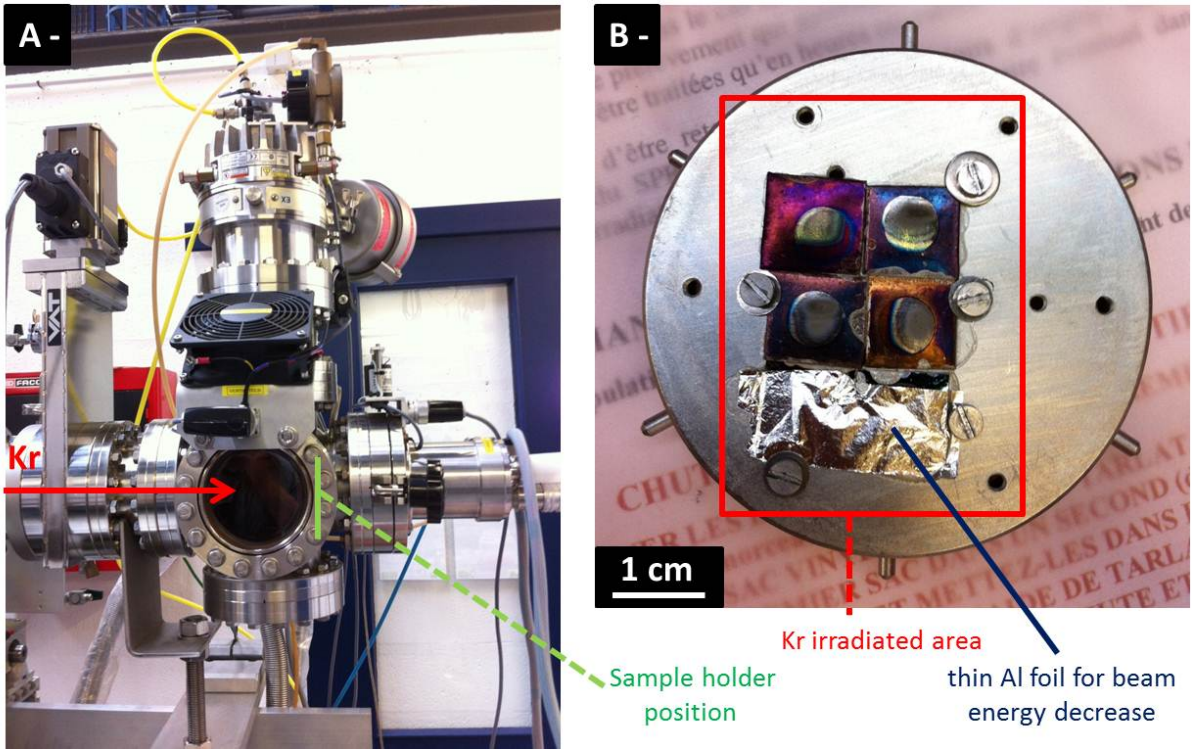

Figure 10.2.: *Images of the IRRSUD beamline setup at GANIL: (A-) Irradiation chamber. The Kr beam (highlighted in red) traverses the vacuum chamber centrally. At the end of this chamber, the beam hits the sample holder carrying the specimens perpendicularly. (B-) Sample holder with 6 specimens before irradiation. 2 samples had a thinner U-Mo and/or IDL layer thickness and were covered by a 0.8µm thin Al foil for reducing beam energy. The red rectangle indicates the beam footprint on the sample carrier as observed after irradiation. As depicted, the whole sample surface was exposed to the beam.*

comparable.
To provide a reliable post-implantation analysis of these samples, a high amount of inert gas has to be detected and observed in the analysed areas. Therefore, the choice of Kr as implantation element was made with a particle energy of 45 MeV. Furthermore, the gas release kinematics from the IRIS4 fuel presented in chapter 7 were also measured with Kr. Based on the shown SRIM calculations in chapter 10.1, this energy is enough to implant Kr through a 4μm thick U-Mo layer, with a peak deposition rate before the IDL at a total depth of around 3.3μm. In total, 6 heavy ion irradiated U-Mo/Al samples with the according U-Mo layer thicknesses were further irradiated. To compensate slight thickness deviations of the U-Mo and/or IDL layers, the effective particle energy on the sample had to be adjusted for each individual sample to guarantee that the main Kr stopping peak is inside the IDL. This has been realised by a 0.8μm thin 99.99% pure Al foil placed in front of the irradiation surface (see fig. 10.2 - B).
Implantation itself was carried out by a $^{82}Kr^{13+}$ beam with an according particle flux of $1.8 \cdot 10^{10}$ $^{ions}/_{s \cdot cm^2}$. All samples were irradiated simultaneously (see fig. 10.2 - B). After

40 hours of irradiation, a final fluence of $2.56 \cdot 10^{15}$ $^{ions}/_{cm^2}$ was reached. A comparison between Kr and I implantation parameters is provided in tab. 10.2. Furthermore, the resulting beam power alone was sufficient to heat up the sample carrier, and therefore the samples themselves, to final temperature of 141 ± 2 °C; a value which was reached after nearly 2 hours of irradiation. This means that both I and Kr irradiation temperatures were the same.

10.3. SEM analyses

Just like in the case of Iodine irradiation, the first experimental investigations were carried out by SEM. An exemplary result is shown in fig. 10.3. This sample was covered by the thin Al foil during the Kr implantation. First, EDX measurements confirmed the presence of Kr inside the U-Mo and the IDL with a gradually decreasing amount throughout the IDL towards the Al substrate (fig. 10.3 - D). A homogeneous Kr distribution inside the U-Mo layer is evident. This is in contrast to the distribution expected according to SRIM calculations.
A more striking feature is the observation of micrometer sized porosities in the IDL. Moreover, at higher magnification, it can be seen that additional porosities are visible inside the larger ones (see circles in fig. 10.3 - B). It is evident that a network of interconnected porosities exists inside the bulk material. This is in full agreement with observations made after thermal annealing tests on in-pile irradiated IRIS4 fuel, where this observation was also made (see chapter 7). It has to be stressed that these observed large porosities were only visible in areas exposed to both Iodine and Krypton irradiation. Areas irradiated with Iodine only showed a homogeneous, porosity-free IDL, while those irradiated only with Kr, but not with Iodine, showed neither an IDL, nor porosities at the U-Mo/Al interfaces (see fig. 10.3 - C).
Additionally, the IDL itself is no longer of homogeneous thickness compared to observations made in chapter 9.1. Indeed, Kr implantation has deformed the IDL. A more detailed discussion is given in chapter 10.5.

10.4. SIMS measurements

Just like in the case of the IRIS4 experiments, SEM can only deliver sample surface information (see chapter 5.1). Therefore, SIMS was utilized to quantify the amount of Kr inside the bulk material (see chapter 5.6). According dynamic-SIMS (D-SIMS) measurements were carried out at the "Centre de la recherche publique - Gabriel Lippmann" (CRP-GL) in Esch-sur-Alzette, Luxembourg. To achieve a high spatial resolution in the 500nm range and a depth resolution in the 10nm range, a CAMECA-SC-Ultra-SIMS was utilized with a Cs^+ beam at 4kV and a current of 60nA.

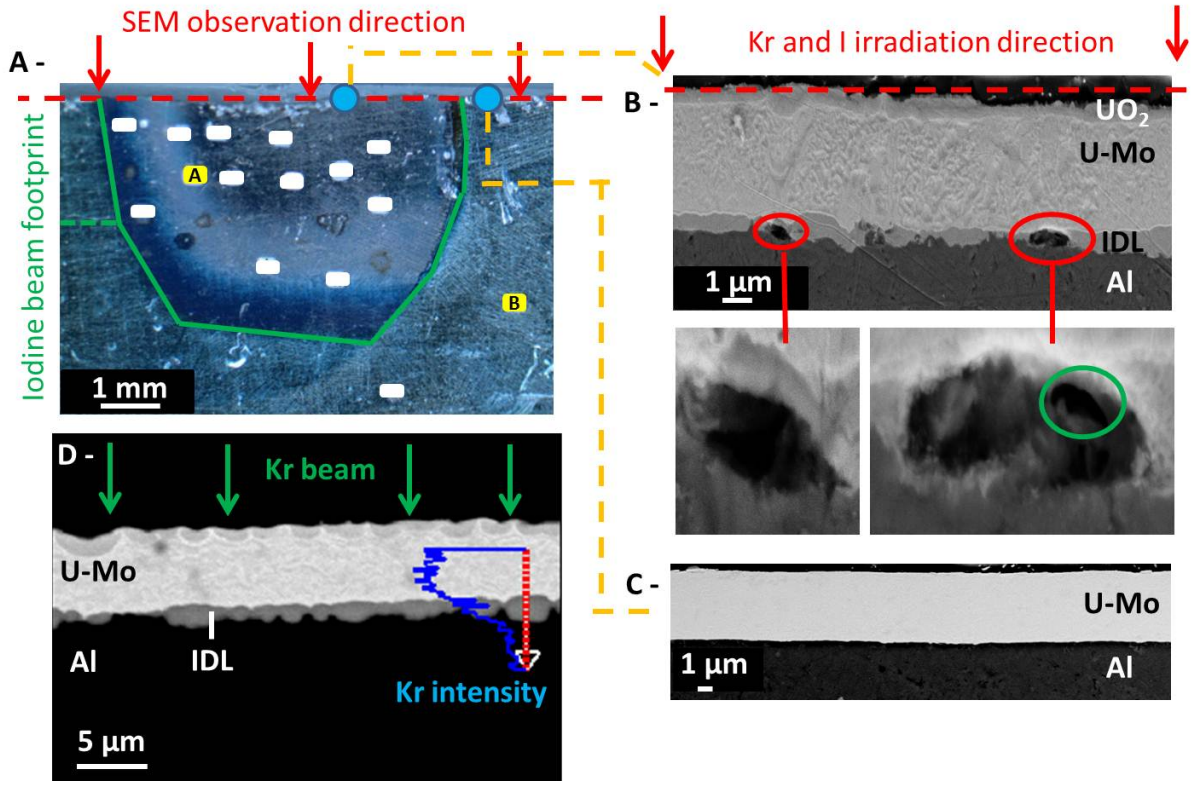

Figure 10.3.: *(A-) Optical microscopy of the analyzed sample. The sample was cut in two pieces along the red dashed line. One half was embedded for SEM investigation. White rectangles indicated the locations chosen for SIMS analysis. The two yellow rectangles labelled "A" and "B" indicate areas presented in chapter 10.4. (B-) SEM BSE image of the sample part which was exposed to both I and Kr irradiation. At the IDL/Al interface, µm-sized porosities are observed (see red circles). A magnified image of the right porosities shows some smaller porosities inside (see green circle) indicating and interconnected network of porosities. (C-) SEM SE image of a sample part which was only exposed to Kr irradiation. No IDL and no porosities are found. (D-) EDX linescan along the U-Mo/IDL/Al part showing the detected Kr signal.*

I and Kr concentrations

As indicated in fig. 10.3 - A, 20 areas of the sample were investigated both in the Iodine and in the non-Iodine irradiated part. Fig. 10.4 shows the Kr and I concentration depending on sample depth in (A-) an area exposed to both I and Kr irradiation, and (B-) an area exposed only to Kr irradiation. The according Kr and I concentrations are listed in tab. 10.1. For completeness, Al and U is shown as well to indicate the UO_2, U-Mo, IDL and Al substrate regions. As Al and U was not quantified, no concentrations are provided, and fig. 10.4 shows only the according counts.

- The different layer thicknesses for UO_2 (0.5μm), U-Mo (4μm), IDL (0.8μm) and Al are in good agreement with the SEM observation presented in fig. 10.3 - B and - C.

- For all detected elements, an increased concentration can be detected at the sample surface. This observation cannot be fully explained. However, the following interpretations are provided: First, an increased uranium concentration at the sample surface can be excluded. Otherwise, the according SEM BSE image shown in fig. 10.3 - B would have a higher contrast than the U-Mo layer which is not the case. Second, this increased uranium concentration decays over around 0.5μm which is in good agreement with the UO_2 layer thickness. A conclusion is that the UO_2 is sputtered more swiftly than the U-Mo layer which may be caused by the different compound densities, which are 17.6 $^{g}/_{cm^3}$ for U-8Mo [24] and 10.97 $^{g}/_{cm^3}$ for UO_2 [159].

- Throughout the UO_2 and U-Mo layer, the presence of Al is detected with a local maximum inside the oxide layer and an decreasing amount inside the U-Mo. This is attributed to the Al foil which was placed on top of the U-Mo to decrease the Kr energy during the implantation (see chapter 10.2.2). During the implantation, Al from the foil was implanted in the sample as well.

- Likewise, the presence of U in the Al substrate, even in the area which was not exposed to Iodine irradiation (see fig. 10.4 - B). U-Mo/Al thermal diffusion couple experiments at 580°C for 0.5 to 2 hours indicated an interaction length of 30 to 50μm on average [56] which could explain this observation. However, no IDL can be detected by SEM (see fig. 10.3 - C). Although an U diffusion occurred, the concentrations are too low to result in a common IDL (see chapters 3.2.2 and 3.2.3).

- Furthermore, a strong Kr and I concentration is observed in the oxide layer. A thermal diffusion of these two elements during the implatations is made responsible for this observation resulting in the accumulation inside the ceramic UO_2 layer[2] which is known to have more porosities than the metallic U-Mo layer.

- **Region A**: For **I**, three major concentration peaks are detected: The first one in the UO_2 layer with a peak value of $2.0 \cdot 10^{20}$ $^{atoms}/_{cm^3}$, the second one with a value of $7.9 \cdot 10^{20}$ $^{atoms}/_{cm^3}$ at the U-Mo/IDL interface, and a third peak value of $5.9 \cdot 10^{17}$ $^{atoms}/_{cm^3}$ inside the Al substrate at a depth of 7.2μm. The later two concentrations are in good agreement with SRIM calculations which predict an according concentration $4.1 \cdot 10^{20}$ $^{atoms}/_{cm^3}$ of at the U-Mo/Al interface and $3.6 \cdot 10^{20}$ $^{atoms}/_{cm^3}$ inside the Al (see fig. 9.3). However, the Iodine concentration inside the UO_2 layer cannot be explained by implantation effects, as particle stopping in this depth is mainly caused electronically instead of nuclear (see chapter 8.1.2). As explained, this does not result in the final particle stopping which is caused by nuclear stopping. Both the

[2]The ceramic nature of UO_2 was not further verified.

ceramic nature of the UO_2 layer, as well as its increase in porosities during irradiation are well known in literature [119, 160]. As no μm-sized porosities were observed by SEM (see fig. 10.3), it is concluded that the Iodine particles accumulated in nm-sized porosities inside the ceramic UO_2 layer during Kr implantation at 140°C (I back-diffusion).
The **Kr** intensity reaches a maximum of $1.1 \cdot 10^{20}$ $^{\text{atoms}}/_{\text{cm}^3}$ inside the IDL followed by an exponential decrease inside the Al. According SRIM calculations indicate a concentration of $1.0 \cdot 10^{20}$ $^{\text{atoms}}/_{\text{cm}^3}$, which shows a good agreement between simulation and experiment. Inside the UO_2, a peak concentration of $0.2 \cdot 10^{20}$ $^{\text{atoms}}/_{\text{cm}^3}$ is measured. The interpretation for the observed Kr accumulation follows the one for Iodine discussed above.

- **Region B**: **I** is not expected in areas not exposed to the I beam. However, two small I peaks can be detected. The first one with a concentration of $1.8 \cdot 10^{17}$ $^{\text{atoms}}/_{\text{cm}^3}$ at the U-Mo/Al interface, and a second one at a depth of 12.7μm with a concentration of $4.1 \cdot 10^{17}$ $^{\text{atoms}}/_{\text{cm}^3}$. Considering the distance of region "B" from the Iodine beam footprint of 1.5mm, it is once more assumed that an Iodine diffusion has occurred. Considering an Iodine diffusion coefficient in the range of 10^{-5} $^{\text{cm}^2}/_{\text{s}}$ at 140°C [161], this observation is expected.
  Two concentration peaks are also found for **Kr**: The first one inside the UO_2 layer with a concentration of $4.1 \cdot 10^{17}$ $^{\text{atoms}}/_{\text{cm}^3}$. The second peak with a concentration of $2.5 \cdot 10^{18}$ $^{\text{atoms}}/_{\text{cm}^3}$ is found at the U-Mo/Al interface with an exponential decrease inside the Al. Compared to the IDL zone in region "A", this value at the U-Mo/Al interface is lower by a factor of 1000.
  Both I and Kr show a peak at the U-Mo/Al interface. It is concluded that enhanced stress due to the different lattice parameters (3.43Å for U-8Mo [24] and 4.04Å for Al) lead to accumulation inside voids, which are slightly larger at the interface than inside the surrounding bulk material.

Particle concentration in $^{\text{atoms}}/_{\text{cm}^3}$	I + Kr irradiated area			Kr irradiated area	
	UO_2	IDL	Al	UO_2	U-Mo/Al interface
^{127}I	$2.0 \cdot 10^{20}$	$7.9 \cdot 10^{20}$	$5.9 \cdot 10^{20}$	$1.8 \cdot 10^{17}$	$1.1 \cdot 10^{17}$
^{82}Kr	$0.2 \cdot 10^{20}$	$1.1 \cdot 10^{20}$		$4.1 \cdot 10^{17}$	$2.5 \cdot 10^{18}$

Table 10.1.: *I and Kr peak concentrations in the different layers.*

Conclusion about SIMS

It has been verified that the μm-sized porosities in the IDL as observed by SEM show a strong Kr accumulation. An according accumulation at the U-Mo/Al interfaces where no IDL was generated exhibits a 1000 times lesser concentration. TEM measurements are

encouraged to observe the Kr behaviour at the U-Mo/Al interfaces and inside the U-Mo, e.g. whether the Kr has formed a superlattice structure inside the U-Mo as observed after in-pile irradiation (see chapter 4.2.1).

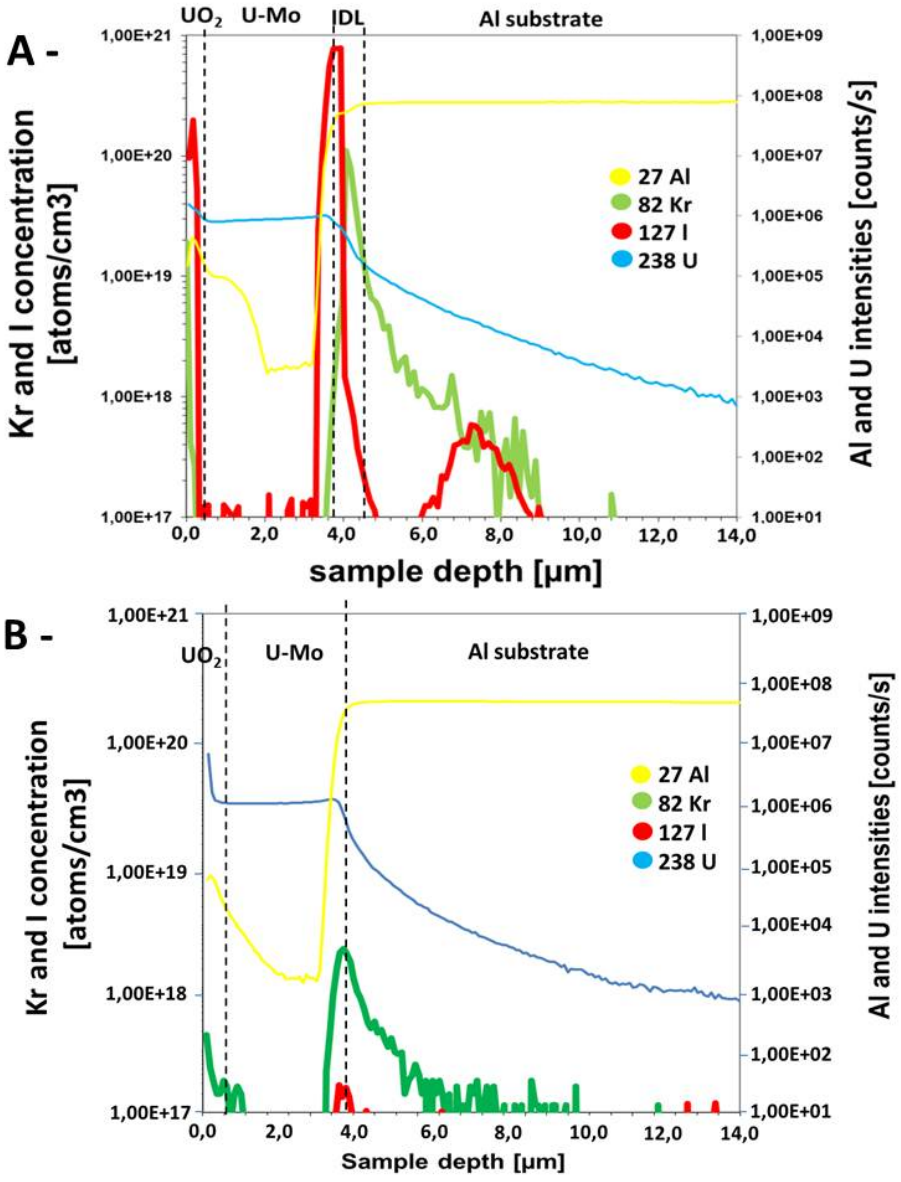

Figure 10.4.: *SIMS quantification of the elements I and Kr depending on sample depth. U and Al intensities are shown to indicate U-Mo/Al, U-Mo/IDL and IDL/Al interfaces according to SEM images depicted in fig. 10.3 -B and -C. (A-) Quantification of anIodine and Krypton implanted location taken in area "A" in fig. 10.3 - A. (B-) Quantification of a pure Krypton implanted area labelled "B" in fig. 10.3 - A.*

10.5. Comparison between Iodine and Krypton irradiation

The Kr implantation temperature of 140°C fits well with the applied Iodine irradiation temperature ranging from 120 to 160°C. This ensures that both Iodine irradiation and Kr implantation were carried out in the same temperature range. Therefore, the temperature dependent observations on both particle bombardment techniques can be compared to each other. However, not all irradiation parameters were in the same scale for these two irradiations. An according overview and comparison of all parameters is given in tab. 10.2. In particular, the final fluence of Kr ions was just 1/100 of the Iodine one[3]. This in turn means that **far less dpa's have occurred during Kr implantation than during Iodine irradiation**.
Another observation made after Kr implantation was the IDL deformation. This is not attributed to the implantation experiment itself. During implantation, both particle energy and flux were lower than during Iodine irradiation (see also tab. 10.2). If this deformation would be the result of irradiation and/or implantation, i.e. the result of damage cascades, then this IDL deformation would have been more prominently observed after Iodine irradiation, as both particle flux and final fluence were higher after Iodine irradiation than after Kr implantation. Therefore, this observation is attributed to Kr gas mechanics inside the IDL. The gas pressure of these large bubbles is assumed to be the reason for this strong IDL deformation. Indeed, when recalling chapter 4.1.2, it is concluded that the implanted amount of gas is sufficient to trigger bubble growth resulting in bubble mass coalescence. Further Kr implantation experiments are encouraged at lower fluences to verify whether the implantation parameters in this work triggered bubble growth behaviour according to "case III" in fig. 4.1. If this behaviour is not observed at lower fluences, i.e. the bubbles are in the nm-scale range, then it can be assumed that a growth behaviour according to "case I" is observed. If "case I" would be observed, this would mean that in this work the amount of implanted Kr was high enough to result in initial bubbles above the critical radius labelled R_c^V in fig. 4.1.

Particle	Beam Energy [MeV]	Flux $[\frac{ions}{s \cdot cm^2}]$	Final Fluence $[\frac{ions}{cm^2}]$	Irradiation Temperature [°C]
$^{127}I^{6+}$	80	$7.0 \cdot 10^{11}$	$1.0 \cdot 10^{17}$	140
$^{82}Kr^{13+}$	40 - 45	$1.8 \cdot 10^{10}$	$2.56 \cdot 10^{15}$	140

Table 10.2.: *Overview and comparison between the irradiation parameters for both Iodine irradiation and Kr implantation.*

[3]After thermal U fission, the Kr yield is 1.5%, while I yields 15.9% (see tab. 2.1). This means that the ratio Kr:I during the implantations is by 1/10 lower than the one occurring during in-pile irradiation.

10.6. Comparison with other recent heavy ion irradiation studies

Recent studies were performed at TUM regarding possible diffusion barrier elements which were manufactured between the U-Mo and the Al substrate. Successively, heavy ion irradiation with the same parameters as in this thesis was carried out on the trilayer systems [162]. In an according STEM image shown in fig. 10.5, the growth of an IDL between the U-Mo and the Al layer is observed. Inside this IDL close to the IDL/Al interface, a 100nm thick layer containing several nm-sized porosities is detected. It was concluded that the Kirkendall effect is responsible for this observation. This in turn leads to the conclusion that these porosities are the starting point for the Kr gas accumulation observed in the present work.

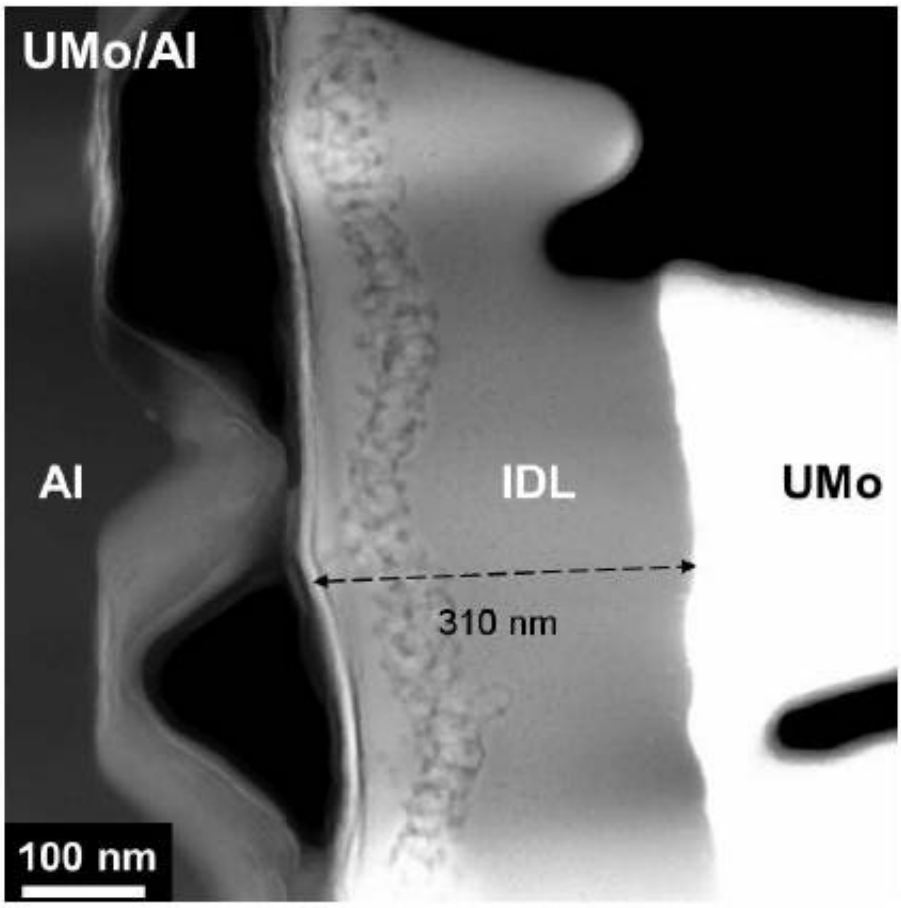

Figure 10.5.: *STEM image of a heavy ion irradiated U-Mo/Al system obtained during a recent thesis[162]. Inside the IDL close to the IDL/Al interface, a 100nm thick layer containing many porosities is observed.*

10.7. Comparison with in-pile irradiated layer systems

When compared to the RERTR6 in-pile irradiation test on monolithic fuel, porosities of the same size are visible after these in-pile tests. Accordingly, fig. 10.6 shows comparative images of both out-of-pile and in-pile tests. A further comparison of this observations can be backed up by the irradiation parameters listed in tab. 10.3. While the irradiation temperatures are in good agreement, the burnup is quite different. Nevertheless, the amount of implanted Kr together with its strong diffusion showed comparable results to the monolithic in-pile test.

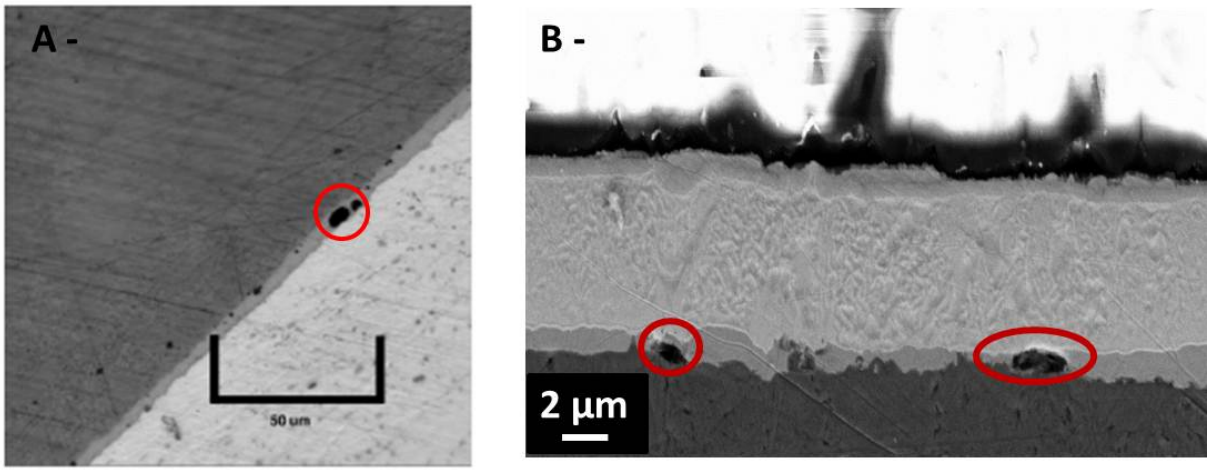

Figure 10.6.: *Comparison between (A-) in-pile irradiated monolithic U-Mo/Al systems (RERTR6 [37]) and (B-) out-of-pile irradiated ones. In both cases, porosities have formed at the IDL/matrix interfaces (see red circles).*

10.8. Comparison with IRIS4 experiment

When comparing the IRIS4 experiment (see chapter 7) with the results obtained by heavy ion irradiation in combination with Kr implantation, the following results are observed (see also tab. 10.3):

- **Interconnected porosities**: Both the thermal treated irradiated IRIS4 fuel samples and the ion and inert gas bombarded samples show interconnected porosities in the range of several 100nm up to $2\mu m$ (see fig. 7.5 and fig. 10.3). These porosities are found in regions of fission gas presence. In both out-of-pile and in-pile irradiated samples, these porosities are found inside the IDL and at the IDL/matrix interfaces. In particular, no porosities are found inside the U-Mo layer after Kr implantation although a homogeneous Kr distribution was found there (see fig. 10.3 - A).

- **Fission density comparison**: In the analyzed IRIS4 samples, a fission density of $3.76 \cdot 10^{21}$ f/cm³ was calculated. The Kr implantation was carried out until a final fluence of $2.56 \cdot 10^{15}$ ions/cm². Similar calculations to those presented in chapter 8.1.2 lead to an equivalent fission density of $0.002 \cdot 10^{21}$ f/cm³ when considering the deposited energy in the material.

- **Gas quantitiy in porosities**: SIMS analysis delivered a peak Kr density of $1.1 \cdot 10^{20}$ particles/cm³ at the IDL/Al interface in the particle bombarded layer systems. Considering the gas quantity alone, this amount would be equal to 3% burnup of the IRIS4 test. According SIMS analysis on in-pile irradiated U-Mo/Al based fuel at the same locations could deliver the according gas quantitiy which would provide a definitive comparison between the two techniques of in-pile and out-of-pile irradiation.

- However, the **temperature measurement** is not exact, especially during in-pile tests where only the cladding temperature can be calculated. Until now, no according data is available concerning the irradiation temperature inside the U-Mo particles or at the U-Mo/Al interfaces. During the out-of-pile irradiations, the temperature was 140°C, and therefore 40°C higher than during the IRIS4 in-pile irradiation.

- The out-of-pile generated IDL at these flux conditions is amorphous and therefore in full agreement with according in-pile data.

Irradiation	Fission/Implantation density (10^{21} f/cm^3)	Irradiation Temperature [°C]
RERTR6	2.8 - 3.9	<200
IRIS4	3.76	100
Iodine irradiation	0.05	140
Kr implantation	0.002 (deposited energy) / 0.11 (gas quantity)	140

Table 10.3.: *Comparison of irradiation parameters of the RERTR6 test and this work (IRIS4 and particle bombardment). The fission density value for the I irradiation is calculated based on the damage to the material caused by implantation (deposited energy). For Kr, bth values considering deposited energy and gas quantity are listed.*

10.9. Conclusion

A conclusion of this comparison is that a comparative low amount of implanted inert gas ($2.56 \cdot 10^{15}$ $^{particles}/_{cm^2}$) is enough to result in bubble growth, and therefore in the formation of large porosities which are interconnected to each other. TEM would enable analysis of the microstructure and would indicate whether a bubble superlattice structure has formed in the particle bombarded samples. By the combination of the TEM and SIMS technique, it would be possible not only to obtain sample surface information and gas quantitiy inside the bulk material, as provided by SEM and SIMS, but also microstructural investagtion of the Kr behaviour inside the U-Mo. Especially, it is of high interest to compare TEM superlattice investigation with the Kr implantation study described in chapter 4.2.2.

Part IV.

Summary

11. Summary of results

In this thesis, samples consisting of both atomized U-Mo powder particles and of monolithic U-Mo layers were investigated. In the following, both experimental approaches are shortly summarized and compared to each other. It is concluded how comparable the presented out-of-pile techniques are to simulate in-pile fuel behaviour.

11.1. Atomized U-Mo powder

Post-irradiation examinations were carried out on **atomized U-7wt%Mo particles** which were irradiated in the **IRIS4** campaign. The particles were coated with an UO_2 layer and were further embedded in an Al(2wt%Si) matrix. Goal of this project was to investigate microstructural evolution of irradiated fuel under thermal treatments. In total, three samples were cut from a high burnup region of the fuel plate ($3.76 \cdot 10^{21}$ f/cm³). The first sample was heated up to a final temperature of 1800°C inside an induction furnace. During this thermal run, two temperatures, **500** and **670°C**, were identified where a strong fission gas release from the sample was detected. Consequently, two additional thermal runs were carried out up to these two temperatures, and once again a strong fission gas output could be detected at these values. Successive SEM, XRD and EPMA measurements were performed on the annealed samples.
At 500°C, fissures inside the U-Mo particles and the IDL were observed, while at some spots the IDL and matrix were no longer in contact. Also, a strong Si diffusion towards the particles and into the IDL was detected. Considering Xe fission gas, a **precipitation towards the particle/IDL interface** became evident where it gathered in large micrometer sized bubbles. However, the inner particle cores are depleted in Xe. In strong contrast to this observation is the Xe distribution inside the IDL, where a homogeneous concentration could be observed. By measuring the Xe quantity in the investigated areas, it is concluded that a **fission gas release from the IDL** occurred during these thermal runs, as the gas quantitiy in the IDL is lower than before the thermal annealing experiments.
Results of the 670°C samples showed a **strong U-Al interaction** with increasing magnitude the more Al was available for interaction, i.e. near the meat/cladding interfaces. At these interfaces, all particles were affected and no clear particle shape remained. In the meat center, fissures of the same size as in the 500°C case were visible as well. Si itself more strongly diffused and could now be detected inside the remaining particles. New

compounds have formed inside the particles in the meat center. EPMA showed that areas rich in U lacked Mo and vice versa indicating U-Mo phase decomposition. No Xe could be detected any longer in areas of strong U-Al interaction. In the meat center, some Xe could still be detected in the IDL with only a very faint amount in the particles. Indeed, the total quantity strongly decreased in all regions when compared to the 500°C case. The second strong Xe release peak at 670°C is therefore assumed to be related to the strong U-Al interaction.

11.2. Monolithic U-Mo/Al

Experiments on **monolithic U-8wt%Mo/Al** layer systems were performed out-of-pile by particle bombardment. First, U-Mo/Al layer systems were produced by PVD sputter coating, consisting of either a 2μm or 4μm thick U-Mo layer on a pure Al substrate. Second, these samples were exposed to heavy ion irradiation with ^{127}Iodine at 80 MeV until a final fluence of $1.0 \cdot 10^{17}$ $^{\text{ions}}/_{\text{cm}^2}$ each. Goal of this study was to observe the IDL growth dependence on irradiation temperature and particle flux and to prepare and understand systems for fission gas implantation. In total, three measurement series were carried out:

- At a particle flux of $7.0 \cdot 10^{11}$ $^{\text{ions}}/_{\text{s}\cdot\text{cm}^2}$ at temperatures from 100 to 180°C. Here, both 2 and 4 μm thick U-Mo layers were utilized.
- At a particle flux of $2.0 \cdot 10^{11}$ $^{\text{ions}}/_{\text{s}\cdot\text{cm}^2}$ at temperatures from 100 to 200°C. This series was performed on 2 μm thick U-Mo layers.

A global result was that a necessary temperature of 110°C is mandatory in order to grow an IDL with this technique. Depending on the temperature, the IDL thickness ranged from 0.2μm at 110°C to 1.1μm at 190°C. If the flux is reduced to 1/3 of its original value, the final IDL growth is also only 1/3 of the initial one. Comparing the generated IDL thicknesses to those obtained after in-pile irradiation of monolithic U-Mo fuels, these thicknesses are in good agreement, although the values $^{\text{f}}/_{\text{cm}^3}$ and $^{\text{Iodine}}/_{\text{cm}^3}$ strongly differ from each other. It is concluded that the grown IDL thickness is **directly proportional to both irradiation temperature and particle flux**.
Furthermore, TEM and high energy XRD measurements were carried out on the generated IDLs. Both techniques identicated the **amorphous nature of the IDL** with a nearest neighbour distance of 0.251 nm. This is as well in excellent agreement with IDLs obtained after in-pile irradiation which were also fully amorphous and showed an almost identical nearest neighbour distance.

Kr implantation

In a final step, Kr was implanted into these created IDLs to observe the according inert gas behaviour. This irradiation was carried out until a final fluence of $2.56 \cdot 10^{15}$ $^{\text{particles}}/_{\text{cm}^2}$ with ^{85}Kr at 45 MeV at a temperature of 140°C. In a recent work, inside the IDL, a 100nm thick layer consisting of several porosities on the nm-scale was detected. This effect was attributed to the Kirkendall effect leading to the conclusion that these porosities are the starting point for the Kr accumulation observed in the present work. SEM investigations in the present study confirmed large micrometer sized porosities in the IDL which can be attributed to Kr kinetics. No porosities were visible in areas exposed to Kr, but not to Iodine irradiation, i.e. no porosities were observed in areas where no IDL was generated. The porosity sizes are also in good agreement with those observed after in-pile irradiation of monolithic layer systems. Moreover, the observed porosities indicate that they are interconnected with each other. Successive SIMS measurements confirmed that the porosities inside the IDL show a peak Kr accumulation $1.1 \cdot 10^{20}$ $^{\text{atoms}}/_{\text{cm}^3}$. According U-Mo/Al interfaces which lack IDLs show a 1000 times lesser Kr concentration. SIMS measurements on in-pile irradiated fuel is encouraged to compare these values. Furthermore, additional Kr implantation experiments at different final fluences could provide a detailed study of the bubble growth behaviour in these layer systems which in turn supports the understanding of fission gas dynamics in in-pile irradiated U-Mo fuels.

11.3. Comparison

In both parts of this thesis fission gas accumulation in large bubbles was observed in the according IDLs. This was inidicated by large μm-scaled porosities at the U-Mo/IDL interfaces. Although the Kr implantation density in the heavy ion bombarded samples was a factor of 5 lower than the according fission density in the IRIS4 experiment, this Kr gas amount is already high enough to result in large porosities. Additional Kr implantation experiments at different final fluences are encouraged to investigate this behaviour further.

11.4. Conclusion

Both presented techniques enhance the understanding of post-irradiation examinations made on both dispersed powder and monolithic fuels. For the thermal runs on the IRIS4 fuel samples, it has been shown that fission gas tends to diffuse from inside the particles towards the IDL where it can be contained to even high temperatures. Heavy ion irradiation confirms that, if the irradiation parameters are properly chosen, IDLs can be generated which are very similar to those obtained after in-pile irradiation. This in turn

qualifies heavy ion irradiation combined with Kr implantation as an appropriate method to predict some in-pile irradiation effects on the material. Considering the fact that both particle bombardment methods are economic and time-efficient as no further activation of the samples occurs, both techniques are an excellent option to pre-qualify future fuels before actual in-pile irradiation experiments are carried out.

12. Outlook

Both the IRIS4 experiment as well as the out-of-pile studies provide information regarding inert gas behaviour and microstructural evolution of the fuel samples when exposed to elevated temperatures or particle bombardment. However, as mentioned in chapter 11, several data gaps are remaining. Therefore, the following experiments on both topics are strongly encouraged:

- For the IRIS4 experiments, SEM and EPMA can only provide sample surface information. However, during the sample preparation processes, micrometer sized gas bubbles close to the investigated areas were most likely cut open, and according porosities located in these areas lack fission products. To obtain data from inside the bulk material, secondary ion mass spectrometry (**SIMS**) is proposed. With this method, fission gas location and quantity from areas below the investigated surface could be acquired, and a more global overview over temperature dependent fission gas location and behaviour could be provided. To fill the remaining data gaps, the according measurements should be undertaken inside the IDLs before any thermal run, as well as inside the U-Mo particles after thermal annealing until 500°C.

- Iodine irradiation was performed until a final fluence of $1.0 \cdot 10^{17}\ {}^{\text{ions}}/_{\text{cm}^2}$. However, studying the IDL growth at lower final fluences in order to provide a definitive conclusion about the growth dependence on the final fluence, and comparing these values to in-pile data is strongly encouraged. A clear answer could be given whether the growth is **directly proportional to fluence**. Moreover, in the framework of the HERACLES project, Iodine irradiation until higher final fluences is also of interest to study the U-Mo particle and coating behaviour itself under simulated very high fission densities. For Kr implantation, the combination of SEM and SIMS proved that μm-sized porosities found in the heavy ion generated IDL show an accumulation of Kr gas with a peak value of $1.1 \cdot 10^{20}\ {}^{\text{atoms}}/_{\text{cm}^3}$. TEM measurements are encouraged to clearify whether Kr has accumulated in nm-sized bubbles forming a superlattice structure inside the U-Mo, as observed after in-pile irradiation. Also, studying the bubble size dependence on fluence and implantation temperature could enable a more global understanding over the behaviour.

Part V.

Appendices

List of Figures

1.1. Cross-section view of FRM II's reactor [1]. 12
1.2. Sketch of FRM II's fuel element [1]. 12
1.3. Exemplary fuel plate swelling curves for the E-FUTURE (left branches) and the SELENIUM (right branches) irradiation tests (see also tab. 1.1) [44]. In the E-FUTURE campaign, abnormal swelling started at around $1.75 \cdot 10^{21}\,\mathrm{f/cm^3}$, whereas in the SELENIUM campaign this swelling onset is delayed until $4.5 \cdot 10^{21}\,\mathrm{f/cm^3}$. 16
1.4. (A-) cross-section overview of an irradiated IRIS2 fuel plate [34]. At high flux regions, the matrix shows strong evidence of disbandment. Further SEM investigations on the fuel microstructures are shown for (B-) atomized powder [54], (C-) ground powder [40] and (D-) monolithic layers [37]. All images were taken in 50% burn-up regions. In all cases an IDL has been generated during irradiation between the U-Mo and the surrounding matrix/cladding. Moreover, in all cases excessive porosity formation is visible both in the particles and in the IDL (indicated by red circles). . . . 17

2.1. Average nucleon binding energy per nucleon versus atomic number. Elements found left of the most stable element Fe could become more stable by core fusion, while those on the right of Fe would undergo core fission [9]. 22
2.2. Occuring fission fragments after ^{236*}U fission. Please note that this distribution is normalized to 200%, as two fission fragments are generated [7]. 23
2.3. Sketches of the lattice structures of (A-) α-, (B-) β- and (C-) γ - phase uranium, as well as (D-) γ^0-U-Mo. Purple spots in (D-) mark the position of Mo atoms [13], [143]. 24
2.4. Image of α-U deformation. After around 3000 cycles at temperatures between 50 and 550°C, the solid bulk (A-) of highly textured uranium has grown around six times in size (B-) [15]. 24
2.5. Relationship between γ-U stability and U density for different alloys at $500°C$. U-Mo exhibits the highest density of all the three alloys [24]. 25
2.6. (A-) U-Mo binary phase diagram [24]. The two red lines correspond to U-7wt%Mo and U-8wt%Mo respectively. (B-) TTT diagram for a U-8wt%Mo compound. Grey lines indicate measurements from the 1960s [31], while black lines indicate recent studies [133]. 27

3.1. Time scale for damage evolution and according time intervalls [45]. 30

3.2. Comparison of projectile trajectories by high (a) and low (b) energetic ions inside a solid [45]. 33

3.3. Zones of electronic and nuclear stopping dominance [45]. 34

3.4. Gaussian distribution of the implanted ions inside the material. R_p is the average projectile penetration depth, while ΔR_p is the standard deviation and N_p the maximum concentration of implanted ions at the distance x [45]. 34

3.5. Model graph indicating the strength of U-Al interaction dependeing on fission rate and temperature [66]. Both high temperatures and high fission rates lead to crystalline IDLs. 37

3.6. SEM cross section view of an heavy ion irradiated atomized U-Mo/Al sample. Between the U-Mo particles and the Al matrix an IDL has formed up (see green circles). The yellow dashed line indicates the sample surface which was exposed to the ^{127}Iodine particle bombardment. The red dashed line shows the maximum penetration depth of Iodine into Al of 13μm. Based on [143, 67]. 38

4.1. Growth rate depending on the cavity radius with an increasing amount of gas atoms inside [45]. 47

4.2. Sketch of the dislocation loop punching mechanism. A bubble can further grow by using its gas pressure p on the lattice structure to force dislocations nearby to be moved out of position [75]. 48

4.3. Microstructural investigations on irradiated FUTURE fuel samples. (A -) Optical microscopy on U-Mo. Inside the particles, grain subdivision has occurred. At these intergranular cell boundaries, porosities can be detected which are filled with fission gas. (B -) An EPMA mapping showing the Mo concentrations inside the particles. Inside the intergranular cells, a larger Mo amount can be detected than at the cell boundaries. TEM dark field imaging (C -) and a corresponding TEM diffraction pattern (D -) obtained in the area highlighted in red in (C -). The U-Mo's granular structure is well observed. (E -) and (F -): TEM bright field images of two different U-Mo particles. The bubble superlattice structure is evidenced [35, 63]. . . 51

4.4. Microstructural investigations on irradiated IRIS-TUM fuel samples. (A -) SEM BSE image of a U-Mo particle where a grain subdivision has occurred. Also at these intergranular cell boundaries, the detected porosities are filled with fission gas. (B -) A corresponding TEM diffraction pattern showing a gas bubble superlattice structure [40]. 52

4.5. TEM investigations on irradiated RERTR7 fuel on both (A -) low flux and (B -) high flux regions. High flux regions show significantly bigger fission gas bubbles (see red circles). (C -) Inside the U-Mo particles of the RERTR6 fuel plates a bubble superlattice is seen as well. (D -) Large bubbles are visible inside the amorphous interaction layer (see blue circles) [105, 64]. . 53

5.1. Sketches of SEM mechanisms. (A-) A general overview of how primary electrons emitted from the gun (indicated in light blue) hit the sample structure. Based on the primary electron energy, i.e. the accelerating voltage, the penetration depth is up to 2 μm. While traversing the sample, several secondary effects inside the sample are triggered (see also (B-)). From a depth of up to 10 nm inside the material, low energetic secondary electrons (SE) can leave the sample and are attracted to and absorbed by a positively charged SE detector. Backscattered electrons (BSE) from a depth of up to 2 μm are high energetic and mainly emitted in trajectory close to the primary electron beam where they can be detected by a backscattered electron detector. (C-) Also, incident beam electrons can excite electrons from atom shells inside the material. Upon relaxation, the electron can emit an x-ray photon that can also be detected. Therefore, information about the elemental composition inside the bulk material can be acquired. (B) is directly taken from [127], while (C-) is based on [127]. 57

5.2. Sketch of FIB operation: The specimen is tilted inside a SEM system so that the sample surface and the ion beam include a 90° angle. Normally, FIB and SEM include a 45° angle. On the same time as FIB imaging, SEM imaging can be performed under a 45° angle to the sample surface. The distance between SEM gun and sample observation is normally around 5 mm. This ensures that FIB and SEM show exactly the same spot on the sample surface when FIB milling is undergoing. A gas inlet system can provide working gas for the operation processes. With a low FIB current, gas material can be deposited on the sample, while a high FIB current ensures sample milling. In the later case, the working gas assists the milling process. The final result of FIB milling are very small objects in the nm scale. The sketch is based on [127]. 59

5.3. (A-) In TEM, electrons are accelerated by a high voltage ranging from 300 to 500 kV. The primary electrons' beam trajectories are considered as parallel to each other due to the beam size. When traversing an average 80 - 100 nm thin foil, the electrons are diffracted and can be focussed by objective lenses. A diffraction pattern can be acquired which shows the crystal structure of the examined area. (B-) In STEM, the primary beam is highly focussed so that point-by-point scanning of the specimen can be achieved. The transmitted electrons can be observed by bright field analysis technique or by high angular annular dark field (HAADF) analysis. The later technique allows phase analysis as the scattered electrons detected by HAADF are strongly dependent on the density of the scanned material. . 60

5.4. Sketches describing Bragg's law: (A-) Incident x-rays can penetrate into the specimen where they interact with the material atoms' electronic shells. In a lattice structure, all the reflected x-rays are diffracted under the same angle which results in a path difference between those rays being emitted from inside the material and those which are reflected at the sample surface. This path difference depends on the lattice constant d. XRD patterns can very well be collected for rays of constructive interference. (B-) Sketch to visualize the aforementioned derivation of Bragg's law [132]. The angle between incident and reflected beam is 180° - 2θ. 62

5.5. Sketch of the Bragg-Brentano setup, a θ-2θ powder diffraction method. To detect each individual phase, both x-ray source and detector of this phase have to be placed on their own goniometric circle. Two exemplary goniometric circles are highlighted in green and blue. As the specimen itself is placed in the center of its own goniometric circle, both the x-ray source and the according detectors are to be situated at this goniometric circle's radius (highlighted in black). A common method is to rotate the specimen while the source and the detector are fixed in place [132]. 63

5.6. Sketch of the Debye-Scherrer method. The incoming x-ray beam can traverse the specimen if the beam energy is high enough and the sample thin enough. Due to the different phases and according spatial orientations inside, diffraction rings may be acquired on a flat detector behind the sample. Sketch is based on [133]. 64

5.7. Sketch of the SIMS technique: An incident primary ion beam sputters the target material. Around 1% of the sputtered material is charged and can be analyzed by mass spectrometry [157]. 65

6.1. Illustration of the IRIS4 fuel manufacturing process. The oxide coated U-Mo particles are embedded in an Al matrix with a 2.1wt% Si addition. The created meat is then enclosed by an AG3NE frame and an AlFeNi cladding on both sides to prevent fission products to evade into the primary circuit. The image on the bottom left shows a cross-section view of the final fresh fuel plate. 70

6.2. EPMA SE imaging and elemental mapping of fresh IRIS4 fuel meat. The different elements contributing to the meat can be distinguished from each other: U, Si, Mo, Al, N and O. A slight Si accumulation at the oxide layer around the particles can be seen (see red circle). Indicated in the Mo map is the intergranular grain subdivision leading to a Mo depletion at the grain boundaries inside the U-Mo particles. 71

6.3. SEM BSE characterisation of fresh IRIS4 meat. The presence of a nitride layer which has grown on top of the oxidized particles is confirmed by EDX elemental mapping. The nitride layer exhibits cracks. 72

6.4. (A-) Optical microscopy and (B-) EPMA SE images taken in the main meat region of irradiated IRIS4 fuel [54]. (A-) The growth of an IDL around the particles is evidenced. (B-) Inside the particles and at the U-Mo/IDL interfaces, a large amount of porosities is visible. As shown in fig. 6.5, these porosities are filled with Xe gas. 74
6.5. (A-) EPMA elemental mapping of irradiated IRIS4 fuel. All images were obtained in the meat center. A BSE image is shown together with X-ray maps for U, Xe, O, Si, Al, Zr and Mo. Indicated in the BSE image is the direction of the EPMA linescan shown in (B-). This scan indicates the Zr and Xe weight fractions inside the Al, the IDL and the U-Mo particle. . . . 75

7.1. Sketch of the IRIS4 fuel plate no. 8043 indicating the regions from the samples were cut for further thermal treatments. The PIEs presented in the last chapter were performed on MA432 which was exposed the same irradiation conditions as TMG434, TMD433 and TMD434. The later three samples are heated up until 1800°C (TMG434), 670°C (TMD433), and 500°C (TMD434) respectively. 78
7.2. Sketch of the MERARG setup for thermal treatments and online fission gas release observation [114]. 78
7.3. Measured ^{85}Kr release during the three different thermal treatment runs using similar irradiated IRIS4 fuel samples. The treatments were performed until a final temperature of (A-) 1800°C, (B-) 500°C, and (C-) 670°C. In each curve, the detected release peaks are indicated by a digit. 81
7.4. Global optical microscopy overview of transversal cross sections cut from the ThT500 (A-) and ThT670 sample (B-). Analyzed areas are highlighted in green. To gain an artificially magnified view of the meat region, the cross sections were not cut perpendicular to the cladding surface, but rather in a slight angle (see sketch). 82
7.5. Two SEM images from the irradiated and thermally treated IRIS4 ThT500 sample: The middle image is representative for the meat center region, while the image at the right represents the meat/cladding regions. Highlighted in red are areas inside the sample where fissures occurred during the thermal run. Also, highlighted in blue are areas ("holes") where the IDL and the matrix lost contact with each other. These holes are also visible in non-irrdiated U-Mo/Al fuels after thermal treatments. An image of this behaviour is shown on the right [117]. Please note that the right image was taken in BSE mode, while the other two were taken in SE mode. 84
7.6. Al, Si, O and Mo EPMA elemental maps of the ThT500 sample and comparison with the pre-ThT state. On the left, the regions in which these maps were acquired are highlighted by green rectangles. In the Mo map, intergranular grains are visible inside the U-Mo particles. Si accumulation is well observed inside the IDL after thermal treatment. Red circles represent areas of massive Si accumulation. The two maps of the pre-ThT are taken from [54]. 85

7.7. EPMA mapping of Xe, Nd and Zr distribution in the same regions already shown in fig. 7.6. Indicated by a red arrow is the direction of a linescan to determine the quantity of these elements inside the U-Mo particle, the IDL, and the matrix. 86

7.8. Xe and Zr average weight fractions in the (A-) meat center region and (B-) at the meat/cladding interface after the different thermal treatments. . . . 88

7.9. XRD refinement on the ThT500 sample. Identified phases include α-U, γ-U-Mo, UAl_3, Al, Sn and Bi. Please note the significant discrepancies between the expected peak height (in color) and the measured ones (in black). 89

7.10. SE images of the ThT670 sample taken (A-) at the meat/cladding interface and (B-) in the meat center region. While the fuel microstructure can still be detected in the meat center, a total interaction occurred at the meat/cladding interface. 90

7.11. EPMA elemental mapping of the ThT670 sample in large scale. The left side of each map shows the meat/cladding interface while the right hand side shows the meat center. Elemental maps show the distribution of Mg, Al, O, Si, U and Xe. In the Xe map, five orange boxes are highlighted which mark the region for further small scale Xe investigations shown lateron. 93

7.12. (A-) EPMA mapping of U. Indicated are 4 regions where a small scale investigation has been performed. (B-) Evolution of inceased U-Al interaction the closer one gets to the meat/cladding interface. 94

7.13. EPMA SE images (A- and I-) and EPMA small scale elemental mapping for the ThT670 sample. On the left hand side, the meat/cladding interface is shown, while on the right hand, the meat center is pictured. White circles in (K-) represent areas of starting Al diffusion into the U-Mo particles. . . 95

7.14. EPMA elemental mapping of Xe distribution. Below, small scale images of the same five selected regions as in fig. 7.12 are shown. Indicated by orange arrows are the direction of EPMA linescans performed in these regions in order to calculate Xe weight fractions and Xe/Nd weight ratios. In region 3 no linescan was obtained as this area was considered identical to region 2. . 96

7.15. EPMA linescans showing the Xe and Nd weight fractions at (A-) the meat cladding interface and (B-) the meat center. Linescan directions are highlighted by arrows in according images. Image (A-) corresponds to region no. 1 and image (B-) to region no. 5 in fig. 7.14. 97

8.1. (A-) Sketch of the DC magnetron sputtering technique. (B-) Drawing of the used sputtering setup. Both sketches are taken from [137]. 108

8.2. SRIM calculations showing the impact of Iodine ions with an energy of 80 MeV into an U-8wt%Mo layer. (A-) A two-dimensional plot showing the Iodine penetration depth into a pure U-8wt%Mo layer. The average maximum penetration depth is located at 4.95 μm. (B-) The ionization due to recoils is also at its maximum at this depth. (C-) to (E-): Ionization plots calculated for U-Mo layers of various thicknesses: (C-) 2 μm, (D-) 4 μm, (E-) 5 μm. Ionization by both ions and recoils are plotted [143]. Green lines indicate Bragg peaks for nuclear stopping power. 110

8.3. Overview of the MLL Tandem accelerator facility. Negative charged ions are generated in the ion source, while the main acceleration to the final energy and charge state takes place in the main Tandem tube. Afterwards, a 90° magnet leads the beam to hall 1. There, a switcher magnet guides the beam to the experimental setup at the +10° tube [140]. 112

8.4. Sketches explaining the basic mechanism of Tandem acceleration. (A-) shows the method of particle extraction from a target via sputtering. Before entering the mean acceleration system shown in (B-) the particles are negatively charged. In the acceleration "tank", the particles are first accelerated towards a terminal voltage in the range of 3 to 15 MV. There, the particles traverse a "stripping" system after which they are positively charged. Then the second acceleration step forces the particles towards the experiment. As high voltages are applied, both an isolator and an SF_6 isolation gas have to be used to shield the beam tube from the environment. (B-) is based on [140]. 114

8.5. (A-) Image of the sample holder. Three irradiation position are possible. The samples are fixed to the holder by a thin Al sheet with a 6mm wide hole. This ensures the beam footprint on the sample is exactly of this size. The irradiation temperature is measured by a PT100 sensor positioned between the Al sheet and the sample holder ($\approx$ 1mm distance to beam footprint). On the bottom of the sample holder, a 6mm wide hole was drilled. This is meant for beam adjustments and allows for on-line beam monitoring. Sample heating is achieved by both the beam power and an electrical heating wire on the sample holder's flank. (B-) Overview of the irradiation chamber. The beam traverses the chamber centrally where the irradiated sample is to be positioned. The sample holder is mounted on a translateable rod which can move the holder vertically. Integrated in the rod is a cooling tube. A turnable quartz crystal together with an IR camera allows for on-line beam spot monitoring. 117

9.1. (A-) Optical microscopy image of a heavy ion irradiated monolithic U-Mo/Al sample. The beam footprint on the sample is uniformly 6mm in diameter. The red line indicates the intersection for successive SEM cross section preparation. The right, smaller part of the sample was embedded. Two representative SEM BSE images are shown in (B-): for the non-irradiated and in (C-): for the irradiated part. In the irradiated area, a 400nm thick IDL has grown between the Al substrate and the 2μm thick U-Mo layer. 119

9.2. (A-) Plot showing the IDL thickness evolution with increasing temperature for both 2μm (in blue) and 4μm (in red) thick U-Mo layers. (B-) Plot comparing the influence of flux on 2μm U-Mo systems. The blue line indicates the high flux condition (6+) already shown in (A-), while the red one represents the low flux condition (7+). All sample types were irradiated until a final fluence of $1.0 \cdot 10^{17} \frac{ions}{cm^2}$. Large error bars on the x-axis indicate irradiations performed with the old setup (see chapter 8.2.2). Linear fits with 95% confidence bands are shown. 124

9.3. SRIM calculations performed on Iodine irradiation on a 5μm thick U-Mo layer on an Al substrate. (A-) Iodine distribution and (B-) energy loss are depicted. The blue line indicates the U-Mo/Al interface. 126

9.4. (A-) SEM BSE image of a sample irradiated at 140°C (charge state 6+). A 0.7μm thick IDL has formed during irradiation. The region highlighted in red represents the area from which a 100nm thin foil for TEM investigations was prepared. (B-) STEM HAADF image of the mentioned foil well indicating the three different layers. The left hand side in (B-) does not show a uniform layer thickness. This is an artefact produced by thin foil preparation. . . . 126

9.5. (A-) STEM HAADF image of the thin foil with indicating the areas for EDX linescan direction (B-) and TEM diffraction pattern collection of the U-Mo, IDL and Al layer (C- to E-). The literature diffraction pattern for the U-Mo (1 0 0) crystall axis is shown in (F-) [151]. A slight shift of approximately 10° between the two directions A and B is observed in the sample's U-Mo pattern when compared to the (1 0 0) literature diffraction pattern. 127

9.6. Nano-XRD diffraction patterns of the (A-) U-Mo layer and (B-) the IDL layer as analysed by the Rietveld method. For both patterns, the original acquired 2D diffraction pattern is added as an inset on the top right of each image. Both patterns show a significant Cu contribution due to the TEM sample holder on which the thin foil was glued on. (B-) In the IDL layer, the contribution of the amorphous phase is plotted seperately as it has a very strong share of the pattern. 130

9.7. Comparison between TEM images obtained inside IDLs generated as a result of either in-pile irradiation ((A-, [63]) and (B-, [105])) or heavy ion irradiation (C-). No scale for image (B-) is indicated in the according reference. 132

10.1. SRIM full damage calculations performed on layer systems consisting of a 0.5μm UO_2 layer, an either 2 (A- and B-) or 4μm (C- and D-) thick U-8wt%Mo layer, a 0.8μm thick IDL and an Al substrate. (A-) The mean Kr implantation depth for the thinner U-Mo layer lies at the U-Mo/IDL interface, while knock-on collisions may occur until a depth of 7μm. (B-) Ionization calculation by ions and recoils. Recoil damage is at its maximum at the U-Mo/IDL interface. (C-) For the thicker U-Mo layers, the mean implantation depth lies 0.5μm before the U-Mo/IDL interface, which is further verified by the calculation of ionization and recoil damage (D-). . . 134

10.2. Images of the IRRSUD beamline setup at GANIL: (A-) Irradiation chamber. The Kr beam (highlighted in red) traverses the vacuum chamber centrally. At the end of this chamber, the beam hits the sample holder carrying the specimens perpendicularly. (B-) Sample holder with 6 specimens before irradiation. 2 samples had a thinner U-Mo and/or IDL layer thickness and were covered by a 0.8μm thin Al foil for reducing beam energy. The red rectangle indicates the beam footprint on the sample carrier as observed after irradiation. As depicted, the whole sample surface was exposed to the beam. 136

10.3. (A-) Optical microscopy of the analyzed sample. The sample was cut in two pieces along the red dashed line. One half was embedded for SEM investigation. White rectangles indicated the locations chosen for SIMS analysis. The two yellow rectangles labelled “A” and “B” indicate areas presented in chapter 10.4. (B-) SEM BSE image of the sample part which was exposed to both I and Kr irradiation. At the IDL/Al interface, μm-sized porosities are observed (see red circles). A magnified image of the right porosities shows some smaller porosities inside (see green circle) indicating and interconnected network of porosities. (C-) SEM SE image of a sample part which was only exposed to Kr irradiation. No IDL and no porosities are found. (D-) EDX linescan along the U-Mo/IDL/Al part showing the detected Kr signal. 138

10.4. SIMS quantification of the elements I and Kr depending on sample depth. U and Al intensities are shown to indicate U-Mo/Al, U-Mo/IDL and IDL/Al interfaces according to SEM images depicted in fig. 10.3 -B and -C. (A-) Quantification of anIodine and Krypton implanted location taken in area “A” in fig. 10.3 - A. (B-) Quantification of a pure Krypton implanted area labelled “B” in fig. 10.3 - A. 141

10.5. STEM image of a heavy ion irradiated U-Mo/Al system obtained during a recent thesis[162]. Inside the IDL close to the IDL/Al interface, a 100nm thick layer containing many porosities is observed. 143

10.6. Comparison between (A-) in-pile irradiated monolithic U-Mo/Al systems (RERTR6 [37]) and (B-) out-of-pile irradiated ones. In both cases, porosities have formed at the IDL/matrix interfaces (see red circles). 144

A.III.(A-) New sample holder design with a closeup image of the specimen carrier. Here, it is possible to move the whole sample holder in $\hat{z}$ direction which allows mounting of three samples at the same time. Heating of the specimen carrier can be realised by beam power and also by an electrical heating wire. Cooling is achieved by a flow pass through the backside of the specimen carrier. Both electrical heating and cooling flow can be regulated by PLC controlling. In both cases temperature is measured with a PT100 sensor positioned between the Al sheet and the sample. Shown in (B-) is the irradiation chamber overview indicating beam direction and relevant positions for irradiation monitoring and control. 198

A.IV.(A-) TEM diffraction pattern of the Al region obtained in a thin foil prepared by FIB. (B-) According diffraction pattern from literature indicating the (h k l) values' diffraction rings [151]. (C-) TEM diffraction pattern of the amorphous IDL. Two distances of the broad amorphous ring were taken into account for calculation of nearest neighbour distance. 203

List of Tables

1.1. Overview of selected previous in-pile test irradiations on ground and atomized U-Mo dispersion fuel, as well as for monolithic fuel, showing the evolution of fuel manufacturing and irradiation history over the years. Final fission density, burnup, temperature and heat flux values are given for maximum flux planes (MFP). In some cases, an additional element was added to the matrix to improve irradiation performance. The IRIS4 irradiation campaign is described in greater detail in chapter 6.2. 15

2.1. List of the most prominent elements occurring after thermal uranium fission [11]. 22

3.1. IDL information obtained during post irradiation examinations for some exemplary irradiations (see also tab. 1.1). The nomenclature n.m. stands for "not measured". Fission density values are given for the examined area. 36

4.1. Exemplary PIE data on fission gas distribution inside U-Mo fuel. 49

6.1. Summary of the in-pile irradiation conditions IRIS4 plates no. 8043 and 8044 (2.1wt% Si in matrix). Samples analyzed in this thesis were taken from plate no. 8043. 73

7.1. Melting temperatures of materials that could be present in thermally treated IRIS4 fuel. U-Al_x compounds are common U-Al interaction products occurring after in-pile irradiation. The exact cladding melting point depends on the wt% mixture of the different elements inside. 79

7.2. Measured fission gas release fraction in each temperature interval for the ThT 1800°C run. 80

7.3. Integral fission gas release values during the ThT1800°C, the ThT500°C and the ThT670°C run. The unit "g" indicates that Kr release was normalized to the meat weight of each sample. 80

7.4. Surfrace fraction of U-Mo, IDL, and Al in the meat center determined by X-ray mapping analysis of Al and U. Large porosities are excluded from this analysis. No surface calculations were made in the ThT670 sample, as its microstructure is no longer homogeneous. 83

7.5. Thermal expansion coefficients for U-Mo and Al at 500°C [24]. At this temperature, Al has 1.6 times the value of U-Mo. 84

7.6. IDL elemental composition as determined by quantitative EPMA linescans in in-pile irradiated IRIS4 fuels. Comparison between as irradiated and post-thermally treated fuel samples up to 500°C and 670°C respectively. In the 670°C case, no distinction is made between internal and external IDL; atomic ratio values show the evolution from the meat towards the cladding area. Accordingly, Si concentrations in the 670°C case are only releveant for IDLs around particles in the meat center (see also subchapter 7.6). . . . 88
7.7. Xe:Zr weight fractions as measured by EPMA at the three different states: as-irradiated, after ThT500 and after ThT670. 88
7.8. Measured total fission gas release and assumption of release locations inside the material. 98
7.9. Measured reactions heat depending on U loading inside U/Al compacts [124].100
7.10. Assumed fission gas release from compounds melting at temperatures above 670°C (see also tab. 7.1). 101
7.11. Summary of EPMA and XRD analysis after in-pile irradiation [54], after thermal treatment at 500°C and after thermal treatment at 670°C. 102

8.1. Overview of the electronegativity of frequent elements after thermal fission of ^{235}U (see also tab. 2.1). Cs which has one of the lowest electronegativites of all elements is put in first place as it is an essential part of Tandem accelerator operation and is therefore considered as a reference. For consistency, the total elemental yield after thermal uranium fission is shown as well. All values are according to Pauling's classification and are therefore without unit [139]. 113
8.2. Summary of heavy ion irradiation conditions and calculated deposited energy at the U-Mo/Al interface. 117

9.1. Comparison of the obtained IDL thicknesses after in-pile irradiation and after heavy ion irradiation. 123
9.2. Overview and comparison of IDL characteristics obtained either by in-pile irradiation or by heavy ion irradiation. Irradiation conditions (temperature, final fission density) are mentioned as well. The nearest neighbour distance inside the IDL obtained by heavy ion irradiation is in good agreement with those obtained in-pile. 131

10.1. I and Kr peak concentrations in the different layers. 140
10.2. Overview and comparison between the irradiation parameters for both Iodine irradiation and Kr implantation. 142
10.3. Comparison of irradiation parameters of the RERTR6 test and this work (IRIS4 and particle bombardment). The fission density value for the I irradiation is calculated based on the damage to the material caused by implantation (deposited energy). For Kr, bth values considering deposited energy and gas quantity are listed. 145

A.IV.Parameters of the Al. As a cubic structure lattice parameters a,b,c and several (hkl) directions are identical. 201
A.IV.Calculated values for the Al pattern shown in fig. A.IV - A and - B. 202

A.VI.Utilized sample grinding and polishing recipe for successive SEM analyses. 207

Bibliography

[1] Homepage of the FRM II: `http://www.frm2.tum.de`, URL link as of April 2014.

[2] A. Röhrmoser: *Neutronenohysikalische Optimierung und Auslegung eines Forschungsreaktors mittlerer Leistung mit Zielsetzung auf einen hohen Fluß für Strahlrohrexperimente*, PhD Thesis, Technische Universität München, 1991.

[3] A. Röhrmoser, W. Petry, K. Böning, N. Wieschalla: *Reduced Enrichment Program for the FRM-II*, Proceedings of the 23rd International Topical Meeting on Reduced Enrichment for Research and Test Reactors (RERTR), Vienna, Austria, 2004.

[4] R. Jungwirth, T. Zweifel, H.-Y. Chiang, W. Petry, A. Leenaers, S. van den Berghe: *Heavy ion irradiation of UMo/Al samples PVD coated with Si and ZrN layers*, Journal of Nuclear Materials Vol. 434 (2013), 296 - 302.

[5] J.P. Durand, Y. Fanjas: *LEU Fuel Development at CERCA: Status of October 1993*, Proceedings of the 17th International Topical Meeting on Reduced Enrichment for Research and Test Reactors (RERTR), Oarai, Japan, 1994.

[6] J.L. Snelgrove, G.L. Hofman, C.L. Trybus, T.C. Wiencek: *Development of very high density low-enriched-uranium fuels*, Proceedings of the 19th International Topical Meeting on Reduced Enrichment for Research and Test Reactors (RERTR), Seoul, South Korea, 1996.

[7] D. Emendörfer: *Theorie der Kernreaktoren - Band 1*, 2nd printing, B.I. Wissenschaftsverlag, Heidelberg, 1982.

[8] M.F. L'Annunziata: *Handbook of Radioactivity Analysis*, 3rd edition, Academic Press, 2012.

[9] `http://en.wikipedia.org/wiki/File:Binding_energy_curve_-_common_isotopes.svg`, URL link as of October 2013.

[10] N.J. Carron: *An Introduction to the Passage of Energetic Particles through Matter*, Taylor Francis Group, New York, 2007.

[11] IAEA homepage: *Cumulative Fission Yields* , `https://www-nds.iaea.org/sgnucdat/c3.htm`, URL link as of December 2013.

[12] J. Lehmann, R.F. Hills: *Proposed nomenclature for phases of Uranium alloys*, Journal of Nuclear Materials Vol. 2 (1960), pp 261.

[13] Fachinformationszentrum Karlsruhe, FindIt, version 1.4.6, 2009.

[14] D. Blake, R.F. Hehemann: *Transformation of Uranium base alloys*, Physical Metallurgy of Uranium alloys, Brook Hill Publishing Company, Charlotte, 1976.

[15] F.G. Foote: *Physical metallurgy of Uranium and its alloys*, Proceedings of the 1st International Conference on the peaceful uses of atomic energy, United Nations, New York, 1955.

[16] B. Blumenthal: *The transformation temperature of high-purity Uranium*, Journal of Nuclear Materials Vol. 2 (1960), pp. 23.

[17] A.C. Lawson, C.E. Olsen, J.W. Richardson, M.H. Mueller, G.H. Lander: *Structure of β-uranium*. Acta Crystallographica B Vol. 44 (1988), pp. 89.

[18] P. Chiotti et al.: *Lattice parameters of uranium from 25 to 1132°C*. Transactions of the American society for metals Vol. 51 (1959), pp. 772.

[19] A.D. Dwight: *The Uranium-Molybdenum equilibrium diagram below 900°C*, Journal of Nuclear Materials Vol. 2 (1960), pp. 81.

[20] K. Tangri: Memoire No. 90, Journees Metallurgiques d'Automne, Paris, 1960.

[21] K. Tangri, G.I. Williams: *Metastable phases in the uranium-molybdenum system and their origin*, Journal of Nuclear Materials Vol. 2 (1961), pp. 226.

[22] K. Tangri, D.K. Chaudhuri: *Metastable phases in the uranium alloys with high solute solubility in the bcc gamma phase, part 1 - the system U-Nb.*, Journal of Nuclear Materials Vol. 4 (1965), pp. 278.

[23] K. Tangri, D.K. Chaudhuri: *Metastable phases in the uranium alloys with high solute solubility in the bcc gamma phase, part 2 - the system U-Ru.*, Journal of Nuclear Materials Vol. 4 (1965), pp. 288.

[24] J. Rest, Y.S. Kim, G.L. Hofman, M.K. Meyer, S.L. Hayes: *U-Mo fuels handbook*, Internal Report ANL-09/31, Argonne National Lab, November 2009.

[25] J.T. Creasy: *Thermal Properties of Uranium-Molybdenum alloys: Phase decomposition effects of heat treatments*, Master Thesis, AM University of Texas, USA, 2011.

[26] G.L. Hofman, M.K. Meyer: *Design of high density gamma-phase uranium alloys for LEU dispersion fuel applications*, Proceedings of the 21st International Topical Meeting on Reduced Enrichment for Research and Test Reactors (RERTR), Sao Paulo, Brazil, 1998.

[27] R.J. Jackson, W.L. Larsen: *Transformations and structures in the uranium-rhenium system - part 1.*, Journal of Nuclear Materials Vol. 21 (1967), pp. 263.

[28] R.J. Jackson, W.L. Larsen: *Transformations and structures in the uranium-rhenium system - part 2.*, Journal of Nuclear Materials Vol. 21 (1967), pp. 277.

[29] R.J. Jackson, W.L. Larsen: *Transformations and structures in the uranium-rhenium system - part 3.*, Journal of Nuclear Materials Vol. 21 (1967), pp. 282.

[30] J. Bloch: *Changement de phase et mise en desordre par irradiation du compose U_2Mo*, Journal of Nuclear Materials Vol. 1 (1960), pp. 91-92.

[31] P.E. Repas, R.H. Goodenow, R.F. Hehemann: *Transformation characteristics of U-Mo and U-Mo-Ti alloys*, Transactions of the American Society for Metals Vol. 49 (1957), 588-619.

[32] F. Huet, B. Guigon, P. Lemoine, C. Jarousse, F. Wijitsma, G. Dassel, G. Hofman, J. Snelgrove: *The UMUS failure: Facts and Analyses*, Proceedings of the 7th International Topical Meeting on Research Reactor Fuel Management (RRFM), Aix-en-Provence, France, 2003.

[33] F. Huet, V. Marelle, J. Noirot, P. Sacristan, P. Lemoine: *Full-sized plates irradiation with high UMo fuel loading - Final results of IRIS1 experiment*, Proceedings of the 24th International Topical Meeting on Reduced Enrichment for Research and Test Reactors (RERTR), Chicago, USA, 2003.

[34] F. Huet, J. Noirot, V. Marelle, S. Dubois, P. Boulcourt, P. Sacristan, S. Naury, P. Lemoine: *Post irradiation examinations on UMo full sized plates - IRIS 2 experiment*, Proceedings of the 9th International Topical Meeting on Research Reactor Fuel Management (RRFM), Budapest, Hungary, 2005.

[35] A. Leenaers, S. Van den Berghe, E. Koonen, C. Jarousse, F. Huet, M. Trotabas, M. Boyard, S. Guillot, L. Sannen, M. Verwerft: *Post-irradiation examination of uranium-7wt% molybdenum atomized dispersion fuel*, Journal of Nuclear Materials, Vol. 335 (2004), 39-47.

[36] M. Ripert, S. Dubois, P. Boulcourt, S. Naury, P. Lemoine: *IRIS3 experiment - Status and results of thickness increases*, Proceedings of the 10th International Topical Meeting on Research Reactor Fuel Management (RRFM), Sofia, Bulgaria, 2006.

[37] A.B. Robinson, D.M. Perez, D.L. Porter, G.L. Chang, D.D. Keiser, D.M. Wachs, G. Hofman: *Irradiation performance of U-Mo alloy based monolithic plate-type : Design Selection Update*, INL external report no. INL/EXT-09-16807, 2013.

[38] M.R. Finlay, D. Wachs, G.L. Hofman: *Post irradiation examination of monolithic mini fuel plates from RERTR6*, Proceedings of the 26th International Topical Meeting on Reduced Enrichment for Research and Test Reactors (RERTR), Cape Town, South Africa, 2006.

[39] D. Perez, M. Lillo, G. Chang, G. Roth, N. Woolstenhulme, D. Wachs: *RERTR-7 Irradiation Summary Report*, INL/EXT-11-24283, Idaho National Lab, USA, 2011.

[40] A. Leenaers, S. Van den Berghe, W. Van Renterghem, F. Charollais, P. Lemoine, C. Jarousse, A. Röhrmoser, W. Petry: *Irradiation behavior of ground U(Mo) fuel with and without Si added to the matrix*, Journal of Nuclear Materials Vol. 412 (2011), 41-52.

[41] S. Van den Berghe, Y. Partheons, F. Charollais, Y.S. Kim, A. Leenaers, E. Koonen, V. Kuzminov, P. Lemoine, C. Jarousse, H. Guyon, D. Wachs, D. Keiser Jr, J. Stevens, G. Hofman: *Swelling of U(Mo)-Al(Si) dispersion fuel under irradiation : Non-destructive analyses of the LEONIDAS E-FUTURE plates*, Journal of Nuclear Materials Vol. 430 (2012), 246-258.

[42] H. Palancher, X. Iltis, A. Bonnin, F. Charollais, P. Lemoine, S. Van den Berghe, A. Leenaers, E. Koonen, B. Stepnik, C. Jarousse, Y. Calzavara, H. Guyon: *LEONIDAS E-FUTURE II: Characteristics of the fresh fuel plates*, Proceedings of the 16th International Topical Meeting on Research Reactor Fuel Management (RRFM), Prague, Czech Republic, 2012.

[43] S. Van den Berghe, Y. Parthoens, G. Cornelis, A. Leenaers, E. Koonen, V. Kuzminov, C. Detavernier: *Swelling of U(Mo) dispersion fuel under irradiation: Non-destructive analyses of the SELENIUM plates*, Journal of Nuclear Materials Vol. 442 (2013), 60-68.

[44] B. Ye, Y.S. Kim, G. Hofman, J. Rest: *Modeling of U-Mo fuel swelling to high burnup*, Proceedings of the 18th International Topical Meeting on Research Reactor Fuel Management (RRFM), Ljubljana, Slovenia, 2014.

[45] G.S. Was: *Fundamentals of Radiation Materials Science*, Springer Verlag, Heidelberg, Germany, 2007.

[46] D.S. Billington: *Radiation Damage in Solids*, Princeton University Press, New Jersey, US, 1961.

[47] W. Schilling: *Physics of Radiation Damage*, Material Science and Technology Vol. 10B, VCH Verlagsgesellschaft mbH, Weinheim, Germany, 1994.

[48] F. Seitz: *Displacement of atoms during irradiation*, Solid State Physics 2, Academic Press, 1956.

[49] H. Ullmeier: *Radiation damage in metallic reactor materials*, Physics of Modern Materials Vol. 1, IAEA, Vienna, Austria, 1980.

[50] J. Lindhard: *Approximation method in classical scattering by screened Coulomb fields*, Mat.Fys.Medd.Dan.Vid. Vol. 36 (1968), pp. 10.

[51] J. Lindhard, A. Winther: *Stopping power of electron gas and equipartition rule*, Mat.Fys.Medd.Dan.Vid. Vol. 34 (1964), 1-24.

[52] H.L. Heinisch: *Atomic-Scale modeling of radiation-damage by SAS*, Journal of Metals Vol. 48 (1996), 38-41.

[53] J.F. Ziegler: *The Stopping and Range for Ions in Solids*, Pergamon Press, New York, 1996.

[54] Ch. Valot, I. Aubrun, J. Lamontagne, Th. Blay, L. Brunaud, P. Delion, N. Monchalin, M. Ripert, F. Charollais, M. C. Anselmet, P. Lemoine: *IRIS4 experiment: PIE on oxidized U-Mo Dispersion fuel*, Proceedings of the 30th International Topical Meeting on Reduced Enrichment for Research and Test Reactors (RERTR), Santiago de Chile, Chile, 2011.

[55] L. Xiao, L. Tie-Cheng, X. Zhong-Hu, Q. Da-Zhi: *Modelling the swelling performance of U-Mo alloys for Al-matrix dispersion fuel*, Journal of Alloys and Compounds Vol. 509 (2011), 6589-6594.

[56] M.I. Mirandou, S.N. Balart, M. Ortiz, M.S. Granovsky: *Characterization of the reaction layer in U-7wt%Mo/Al diffusion couples*, Journal of Nuclear Materials Vol. 323 (2003), 29 - 35.

[57] A. Leenaers, S. van den Berghe, E. Koonen, C. Jarousse, F. Huet, M. Trotabas, M. Boyard, S. Guillot, L. Sannen, M. Verwerft: *Post-irradiation examination of uranium 7wt% molybdenum atomized dispersion fuel*, Journal of Nuclear Materials Vol. 335 (2004), 39-47.

[58] K. Colon, D. Sears: *Neutron powder diffraction of UMo fuel irradiated to 60 at% ^{235}U burnup*, Proceedings of the 11th International Topical Meeting on Research Reactor Fuel Management (RRFM), Lyon, France, 2007.

[59] K. Colon, D. Sears: *Structure studies of dispersed U-Mo fuel after irradiation and isochronous annealing within the temperature range of 150 - 580°C by the neutron diffraction method*, Proceedings of the 11th International Topical Meeting on Research Reactor Fuel Management (RRFM), Lyon, France, 2007.

[60] M.K. Meyer, G.L. Hofman, R.V. Strain, C.R. Clark, J.R. Stuart: *Irradiation Behavior of U-Mo Dispersion Fuel: Fuel Performance Data from RERTR-3*, Proceedings of the 19th International Topical Meeting on Reduced Enrichment for Research and Test Reactors (RERTR), Santiago de Chile, Chile, 2000.

[61] F. Huet, J. Noirot, V. Marelle, S. Dubois, P. Boulcourt, P. Sacristan, S. Naury, P. Lemoine: *Post-irradiation experiments of UMo full sized plates - IRIS 2 experiment*, Proceedings of the 9th International Topical Meeting on Research Reactor Fuel Management (RRFM), Budapest, Hungary, 2005.

[62] J.M. Park, H.J. Ryu, Y.S. Lee, D.B. Lee, S.J. Oh, B.O. Yoo, Y.H. Jung, D.S. Sohn, C.K. Kim: *An Investigation on the Irradiation Behavior of Atomized U-Mo/Al Dispersion Rod Fuels*, Proceedings of the 23rd International Topical Meeting on Reduced Enrichment for Research and Test Reactors (RERTR), Vienna, Austria, 2004.

[63] S. Van den Berghe, W. Van Renterghem, A. Leenaers: *Transmission electron microscopy investigation of irradiated U7wt%Mo dispersion fuel*, Journal of Nuclear Materials Vol. 375 (2008), 340-346.

[64] J. Gan, D.D. Keiser Jr., B.D. Miller, A.B. Robinson, J.F. Jue, P. Medvedev, D.M. Wachs: *TEM characterization of U7Mo/Al2Si dispersion fuel irradiated to intermediate and high fission densities*, Journal of Nuclear Materials Vol. 424 (2012), 43-50.

[65] G.L. Hofman, L.A. Neimark, F.L. Olquin: *The effects of fabrication variables on the irradiation performance of uranium-solicide dispersion fuel plates*, Nuclear Technologies Vol. 77 (1987), 110 - 122.

[66] H.J. Ryu, Y.S. Kim, G.L. Hofman: *Amorphization of the interaction products in U-Mo/Al dispersion fuel during irradiation*, Journal of Nuclear Materials Vol. 385 (2009), 623-628.

[67] E. Welcomme, H. Palancher, C. Sabathier, Ph. Martin, J. Allenou, C. Valot, F. Charollais, M.C. Anselmet, R. Jungwirth, W. Petry, L. Beck, C. Jarousse, R. Tucoulou, P. Lemoine: *Heavy ion irradiation of UMo7/Al fuel: methodological approach*, Proceedings of the 13th International Topical Meeting on Research Reactor Fuel Management (RRFM), Vienna, Austria, 2009.

[68] H. Palancher, N. Wieschalla, P. Martin, R. Tucoulou, C. Sabathier, W. Petry, J.-F. Berar, C. Valot, S. Dubois: *Uraniumâmolybdenum nuclear fuel plates behaviour under heavy ion irradiation: An X-ray diffraction analysis*, Journal of Nuclear Materials Vol. 385 (2009) 449â455.

[69] S. van den Berghe, A. Leenaers, C. Detavernier: *SELENIUM fuel: Surface engineering of U(Mo) particles to optimise fuel performance*, Proceedings of the 14th International Topical Meeting on Research Reactor Fuel Management (RRFM), Marakesh, Marocco, 2010.

[70] F.F. Abraham: *Homogeneous nucleation theory*, Academic Press, New York, USA, 1974.

[71] J. Rest: *The Prediction of Transient Fission-Gas Release and Fuel Microcracking Under Severe Core-Accident Conditions*, Nuclear Technologies Vol. 56 (1982), 553-564.

[72] J. Rest: *Evaluation of Volatile and Gaseous Fission Product Behavior in Water Reactor Fuel Under Normal and Severe Core Accident Conditions*, Nuclear Technologies Vol. 61 (1983), 33-48.

[73] J. Rest: *An improved model for fission product behaviour in nuclear fuel under normal and accident conditions*, Journal of Nuclear Materials Vol. 124 (1983), 195-212.

[74] H. Trinkaus: *Energetics and formation kinetics of helium bubbles in metals*, Radiation Effects Vol. 78 (1983), 189-211.

[75] J.H. Evans: *The role of implanted gas and lateral stress in blister formation mechanisms*, Journal of Nuclear Materials Vol. 76-77 (1978), 228-234.

[76] K.C. Russell: *Nucleation of voids in irradiated metals*, Acta Metallurgica Vol. 19 (1971), 753-758.

[77] J.L. Brimhall, H.E. Kissinger, G.L. Kulcinski: in: Proceedings of Radiation-induced Voids in Metals, Oak Ridge, USA, 1972, 338.

[78] G.L. Hofman: *A short note on high density fuel*, Argonne National Lab, 1996.

[79] E. Perez, B. Yao, Y.H. Sohn, D. Keiser: *Interdiffusion in Diffusion Couples: U-Mo vs. Al and Al-Si*, Proceedings of the 30th International Topical Meeting on Reduced Enrichment for Research and Test Reactors (RERTR), Beijing, China, 2009.

[80] B.N. Singh, S.I. Golubov, H. Trinkaus, A. Serra, Y. Osetsky, A.V. Barashev: *Aspects of microstructure evolution under cascade damage conditions*, Journal of Nuclear Materials Vol. 251 (1997), 107-122.

[81] N.M. Ghoniem, D.J. Walgraef, S. Zinkle: *Theory and experiment of nanostructure self-organization in irradiated materials*, Journal of Computer-Aided Materials Design Vol. 8 (2002), 1â38.

[82] C.H. Woo, W. Frank: *A theory of void-lattice formation*, Journal of Nuclear Materials Vol. 137 (1985), 7-21.

[83] A.D. Brailsford, R. Bullough: *The stress dependence of high temperature swelling*, Journal of Nuclear Materials Vol. 48 (1973), 87 - 106.

[84] Y.S. Kim, G.L. Hofman, J.S. Cheon: *Recrystallisation and swelling of U-Mo fuel during irradiation*, Proceedings of the 16th International Topical Meeting on Research Reactor Fuel Management (RRFM), Prague, Czech Republic, 2012.

[85] J. Gan, D.D. Keiser, B.D. Miller, D. Wachs, T.B. Allen, M. Kirk, J. Rest: *Mircostructure of RERTR DU alloys irradiated with Kr ions up to 100 dpa*, Journal of Nuclear Materials Vol. 411 (2011), 174-180.

[86] J.A.T. Jones, B. Bowman, P.A. Lefrank: *Electric Furnace Steelmaking*, The Making, Shaping and Treating of Steel, 11th edition, The AISE Steel Foundation, Pittsburg, USA, 1998.

[87] J.M. Park, H.J. Ryu, K.H. Kim, D.B. Lee, Y.S. Lee, J.S. Lee, B.S. Seong, C.K. Kim, M. Cornen: *Neutron diffraction analyses of U(6 - 10wt%)Mo alloy powders fabricated by centrifugal atomization*, Journal of Nuclear Materials, Vol. 397 (2010), 27-30.

[88] F. Charollais, M. Ripert, M.C. Anselmet, P. Boulcourt, X. Tiratay, P. Lemoine, C. Jarousse: *IRIS program: IRIS4 first results*, Proceedings of the 13th International Topical Meeting on Research Reactor Fuel Management (RRFM), Vienna, Austria, 2009.

[89] Y.S. Kim: *Uranium Intermetallic Fuels (U-Al, U-Si, U-Mo)*, Comprehensive Nuclear Materials, Vol. 3 (2012), 391-422.

[90] M. Wintergerst, N. Dacheux, F. Datcharry, E. Herms, B. Kapusta: *Corrosion of the AlFeNi alloy used for the fuel cladding in the Jules Horowitz research reactor*, Journal of Nuclear Materials, Vol. 393 (2009), 369-380.

[91] M.D. Kaminski: *Aqueous Corrosion of Aluminum-Based Nuclear Fuel*, Open Report ANL-CMT-03/1, Argonne National Lab, USA, April 2003.

[92] Aalco: *Aluminium alloys - Aluminium 5754 Properties, Fabrication and Application, Supplier Data*, `http://www.azom.com/article.aspx?ArticleID=2806#_Chemical_Composition_of`, URL link as of April 2014.

[93] H. Palancher, A. Bonnin, V. Honkimaki, H. Suhonen, P. Cloetens, T. Zweifel, R. Tucoulou, A. Rack, M. Voltolini: *Coating thickness determination in highly absorbent core-shell systems*, Journal of Applied Crystallography, Vol. 45 (2012), 906-913.

[94] H. Palancher, A. Bonnin, V. Honkimaki, T. Buslaps, M. Grasse, B. Stepnik, T. Zweifel: *Quantitative crystallographic analysis of as-fabricated full size UMo/Al(Si) nuclear fuel plates*, Journal of Alloys and Compounds, Vol. 527 (2012), 53-65.

[95] M. Ripert, V. Marelle, X. Iltis, H. Palancher, Ch. Valot, F. Charollais, M.C. Anselmet, X. Tiratay, P. Lemoine, S. van den Berghe, A. Leenaers, C. Jarousse: *Synthetic review of the IRIS3 experiment*, Proceedings of the 15th International Topical Meeting on Research Reactor Fuel Management (RRFM), Rome, Italy, 2011.

[96] D.D. Keiser, Y.F. Yue, B. Yao, E. Perez, Y.H. Sohn, C.R. Clark: *Microstructural characterization of U7Mo/AlSi alloy matrix dispersion fuel plates fabricated at 500° C*, Journal of Nuclear Materials, Vol. 412 (2011), 90-99.

[97] Y.S. Kim, G.L. Hofman, J.S. Cheon: *Recrystallization and fission-gas-bubble swelling of UMo fuel*, Journal of Nuclear Materials, Vol. 436 (2013), 14-22.

[98] G.L. Hofman: *A short note on high density dispersion fuel*, Argonne National Lab, 1996.

[99] A. Leenaers, J. Van Eyken, S. Van den Berghe, E. Koonen, F. Charollais, P. Lemoine, Y. Calzavara, H. Guyon, C. Jarousse, B. Stepnik, D. Wachs, A. Robinson: *LEONIDAS E-FUTURE: Results of the Destructive Analyses of the U(Mo)-Al(Si) Fuel Plates*, Proceedings of the 16th International Topical Meeting on Research Reactor Fuel Management (RRFM), Prague, Czech Republic, 2012.

[100] E. Perez, B. Yao, Y.H. Sohn, D.D. Keiser: *Interdiffusion in Diffusion Couples: U-Mo vs. Al and Al-Si*, Proceedings of the 31st International Topical Meeting on Reduced Enrichment for Research and Test Reactors (RERTR), Beijing, China, 2009.

[101] A.F. Hollemann, N. Wiberg: *Lehrbuch der Anorganischen Chemie*, de Gruyter Verlag, Berlin, 2007.

[102] D.D. Keiser, A.B. Robinson, J.F. Jue, P. Medvedev, D.M. Wachs, M.R. Finlay: *Microstructural development in irradiated U-7Mo/6061 Al alloy matrix dispersion fuel*, Journal of Nuclear Materials, Vol. 393 (2009), 311-320.

[103] X. Iltis, F. Charollais, M.C. Anselmet, P. Lemoine, A. Leenaers, S. van den Berghe, E. Koonen, C. Jarousse, D. Geslin, F. Frery, H. Guyon: *Microstrucural characterization of the E-FUTURE fresh fuel plates*, Proceedings of the 32nd International Topical Meeting on Reduced Enrichment for Research and Test Reactors (RERTR), Lisbon, Portugal, 2010.

[104] M. Ripert, F. Charollais, M.C. Anselmet, X. Tiratay, P. Lemoine: *Results of the IRIS4 irradiation in the OSIRIS reactor: oxidized U-Mo particles dispersed in Al (with 0 or 2.1 wt%Si)*, Proceedings of the 31st International Topical Meeting on Reduced Enrichment for Research and Test Reactors (RERTR), Beijing, China, 2009.

[105] J. Gan, D.D. Keiser, D.L. Wachs, A. Robinson, B.D. Miller, T.R. Allen: *Transmission electron microscopy characterization of irradiated U7Mo/Al2Si dispersion fuel*, Journal of Nuclear Materials, Vol. 396 (2010), 234-239.

[106] R. Jungwirth, H. Palancher, A. Bonnin, C. Bertrand-Drira, C. Borca, V. Honkimäki, C. Jarousse, B. Stepnik, S.H. Park, X. Iltis, W. Schmahl, W. Petry: *Microstructure of as-fabricated UMo/Al(Si) plates prepared with ground and atomized powder*, Journal of Nuclear Materials, Vol. 438 (2013), 246-260.

[107] Y.J. Jeong, J.M. Park, H.J. Ryu, Y.S. Lee, R. Jungwirth, H.-Y. Chiang, T. Zweifel, W. Petry, W.J. Kim: *Heavy ion irradiation of nitride and silicon coated U-Mo/Al and U-Mo-Ti/Al fuel*, Proceedings of the 17th International Topical Meeting on Research Reactor Fuel Management (RRFM), St. Petersburg, Russia, 2013.

[108] H.J. Ryu, J.M. Park, K.H. Lee, B.O. Yoo, Y.H. Jung, Y.J. Jeong, Y.S. Lee: *Post-irradiation examination of the KOMO-5 irradiation test for U-Mo dispersion fuel*, Proceedings of the 17th International Topical Meeting on Research Reactor Fuel Management (RRFM), St. Petersburg, Russia, 2013.

[109] G.A. Birzhevoy, V.V. Popov, O.A. Golosov, V.V. Shushlebin, V.Đ. Rychkov, Đ.S. Lyutikova: *Results of post-irradiation examination of the (U-Mo)-Aluminium matrix interaction rate*, Proceedings of the 17th International Topical Meeting on Research Reactor Fuel Management (RRFM), Proceedings of the 11th International Topical Meeting on Research Reactor Fuel Management (RRFM), Lyon, France, 2007.

[110] `http://enterprise.astm.org/filtrexx40.cgi?+REDLINE_PAGES/E321.htm`, URL link as of October 2013.

[111] A. Leenaers, S. van den Berghe, J. Van Eyken, E. Koonen, F. Charollais, P. Lemoine, Y. Calzavara, H. Guyon, C. Jarousse, D. Geslin, D. Wachs, D. Keiser, A. Robinson, G. Hofman, Y.S. Kim: *Microstructural evolution of U(Mo) - Al(Si) dispersion fuel under irradiation - Destructive analyses of the LEONIDAS E-FUTURE plate*, Journal of Nuclear Materials, Vol. 441 (2013), 439-448.

[112] Y. Pontillon, S. Ravel, D. Parrat, M.P. Ferroud-Plattet, Y. Guerin: *Fission gas release under fast transient and local conditions: Analytical devices implemented at the Commissariat a l'Energie Atomique*, Proceedings of the IAEA technical committee meeting, Halden, Norway, 2001.

[113] Y. Pontillon, L. Desgranges, A. Poulesquen: *ADAGIO technique: From UO_2 fuels to MOX fuels*, Journal of Nuclear Materials, Vol. 385 (2009), 127-141.

[114] P. Menegon, L. Desgranges, Y. Pontillon, A. Poulesquen: *Evidence of two gas release kinetics during the oxidation of an irradiated PWR UO_2 fuel*, Journal of Nuclear Materials, Vol. 378 (2008), 1-8.

[115] J.L. Murray, J. McAlister: *The Al-Si (Aluminium-Silicon) system*, Bulletin of Alloy Phase Diagrams, Vol. 5 (1984), 74-84.

[116] `http://asm.matweb.com/search/SpecificMaterial.asp?bassnum=MA6061t6`, URL link as of April 2014.

[117] A. Bonnin, H. Palancher, V. Honkimaki, R. Tucoulou, Y. Calzavara, C.V. Colin, J.F. Berar, N. Boudet, H. Rouquette, J. Raynal, C. Valot, J. Rodriguez-Carvajal: *UMo/Al nuclear fuel quantitative analysis via high energy X-ray diffraction*, Zeitschrift fur Kristallographie, Vol. 1 (2011), 29-34.

[118] P.E. Repas, R.H. Goodenow, R.F. Hehemann: *Transformation characteristics of the U-Mo and U-Mo-Ti alloys*, Transactions of the ASM, Vol. 57 (1964), 150-163.

[119] S.G. Prussin, D.R. Olander, W.K. Lau, L. Hansson: *Release of fission products (Xe, I, Te, Cs, Mo and Tc) from polycrystalline UO2*, Journal of Nuclear Materials, Vol. 154 (1988), 25-37.

[120] A. Leenaers, F. Joppen, S. van den Berghe: *Microstructural analysis of MTR fuel plates damaged by a coolant flow blockage*, Journal of Nuclear Materials, Vol. 394 (2009), 87-94.

[121] M.L. Bleiberg: *Effect of fission rate and lamella spacing upon the irradiation-induced phase transformation of U-9wt%Mo alloy*, Journal of Nuclear Materials, Vol. 1 (1959), 182-190.

[122] H. Palancher, P. Martin, V. Nassif, R. Tucoulou, O. Proux, J.-L. Hazemann, O. Tougait, E. LaheÂ´ra, F. Mazaudier, C. Valot, S. Dubois: *Evidence for the presence of UMoAl ternary compounds in the UMo/Al interaction layer grown by thermal annealing: a coupled micro X-ray diffraction and micro X-ray absorption spectroscopy study*, Journal of Applied Crystallography, Vol. 40 (2007), 1064-1075.

[123] H.J. Ryu, Y.S. Han, J.M. Park, S.D. Park, C.K. Kim: *Reaction layer growth and reaction heat of U-Mo/Al dispersion fuels using centrifugally atomized powders*, Journal of Nuclear Materials, Vol. 321 (2003), 210-220.

[124] H.J. Ryu, Y.S. Kim, G.L. Hofman, J.M. Park, C.K. Kim: *Heats of formation of $(U,Mo)Al_3$ and $U(Al,Si)_3$*, Journal of Nuclear Materials, Vol. 358 (2006), 52-56.

[125] T.R. Marrero, E.A. Mason: *Gaseous Diffusion Coefficients*, Journal of Physical Chemistry, Vol. 1 (1972), 1-117.

[126] American Society for Metals: *Binary Alloy Phase Diagrams*, `www.asminternational.org`, URL link as of June 2014.

[127] Unknown author: *Einführung in die Elektronenmikroskopie - Instrumentation*, `http://www.zmb.uzh.ch/resources/download/EMinstrumentation.pdf`, University of Zurich, 2007. URL link as of October 2013.

[128] A.N. Danilewsky: *Einführung in die Rasterelektronenmikroskopie*, Vorlesung und Praktikum, Universität Freiburg, October 2006, `http://www.krist.uni-freiburg.de/studium/Praktikum/REM_EBSD.php`. URL link as of October 2013.

[129] G. Bertsche: *Das Rasterelektronenmikroskop*, Anleitung zum F-Praktikumsversuch, Universität Tübingen, Tübingen, unknown date, `http://www.uni-tuebingen.de/Teilchenoptik/html/fprakt/pdf/AnleitungREM.pdf`. URL link as of October 2013.

[130] G. Völksch: *Rasterelektronenmikroskopie und Elektronenstrahlmikroanalyse*, Anleitung zum Praktikum, Universität Jena, year unknown, `http://www.chemie.uni-jena.de/institute/glaschemie/Anleitung_REM.pdf`. URL link as of October 2013.

[131] N. Yao, Z.L. Wang: *Handbook of Microscopy for Nanotechnology*, Kluwer Academic Publishers, USA, 2005.

[132] W. de Boer: *Atomphysik - 2*, Vorlesung für Studierende der Physik - 2010, Universität Karlsruhe, `http://www-ekp.physik.uni-karlsruhe.de/~deboer/html/Lehre/Atomphysik_2010_old/VL2_rutherford_sw.pdf`. URL link as of October 2013.

[133] S. Säubert: *Isothermal transformation kinetics in uranium molybdenum alloys*, Master Thesis, Technische Universität München, October 2013.

[134] H. Hammersley: `http://www.esrf.eu/computing/scientific/FIT2D/`, URL link as of December 2013.

[135] J. Rodriguez-Carvajal: `http://www.ill.eu/sites/fullprof/`, URL link as of December 2013.

[136] T. Zweifel, H. Palancher, A. Leenaers, A. Bonnin, V. Honkimaki, R. Tucoulou, S. van den Berghe, R. Jungwirth, F. Charollais, W. Petry: *Crystallographic study of Si and ZrN coated U-Mo atomised paericles and their interaction with Al under thermal annealing*, Journal of Nuclear Materials Vol. 442 (2013), 124-132.

[137] W. Schmid: *Construction of a sputtering reactor for the coating and processing of monolithic U-Mo nuclear fuel*, PhD Thesis, Technische Universität München, 2012.

[138] A. Heldmann: *Energie- und Gitterschädenverteilung am Übergang UMo-Al: Vergleich von Spaltprodukten und Schwerionen*, Bachelor Thesis, Technische Universität München, 2012.

[139] *Elektronegativität*, Lexikon der Elemente, `http://www.uniterra.de/rutherford/tab_en.htm`, URL link as of November 2013.

[140] L. Beck: *Prinzip der Ionenbeschleunigung*, MLL Tandem accelerator homepage, `http://homepages.physik.uni-muenchen.de/~Ludwig.Beck/index-Dateien/Page359.htm`, URL link as of November 2013.

[141] K. Shima, N. Kuno, M. Yamanouchi, H. Tawara: *Equilibrium charge fractions of ions of Z=4-92 emerging from a carbon foil*, Atomic data and nuclear data tables Vol. 51 (1992), 173-241.

[142] N. Wieschalla: *Heavy ion irradiation of U-Mo/Al dispersion fuel*, PhD Thesis, Technische Universität München, 2006.

[143] R. Jungwirth: *Irradiation behaviour of modified high performance nuclear fuels*, PhD Thesis, Technische Universität München, 2011.

[144] H.D. Baehr, K. Stephan: *Wärme- und Stoffübertragung*, Springer press, Berlin, 2004.

[145] H. Breitkreutz: *Coupled Neutronics and Thermal Hydraulics of High Density Cores for FRM II*, PhD Thesis, Technische Universität München, 2011.

[146] A. Leenaers: *Surface-engineered low-enriched Uranium-Molybdenum fuel for research reactors*, PhD Thesis, University of Ghent, Belgium, 2014.

[147] Y.S. Kim, G.L. Hofman, H.J. Ryu, J.M. Park, A.B. Robinson, D. Wachs: *Modeling of interaction layer growth between U-Mo particles and an Al matrix*, Nuclear Engineering and Technology Vol. 45 (2013), 827-838.

[148] E. Perez, D.D. Keiser Jr., Y.H. Sohn: *Phase Constituents and Microstructure of Interaction Layer Formed in U-Mo Alloys vs Al Diffusion Couples Annealed at 873 K (600 °C)*, Metallurgical and Materials Transactions A, Vol. 42 (2011), 3071-3083.

[149] E. Perez, Y.H. Sohn, D.D. Keiser Jr.: *Role of Si on the Diffusional Interactions Between U-Mo and Al-Si Alloys at 823 K (550 °C)*, Metallurgical and Materials Transactions A, Vol. 44A (2013), 584-595.

[150] B.D. Miller, J. Gan, J. Madden, J.F. Jue, A. Robinson, D.D. Keiser: *Advantages and disadvantages of using a focused ion beam to prepare TEM samples from irradiated Uâ10Mo monolithic nuclear fuel*, Journal of Nuclear Materials Vol. 424 (2012), 38-42.

[151] Digital Micrograph software: `http://www.gatan.com/imaging/dig_micrograph.php`, URL link as of November 2012.

[152] G. Martinez-Criado, R. Tucoulou, P. Cloetens, P. Bleuet, S. Bohic, J. Cauzid, I. Kieffer, E. Kosior, S. Laboure, S. Petitgirard, A. Rack, J.A. Sans, J. Segura-Ruiz, H. Suhonen, J. Susini, J. Villanova: *Status of the hard X-ray microprobe beamline ID22 of the European Synchrotron Radiation Facility*, Journal for Synchrotron Radiation Vol. 19 (2012), 10-18.

[153] B.S. Seong, C.H. Lee, J.S. Lee, H.S. Shim, K.H. Kim, C.K. Kim, V. Em: *Neutron diffraction study of U10wt% Mo alloy*, Journal of Nuclear Materials Vol. 277 (2000), 274-279.

[154] G. Rousseau, L. Desgranges, F. Charlot, N. Millot, J.C. Niepce, M. Pijolat, F. Valdivieso, G. Baldinozzi, J.F. Berar: *A detailed study of UO_2 to U_3O_8 oxidation phases and the associated rate-limiting steps*, Journal of Nuclear Materials Vol. 355 (2006), 10-20.

[155] Understanding of GANIL, Homepage of the Grand Accelerateur National d'Ions Lourds (GANIL), `http://www.ganil-spiral2.eu/science-us/understand-ganil/fundamental-principles`, URL link as of December 2013.

[156] C. Grygiel, IRR-SUD beamline scientist at the Grand Accelerateur National d'Ions Lourds (GANIL), private communication, October 2012.

[157] Unknown author: *An Introduction to Secondary Ion Mass Spectrometry*, Millbrook Instruments Limited, 2004. `http://www.minisims.com/docs/introduction_to_sims.pdf`, URL link as of July 2014.

[158] N. Valle, Centre de la recherche publique - Gabriel Lippmann (CRP-GL), private communication, June 2014.

[159] S.G. Popov, J.J. Carbajo, V.K. Ivanov, G.L. Yoder: *Thermophysical properties of MOX and UO2 fuels including the effects of irradiation*, external document no. ORNL/TM-2000/351, Oak Ridge National Lab, United States of America, 1996.

[160] D.A. Banks: *Some observations of density and porosity changes in UO_2 fuel irradiated in water-cooled reactors*, Journal of Nuclear Materials Vol. 54 (1974), 97-107.

[161] L. Cantrel, R. Chaouche, J. Chopin-Dumas: *Diffusion Coefficients of Molecular Iodine in Aquaeous Solutions*, Journal of Chemical Engineering Vol. 42 (1997), 216-220.

[162] H.Y. Chiang: *Material Selection of UMo Fuel: Swift Heavy Ion Irradiation Studies*, PhD Thesis, Technische Universität München, 2014.

[163] Harry H. Binder: *Lexikon der chemischen Elemente*, S. Hirzel Verlag, Stuttgart, 1999.

[164] Harry H. Binder: *Lexikon der chemischen Elemente*, S. Hirzel Verlag, Stuttgart, 1999.

[165] G.E. Totten, K. Funatani, L. Xie: *Handbook of Metallurgical Process Design*, Marcel Dekker Inc., United States of America, 2004.

[166] M. Dodenhöft: *Metallographische Präparation von Uran-Molybdän*, Bachelor Thesis, Technische Universität München, 2014.

A. JNM article of SELENIUM particles analysed with high energy XRD

Journal of Nuclear Materials 442 (2013) 124–132

Contents lists available at ScienceDirect

Journal of Nuclear Materials

journal homepage: www.elsevier.com/locate/jnucmat

Crystallographic study of Si and ZrN coated U–Mo atomised particles and of their interaction with al under thermal annealing

T. Zweifel [a,b], H. Palancher [a,*], A. Leenaers [c], A. Bonnin [d], V. Honkimaki [d], R. Tucoulou [d], S. Van Den Berghe [c], R. Jungwirth [b], F. Charollais [a], W. Petry [b]

[a] CEA, DEN, DEC, F-13108 St. Paul Lez Durance Cedex, France
[b] Forschungsneutronenquelle Heinz Maier-Leibnitz (FRM II), Technische Universität München Lichtenbergstr. 1, D-85747 Garching, Germany
[c] SCK-CEN, Boeretang 200, B-2400 MOL, Belgium
[d] ESRF, 6 rue Jules Horowitz, 38042 Grenoble, France

ARTICLE INFO

Article history:
Received 10 May 2013
Accepted 19 August 2013
Available online 2 September 2013

ABSTRACT

A new type of high density fuel is needed for the conversion of research and test reactors from high to lower enriched uranium. The most promising one is a dispersion of atomized uranium-molybdenum (U–Mo) particles in an Al matrix. However, during in-pile irradiation the growth of an interaction layer between the U–Mo and the Al matrix strongly limits the fuel's performance. To improve the in-pile behaviour, the U–Mo particles can be coated with protective layers. The SELENIUM (Surface Engineering of Low ENriched Uranium–Molybdenum) fuel development project consists of the production, irradiation and post-irradiation examination of 2 flat, full-size dispersion fuel plates containing respectively Si and ZrN coated U–Mo atomized powder dispersed in a pure Al matrix. In this paper X-ray diffraction analyses of the Si and ZrN layers after deposition, fuel plate manufacturing and thermal annealing are reported.

It was found for the U–Mo particles coated with ZrN (thickness 1 μm), that the layer is crystalline, and exhibits lower density than the theoretical one. Fuel plate manufacturing does not strongly influence these crystallographic features. For the U–Mo particles coated with Si (thickness 0.6 μm), the measurements of the as received material suggest an amorphous state of the deposited layer. Fuel plate manufacturing strongly modifies its composition: Si reacts with the U–Mo particles and the Al matrix to grow $U(Al, Si)_3$ and U_3Si_2 phases. Finally both coatings have shown excellent performances under thermal treatment by limiting drastically the U–Mo/Al interdiffusion.

1. Introduction

The international program on reduced enrichment for research and test reactors (RERTR) encourages reducing the ^{235}U enrichment in nuclear fuels to values below 20 wt%. The most promising candidate is an Uranium–Molybdenum (U–Mo) alloy with 7–10 wt% Mo [1,2]. The addition of Mo is necessary in order to stabilize at room temperature the high temperature γ phase of Uranium. Its cubic structure should ensure an isotropic swelling under irradiation [2]. In the disperse case, the U–Mo fuel particles are produced either by grinding [3,4] or atomization techniques [5]. These powders are then dispersed in an Al matrix (the resulting compound is often referred to as the "meat"). The meat is then further enclosed by an Al cladding which finally results in a fuel plate. A fuel element consists of many such fuel plates.

During in-pile test irradiations, the growth of an interaction layer (IL) between the dispersed U–Mo fuel particles and the surrounding matrix strongly limits this fuel's performance [6,7]. One major goal of U–Mo development is finding solutions for suppressing this IL. Among these, modification of the Al matrix composition (e.g. Si addition [8–12]) or protecting U–Mo particles with diffusion barrier (e.g. UO_2 [13], UN [14], ZrN [15], Si [16] etc.) have been proposed. A significant enhancement of the in-pile performances has been obtained especially by adding Si to the matrix [17–22,4]. This improvement is attributed to first Si diffusion towards U–Mo particles then interaction during both manufacturing and in-pile irradiation thereby delaying the IL build-up. The result of Si interaction with U–Mo particles during fuel plate manufacturing or more generally during a thermal treatment is often written SiRDL for Si rich diffusion layers. However post-irradiation examinations on such U–Mo/Al(Si) plates have suggested some limits for this concept: in very aggressive irradiation conditions an excessive plate swelling can be still observed, and accessibility issues for Si towards U–Mo particles have been evidenced. To solve this last problem U–Mo particle coating would be well suited.

To coat U–Mo atomised particles with materials exhibiting enhanced capacities to limit IL growth (i.e. Si, ZrN, etc), physical vapour deposition (PVD) techniques can be used. In 2008 SCK.CEN

* Corresponding author. Tel.: +33 (0)4 42 25 75 55.
E-mail address: herve.palancher@cea.fr (H. Palancher).

selected this option for developing a new U–Mo nuclear fuel [23]: this project is referred to as SELENIUM (i.e. Surface Engineering of Low ENrIched Uranium–Molybdenum). The feasibility of first particle coating and then full size plates manufacturing with such PVD coated particles has been demonstrated and the in-pile behaviour of these fuels has been tested in the BR2 reactor between April and October 2012 [24]. Post-irradiation examinations are undergoing.

In this paper, the evolution in crystallographic composition of PVD coated particles due to the fuel plate manufacturing conditions is first discussed. To reach this objective, a methodology combining high energy X-ray diffraction (HE-XRD) [12,25] and nano-XRD [26,27] has been chosen. This approach has been previously validated by analysis of U–Mo atomised particles protected by oxide and silicide layers.

Second the efficiency of such a coating to prevent U–Mo/Al interdiffusion during thermal treatments is analysed. This last study consists in reinvestigating annealed compacts [29].

2. Experimental methods

2.1. Sample manufacturing by PVD sputter coating

U-7Mo[1] powders used in this work have been produced by centrifugal atomisation by KAERI (Korea Atomic Energy Research Institute) [5]. At SCK.CEN they were coated by PVD with either ZrN or Si. The developed instrumentation (which includes a rotating drum) and procedures are detailed in another document [23]. Note that if Si has been deposited under high-purity Ar flow for Si coating, N_2 was added to the Ar flow during Zr deposition to get ZrN coating. Destructive examinations after PVD coating revealed an homogeneous coating around U–Mo particles. Coating thicknesses have been measured to 1 and 0.6 μm for ZrN or Si respectively. These coated powders (abbreviated as U–Mo(Si) and (U–Mo(ZrN)) have subsequently been used to prepare U–Mo/Al compacts or to manufacture full size fuel plates.

Fifteen cylindrical compacts with pure Al powder as a matrix have been prepared: 5 with U–Mo(Si), 5 with U–Mo(ZrN) and 5 with regular un-coated U–Mo atomised powders. Since very few coated U–Mo powder was available for this study, the U–Mo weight fraction inside each sample was limited (much lower than in the fuel plate meat for example) and may fluctuate from one sample to another. To overcome this problem, U loading inside each sample will be determined (see Section 2.3.2.2). Even if full description of compacts production procedure is given elsewhere [29], note that the size of these compacts were 8 mm in diameter and about 5 mm in height and that compaction has been performed manually using an hydraulic press, applying a force of 5 tons/in.

For each kind of compacts, 4 were annealed (340 °C for 130 days, 450 °C for 4 h, 550 °C for 2 and 4 h respectively) the last one being kept as a reference [29]. After annealing scanning electron microscopy (SEM) and electron probe micro analysis (EPMA) examinations have been performed [29]. At this step only fourteen compacts remained[2]. From each of them 1 mm thick slices have been cut perpendicular to the compression axis. Upper and lower surfaces were diamond polished. The resulting samples have been directly used for HE-XRD characterisations.

From the SELENIUM fuel plates (abbreviated as U–Mo(Si)/Al and U–Mo(ZrN)/Al) manufactured by hot rolling, $10 \times 10\ mm^2$ samples have been cut. The cladding has been removed by mechanical polishing to obtain the pure meat for HE-XRD analysis [25]. As a reminder, such a fuel plate meat is a mixture of U–Mo and Al powders with respective weight fractions of about 87–13 wt%. Indeed with these values the required high U loading ($8\ g\ cm^{-3}$) is obtained. More details about fuel plate manufacturing can be found for example in [3].

Finally particles taken from powders (U–Mo(Si) and U–Mo(ZrN)) or extracted from the related fuel plates (U–Mo(Si)/Al and U–Mo(ZrN)/Al) were isolated and glued on top of quartz capillaries for nano-XRD experiments [26]. After gluing, SEM images were taken on both kinds of particles (see Fig. 1). First, particles taken from powders are described. It can be seen that in the case of Si coating, some areas can be found where the coating has detached (red circle in Fig. 1A). Contrary, no detachment and very few cracks are visible in the ZrN coatings (see Fig. 1C). On both particles retrieved from the fuel plates, some Al is still attached to the particles (indicated by dark grey in Fig. 1) thus making the observation of the coating more difficult. However SEM observations of the as-fabricated fuel plates have demonstrated first the full coverage of particles and the presence of cracks in the ZrN coating of U–Mo(ZrN)/Al fuel plate particles [30].

In the following "C" and "P" letters have been added to sample designations to distinguish compacts from fuel plates.

2.2. X-ray diffraction

HE-XRD and nano-XRD measurements were performed at the ESRF (Grenoble, France). In each case diffraction data were collected in transmission mode using a two dimensional detector.

HE-XRD macroscopic measurements have been carried out on the ID15B beamline using a 87 keV X-ray beam which has a size of about 300 μm × 300 μm. Since fuel plate meat samples and compacts do not exhibit any texture, the only constraint for sample orientation was that X-rays had to travel through the smallest sample direction. In other words X-Ray beam path was set along slice thickness (parallel to the compression axis) for compacts and along the fuel plate meat thickness (normal to hot-rolling

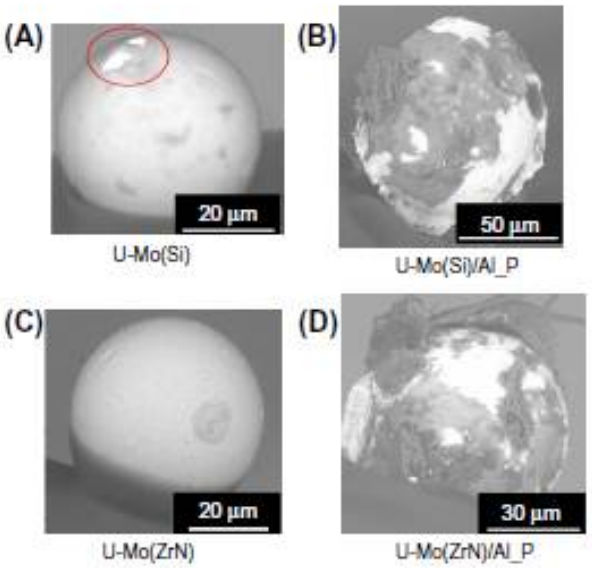

Fig. 1. SEM images of coated U–Mo powder particles ((A) U–Mo(Si) and (C) U–Mo(ZrN)) and of particles extracted from fuel plates ((B) U–Mo(Si)/Al_P and (D) U–Mo(ZrN)/Al_P). (A): Indicated by a red circle are spots on the U–Mo(Si) particle where the Si coating has detached itself. (B) and (D): On the particles extracted from the fuel plates some amount of Al is still attached to the particles.

[1] This refers to 7 wt% (i.e. about 16 at%) of Mo in the U-Mo alloy.
[2] The non-annealed U-Mo(Si)/Al compact has been lost during fabrication.

Table 1
SELENIUM samples characterised using HE-XRD (indicated by "x") and nano-XRD (indicated by "•").

	U–Mo powders	U–Mo compacts					Fuel plates
		Un-annealed	340 °C for 130 days	450 °C for 4 h	550 °C for 2 h	550 °C for 4 h	
U–Mo		×	×	×	×	×	
U–Mo(Si)	×•		×	×	×	×	×•
U–Mo(ZrN)	×•	×	×	×	×	×	×•

plane). At least 20 locations per sample have been characterized to be less sensitive to sample local heterogeneities.

For nano-XRD measurements the ID22Ni beamline has been selected [31]. A 29 keV monochromatic beam was used; its size was 0.1 μm × 0.15 μm. During these measurements only the outer part of U–Mo single particle has been probed: these analyses are used to characterise in details the crystallographic particle coating composition.

Table 1 recaps the characteristics of the samples analysed by HE-XRD and nano-XRD.

2.3. Data interpretation

Diffraction patterns have been analysed with the FullProf software which uses the Rietveld method [32]. At least 10 phases have been taken into account in the refinement. The thermal treatments detailed previously may result in the destabilisation of the U–Mo alloy to form α-U, U_2Mo and two γ-U–Mo phases (written γ-U–Mo-a and γ-U–Mo-b, with different Mo contents), and a U–Mo/Al interaction layer. This layer usually may consist of $U_6Mo_4Al_{43}$, $U(Mo,Al)_2$ and UAl_3 [25,26]. In case of Si coating, two additional phases, $U(Al,Si)_3$ and U_3Si_5 are considered as their presence has been reported in U–Mo/AlSi fuel plates around UMo particles [3,12]. UO_2 is also considered as the U–Mo samples naturally oxidise over time. Last but not least the two crystal structures associated with Si (Fd3m, a_0 = 5.43 Å) and ZrN (Fm3m, a_0 = 4.58 Å) potentially located in the coating of U–Mo particles and Al for the matrix are also taken into account. Table 2 gathers the crystallographic composition derived from the HE-XRD analysis of all SELENIUM samples.

2.3.1. Powders and fuel plates

For powders and fuel plates a synopsis of the analysed nano-XRD and HE-XRD patterns is shown in Figs. 2 and 3 respectively. In all measured patterns presented in this paper, the background has been removed. Because of the better sampling statistics for HE-XRD, the agreement between measured and calculated data is better for HE-XRD patterns than for nano-XRD patterns.

HE-XRD measurements are shown to provide the quantitative composition of U–Mo/Al based samples [25]. The obtained weight fractions can basically be used to determine an average coating thickness assuming some hypotheses on particle geometry and granulometry [12,27]. Since the granulometry of U–Mo atomised powders is not available, it has been considered that it equals the granulometry of U–Mo powders used for manufacturing IRIS plates [12]. This hypothesis makes sense since these plates were produced by the same supplier.

2.3.2. Compacts

2.3.2.1. Evaluation of the initial U–Mo and Al weight fractions. The crystallographic composition of annealed compacts has not been measured before thermal treatment. However this can be estimated based on HE-XRD analyses performed after thermal

Table 2
Crystallographic composition of the SELENIUM samples studied by HE-XRD (2 powders, 2 fuel plates and 14 compacts).

Sample type and composition	Annealing conditions	Crystallographic composition (wt%)											
		U–Mo particle core				U–Mo particle surrounding shell				Interaction layer		Matrix
		γ-U–Mo	α-U[a]	U_2Mo	UC	UO_2	UAl_3 or $U(Al,Si)_3$	U_3Si_5	ZrN	UAl_3	$U_6Mo_4Al_{43}$	Al
Powders												
U–Mo(Si)		97.9			0.9	0.4						0.8
U–Mo(ZrN)		96.7			0.7	0.3			1.2			0.9
Plates												
U–Mo(Si)/Al_P		71.0	10.2	0.4	0.6	0.3	0.1	0.2				17.2
U–Mo(ZrN)/Al_P		70.7	11.6	0.5	0.7	0.3						16.2
Compacts												
U–Mo/Al_C	Un-annealed	7.3	0	0	0.1	0.1	0					92.4
	340 °C for 130 d	4.2	7.1	7.7	0.1	1.6	0					79.3
	450 °C for 4 h	8.9	3.4	1.0	0.1	0.9						85.6
	550 °C for 2 h	8.4	2.4	0	0.1	0.6	2.9			0.2	1.2	84.2
	550 °C for 4 h	12.1	4.6	0	0.1	0.8	8.2			0.4	4.5	69.3
U–Mo(Si)/Al_C	Un-annealed	–	–	–	–	–	–	–	–	–	–	–
	340 °C for 130 d	1.5	2.5	2.3	0.1	0.8	0			0	0	92.9
	450 °C for 4 h	3.5	2.0	1.4	0.1	0.5	0			0	0	91.7
	550 °C for 2 h	8.3	2.2	0	0.1	0.6	0.1			0	0	88.9
	550 °C for 4 h	4.4	1.6	0	0.1	0.4	0.1			0.1	0	93.5
U–Mo(ZrN)/Al_C	Un-annealed	7.6	0	0	0.1	0.1				0	0	92.0
	340 °C for 130 d	2.4	4.7	5.2	0.1	0.6	0			0	0	87.0
	450 °C for 4 h	2.3	1.5	1.0	0.1	0.1	0			0	0	95.0
	550 °C for 2 h	4.0	1.0	0	0.1	0.2	0.1			0	0	94.7
	550 °C for 4 h	6.3	2.4	0	0.1	0.3	0.1			0	0	90.9

[a] α-U stands either for α'-U or for α"-U, as defined in the text.

Table 3
Initial U–Mo weight fraction, U loading and oxidation (written $W^{initial}_{U-Mo}$, $\rho^{compact}_{U}$ and W_{oxid} respectively in the text) in each analysed SELENIUM compact. Note that variations in U–Mo weight fractions and U loading are due to initial compact manufacturing conditions and not to the thermal treatments, these samples may have subsequently undergone.

Sample designation	Annealing conditions	Initial U–Mo weight fraction (wt%)	U loading (g cm^{-2})	Oxidation (%)
U–Mo/Al_C	Un-annealed	7.5	0.2	0.5
	340 °C for 130 days	20.5	0.6	7.4
	450 °C for 4 h	14.1	0.4	6.2
	550 °C for 2 h	14.5	0.4	3.8
	550 °C for 4 h	26.7	0.8	2.9
U–Mo(Si)/Al_C	Un-annealed	–	–	–
	340 °C for 130 days	7.0	0.2	10.4
	450 °C for 4 h	7.4	0.2	6.1
	550 °C for 2 h	11.1	0.3	4.8
	550 °C for 4 h	9.6	0.2	4.4
U–Mo(ZrN)/Al_C	Un-annealed	7.9	0.2	0.6
	340 °C for 130 days	13.0	0.3	4.7
	450 °C for 4 h	7.5	0.2	1.2
	550 °C for 2 h	5.2	0.1	3.0
	550 °C for 4 h	9.1	0.2	2.9

annealing. Indeed assuming that identified crystallographic phases are stoichiometric and that annealing does not modify the global compact elemental composition, Al and U–Mo initial weight fractions can be calculated using two simple relations:

$$W^{initial}_{Al} = \sum_i W_i \times X_i(\mathrm{Al}) \text{ and } W^{initial}_{U-Mo} = W^{initial}_{U} + W^{initial}_{Mo} = \sum_i W_i \times (X_i(U) + X_i(Mo))$$

with W_i weight fraction of the crystallographic phase i, X_i(U), X_i(Mo), X_i(O), X_i(C) and X_i(Al) mean weight fractions of U, Mo and Al in the i crystallographic phase. Note that for this calculation, the presence of coating elements (namely Si, Zr and N elements) has not been taken into account. The so-calculated initial U–Mo weight fractions are given in Table 3.

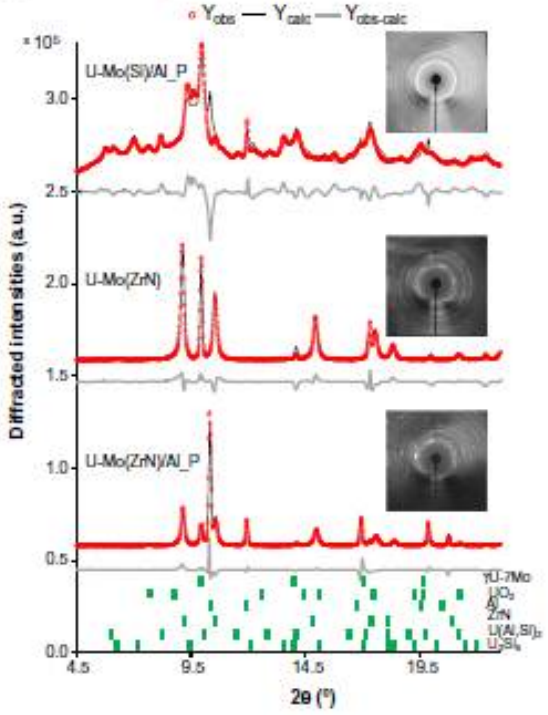

Fig. 2. Synopsis of nano-XRD patterns collected on U–Mo(ZrN) powder particles and U–Mo(Si)/Al_P and U–Mo(ZrN)/Al_P particles from fuel plates.

2.3.2.2. *U loading determination.* The volume of fresh compacts (as in fuel plate meat) consists of three parts: Al matrix, U–Mo particles and porosities. Associated volume fractions are written V_{Al}, V_{U-Mo} and V_{poro} respectively. V_{U-Mo} can be determined using the U–Mo weight fraction (written W_{U-Mo}) inside the compact as derived from HE-XRD analyses (see Section 2.3.2.1):

$$V_{U-Mo} = (1 - V_{poro}) \times \frac{W_{U-Mo}}{W_{U-Mo} + \frac{\rho^{pure}_{U-Mo}}{\rho^{pure}_{Al}} \times (1 - W_{U-Mo})}$$

In the previous equation ρ^{pure}_{U-Mo} and ρ^{pure}_{Al} refer to Al and U–Mo density in pure U–Mo and Al samples and equal to 17.7 and 2.7 g cm^{-3} respectively. The U loading inside a compact written here $\rho^{compact}_{U}$ can be calculated as:

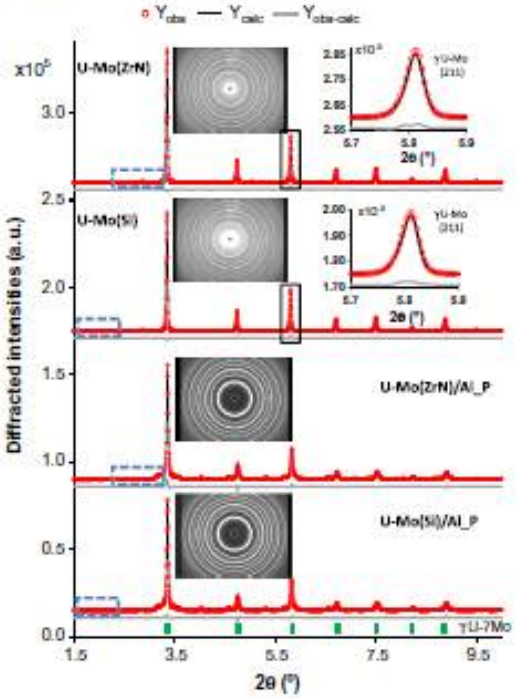

Fig. 3. HE-XRD patterns collected on U–Mo(Si) and U–Mo(ZrN) powder particles and U–Mo(Si)/Al_P and U–Mo(ZrN)/Al_P fuel plates. Insets show zooms in the vicinity of the (211) γU–Mo Bragg line for U–Mo powders. Dashed blue boxes indicate the zoomed-in regions shown in Fig. 4 and Fig. 5.

$\rho_U^{compact} = \rho_{U-Mo}^{compact} \times W_U^{U-Mo}$ with $\rho_{U-Mo}^{compact} = \rho_{U-Mo}^{pure} \times V_{U-Mo}$ and W_U^{U-Mo} the U weight fraction inside U–Mo alloy which is about 93% in this case (see Section 2.1).

To sum-up, it is demonstrated that the U loading inside a compact (as in the meat of fuel plates) can be estimated using U–Mo initial weight fractions and porosity volume fraction: $\rho_U^{compact} = (1 - V_{pore}) \times f(W_{U-Mo})$ where $f(W_{U-Mo})$ is a well-defined function of (W_{U-Mo}). If V_{pore} has not been measured in this study, a 5% value has been assumed. This is at least twice higher than the usual porosity volume fraction in the meat of fuel plates. The last equation shows however that this uncertainty leads to a limited error for calculating U loading (estimated to a few percents). Table 3 gathers the U loadings estimated for each compact.

2.3.2.3. IL fraction, destabilisation and oxidation level. Figs. 6–8 show a comparison between measured and calculated HE-XRD patterns for the U–Mo/Al_C, U–Mo(ZrN)/Al_C and U–Mo(Si)/Al_C compacts respectively. In this paper their crystallographic composition is discussed through the quantity of IL present in the sample and through the destabilisation of the γ-U–Mo phase. Since the initial U–Mo powder weight fraction in a compact may fluctuate from one sample to another, the IL weight fraction in the compact has been normalised using the following relation:

$W_{IL} = \frac{\sum_j W_j}{\sum_j j W_j + W_{U-Mo}^{initial}}$ with W_j the crystallographic weight fraction of phases j in the IL. To follow the γ-U–Mo destabilisation, it has been chosen to consider the α-U (α′-U or α‴-U) weight fraction inside U–Mo particle cores defined as: $\alpha U\_ratio = \frac{W_{\alpha U}}{(W_{\alpha U} + W_{U_2Mo} + W_{\gamma\text{-}UMo\text{-}\alpha''} + W_{\gamma\text{-}UMo\text{-}\gamma'})}$. Finally the oxidation level of U–Mo particles has been evaluated using the following relation: $W_{oxid} = \frac{W_{UO_2}}{W_{UO_2} + W_{U-Mo}^{initial}}$ (See Fig. 7).

3. Results and discussion

3.1. Si and ZrN coated powders (U–Mo(Si) and U–Mo(ZrN))

3.1.1. HE-XRD

The patterns measured on the coated U–Mo particles confirm that no destabilisation of γ-U–Mo phase has occurred during the PVD process. No trace of α-U has been found in both samples as usually observed in as-fabricated U–Mo atomised [33,34,27] and ground powders [3]. Note the asymmetry of γ-U–Mo Bragg lines as shown in Fig. 3 for the example of the (211) Bragg line: this observation is in agreement with the presence of two γ-U–Mo phases related to Mo-depleted zones in the vicinity of grain boundaries. Indeed difference in the Mo content of γ-U–Mo phase will cause a shift in lattice parameter.

Moreover some contaminations have been identified in the U–Mo particles. As already reported in [27], the UC and UO_2 phases have been detected within the expected concentration range (about 1 and 0.3 wt% respectively) (see Table 2): the PVD treatment did not induce an important additional U–Mo particle oxidation. The presence of Al (1 wt%) is more surprising but could be the result of a contamination during preparation.

Finally the presence of low intensity diffraction Bragg lines must be mentioned at 2.78, 1.84, 1.62 and 1.35 Å (d_{hkl} values). It remains still difficult to definitely attribute them either to a γ-U–Mo ordered metastable phase ($U_{2.2}Mo_3$ or U_3Mo) [33] or to an unidentified pollution trace phase [27].

On top of the results obtained on the U–Mo particle core, HE-XRD measurements are also sensitive to U–Mo particle coatings (see Figs. 4 and 5). In the case of Si deposition, it has not been possible to assess the presence of the Si phase. Indeed the peaks of this phase systematically overlap with the UO_2 broad ones thus making a definitive conclusion difficult. It has been shown that the Si quantity in a 0.6 μm thick Si coating is equivalent to that found in the meat of a U–Mo/Al(Si) fuel plate with a matrix containing 5 wt% Si [23,35]. Considering that the matrix fraction in the meat is about 13 wt% (in conventional 8 gU cm^{-3} U–Mo/Al fuel plates), the Si weight fraction in this U–Mo powder should yield about 0.5 wt%. However HE-XRD pattern simulations have demonstrated that such a quantity of crystalline Si is not present in the analysed powder.

In the case of ZrN coatings, Bragg lines can be unambiguously attributed to the ZrN cubic structure [36]. The amount of this phase (about 1.2 wt%) is however lower than expected if one considers both the measured thickness (1 μm) and density (about 7.3 g cm^{-3}).

3.1.2. Nano-XRD

To complement HE-XRD studies successive nano-XRD measurements were made on U–Mo(Si) and U–Mo(ZrN) particle to characterize their coating crystallographic composition (see Fig. 2).

For U–Mo(ZrN) particles, only one crystallographic phase has been found in the coating: the cubic ZrN structure. Moreover the measured 2D pattern shows that this phase is strongly textured with complex crystallographic relation with U–Mo grains on which this phase has been deposited. Such texture relationships between outer shell crystallites and U–Mo grains have already been reported for U–Mo surrounded by a micrometre thick UO_2 layer [27].

For U–Mo(Si) particles, the numerous nano-XRD measurements in the outer part of the samples do not reveal the presence of any crystallographic compound except some UO_2 traces which are often found in atomised U–Mo particles. Since the presence of Si coating is demonstrated (see Fig. 1A), it can be reasonably proposed that Si PVD coating is amorphous in these powders. Indeed the contribution of a thin layer of an amorphous compound made with low Z elements (Si) is expected to be very limited and thus difficult to identify in a nano-XRD pattern measured at relatively high energy (29 keV).This proposition is supported by the existence of a non-crystalline allotropic form of silicon (written a-Si in literature) and by the demonstration that such compound can be deposited by PVD in thin films (see for instance reference [28]).

3.2. Full size fuel plates (U–Mo(Si)/Al_P and U–Mo(ZrN)/Al_P)

3.2.1. HE-XRD

The destabilisation ratios observed in the two analysed fuel plates (U–Mo(Si)/Al_P and U–Mo(ZrN)/Al_P) are low but in agreement with those reported for fuel plates manufactured under similar conditions [12,3]. The weight fraction of the α‴-U phase in the U–Mo particle core (α‴-U_ratio) is close to 14 wt% (see Table 2).

The HE-XRD measurements on the as-fabricated U–Mo(ZrN)/Al_P fuel plate do not enable the study of the ZrN crystal structure. The reason is that ZrN's most intense peaks overlap with α‴-U Bragg lines which exhibit a higher intensity (see Fig. 3).

The analysis of the U–Mo(Si)/Al_P fuel plate is much more fruitful. HE-XRD measurements definitely show the presence of two uranium Silicide phases:

- $U(Al,Si)_3$ with two lattice parameters (4.16 Å and 4.21 Å),
- A distorted U_3Si_5 phase.

Note that these phases were not present in the U–Mo(Si) powders. These phases are usually found in the Silicon rich diffusion layer (SiRDL) obtained in dispersed fuels (as-manufactured U–Mo/Al(Si) fuel plates [12,3] or annealed UMo(Si)/Al fuel rods [40]) as well as in diffusion couples (U–Mo/Al(Si7) [37–39] or U–Mo/Si [41]). This analysis is furthermore in full agreement with the SEM/EDX characterisations which have highlighted the growth of a SiRDL in these U–Mo(Si)/Al_P fuel plates [30]. However it must be stressed that the amount of these $U(ALSi)_3$ and U_3Si_5 crystalline phases (about 0.3 wt%) is lower than the one obtained for fuel

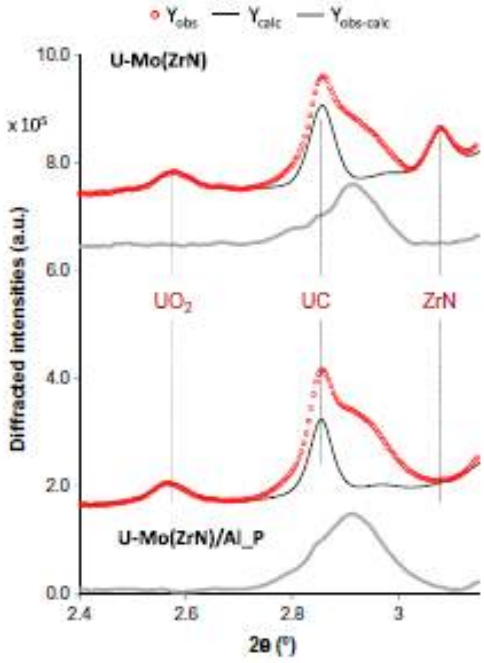

Fig. 4. Comparison between HE-XRD patterns associated with U–Mo(ZrN) and U–Mo(Si) powders. Zoom in the [2.4–3.1] 2θ range of the measured and calculated diagrams shown in Fig. 3.

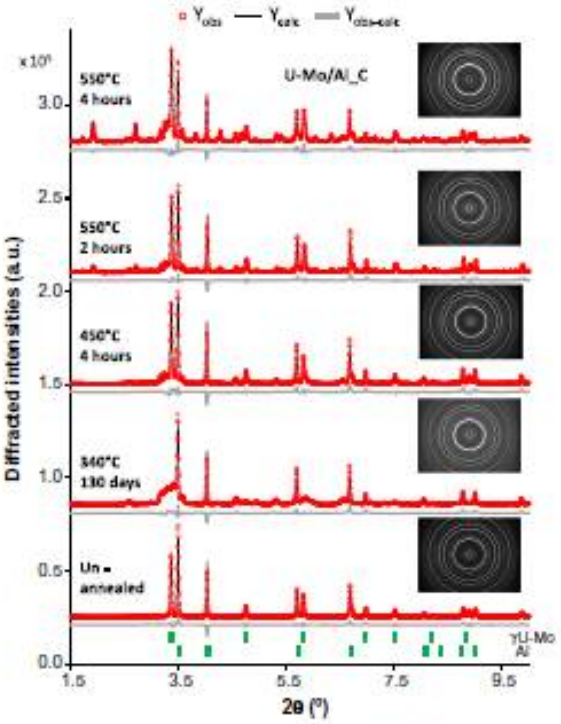

Fig. 6. Comparison between measured and calculated HE-XRD patterns related to U–Mo/Al_C compacts (with uncoated U–Mo particles) annealed under different conditions.

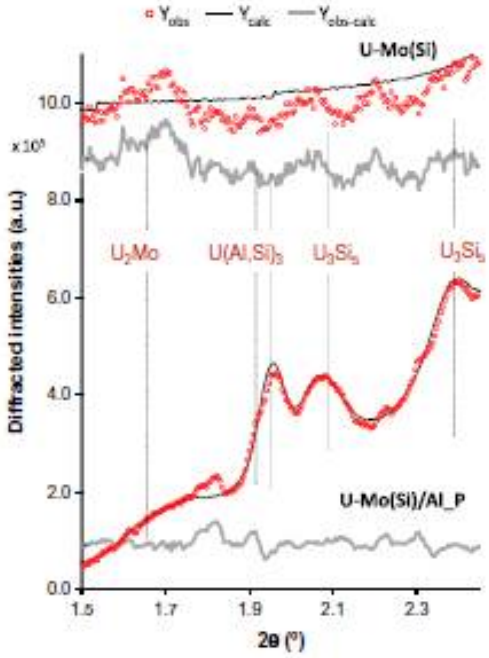

Fig. 5. Influence of fuel plate manufacturing process on the Si coating crystallographic composition: comparison between HE-XRD patterns associated with U–Mo(Si) powders and U–Mo(Si)/Al_P fuel plates in the as-manufactured state. Zoom in the [1.5–2.4] 2θ range of measured and calculated diagrams shown in Fig. 3.

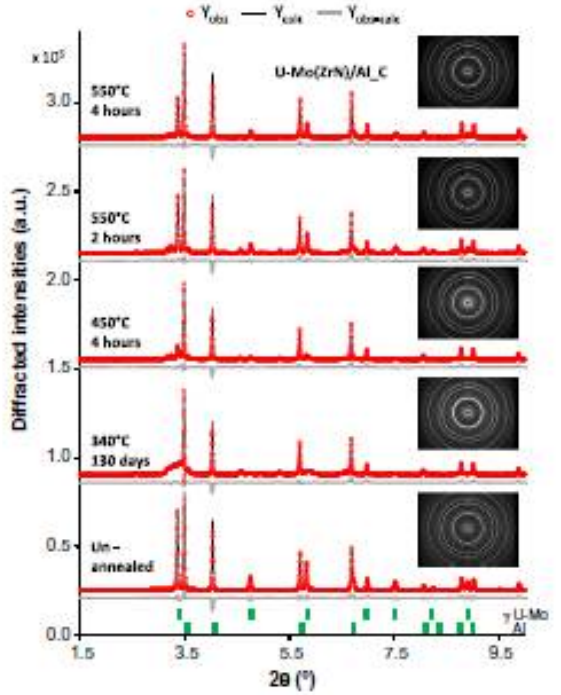

Fig. 7. Comparison between measured and calculated HE-XRD patterns related to U–Mo(ZrN)/Al_C compacts annealed under different conditions.

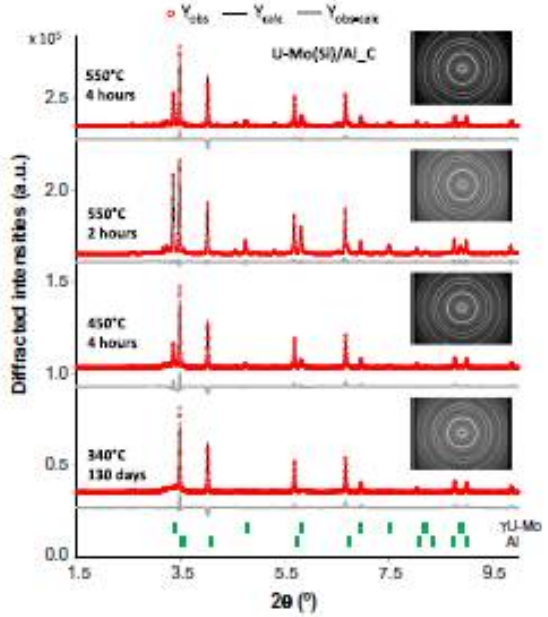

Fig. 8. Comparison between measured and calculated HE-XRD patterns related to U–Mo(Si)/Al_C compacts annealed under different conditions.

plates containing 4–6 wt% Si in the matrix [12]. It equals to the SiRDL amount measured in the IRIS4_2.1%Si fuel plate. Using these HE-XRD measurements, the Si concentration in SiRDLs is evaluated to 51 at%. This value is somewhat higher than when measured by EDX: it has been estimated to 40 at% in [30].

3.2.2. Nano-XRD

Nano-XRD measurements on the outer part of U–Mo(ZrN)/Al_P particles have definitely confirmed the presence of crystalline ZrN phases whose characteristics are very close to those obtained on U–Mo(ZrN) particles.

Characterisations using nano-XRD have been undertaken on a Si coated U–Mo particle retrieved from a fuel plate. In the refined pattern shown in Fig. 2, it is obvious that U_3Si_5 and $U(AlSi)_3$ phases are present in the shell surrounding these U–Mo(Si)/Al_P particle. Since these shells are very thin, phases from the U–Mo core as well as from the Al matrix can be also seen in the nano-XRD pattern. Finally note that U_3Si_5 Bragg lines show very intense broadening indicating a very small crystallite size (in the 10 nm range). Recent TEM characterisations on U–Mo/Al(Si7) fuel plates have reported the presence of amorphous compounds in such uranium silicide layers [42], which is difficult to confirm based on these nano-XRD patterns.

3.3. Compacts

3.3.1. Specificities of annealed compacts

As shown in Table 3, the U loading is particularly low in the analysed compacts 0.3 (0.3 g cm^{-3} in average) compared to U loadings in the fuel plate meat (8 gU cm^{-3}) respectively. As a consequence of the low U–Mo powder amount in the analysed samples, the composition of the coatings became very difficult to analyse: they will not be discussed in this paper. Moreover it can be seen in Table 3 that compact annealing has induced a slight U–Mo particle oxidation which is stronger for low temperature thermal treatments (at 340 and 450 °C). The oxidation levels are however higher on these compacts than on fuel plates: after annealing of fuel plates during 50 h at 425 °C, the oxidation level was found to be about 1% [43]. Since U–Mo(ZrN)/Al_C compacts are less affected by the presence of UO_2 than U–Mo(Si)/Al_C and U–Mo/Al_C samples, it is likely that a ZrN coating preserves U–Mo particles from oxidation.

3.3.2. γ-U–Mo destabilisation under thermal treatments

Whatever the coating composition, U–Mo destabilisation products after thermal annealing are mainly:

- U_2Mo and α″-U phase for compacts annealed at 340 °C,
- U_2Mo and α′-U phase for compacts annealed at 450 °C [43],
- γ-U–Mo and α′-U for compacts annealed at 550 °C.

These results obtained on compacts are in good agreement with previous works performed on U–8Mo ingots (see Fig. 9A) -even if some differences in the α-U phase structure must be mentioned - and in very close agreement with recent studies on thermally annealed U–Mo/Al fuel plates. Indeed destabilisation products found in this work are identical to those identified after fuel plate annealing at 550 °C [25] and 450 °C [43]. Moreover this work helps establishing that destabilisation products are U_2Mo and α″-U at

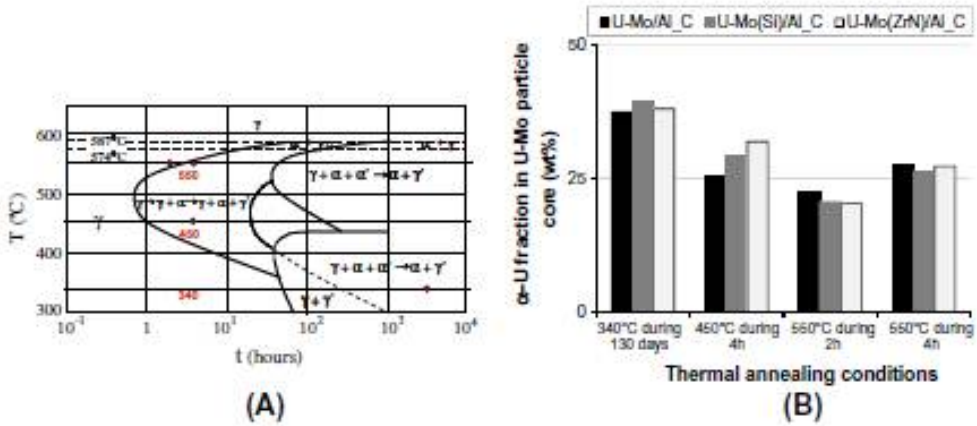

Fig. 9. Destabilisation of the γ-U–Mo phase in the analysed compacts. Superimposition of the compact annealing conditions (red circles) with the U–Mo8 TTT curve taken from [44] and references therein (A). Normalised α-U fraction in the particle core after annealing as determined by HE-XRD (B). (For interpretation of the references to colour in this figure legend, the reader is referred to the web version of this article.)

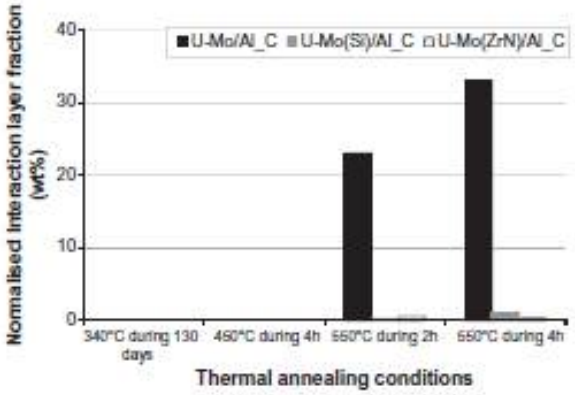

Fig. 10. Normalised IL weight fractions in U–Mo/Al_C, U–Mo(Si)/Al_C and U–Mo(ZrN)/Al_C compacts. Definition of the normalised IL weight fraction is given in Section 2.3.2.2.

lower temperatures (below 450 °C). This was first demonstrated on fuel plates annealed at 425 °C for more than 50 h [43] and this is confirmed here with the analysis of the compacts annealed at 340 °C during 130 days. Note finally that whatever the presence of a coating, destabilisation ratios are very close in compacts annealed in the same conditions (see Fig. 9B) and that destabilisation ratios show the expected increase between 2 and 4 h annealing at 550 °C.

3.3.3. *PVD coatings for limiting the IL growth*

It must be first mentioned that no significant amount of IL has grown in any compact annealed at 340 (during 130 days) and 450 °C (during 4 h). This IL in significant amounts has only been found in U–Mo/Al compacts after thermal treatment at 550 °C for 2 and 4 h. After both durations the IL crystallographic composition has been found to be identical: it is made of UAl_3, $U_6Mo_4Al_{43}$ and UAl_2 as expected from literature [25,26,43]. From Fig. 10, it is clear that both ZrN and Si coatings are very efficient in limiting the growth of the U–Mo/Al IL: for thermal treatments at 550 °C, almost no IL could be found in U–Mo(Si)/Al_C and U–Mo(ZrN)/Al_C. HE-XRD measurements therefore confirm not only SEM/EPMA analyses on these annealed compacts but also recent heavy ion irradiation experiments performed on the related fuel plates [30].

4. Conclusion

In this paper, Si and ZrN coated atomized U–Mo powders, full size test plates and annealed compacts have been studied using high energy and nano-X-ray diffraction.

For the coated powders, the PVD sputtering process is shown to avoid both destabilisation of the γ-U–Mo phase and surface oxidation of the U–Mo particles. Evidence has been provided for the presence of the crystalline ZrN in U–Mo(ZrN) powders. It has been demonstrated that conventional fuel plate manufacturing process induced minor evolutions in the crystallographic structure of the coating. However previous SEM investigations of the fuel meat have suggested that this step could induce numerous cracks in ZrN layer [30]. To define whether those cracks are induced by sample preparation methods or by the manufacturing process, it would be pertinent to image the coating of such U–Mo(ZrN)/Al particles using nano-CT [26].

On the contrary, manufacturing process has a huge influence on the coating crystallographic composition of U–Mo(Si) particles. Indeed it has been demonstrated that during this step a reaction occurs between the initially amorphous Si coating and the U–Mo particle. SiRDLs are formed: they consist of $U(Al,Si)_3$ and U_3Si_5.

Macroscopic investigations performed on annealed U–Mo/Al_C, U–Mo(Si)/Al_C and U–Mo(ZrN)/Al_C compacts have demonstrated that the 1 μm ZrN coating as well as 0.6 μm Si coatings are very efficient for preventing the growth of an IL under thermal treatments. It would be very interesting to supplement this work with more local characterisations to determine crystallographic evolutions in the coating of these U–Mo particles whose presence after thermal treatments has been assessed by EPMA [23].

Acknowledgments

This work was supported by a combined Grant (FRM0911) of the Bundesministerium für Bildung und Forschung (BMBF) and the Bayerisches Staatsministerium für Wissenschaft, Forschung und Kunst (StMWFK). This work is also part of the ESRF long term project MA1063.

References

[1] J.L. Snelgrove, G.L. Hofman, C.L. Trybus, T.C. Wiencek in: Proceedings of the 19th International Topical Meeting on Reduced Enrichment for Research and Test Reactors (RERTR), Seoul, South Korea, 1996.
[2] M.K. Meyer, G.L. Hofman, S.L. Hayes, C.R. Clark, T.C. Wiencek, R.V. Strain, K.-H. Kim, J. Nucl. Mater. 304 (2002) 221–236.
[3] R. Jungwirth, H. Palancher, A. Bonnin, C. Bertrand-Drira, C. Borca, V. Honkimaki, C. Jarousse, B. Stepnik, S.H. Park, X. Iltis, W. Schmahl, W. Petry, J. Nucl. Mater. 438 (2013) 246–260.
[4] A. Leenaers, S. Van den Berghe, W. Van Renterghem, F. Charollais, P. Lemoine, C. Jarousse, A. Röhrmoser, W. Petry, J. Nucl. Mater. 412 (2011) 41–52.
[5] C.K. Kim, J.M. Park, H.J. Ryu, Nucl. Eng. Technol. 39 (2007) 617.
[6] A. Leenaers, S. Van den Berghe, E. Koonen, C. Jarousse, F. Huet, M. Trotabas, M. Boyard, S. Guillot, L. Sannen, M. Verwerft, J. Nucl. Mater. 335 (2004) 39–47.
[7] P. Lemoine, J.L. Snelgrove, N. Arkhangelsky, L. Alvarez in: Proceedings of the 8th International Topical Meeting on Research Reactor Fuel Management (RRFM), Munich, Germany, 2004.
[8] G.L. Hofman, A.B. Robinson, Proceedings of the 13th International Topical Meeting on Research Reactor Fuel Management (RRFM), Austria, Vienna, 2009. March.
[9] D.D. Keiser Jr., J-F. Jue, N.E. Woolstenhulme, A. Ewh, J. Nucl. Mater. 419 (2011) 226–234.
[10] R. Jungwirth, H. Breitkreutz, W. Petry, A. Rohrmoser, W. Schmid, H. Palancher, C. Bertrand-Drira, C. Sabathier, X. Iltis, N. Tarisien and C. Jarousse in: Proceedings of the 31th International Meeting On Reduced Enrichment For Research And Test Reactors (RERTR), Beijing, China, 2009.
[11] X. Iltis, F. Charollais, M. C. Anselmet, P. Lemoine, A. Leenaers, S. Van den Berghe, E. Koonen, C. Jarousse, D. Geslin, F. Frery and H. Guyon in: Proceedings of the 32th International Meeting on Reduced Enrichment for Research and Test Reactors (RERTR), Lisbon, Portugal, 2010.
[12] H. Palancher, A. Bonnin, V. Honkimäki, T. Buslaps, M. Grasse, B. Stepnik, T. Zweifel, J. Alloys Comp. 527 (2012) 53–65.
[13] S. Dubois, F. Mazaudier, H. Palancher, P. Martin, C. Sabathier, M. Ripert, P. Lemoine, C. Jarousse, M. Grasse, N. Wieschalla, W. Petry, in: Proceedings of the 28th International Meeting on Reduced Enrichment for Research and Test Reactors (RERTR), Cape Town, 2006.
[14] J.H. Yang, J.S. Park, W.H. Cho, C.K. Kim, H.J. Ryu, Y.S. Lee, J.M. Park, Proceedings of the 15th International Topical Meeting on Research Reactor Fuel Management (RRFM), Rome, Italy, 2011.
[15] A. Izhutov, V. Alexandrov, A. Novosyolov, V. Starkov, A. Sheldyakov, V. Shishin, V. Iakovlev, I. Dobrikova, A. Vatulin, G. Kulakov, V. Suprun, in: Proceedings of the International Meeting on Reduced Enrichment for Research and Test Reactors (RERTR), Lisbon, 2010.
[16] H.J. Ryu, J.S. Park, J.M. Park, C.K. Kim, Nucl. Eng. Technol. 43 (2011) 159.
[17] D.D. Keiser, A.B. Robinson, J.F. Jue, P. Medvedev, D.M. Wachs, M.R. Finlay, J. Nucl. Mater. 393 (2009) 311–320.
[18] Y. S. Kim, G. Hofman and A. B. Robinson in: Proceedings of the International Topical Meeting on Research Reactor Fuel Management (RRFM), Vienna, Austria, 2009.
[19] M. Ripert, V. Marelle, X. Iltis, H. Palancher, Ch. Valot, F. Charollais, M.-C. Anselmet, X. Tiratay, P. Lemoine, S. Van den Berghe, A. Leenaers, C. Jarousse, Proceedings of RRFM 2011, Roma, Italy, 2011. March.
[20] D.D. Keiser, J.-F. Jue, B. Yao, E. Perez, Y.H. Sohn, C.R. Clark, J. Nucl. Mater. 412 (2011) 90–99.
[21] D.D. Keiser, J. Gan, J.-F. Jue, B.D. Miller, C.R. Clark, Mater. Character. 61 (2010) 1157–1166.
[22] A. Leenaers, S. Van den Berghe, J. Van Eyken, E. Koonen, F. Charollais, P. Lemoine, Y. Calzavara, H. Guyon, C. Jarousse, D. Geslin, D. Wachs, D.D. Keiser, A. Robinson, G. Hofman, Y.S. Kim, J. Nucl. Mater. 444 (2013) 439–448.

[23] A. Leenaers, S. Van den Berghe, C. Detavernier, J. Nucl. Mater. 440 (2013) 220–228.
[24] S. Van den Berghe, A. Leenaers, Detavernier, in: Proceedings of the RERTR, Warsaw, Poland, 2012.
[25] A. Bonnin, H. Palancher, V. Honkimäki, R. Tucoulou, Y. Calzavara, C.V. Colin, J-F. Bérar, N. Boudet, H. Rouquette, J. Raynal, C. Valot, J. Rodriguez-Carvajal, Zeit. Krist. Proc. 1 (2011) 29–34.
[26] H. Palancher, R. Tucoulou, P. Bleuet, A. Bonnin, E. Welcomme, P. Cloetens, J. Appl. Crystallogr. 44 (2011) 1111–1119.
[27] H. Palancher, A. Bonnin, V. Honkimäki, H. Suhonen, P. Cloetens, T. Zweifel, R. Tucoulou, A. Rack, M. Voltolini, J. Appl. Crystallogr. 45 (2012) 906–913.
[28] P.R. Besser, Q. Xiang, M.S. Buynoski, US Patent US6392280 B1, 2002.
[29] A. Leenaers, S. Van den Berghe, C. Detavernier, Proceedings of the 15th International Topical Meeting on Research Reactor Fuel Management (RRFM), Rome, Italy, 2011.
[30] R. Jungwirth, T. Zweifel, H.-Y. Chiang, W. Petry, S. Van den Berghe, A. Leenaers, J. Nucl. Mater. 434 (2013) 296–302.
[31] G. Martinez-Criado, R. Tucoulou, P. Cloetens, P. Bleuet, S. Bohic, J. Cauzid, I. Kieffer, E. Kosior, S. Labouré, S. Petitgirard, A. Rack, J.A. Sans, J. Segura-Ruiz, H. Suhonen, J. Susini, J. Villanova, J. Synchrotron, Radiation 19 (2012) 10–18.
[32] J. Rodriguez-Carvajal, 2001. <http://www.ill.eu/sites/fullprof>.
[33] B.-S. Seong, C.H. Lee, J.-S. Lee, H.-S. Shim, J.-S. Lee, K.H. Kim, C.K. Kim, V. Em, J. Nucl. Mater 277 (2000) 274–279.
[34] J.M. Park, H.J. Ryu, K.H. Kim, D. B Lee, Y.S. Lee, J.S. Lee, B.S. Seong, C.K. Kim, M. Cornen, J. Nucl. Mater. 397 (2010) 27–30.
[35] S. Van den Berghe, A. Leenaers, E. Koonen, L. Sannen, Adv. Sci. Technol. 73 (2010) 78–90.
[36] A.N. Christensen, Acta Chemica Scandanavica 29A (1975) 563–568.
[37] M. Mirandou, S. Arico, M. Rosenbusch, M. Ortiz, S. Balart, L. Gribaudo, J. Nucl. Mater. 384 (2009) 268–273.
[38] J. Allenou, H. Palancher, X. Iltis, M. Cornen, O. Tougait, R. Tucoulou, E. Welcomme, Ph. Martin, C. Valot, F. Charollais, M.C. Anselmet, P. Lemoine, J. Nucl. Mater. 399 (2010) 189–199.
[39] X. Iltis, J. Allenou, B. Verhaege, H. Palancher, O. Tougait, A. Bonnin, R. Tucoulou, J. Nucl. Mater. 433 (2013) 255–264.
[40] W.J. Kim, H. Palancher, H.J. Ryu, J.M. Park, J.M. Nam, A. Bonnin, V. Honkimäki, F. Charollais, P. Lemoine, J. Alloys Compd (2013). submitted.
[41] A. Leenaers, S. Van den Berghe, C. Detavernier, Solid State Sci. 14 (2012) 1133–1140.
[42] B. Yao, E. Perez, D.D. Keiser Jr., J-F. Jue, C.R. Clark, N. Woolstenhulme, Y. Sohn, J. Alloys Comp. 509 (2012) 9487–9496.
[43] H. Palancher, A. Bonnin, C.V. Colin, V. Nassif, V. Honkimäki, C. Ritter, R. Jungwirth, G. Champion, Y. Calzavara, Powder. Diff., accepted, 2013.
[44] C. Prunier, PhD thesis, Reims University, France, 1981.

B. Restart of MLL Tandem accelerator after spark

During irradiation at high voltages above 11 MV, a spark is quite possible to occur. A spark can be identified by any of these observations which should be checked in this order:

- A strong sound like a detonation coming from the Tandem hall.
- Sparks are likely to cause a "blackout" of the controlling devices near the Tandem tube just like an EMP wave. A direct effect could be failure of pumping systems inside the tube resulting in an alarm sound at the controlling stage.
- 4 buttons at the controlling stage indicate the status of the most important Tandem devices: the high/low energy side pumping system and loading system (HE/NE Welle / Kette). If a failure is detected, one or more of these buttons are highlighted in red.
- The Tandem voltage shows a slightly different value, e.g. 10.4 MV instead of 11.3 MV.
- An obvious drop in irradiation temperature as no beam power is available to heat the sample. Likewise, no current is measured. Please note that these two points may not necesserily be related to a spark. Other reasons might be as well responsible for these two effects.

Please keep in mind that it is necessary to check the controlling stage regularly, especially during night shifts when no operator is on duty. In the worst case, the Tandem tube is aired if the pumps are out of order for 10 minutes. Pumping the tank, re-establishing and guiding the beam to the irradiation setup could then result in severe loss of beamtime. To restart the Tandem after a spark follow these steps in exactly this order:

1. If necessary, restart the "NE/HE Welle" which pump the accelerator tube. As mentioned, they are highlighted in red when out of order. Resetting is done by pushing the according buttons until they blink in green. When blinking has finished, the device is fully reset. When not responding they must be resetted manually in

the Tandem hall. On the left and right hand side of the Tandem tube two pumping stacks are installed. Reset the according vacuum pumps.

2. Check whether one of the menues in the computer screen is red. If this is the case, simultaneously push the buttons "Freigabe" and "HE/NE Knoten" until they blink in yellow. This resets the computer interfaces. DO NOT PUSH ANY BUTTONS OR HANDLE MENUES UNTIL BLINKING IS STOPPED. Otherwise the whole controlling system will crash. Resetting of these devices will take around 10 minutes. You can cross-check the status on the screen on the far right of the controlling stage. If the displays indicates "code segment loaded" resetting is finished.

3. If the menue "Corona Spitzen" is grey another device has to be reset. Push "Freigabe" and "Stab-K" at the same time and behave as explained before. NEVER PUSH THE BLUE BUTTON.

4. In the menue field "GVM Gain" push "Disable" to bring the present accelerator voltage on screen again. This should normally be below 1 MV.

5. One of the Faraday cups may also cease operation after a spark. When a cup cannot be operated, the cup controlling system has to be reset. This is done behind the rack on the far left of the controlling stage. Approximately at the height of the head a small lever saying "FC-B1" is visible. Turn the lever for ca. 1 second.

6. Bring the corona online again. In the "Corona Spitzen" menue turn the motor on "EIN". Now the position of the corona should have a negative value of around -100mm. If this is not the case turn off and on the motor again. Set the corona to a value of 0mm. Around 5 minutes pass until this value is reached.

7. Restart the voltage generator. This is done by resetting the "NE/HE Kette" via the according buttons. Behave as before. Now adjust both "HE/NE Ladestrom" to a value of 50μA. This should be equal to a voltage of 7 to 8 MV. Now increase both stepwise and alternating by around 5 - 7 μA each. When these values are increased to fast another spark is likely. Continue until 9 MV are reached.

8. On the computer desktop interface a link saying "Sequencer" exists. The final voltage is reached by utilizing this program. In the program under "Aufgabe wählen" click "Konditionieren". Then type in the desired voltage. Click "Connect" and "Start". When the final voltage is reached click on "Stop" and close the program. The corona current should now be around 50 μA.

9. GVM Gain and Slit Gain on "Enable".

10. Check the current on all the Faraday cups in the right order (from 1 to 5).

11. If no current is detected on Cup1 but particles are well generated in the source, a shutter before the accelerator tube has closed. On the far left of the Tandem tube, right next to the Faraday cage, a small rack is situated. When the shutter is closed the button "NE-Schieber" is red. Pushing it will turn it green together with a characteristic sound of pressurized air.

12. If a good value is seen on Cup4, but no current is detected on Cup5, the 90°-Magnet has to be checked in the Tandem hall. Normally, a "SSV" shutter has closed. Pushing the according button on the nearby rack will open it again. Otherwise the magnet settings have been lost during the spark. This is indicated by swiftly changing values on the display in the same rack. Also push "Hard Reset" or even disconnect the according power supply. In any case the magnet value has to be set in the controlling program. Actual values for the magnet have to be taken from the beamtime protocoll.

13. Check the gas stripper (Menues Tandem $\rightarrow$ Stripper $\rightarrow$ Gas Stripper). The necessary values are 100%, Ventil ca. 40V and Strippergas 7 - 8%. This should equal a vacuum value of $2 - 4 \cdot 10^{-5}$ mbar.

14. Check the vacuum status along the whole beamline. Restart all pumps that failed during the spark.

15. Make a note in the beamtime protocoll indicating the time the spark occurred and the time necessary to bring the machine online again.

C. Heavy ion irradiation setup and beam adjustment procedures

The standard procedure during every beam time was:

1. Beam adjustment in order to guarantee the beam is exactly at the sample position. To fulfill this criteria, a "hole" (see fig. A.III - A is placed at this position. The diameter of the hole can be modified by screwing an Al sheet which in turn has its own hole. For this thesis, the irradiated sample surface was chosen to 6 mm in diameter. By the two Faraday cups before and after the irradiation chamber, the **beam transmission** through the hole can be measured. As a consequence, the exact particle flux on the irradiated surface can be measured.

2. Adjust beam shape to ensure the sample surface is homogenously irradiated. Two possibilities exist to achieve homogeneouty:

   - Either the beam shape itself can be set to a distinct size in diameter. However, this means the beam has to be defocussed on the sample position. The drawback is that in general it is not possible to achieve a perfect circular beam shape resulting in additional beam loss on the target surface. Also, the temperature distribution on the sample would be inhomogeneous as the beam spot center would exhibit a higher temperature as fringe regions.

   - The second possibility, which is the preferred one, is to focus the beam and then move the beam position in x and y direction by electric fields. This method is known as **"focus wobbling"**. This guarantees a more homogeneous temperature distribution on the sample and a full irradiation of the target surface.

   However, to observe the beam shape, a quartz crystal has to be put in the sample position place. This crystal provides an excellent beam shape observation which is visible by an infrared camera.

3. Move sample in beam position.

To conclude, three steps have to be taken into account before irradiation can start. However, the first two steps are only necessary at the beginning of beam time. It became clear that once adjusted the first two points do not change during a week of beam time. For example, the beam diverged only by 1 mm during this period.

Past irradiations in this setup and the according sample holders are fully described in [142] and [143]. The first samples irradiated during this thesis also used one of the samples holders from these previous PhD theses. Only one position on the sample holder was possible. This in turn resulted in opening the irradiation chamber and loss of beamtime. Taking into account preliminary beam adjustments for transmission measurement and beam shape determination, several hours of beamtime had to be invested for these adjustments. Naturally, other sample holders were available which allowed mounting of several samples before the chamber had to be opened again. However, one major goal was the observation of the temperature influence during the irradiation. As a consquence, only the mentioned sample holder could provide temperature adjustment of the sample at all, although by a very basic mechanism. The principal idea of this temperature control mechanism was heating by the constant beam power on the one hand and cooling by filling liquid nitrogen into the sample holder on the other hand. As the holder inlet was made of pure Cu, the heat transfer to the sample holder was very efficient. Two major obvious drawbacks were that there was no method to heat up the sample by other means as beam intensity and that the nitrogen cooling with a liquid temperature of -196°C resulted in a strong drop in temperature. Furthermore, no constant nitrogen flow could be achieved with this sample holder. All the mentioned drawbacks resulted in a strong temperature deviation of ± 20°C. As a consequence, some irradiation results presented in the proceeding chapters show this strong deviation.

Therefore, a setup upgrade has been realised during this thesis and it is described in the following. The two most important issues to be optimized were on the one hand the temperature control of the sample holder, on the other hand mounting of several samples simultaneously was also a mandatory upgrade so that the preliminary beam adjustments could be performed without the need to open the chamber between the different adjustment steps. Both issues have been realised in the sample holder shown in fig. 8.5 - A. This new sample holder itself consists of two main parts: the mean part which is connected to the chamber and made of stainless steel (fig. 8.5 - B). The lower end of the sample holder is made of a stainless steel bulk material containing the cooling pipe flow channel. The bulk itself is connected to the chamber feedthrough via two hollow pipes which are part of the cooling system. The whole sample holder can be translated in $\hat{z}$ direction by a mechanical adjustment system within a 0.5 mm discrepancy[1].
The samples themselves are mounted on a seperate specimen carrier shown in fig. A.III - A

[1] On the first look this discrepancy seems to be non-marginal. However, the combination of a several mm wide beam spot diameter with the possibility to adjust the beam in shape, as well as in $\hat{x}$ and $\hat{y}$ direction, this 0.5 mm discrepancy can be easily countered.

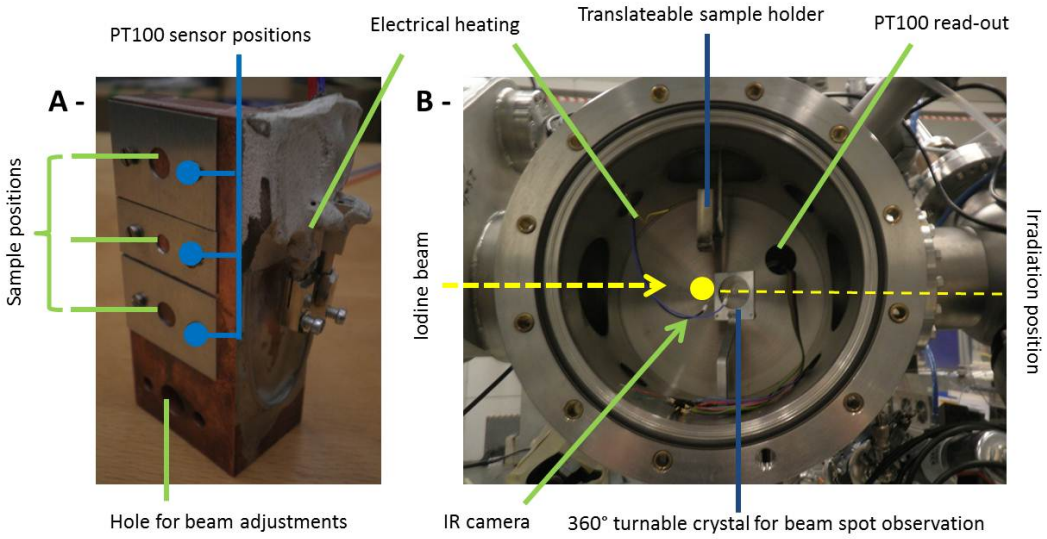

Figure A.III.: *(A-) New sample holder design with a closeup image of the specimen carrier. Here, it is possible to move the whole sample holder in $\hat{z}$ direction which allows mounting of three samples at the same time. Heating of the specimen carrier can be realised by beam power and also by an electrical heating wire. Cooling is achieved by a flow pass through the backside of the specimen carrier. Both electrical heating and cooling flow can be regulated by PLC controlling. In both cases temperature is measured with a PT100 sensor positioned between the Al sheet and the sample. Shown in (B-) is the irradiation chamber overview indicating beam direction and relevant positions for irradiation monitoring and control.*

which is made of pure Cu and can be screwed on the stainless steel bulk material at the end of the sample holder. Three samples can be mounted at the same time. Together with the sample holder translation capability in $\hat{z}$ direction, all three samples can successively be irradiated. The bottom position on the carrier consists of a hole of 8mm in diameter. This is foreseen for necessary beam adjustments before and during the beam time. Together with a quartz crystal, which is mounted on a steel pipe right behind the irradiation position and which can be rotated into and out of the beam trajectory, the beam shape can as well be observed (see fig. 8.5 - B).
Heating of the samples is on the one hand achieved by the beam itself and on the other hand by an electrical heating wire attached to the Cu sample carrier. Through this wire, a heating power between 1 and 20 W can be realized. Both heating and cooling can be regulated by a programmable logic controller (PLC). Together, the electrical heating, the heating by the beam itself and the cooling enable a long term stable irradiation temperature over more than 40 hours within just a slight deviation of $\pm$ 1°C. Sample temperature itself is measured by a PT100 sensor which is directly placed between the Al sheet (for sample fixing on the carrier) and the sample carrier. Only 1 mm of space exists between the sensor and the irradiated zone. Taking into account a several hours lasting irradiation of a sample, the measured temperature is representative for the irradiated areas, even though peak temperature values in the center of the irradiated zones are not

measureable.
For heat dissipation from the sample carrier under high vacuum conditions, two major mechanisms have to be mentioned: the thermal radiation effect and the thermal conductivity via the Cu-steel interface.

- For thermal radiation, Stefan-Boltzmann's law has to be considered:

$$\dot{Q} \;=\; \epsilon\, \sigma\, A\, T^4 \tag{C.1}$$

  Here, $\dot{Q}$ represents emission power, ϵ denotes the emissivitiy of the material (0.03 for non-oxidized Cu [144]), σ is the Boltzmann factor of $5.67 \cdot 10^{-8} \frac{W}{m^2 \cdot K^4}$, A is the total radiating surface ($\approx 20 cm^2$) and T the temperature in Kelvin. As the irradiation temperature was kept between 100 and 200°C (= 373 and 473 K), thermal radiation effects are in the mW range.

- This value is by far outbalanced by thermal conductivity between the two materials. Reminding the formula for thermal conductivity gives:

$$\dot{Q} \;=\; A\, \lambda\, \Delta T\, l^{-1} \tag{C.2}$$

  In this equation, A is the total Cu-steel interface area (6 cm^2), l the thickness of the Cu sample carrier (0.8 cm)[2], λ the materials' specific thermal conductivity values (240 - 400 $\frac{W}{m \cdot K}$ for Cu and 15 $\frac{W}{m \cdot K}$ on average for stainless steel [163]), and ΔT the temperature difference between the carrier and the steel bulk[3]. Assuming the steel bulk material is constantly kept at room temperature (e.g. by pressurized air cooling), ΔT is between 80 and 180 K. Calculating $\dot{Q}$ with these values gives a result in the range of W.

- Comparing the resulting value for both thermal radiation and thermal conductivity, the ratio $\frac{\dot{Q}_{conductivity}}{\dot{Q}_{radiation}}$ is in the range of $1000 : 1$. Concluding, the heat dissipation by conductivity clearly dominates in this temperature range.

Every 20 minutes, the setup-integrated PLC controlling software automatically moved the Faraday cup before the experiment into the beam to measure the beam current for 10 seconds. Afterwards, the cup was also automatically moved out of the beam and the acquired beam current was recorded in a data sheet. By integrating the current values, the total fluence on the sample could be calculated when considering the beam transmission ratio through the target surface which was calculated in the very first step of beam adjustment.

[2] Of course, the carrier is no perfect cuboid. Nevertheless, when measuring the carrier, this is an average value. Furthermore, deviations of this value are as well in the 0.1 cm range resulting only in a marginal change in the total value for $\dot{Q}$.

[3] For completeness, the thermal conductivity of non-irradiated U-8wt%Mo is ≈ 10 $\frac{W}{m \cdot K}$ [24]

Likewise, the irradiation temperature measured by the PT100 sensor was as well automatically recorded. The advantage of this later measurement was that it did not interfere with the beam. Therefore, the temperature was instantly recorded and PLC could make necessary adjustments to the cooling flow and the electrical heating of the sample carrier without delay.

D. TEM diffraction pattern evaluation

Goal is to attain a lattice parameter of an unknown phase (e.g. from an amorphous structure). The following explanations were applied for acquisition of the amorphous IDL nearest neighbour value given in chapter 9.2. Step-by-step approach:

1. Consider a TEM reference pattern taken under the same conditions (acceleration voltage, camera length etc...). The most appropriate way is to do so during the same data acquisition run. In this case an Al region was taken, as its lattice structure and lattice parameter are well known from literature (see fig. A.IV - A and - B):

Space group: F 4/m 3 -2/m	Cubic structure:	(h k l)	d_{khl}[Å]
a = 4.0495 Å	$\alpha = 90°$	(1 1 1)	2.3380
b = 4.0495 Å	$\beta = 90°$	(2 0 0) ≡ (0 2 0) ≡ (0 0 2)	2.0247
c = 4.0495 Å	$\gamma = 90°$	(2 2 0) ≡ (0 2 2) ≡ (2 0 2)	1.4317
		(3 1 1) ≡ (1 3 1) ≡ (1 1 3)	1.2210

Table A.IV.: *Parameters of the Al. As a cubic structure lattice parameters a,b,c and several (hkl) directions are identical.*

2. Obtain the radii in each diffraction ring. If the pattern is already in the center of the image, it's straightforward. Otherwise, use the graphic tools provided by the dm3 program to do so. Please note the scale in the pattern image. The measured distance will give a value in pixel.

3. The formula for evaluation is:

$$L\,\lambda \;=\; d_{hkl}\,R_x \;=\; const. \tag{D.1}$$

L represents the camera length, λ the electron wavelength, R_x the radius measured in pattern. The value L λ should be constant, just like $d_{hkl}R_x$. By measuring the distance in the pattern, you will get a unit "pixel ·Å". While the former gives a unit of m^2, the later one is the same unit when you take into account the image scale. Calculate the average value $d_{hkl} \cdot R_x$. As this value is constant as long as the camera parameters don't change, this average value can further be used to analyse the unknown phase pattern.

4. In our example for Al:

(h k l)	(1 1 1)	(0 0 2)	(0 2 2)	(1 1 3)
$d_{hkl} \cdot R_x$ [Å· pixel]	689.24	677.46	687.22	708.18

Table A.IV.: *Calculated values for the Al pattern shown in fig. A.IV - A and - B.*

Therefore, the average value is 690.5 Å·pixel.

5. Consider now the amorphous phase in fig. A.IV - C. As the diffraction ring is rather broad, two individual distance are measured, labelled R_{min} = 263.9 pixel and R_{max} = 297.2 pixel. This in turn gives d_{hkl} values of 2.67 Å and 2.32 Å. Therefore, the according d_{hkl} value of the amorphous phase lies in between these two values.

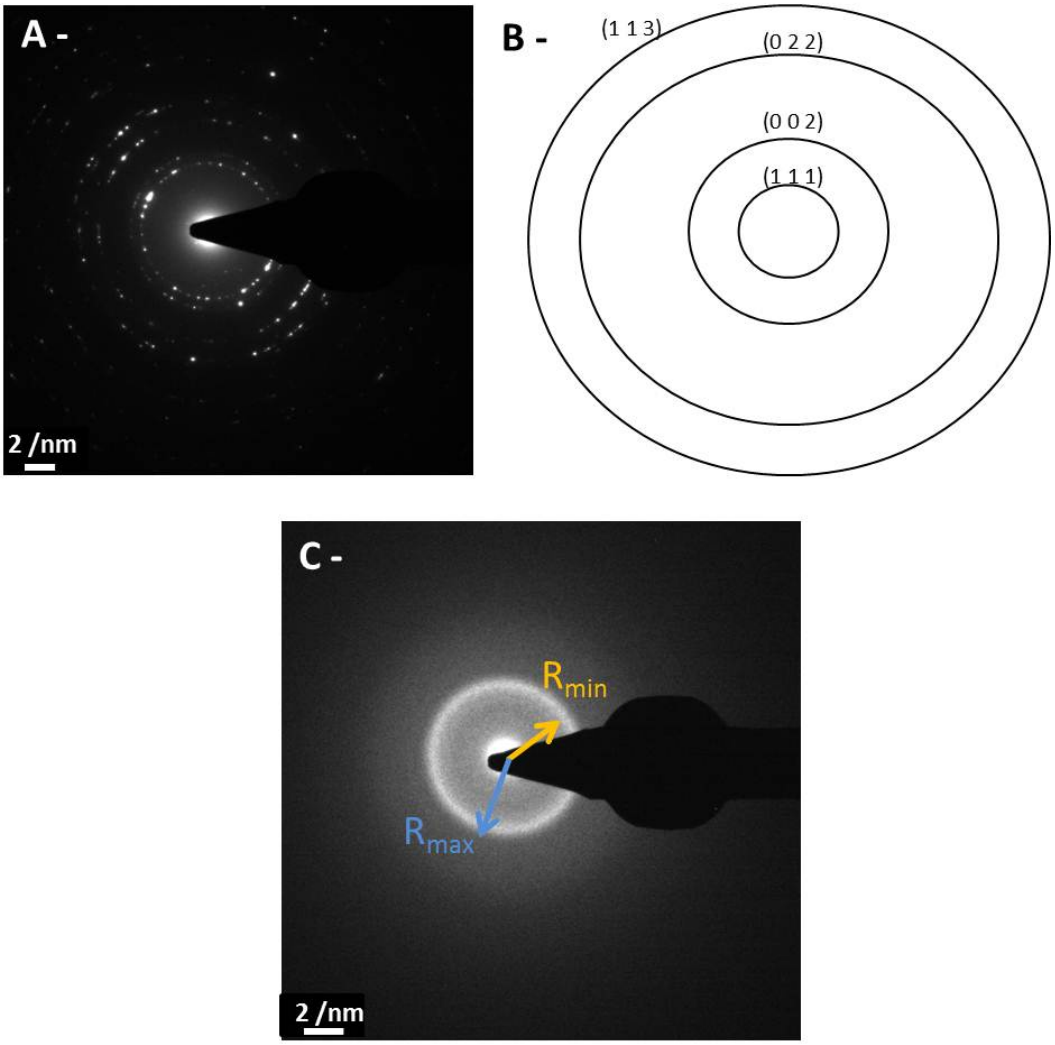

Figure A.IV.: *(A-) TEM diffraction pattern of the Al region obtained in a thin foil prepared by FIB. (B-) According diffraction pattern from literature indicating the (h k l) values' diffraction rings [151]. (C-) TEM diffraction pattern of the amorphous IDL. Two distances of the broad amorphous ring were taken into account for calculation of nearest neighbour distance.*

E. XRD diffraction pattern analysis

Fit2D

First, the obtained 2D diffraction pattern has to be converted into a 1D pattern showing the 2Θ and intensity values. This can be done smoothly via Fit2D.

1. When starting the program the first screen will ask you about the x- and y-dimensions. These values are in pixel and give the program the size of the diffraction pattern. Normally, the default values of 2048 should work well. Ignore the other two options on this screen and say OK.

2. Choose now the "Powder Diffraction" option and use the Input command to load a diffraction pattern into the program.

3. Click OK on the first screen appearing. Then, you are asked to provide dark field, bright field images and a spatial distortion file. Both dark field and bright field images should be acquired during the XRD experiment. Be sure that all three images (diffraction, bright, dark) have the same counting time. The spatial distortion file should be provided by the beamline. Finally, you will see the 2D diffraction image in the Fit2D program. By using the z-Scale option you can change the contrast of the image to more clearly see the diffraction rings. Either attune the image manually or automatically if necessary.

4. Next, say "Integrate" and you will be asked about 8 parameters that were of importance during the measurement. Normally, the beamline can provide the data via a pre-experimental calibration session with a standard sample (e.g. Li_6B crystals or pure Si). On the second screen just say OK.

5. You should now see a 1D diffraction pattern. You can further incease the intensity by the option "Image Processing" → Math. Both are accessible in the main interface of the program.

6. When you are satisfied with the quality of the pattern say "Output" → "Chiplot". You can now save the pattern.

7. In the Windows Explorer rename the .chi-file into a .dat-file. Next, open the .dat-file in a WordPad editor. There, the first line should be changed so that it says "XYdata". Lines 2 and 3 are not important. However, the fourth line should be the starting point for data values.

FullProf data analysis

When the abovementioned steps have been performed, the pattern can now be evaluated in the WinPlotr/FullProf Rietveld data analysis program. Two possibilites exist to do so. On the one hand, the program interface itself provides many input arrays to analyse the pattern. However, no full control over all parameters is possible in this program. Hence, a second method is to manipulate the .pcr-file with a common WordEditor. For both methods, it is strongly suggested to rename the resulting Rietveld output data (labelled .new) and give them comprehensive new file names showing the refinement evolution. These .new-files have to be manually renamed .pcr. On the first look, this might look inconvenient. However, there is no risk of running into a "dead end" where the parameters are far off scale and cannot be refined properly. In any case, Rietveld analysis should follow this scheme:

1. Define excluded regions. This cuts off parts of the 1D diffraction pattern and should exclude beam stop regions and high angle regions. Standard excluded regions in this thesis were 0 to 2.0 and 14 to 180° on the 2Θ axis.

2. Define the first background point. After cutting down the 1D pattern, the first background point (in the low 2Θ regime naturally) is to be defined in the program. This ensures that the following phase analysis is performed with the right intensity values. Do not refine the background at this step.

3. Define all parameters for all phases you want to analyse in the pattern. This includes lattice parameters, lattice structure, spatial structure and so on. Consider literature values whenever possible before doing refinements.

4. Continue with analysis of the most prominent phase. You should have a general idea about the phases inside your sample. For first refinements, only run 1 iteration cycle as divergences are very likely. Every phase analysis is performed in this basic manner:

    - Adjust the scale parameter which stands for the intensity. A value of 1.0e-9 means the program consideres the phase to be not present at all. This might cause problems if this phase has a definitive impact on the pattern.

- Adjust lattice parameters. Please note that, depending on the lattice structure, the three parameters a,b,c might be correlated to each other. For example, in a bcc structure all three parameters are identical and have to be refined at the same time. Try to adjust the calculated peak to the measured one.

- Adjust the shape parameter between 0.1 and 1.0. This tells the program whether the measured peak/phase has a Lorentzian or a Gaussian shape.

- Change u,v,w parameters. FullProf applies a polynomal function over the whole 1D pattern with recalculating u,v,w parameters for each phase individually. u has an impact on the low angle region, v on intermediate values and w on high angle values. Always start with u parameter and observe its impact on the low angle regions.

- You cannot obtain an acceptable analysis of one single phase until all other phases are in rough agreement between measured and calculated shapes. Therefore, when you cannot make progress on the most prominent phase any longer continue with the next one.

- In the word Editor below any parameter value is an additional line saying either 0.0 or 1.0. This tells the pcr file whether the program should refine this parameter (1.0) or not (0.0).

5. When all phases are in good agreement (position and shape) refine the background. This naturally will force you to make further refinements on the phases. As a very last step, manually give the program background points that fit very well and do not refine the background.

6. When all this has been performed and the final pattern shows a good agreement, you can read out the weight% contribution of every phase to the pattern. These values can be found in the .out-file.

F. Sample polishing

Very recently, a Bachelor thesis was carried out at the FRM II whose topic was to specify the optimum grinding and polishing parameters for U-Mo [166]. However, in this thesis the following procedure depicted in tab.A.VI was utilized and is no longer up-to-date:

Preparation step	Grinding/Polishing paper + suspension	Rotations per minute	Force	Time
Grinding	SiC 220 + Water	300	20	30 sec.
Polishing	MD Allegro + DiaPro Allegro/Largo 9μm	200	20	5 min.
Polishing	MD Dac + DiaPro Allegro/Largo 3μm	200	20	5 min.
Polishing	MD Nap + DiaPro Allegro/Largo 1μm	200	20	5 min.

Table A.VI.: *Utilized sample grinding and polishing recipe for successive SEM analyses.*

Publication list

Enlisted below are all journal and conference contributions which have been realised during this thesis.

Journal Papers

- T. Zweifel, Ch. Valot, Y. Pontillon, J. Lamontagne, A. Vermersch, L. Barallier, T. Blay, W. Petry, H. Palancher: *Annealing tests of in-pile irradiated oxide coated U-Mo/Al-Si dispersed nuclear fuel*, Journal of Nuclear Materials Vol. 452 (2014), 533-547.

- T. Zweifel, H. Palancher, A. Leenaers, A. Bonnin, V. Honkimaki, R. Tucoulou, S. van den Berghe, R. Jungwirth, F. Charollais, W. Petry: *Crystallographic study of Si and ZrN coated U-Mo atomised particles and their interaction with Al under thermal annealing*, Journal of Nuclear Materials Vol. 442 (2013), 124-132.

- H. Palancher, A. Bonnin, V. Honkimaki, H. Suhonen, P. Cloetens, T. Zweifel, R. Tucoulou, A. Rack, M. Voltolini, *Coating thickness determination in highly absorbent core-shell systems*, Journal of Applied Crystallography Vol. 45 (2012), 906-913.

- H. Palancher, A. Bonnin, V. Honkimaki, T. Buslaps, M. Grasse, B. Stepnik, T. Zweifel: *Quantitative crystallographic analysis of as-fabricated full size U-Mo/Al(Si) nuclear fuel plates*, Journal of Alloys and Compounds Vol. 527(2012), 53-65.

- H.-Y. Chiang, T. Zweifel, H. Palancher, A. Bonnin, L. Beck, P. Weiser, M. Döblinger, C. Sabathier, R. Jungwirth, W. Petry: *Evidence of amorphous interdiffusion layer in heavy ion irradiated U-8wt%Mo/Al interfaces*, Journal of Nuclear Materials Vol. 440 (2013), 117-123.

- R. Jungwirth, T. Zweifel, H.-Y. Chiang, W. Petry, S. Van den Berghe, A. Leenaers: *Heavy ion irradiation of UMo/Al samples PVD coated with Si and ZrN layers*, Journal of Nuclear Materials Vol. 434 (2013), 296-302.

Conference Proceedings

- T. Zweifel, H. Palancher, R. Jungwirth, A. Bonnin, W. Petry, M.C. Anselmet, F. Charollais, P. Lemoine, L. Beck: *Heavy ion irradiation on U-Mo/Al systems: Temperature influence*, 15th International Topical Meeting on Research Reactor Fuel Management (RRFM), Rome, Italy, 2011.

- T. Zweifel, H. Palancher, A. Bonnin, F. Charollais, A. Leenaers, S. van den Berghe, R. Jungwirth, W. Petry, P. Lemoine: *Study of Si and ZrN coated U-Mo atomised particles using high energy XRD*, 16th International Topical Meeting on Research Reactor Fuel Management (RRFM), Prague, Czech Republic, 2012.

- T. Zweifel, H.-Y. Chiang, R. Jungwirth, W. Petry, H. Palancher, C. Sabathier, M.C. Anselmet, A. Bonnin, L. Beck, P. Weiser, M. Döblinger, P. Lemoine: *Evidence of amorphous interdiffusion layer in heavy ion irradiated u-8wt%Mo/Al interfaces*, 17th International Topical Meeting on Research Reactor Fuel Management (RRFM), St. Petersburg, Russia, 2013.

- T. Zweifel, H. Palancher, Ch. Valot, Y. Pontillon, J. Lamontagne, T. Blay, W. Petry: *In-pile irradiated U-Mo/Al(Si) dispersed nuclear fuel behaviour under thermal annealing: Fission gas release and microstructure evolutions*, 18th International Topical Meeting on Research Reactor Fuel Management (RRFM), Ljubljana, Slovenia, 2014.

- S. Säubert, T. Zweifel, R. Jungwirth, M. Hölzel, M. Hofmann, W. Petry: *Isothermal transformation kinetics in Uranium Molybdnum alloys*, 18th International Topical Meeting on Research Reactor Fuel Management (RRFM), Ljubljana, Slovenia, 2014.

- C. Reiter, H. Breitkreutz, T.K. Huber, T. Zweifel, W. Petry: *Influence of thermal annealing on the specific heat capacity of different dispersion U-(7-8)wt%Mo fuels*, 18th International Topical Meeting on Research Reactor Fuel Management (RRFM), Ljubljana, Slovenia, 2014.

- R. Jungwirth, T. Zweifel, H.-Y. Chiang, W. Petry, S. van den Berghe, A. Leenaers: *Heavy ion irradiation of U-Mo/Al samples with protective Si and ZrN layers (SELENIUM)*, 30th International Topical Meeting on Reduced Enrichment for Research and Test Reactors (RERTR), Santiago de Chile, Chile, 2011.

- H.-Y. Chiang, R. Jungwirth, T. Zweifel, W. Schmid, W. Petry, F. Kraus: *Interactions between U-Mo/Al fuel and diffusion barriers (Nb and TiN) under heavy ion irradiation*, 30th International Topical Meeting on Reduced Enrichment for Research and Test Reactors (RERTR), Santiago de Chile, Chile, 2011.

- R. Jungwirth, T. Zweifel, H.-Y. Chiang, W. Petry, F. Charollais, P. Lemoine, Y. Calzavara, H. Guyon, S. van den Berghe, A. Leenaers, E. Koonen, B. Stepnik, C. Jarousse: *Ion irradiation of U-Mo/Al fuel samples with 7wt% and 12wt% Si inside the matrix (E-FUTURE II)*, 16th International Topical Meeting on Research Reactor Fuel Management (RRFM), Prague, Czech Republic, 2012.

- Y.J. Jeong, J.M. Park, H.J. Ryu, Y.S. Lee, W.J. Kim, R. Jungwirth, H.-Y. Chiang, T. Zweifel, W. Petry: *Heavy ion irradiation of nitride and silicon coated U-Mo/Al and U-Mo-Ti/Al fuel*, 17th International Topical Meeting on Research Reactor Fuel Management (RRFM), St. Petersburg, Russia, 2013.

Acknowledgement

Without the support and help of a lot of people this work could not have been accomplished:

- Prof. Dr. Winfried Petry who enabled this interesting work. Without your backup and continous support a lot of "barriers" would have persisted. Despite your challenging time schedule you always took your time to discuss.

- Dr. Herve Palancher. Not only during my two stays at Cadarache you were always available when I faced a problem. I enjoyed our scientific discussions, especially with regard to the task of XRD refinement and thermal treatment experiments. I wish you all the best.

- Dr. Ludwig Beck, Walter Carli, Wolfgang Hagn, Horst Müller and the whole staff of the MLL Tandem accelerator. Successful beamtimes would not have been accomplished without your exhaustive help. You always were there to offer a helping hand when re-constructing the irradiation setup and did not hesitate to work hard during the weekend.

- The same gratitude is expressed towards Dr. Yves Pontillon, Dr. Christophe Valot, Guillaume Volle and Thierry Blay during the thermal treatment and EPMA experiments.

- My former and present colleagues both at the FRM-II and at CEA: Dr. Harald Breitkreutz, Dr. Wolfgang Schmid, Dr. Rainer Jungwirth, Dr. Rainer Grossmann, Dr. Anton Röhrmoser, Bruno Baumeister, Hsin-Yin Chiang, Alexandra Egle, Tobias Hollmer, Tanja Huber, Christian Reiter, Steffen Säubert, Robert Schenk, and our "army" of bachelor and working students on FRM II side, as well as Dr. Catherine Sabathier, Kiet Hoang, Dario Pieck, Elisabetta Pizzi, Axel Richard, Richard Skorek, Emerson Vathonne, and the whole rest of the LLCC team at CEA.

- Florian Kortmann and Dr. Christoph Lierse of the Radiochemie München for using the SEM/EDX apertures.

- Dr. Clara Grygiel from the GANIL IRRSUD beamline is thanked for fruitful discussions concerning implantation beamtime and help during the actual experiment.

- Dr. Nathalie Valle from CRP-GL for performing the SIMS measurements.

- Peter Weiser from WSI made possible FIB preparation experiments and always found time to fix occurring problems.

- Dr. Markus Döblinger from LMU is appreciated for using TEM analysis methods.

- Thanks also to Alex Egle, Tanja Huber and Christian Reiter for the enjoyable and funny late-evening discussions.

- Kiet Hoang for giving me “shelter” for two weeks at the end of my first stay in Cadarache.